

Molecular engineering of functional materials for optoelectronic applications

Présentée le 5 février 2020

à la Faculté des sciences de base
Groupe SCI SB MN
Programme doctoral en chimie et génie chimique

pour l'obtention du grade de Docteur ès Sciences

par

Nikita DRIGO

Acceptée sur proposition du jury

Prof. U. A. Hagfeldt, président du jury
Prof. M. K. Nazeeruddin, directeur de thèse
Prof. M. Kivala, rapporteur
Dr G. Pozzi, rapporteur
Prof. R. Buonsanti, rapporteuse

ACKNOWLEDGMENTS

First of all I acknowledge my thesis director Prof. Mohammad Khaja Nazeeruddin who had been interested to consider and to accept my application when I applied to EPFL for a PhD position as a graduating master student. It was a great opportunity for me to do my studies in his research group and to face an exciting multidisciplinary research area of optoelectronics and renewable energy technologies. I'm very grateful for challenging my professional skills that made me to grow up as a specialist and as a person and to be very motivated for constant self-development. I really appreciate the research freedom Prof. Nazeeruddin gave to me, so I could bring to life and to develop my own ideas, to make mistakes, to think and to correct them, to bear responsibilities for the decisions taken and to learn a lot. This work would not be possible without his constant encouragement, advices and support.

I also acknowledge all jury members: Prof. Buonsanti, Prof. Hagfeldt, Prof. Kivala and Dr. Pozzi for having dedicated their precious time to read, to give feedback and to evaluate my thesis.

I would like to thank all GMF group members and many visitors I ever had a unique chance to meet, to work with, to have very interesting inspiring discussions and activities out of the laboratory. It is very difficult to mention all present and past group members whom I'd like to acknowledge, but I'm particularly grateful to Dr. Sadig Aghazada and Dr. Kasparas Rakstys for fruitful discussions and many useful advices they gave to me when I was starting my PhD studies. I thank Dr. Paek Sanghyun and Albertus Adrian Sutanto for putting much efforts to make the organic materials I synthesized work in perovskite solar cells. I'm very grateful to our big heartfelt Spanish community: Dr. Cristina Roldàn Carmona, Dr. Maria Cristina Momblona Rincon and Dr. Ines Garcia Benito, for fruitful collaborations, lessons of Spanish and so much joy we had when working and not working together! I deeply acknowledge Prof. Giulia Grancini I've been actively collaborating with only for the very last half-year of my PhD studies. I really appreciate those intense scientific discussions, brainstorming, writing the paper

together and of course your personal support. I learned a lot from you – grazie mille Giulia! I'm very grateful to Valentin who helped me to translate the abstract to French language! Thank you Hobeom, Cansu, Alex, Hiroyuki, Mousa, Aron, Nadja and many-many-many others from GMF for the warmest atmosphere it was a pleasure to work in! I want to thank my cinque-amico-ciciliano Valentino! You brought so much positive energy and prochnost to our group that helped me to wrap up my thesis within two months!

I want to express my exceptional gratitude to all my collaborators from different laboratories and institutions. This work would not exist without any of you! I'm particularly grateful to members from LCMD EPFL lead by Prof. Clémence Corminboeuf: Lin Kun-Han and Dr. Antonio Prlj. Thank you so much for complex exhaustive computations you made! I also thank my collaborators from EP6 University of Würzburg: Liudmila G. Kudriashova, Sebastian Weissenseel, Dr. Andreas Sperlich and Prof. Vladimir Dyakonov, you literally made molecules shine beautiful deep-blue light! Dear Ludmila, thank you very much for unforgettable (non)scientific discussions, walks in Würzburg and amazing book recommendations! I acknowledge our collaborators from FTMC in Lithuania: Dr. Marius Franckevičius, Rokas Gegevičius and Prof. Vidmantas Gulbinas for the profound optical characterization of materials and devices. I acknowledge collaborators from EPFL: Dr. Pascal Schouwink, Dr. Natalia Gassilova and Dr. Mounir Mensi.

I want to express my exceptional gratitude to the best secretary in the world – Géraldine Gfeller. Merci beaucoup à toi Géraldine pour tous ce que tu as fait pour notre groupe ! Merci de nous aider à résoudre nos problèmes administratifs, pour tous les colis que tu as envoyés, pour tous les évènements, les randonnées, les dînes et dégustations que tu as organisés ! Enfin, ma gratitude particulière concerne les encouragements et motivation à apprendre le français !

Furthermore I'm very grateful to all staff of EPFL Valais for making everything to work as harmoniously and as precisely as Swiss watches do! Our work would not be that efficient and pleasing without any of you!

Finally I'd like to thank all my family and many friends who always encouraged and supported me in all difficult life situations. Thank my dear faithful friends for the

precious time I've spent together with you. My special acknowledgment is for Anton, the very best friend of mine who always gave me a lot of positive energy to pass through all challenges of PhD studies. Dear Daniel, Andrzej, Lennart thank you for beers, hikes, barbeques and very interesting discussions we had together!

Так же я хочу поблагодарить Дашу, которая так и не испекла блины, Вженю, пропавшую в Цюрихе, Митю и Диму, Наташу, Макса. Особые слова благодарности моим учителям и преподавателям из МГУ: Вацуро Ивану Михайловичу, Сане, Никитиной Вике, Ливанцовой Людмиле Ивановне, Жиряковой Марине Владимировне, Ольге Витальевне – за тот прочный фундамент знаний и навыков, который мне позволил успешно завершить аспирантуру в одном из лучших университетов Европы.

Спасибо Вам, дорогие Мама и Папа, за то, что дали мне много возможностей и своды выбирать свое будущее! Спасибо всей моей большой семье за все добрые слова, поддержку, сопереживание и мудрые советы, когда они были особенно нужны на нелегком пути аспирантуры! Я вас всех очень люблю!

Thank you all!

Nikita Drigo

Sion, November 2019

ABSTRACT

Organic functional materials are indispensable components for the last generation of light-energy conversion devices. Photo- and electroactive small organic molecules constitute thin active (emitting, transporting, blocking, injecting etc.) layers of organic optoelectronics and often play a decisive role for efficiency of an operating device. Since desired optoelectronic and morphological properties of organic materials can be finely tuned at the molecular level, the relationships between molecular structure, physicochemical properties and, ultimately, performance of the corresponding bulk material in an operating device are subject of extensive research nowadays. Moreover, developing understanding of device operation and physics imposes newer stricter and more challenging requirements for organic functional materials urging the search for new molecular architectures with advanced properties.

Thus, the work presented in this thesis is focused on synthesis, profound characterization and use of new organic functional materials for light-energy conversion devices. I aim eventually to find out the synthetic guidelines for judicious molecular design of organic low-molecular-weight materials with advanced properties for use in optoelectronic devices.

In this work, I introduce rigid bulky symmetric 10H,10'H-9,9'-spirobi[acridine] (SBA) as a universal molecular platform to construct emitting dopants and HTMs for the last generation optoelectronics: thermally-activated delayed fluorescence light-emitting diodes (TADF OLEDs) and perovskite solar cells (PSCs) respectively. The compact **SBABz₄** TADF emitter exhibited pure blue emission via TADF channel and a significant hypsochromic shift as opposed to simpler **DMABz₄** with commonly used "monomeric" donor without the spiro-node. Moreover, stick-like elongated **SBABz₄** demonstrated increased light-outcoupling efficiency.

As the next part of our work, I utilized SBA molecular platform to construct 4 novel HTMs that mimic simultaneously two benchmark materials: 2,2',7,7',-tetrakis-(N,N-dimethoxyphenyl-amine)-9,9'-spirobifluorine (spiro-MeOTAD) and poly(triaryl

amine) (PTAA) monomer fragment. The new HTMs performed on par with spiro-MeOTAD reference, but the corresponding devices demonstrated no current density-voltage (J - V) hysteresis and excellent durability, strongly outperforming the etalon molecule.

Finally, driven by our curiosity to new molecular scaffolds, I explored chemistry and optoelectronic properties of electron excessive polyaromatic heterocycle – ullazine. I performed synthetic optimization and elaborated a straightforward high-yielding protocol towards 3,9-disubstituted ullazine scaffold and a reactive monobromoullazine. Moreover, I developed synthetic approaches towards all possible ullazine monocarbaldehydes and studied the relationships between regioisomerism and photo-/electronic properties of the corresponding conjugates with malonate acceptor. One of the donor-acceptor (D-A) conjugates displayed a suitable energy level and was tested as a small-molecule dopant-free HTM for PSCs without conventional arylamine substituents.

Keywords

Photovoltaic, perovskite solar cells, organic light-emitting diode, organic electronics, hole transport material, thermally activated delayed fluorescence, emitter, cyclisation, polyaromatic heterocycle, organic synthesis.

RÉSUMÉ

Les matériaux organiques fonctionnels sont des composants indispensables pour la dernière génération d'appareils de conversion de la lumière en énergie. Les petites molécules organiques photo- et électroactives constituent de minces couches actives (émission, transport, blocage, injection, etc.) d'appareil optoélectronique organique et jouent souvent un rôle décisif pour l'efficacité d'un appareil en fonctionnement. Les propriétés optoélectroniques et morphologiques souhaitées des matériaux organiques pouvant être affinées au niveau moléculaire, les relations entre la structure moléculaire, les propriétés physico-chimiques et, en fin de compte, la performance globale du matériau dans un appareil en fonction fait, de nos jours, l'objet de recherches approfondies. De plus, le développement de la compréhension du fonctionnement et de la physique des appareils impose de nouvelles exigences plus strictes pour les matériaux fonctionnels organiques, ce qui incite à rechercher de nouvelles architectures moléculaires aux propriétés innovantes.

Ainsi, les travaux présentés dans cette thèse sont axés sur la synthèse, la caractérisation profonde et l'utilisation de nouveaux matériaux organiques fonctionnels pour les dispositifs de conversion de lumière en énergie. Notre objectif à terme est de trouver les lignes directrices synthétiques pour la conception moléculaire judicieuse de matériaux organiques de faible poids moléculaire ayant des propriétés avancées pour l'utilisation dans des appareils optoélectroniques.

Dans ce travail, nous introduisons la 10H,10'H-9,9'-spirobi[acridine] (SBA) comme plate-forme moléculaire universelle pour construire des dopants émetteurs et des matériaux de transport de trous (HTM) pour la dernière génération d'appareil optoélectronique : les diodes électroluminescentes à fluorescence retardée (TADF OLEDs) et les cellules solaires perovskite (PSCs). L'émetteur compact SBABz₄ TADF présentait une émission bleue pure via le canal TADF et un décalage hypsochromique significatif par opposition à un plus simple DMABz₄ avec un donneur "monomère"

couramment utilisé sans noeud spiro. De plus, le SBABz₄ allongé en forme de bâton a démontré une efficacité accrue de couplage de la lumière.

Dans la partie suivante de notre travail, nous avons utilisé la plateforme moléculaire SBA pour construire 4 nouveaux HTMs qui imitent simultanément deux matériaux de référence : 2,2',7,7',-tetrakis-(N,N-diméthoxyphényl-amine)-9,9'-spirobifluorine (spiro-MeOTAD) et fragment monomère poly(triarylamine) (PTAA). Les nouveaux HTM ont fonctionné au même niveau que la référence spiro-MeOTAD, mais sans aucune hystérèse de tension-densité de courant (*J-V*) et une excellente durabilité, surpassant largement les performances de la molécule d'étalon.

Enfin, poussés par notre curiosité pour de nouvelles structures moléculaires, nous avons exploré la chimie et les propriétés optoélectroniques de l'hétérocycle polyaromatique à excès d'électrons - ullazine. Nous avons effectué une optimisation synthétique et élaboré un protocole simple à haut rendement vers une structure ullazine 3,9-disubstitué et une monobromoullazine réactive. De plus, nous avons développé des approches synthétiques de tous les monocarbaldéhydes ullazines possibles et étudié les relations entre le régio-isomérisme et les propriétés photo-/électroniques des conjugués correspondants avec accepteur malonate. L'un des conjugués donneur-accepteur (D-A) présentait un niveau d'énergie approprié et a été testé comme HTM sans dopant pour les PSC sans substituants classiques arylamine.

Mots clés

Photovoltaïque, cellules solaires en pérovskites, diode électroluminescente organique, électronique organique, matériau de transport de trous, fluorescence retardée activée thermiquement, émetteur, cyclisation, hétérocycle polyaromatique, synthèse organique.

SYMBOLS AND ABBREVIATIONS

A	acceptor
abs	absorption
acac	acetylacetonate
Ac	acetyl
Ad	adamantyl
APCI	atmospheric pressure chemical ionization
Boc	<i>tert</i> -butyloxycarbonyl
br	broad
Bu	butyl
CB	conduction band
CIE	Commission internationale de l'éclairage
CT	charge transfer
CV	cyclic voltammetry
D	donor
d	doublet (NMR multiplicity)
DBA	dibenzylideneacetone
DCE	1,2-dichloroethane
DCM	dichloromethane
DG	directing group
DMA or DMAC	9,9-dimethyl-9,10-dihydroacridine
DMAP	4-dimethylaminopyridine
DMF	dimethylformamide
DMF	dimethylformamide
DMPA	dimethoxydiphenyl amine
DMTHF	2,5-dimethoxytetrahydrofuran
DPAC	9,9-diphenyl-9,10-dihydroacridine
DPEPO	bis[2-(diphenylphosphino)phenyl] ether oxide
DSC	differential scanning calorimetry
DSSC	dye-sensitized solar cell
EIL	electron-injection layer
EL	electroluminescence
Em	emission
EML	emissive layer
EQE	external quantum efficiency
ESI	electrospray ionization
Et	ethyl
ETL	electron-transporting layer
ETM	electron-transporting material
FF	fill factor
FMO	frontier molecular orbital
FOLED	fluorescent organic light emitting diode

FTO	fluorine-doped tin oxide
Hex	hexyl
HIL	hole-injection layer
HOMO	highest occupied molecular orbital
HPV	hybrid photovoltaic
HTL	hole-transporting layer
HTM	hole-transporting material
IC	internal conversion
ICT	intramolecular charge transfer
IEA	International Energy Agency
IP	ionization potential
<i>i</i> Pr	<i>iso</i> -propyl
IQE	internal quantum efficiency
IR	infrared
ISC	intersystem crossing
ITO	indium-tin oxide
LE	locally excited
LUMO	lowest unoccupied molecular orbital
m	multiplet
MA	methylammonium
MALDI	matrix-assisted laser desorption/ionisation
mCP	1,3-bis(<i>N</i> -carbazolyl)benzene
MD	molecular dynamics
Me	methyl
Mes	mesityl
MPPT	maximum power point tracking
MS	mass spectrometry
<i>n</i> Bu	normal-butyl
NMR	nuclear magnetic resonance
NSI	nanospray ionization
OC	open circuit
oDCB	ortho-dichlorobenzene
OLED	organic light-emitting diode
Ox	oxidation
PCE	power conversion efficiency
Ph	phenyl
PHA	polycyclic heteroaromatic compound
PhOLED	phosphorescent organic light emitting diode
PL	photoluminescence
PLQY	photoluminescence quantum yield
PMMA	polymethyl methacrylate
PPA	polyphosphoric acid
ppy	2-phenylpyridine
PSC	perovskite solar cell
PTAA	polytriarylamine
PV	photovoltaic

Py	pyridyl
Red	reduction
RESP	restrained electrostatic potential
RH	relative humidity
rISC	reversed intersystem crossing
RT	room temperature
S	singlet (electronic state)
s	singlet (NMR multiplicity)
SBA	10H,10'H-9,9'-spirobi[acridine]
SC	short circuit
SCLC	space-charge limited current
secBu	secondary-butyl
SEM	scanning electron microscopy
SHE	standard hydrogen electrode
SHR	Shockley Read Hall
SOC	spin-orbit coupling
spiro-MeOTAD	2,2',7,7',-tetrakis-(N,N-dimethoxyphenyl-amine)-9,9'-spirobifluorine
ssDSSC	solid-state dye-sensitized solar cell
T	triplet (electronic state)
t	triplet (NMR multiplicity)
TADF	thermally activated delayed fluorescence
TBP	tert-butylpyridine
tBu	tert-butyl
TCO	transparent conductive oxide
TEEDA	N,N,N',N'-tetraethylethylenediamine
Tf	triflate, trifluoromethanesulfonate
TGA	thermogravimetric analysis
THF	tetrahydrofurane
TLC	thin-layer chromatography
TMS	trimethylsilyl
TOF	time of flight
TPA	triphenylamine
TPCD	transient photocurrent decay
TPE	tetraphenyl ethylene
tr	time-resolved
TSPO ₁	diphenyl[4-(triphenylsilyl)phenyl]phosphine oxide
UPS	ultraviolet photoemission spectroscopy
UV	ultraviolet
VB	valence band
VC	vibronic coupling
Xphos	2-dicyclohexylphosphino-2',4',6'-triisopropylbiphenyl
XRD	X-ray diffraction

TABLE OF CONTENTS

Acknowledgments	2
Abstract	5
Résumé	7
Symbols and abbreviations	9
Table of contents	12
Introduction	15
1.1. Light-energy conversion devices. Operation principles	17
1.2. Organic light-emitting diodes – brief overview.....	20
1.3. Principles of molecular design to modulate TADF properties of organic emitters.....	24
1.4. D and A units to construct TADF materials	27
1.5. Perovskite solar cells – brief overview.....	30
1.6. PSC architectures and materials.....	31
1.7. Molecular design of low-molecular-weight HTMs.....	34
1.8. Motivation and outline of the thesis	38
Spiroacridans as light emitters and hole transporters	41
2.1. Synthesis of spiro-fused arylamine compounds	42
2.2. TADF materials based on spiro-acridane compounds	47
2.2.1. Separation of FMOs via spiro-atom	47
2.2.2. Use of a spiro-pendant for construction of donor units	51
2.2.3. Fine tuning of the electronic and emission properties: HOMO level tuning and introduction of new excited states	52
2.2.4. Rigidification and stabilization of a donor conformation	55
2.2.5. Avoiding the concentration quenching	57
2.2.6. Tuning the proportion of horizontally oriented emitting dipoles	59
2.2.7. TADF materials based on spiro-bisacridane core	61
2.3. Hole transporting materials for PSCs	63
Photophysical properties of spirobisacridane-benzonitrile TADF emitters	67
3.1. Introduction	68
3.2. Results and discussion	69
3.3. Conclusion.....	78
Spirobisacridane hole transporting materials for perovskite solar cells	79

4.1. Introduction	80
4.2. Results and discussion	81
4.3. Conclusions	97
Approaches for selective synthesis of ullazine donor–Acceptor systems	99
5.1. Introduction	100
5.2. Results and discussion	101
5.3. Conclusion.....	108
Conclusions and future perspective	109
Appendix	115
6.1. Synthesis and Characterization of Organic Products – General Information	116
6.2. Appendix to chapter 3.....	117
6.2.1. Synthetic details	117
6.2.2. ¹ H- and ¹³ C- NMR spectra of the final compounds	120
6.2.3. Materials Preparation and Measurements Results	124
6.2.4. Quantum efficiencies of components in PL decay	125
6.2.5. Stretched exponential fit for transient PL	126
6.2.6. Performance estimates for SBABz ₄ -based OLEDs	127
6.2.7. RISC activation energy	128
6.3. Appendix to chapter 4	129
6.3.1. Synthetic details	129
6.3.2. ¹ H- and ¹³ C- NMR spectra of the final compounds	134
6.3.3. Single crystal X-ray diffraction data.....	139
6.3.4. Ultraviolet photoelectron spectroscopy	141
6.3.5. Device testing	143
6.3.6. Transient photocurrent measurements.....	145
6.3.7. Photoluminescence lifetime measurements	145
6.3.8. Electric field dependent time resolved photoluminescence and transient photocurrent measurements.....	145
6.3.9. Computational Details and Theoretical Background.....	147
6.3.10. Charge Transport Properties of BuSBA-DMPA and FBU SBA-DMPA	150
6.3.11. Free-volume in Amorphous HTMs	152
6.4. Appendix to chapter 5.....	153
6.4.1. Synthetic details	153
6.4.2. ¹ H and ¹³ C-NMR spectra of intermediate and the final compounds	164
6.4.3. Solar cell fabrication.	183
6.4.4. Photovoltaic characterization.....	183

References	184
Curriculum vitae	210

CHAPTER 1

INTRODUCTION

Global energy demand has become a relevant problem in present societies. The constantly growing energy consumption and the stricter requirements for its environmentally sustainable production urges for the immediate transition to carbon-neutral sources of abundant energy. The International Energy Agency (IEA) estimated the total electricity consumption reaching 21372 TWh with a foreseen growth for the upcoming decades¹. More than 65% of the total world gross generated electricity still originates from chemical energy released and transformed upon fuels combustion and it is accounted for almost 30% of the global greenhouse gas emission^{2,3}.

In such scenario, one of the most environmentally benign sources of ample energy is energy of incident solar light, that still remains vastly underexploited. Each hour the Earth receives light energy in the amount more than consumed yearly by humans⁴, but only 1.8% of the gross world electricity production stands for the solar energy¹. Hence, the potential of photovoltaic (PV) technology is still to be better developed and deployed to become a practical solution for the increasing demand of CO₂-neutral electricity.

On the other hand, responsible consumption of electricity is an additional key factor to achieve the global energy security. This implies a gradual transition to the technologies that allow an efficient conversion of electricity to useful work. This energy-saving advantage was clearly demonstrated by the gradual substitution of incandescent bulbs by fluorescent lamps, and more recently – by light-emitting diodes⁵⁻⁷.

These two paramount energy-security approaches are the basic idea for the contemporary light-energy conversion technologies that includes organic light-emitting diodes (OLED) and hybrid photovoltaics (HPV). These devices have already demonstrated a great promise for as inexpensive large-area, flexible, environmentally friendly and efficient solutions for light-energy transformation. However, further advances in these technologies are inextricably linked to the development of constituting organic materials, and a deeper understanding of relationships between molecular structure and performance in operating devices is the paramount investigation idea placed in the focal point on this thesis.

1.1. Light-energy conversion devices. Operation principles

Nobel Prize in Chemistry in 2000 was jointly awarded to Alan J. Heeger, Alan G. MacDiarmid and Hideki Shirakawa "for the discovery and development of conductive polymers"⁸. Nowadays, almost 20 years later, one can surely witness that the field of organic electronics has spurred immense interest not only of academics, but also entrepreneurs, manufactures and consumers. It has triggered a worldwide highly-competitive research and immediate production boom, giving a birth to a new generation of optoelectronic devices that are already used today. Organic optoelectronics have some significant advantages over their inorganic analogues: relatively low material and fabrication costs, lightweight, prospective for high off-grid autonomy, flexibility, In addition, a facile tuning of materials' electronic properties can be achieved by molecularly engineering thus easily fulfilling the requirements imposed by device architecture, physics or potential customers.

The light-energy conversion devices, I am addressing in this thesis and the materials I am developing for, are thermally activated delayed fluorescence (TADF) organic light-emitting diodes and hybrid organic-inorganic perovskite solar cells (PSC). Both technologies got an immense development impetus during the last decade and have already proven the outstanding efficiencies and great promises for the upcoming future, in big part, thanks to advances in the organic materials constituting them.

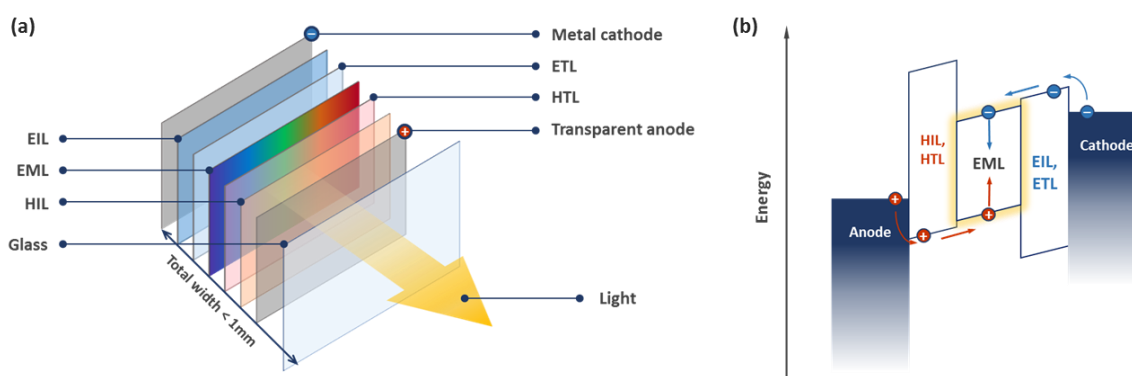


Figure 1. (a) Schematic architecture of a multilayer OLED stack. (b) Schematic energy level diagram of OLED.

OLEDs are electroluminescent (EL) devices converting electrical energy to light, thus enabling applications in display technologies and solid-state large area lighting. Typical OLEDs architecture includes multiple ultra-thin layers of organic semiconductors stacked between two electrodes: cathode and anode (**Figure 1a**). The operating voltage is applied on the electrodes allowing the injection of charge carriers and permitting the current to flow through the semiconductive organic layers (**Figure 1b**). Holes and electrons are then get confined and recombine at the central emissive layer (EML), generating excitons according to the spin statistics (**Figure 2, *vide infra***). Despite the simplest device architectures contain three main components, additional layers are generally required to facilitate carrier injection and current flow towards recombination zone, thus grading the electronic energy profile of a device. . A typical device structure is therefore the combination of an electron injection layer (EIL), an electron transporting layer (ETL), EML, a hole transporting layer (HTL) and a hole injection layer (HIL), all sandwiched between two conductive electrodes. The layer thickness, a type of organic semiconductors are chosen according to the emitter used, energy levels and optimized theoretically and experimentally to achieve the best device performances.

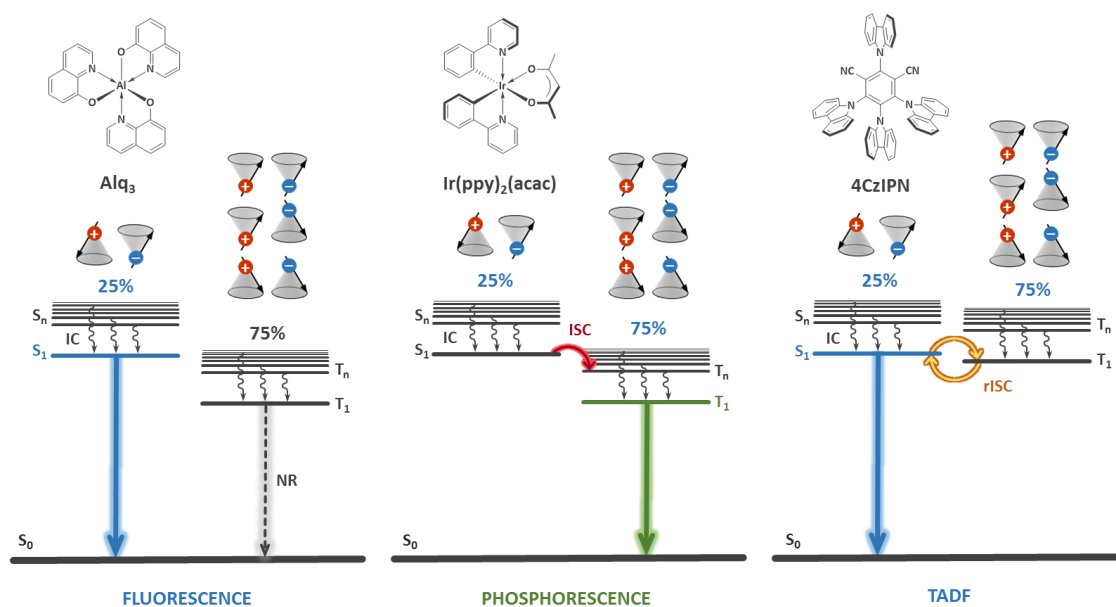


Figure 2. Schematic representation of electroluminescence mechanisms in OLEDs upon electron-hole recombination and structural formulae of the representative emitters.

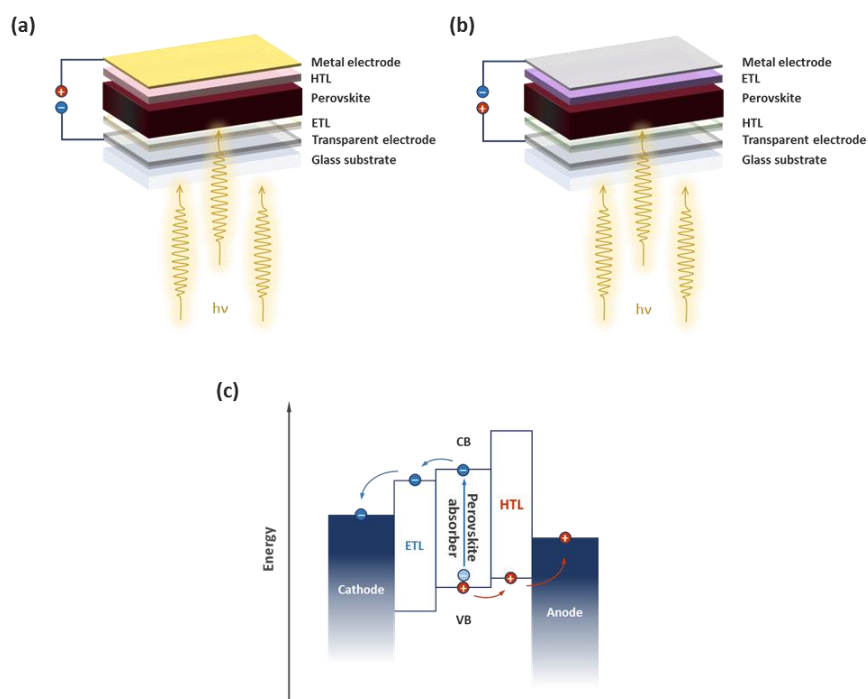


Figure 3. (a) Schematic device structure of a conventional structure PSC. (b) Schematic device structure of an inverted structure PSC. (c) Schematic energy level diagram of PSC.

Organic and hybrid solid-state solar cells, fully opposite to OLEDs by their working principle, are devices that convert energy of light to electricity based on the photovoltaic effect. The HPV device structure nonetheless is somewhat similar to the OLED: multiple thin layers of semiconductors are stacked between two selective electrodes (**Figure 3a, b**). The central layer is an efficient light absorber that harvests incident light, generating weakly-bonded excitons that must be converted into free charges. The adjacent to the absorber layers (HTL and ETL) grade energy barriers, facilitating charge carrier extraction from the photo-absorber and transport to the selective electrodes, that eventually extract the charges and result in current (**Figure 3c**). PSCs without ETLs and HTLs were reported, however they vastly attain significantly lower efficiencies^{9–12}. In this work I focus only on PSCs, employing both ETL and HTL as essential component to achieve advanced device performances.

1.2. Organic light-emitting diodes – brief overview

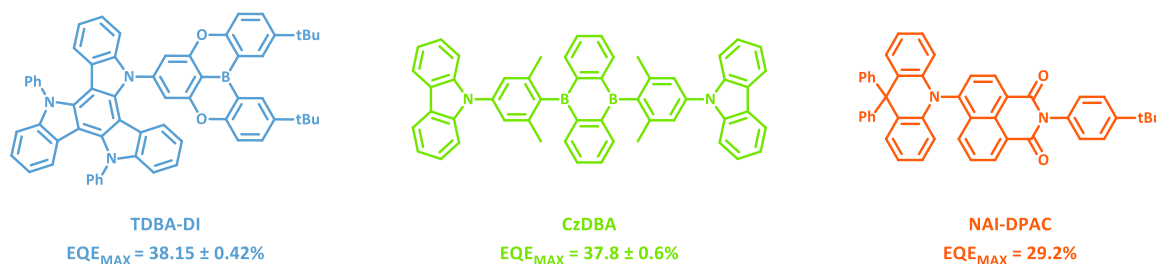
OLEDs technology has stemmed out from the very first studies on electroluminescence (EL) of anthracene crystals and tetracene as a minor impurity in anthracene matrix reported in 1962 by M. Pope (**Figure 4**)¹³. However it took almost 25 years until, C. V. Tang and S. A. VanSlyke described the fabrication and operation of the first conventional fluorescent organic light-emitting diode (FOLED)¹⁴. That pioneering device, containing tris-(8-hydroxyquinoline)aluminum embedded between two electrodes, emitted green light peaking at 550 nm and attained 1% maximum external quantum efficiency (EQE or η_{ext}). Since then, many fluorescent materials, including small molecules and polymers¹⁵, have been developed and applied to OLEDs. Yet none of them could overcome the limitations imposed by spin-statistics for electrogenerated excitons^{16,17} and device light outcoupling efficiency¹⁸. In general, for conventional fluorescent materials, electron-hole recombination generates only 25% of emissive singlet excitons and 75% of “dark” triplets that deactivate non-radiatively, therefore a maximum internal quantum efficiency (IQE or η_{int}) of only 25% is theoretically possible (**Figure 2**). In addition, Lambertian emission with the common 20-30% light outcoupling efficiency limits the maximum EQE up to about 5%.

A significant step forward in the development of efficient OLEDs was made by Baldo et al. in 1998, reporting the first phosphorescent organic light-emitting diode (PhOLED)¹⁹. The authors demonstrated the use of 2,3,7,8,12,13,17,18-octaethyl-21H,23H-porphine platinum(II) complex as the phosphorescent dopant to fabricate a red-emitting phosphorescent OLED attaining maximum EQE of 4% in the operating device. Even though the device was as efficient as a conventional FOLED, it represented a major milestone manifesting the potential advantage of employing direct radiative relaxation from the lowest lying triplet state (T_1) in microsecond time range. The allowed emission and population of T_1 from the lowest singlet state (S_1) occurs thanks to fast intersystem crossing (ISC) facilitated by strong spin-orbit coupling (SOC), induced, in its turn, by presence of a heavy metal atom. Three years later, Adachi et al. demonstrated a PhOLED containing bis(2-phenylpyridine)iridium(III) acetylacetonate phosphorescent dopant, that exhibited IQEs close to unity²⁰. The device emitted green light peaking at 520 nm

and attained maximum EQE of $19.0 \pm 0.5\%$, thus clearly exceeding the limitation imposed by spin statistics for fluorescent materials (**Figure 2, Figure 4**). Since 2001 many organometallic phosphorescent compounds including Ir, Pt, Ru, Os, Re, Au atoms have been reported, demonstrated emission covering the whole visible spectrum^{21,22}. Moreover, red and green Ir cyclometalated complexes have already found vast application in production of OLED-displays, clearly demonstrating the superiority of the new technology in brightness, contrast ratio, wider viewing angles, lightweight, response time and power efficiencies over the preceding concepts. However, effective and stable deep blue-emitting phosphors remain to be scarce²³⁻²⁵, and the best performing OLEDs contain rare noble metals, which are rather disperse and therefore expensive. Additionally, the extensive mining, refinery and use of rare metals may bring about many environmental and economic risks associated with the mass production²⁶.

E-type fluorescence, or TADF is an alternative phenomenon that utilizes “dark” electrogenerated triplet excitons thanks to a tiny energy splitting between S_1 and T_1 , which permits thermally-triggered back-population of S_1 from T_1 thanks to the efficient reversed intersystem crossing (rISC). To the best of my knowledge, TADF has been first reported as early as in 1941 by Lewis G.N. et al, who described the temperature-dependent afterglow of fluorescein in a boric acid matrix²⁷. Few decades later, some other small molecules (eosin, aromatic ketones, thioketones) and fullerenes have been demonstrated to display delayed fluorescence properties in solutions or solid state, however photoluminescence quantum yields (PLQY) were extremely low and not yet suitable for any use in emitting devices²⁸⁻³³. Almost at the same time, light *d*-element complexes (mainly Cu-complexes) with bulky phosphine ligands were synthesized showing a small S_1 - T_1 energy splitting ($\sim 900 \text{ cm}^{-1}$) and a strong delayed temperature-dependent component in their emission³⁴. In contrast to *5d*-element phosphors, lighter Cu-analogues did not display the strong SOC that allow spin-forbidden radiative transition from T_1 to the ground singlet state (S_0). On the contrary, Cu-complexes with sterically congested phosphine ligands have a very small splitting between the lowest singlet and triplet states, allowing thermally triggered rISC, thus resulting in delayed emission via a fluorescent channel. However, molecular design for efficient and stable

Cu- or Ag-based TADF complexes with short delayed emission component (3-5 μ s) remains to be very challenging³⁵. Porphyrin-based Sn⁴⁺-fluoride conjugates were also reported to exhibit TADF emission and used to fabricate the first doped TADF OLED³⁶. The very first OLED with purely organic TADF emitting dopant was reported by Endo et al. in 2011³⁷. However, the EQE of the pioneering device hardly surpassed the conventional maximum EQE values FOLEDs, attaining modest 5.3% and thus remaining as proof of a potential concept rather than a practical methodology to build efficient TADF devices. The “game-changer” was reported by Uoyama H. et al. in 2012 and manifested a surpass of the FOLED maximum EQE limit of $\sim 5\%$ using fully organic EML, and becoming a starting point for the third generation OLEDs based on organic TADF emitters³⁸. The authors proposed a feasible strategy to construct organic TADF materials with tunable electronic properties, eventually demonstrating the full palette of emission colors over the visible spectrum, from sky-blue TADF OLEDs (max. $\eta_{\text{ext}} = 8.0 \pm 1\%$), to green (max. η_{ext} of $19.3 \pm 1.5\%$) and orange-red (max. $\eta_{\text{ext}} = 11.2 \pm 1\%$).



Nowadays, fully organic TADF emitters have broken new records approaching maximum EQEs close to 40% for sky-blue (TDDBA-DI)³⁹ and green (CzDBA)⁴⁰, and 30% for orange-red (NAI-DPAC)⁴¹ OLEDs without any extra light-outcoupling devices. They illustrate the importance of a rational molecular design, and the paramount need of investigating the relationship between molecular structure and the macroscopic properties of the materials.

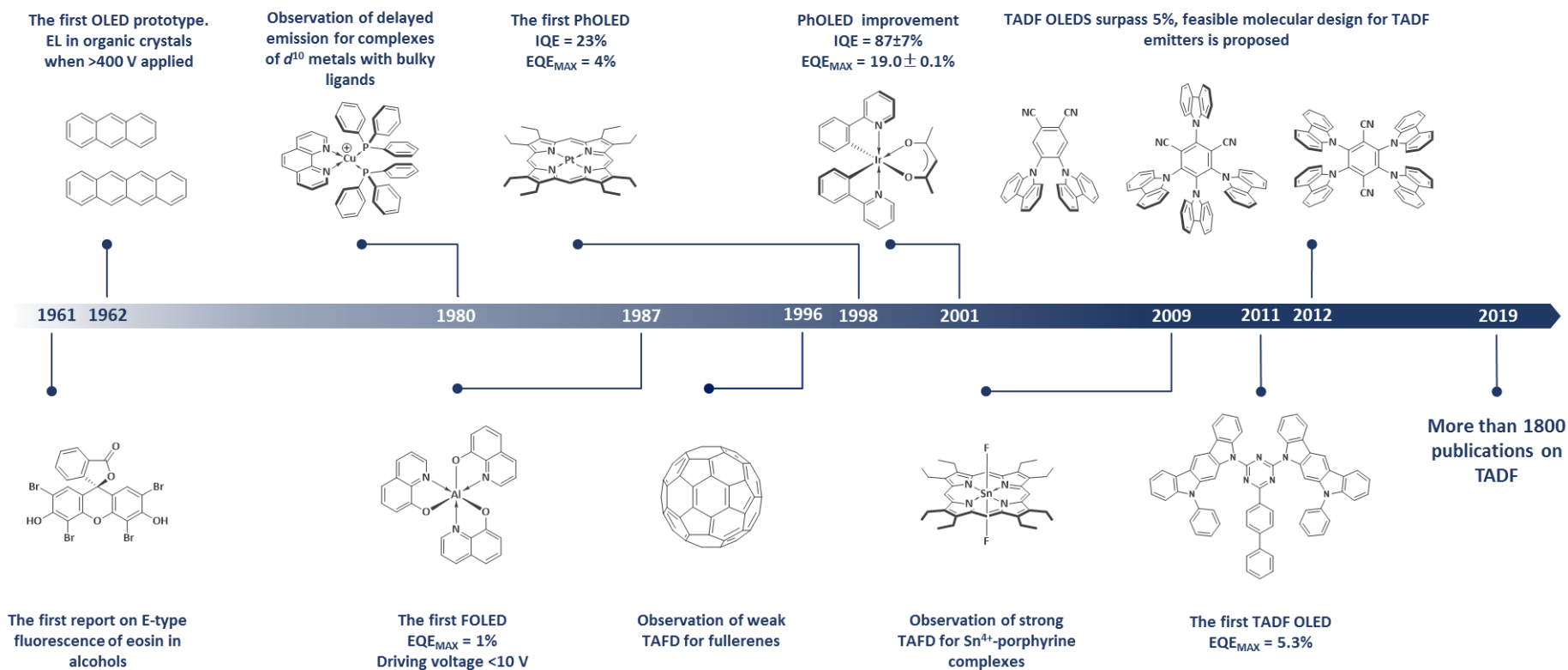


Figure 4. Timeline and the selected milestones of OLED and TADF development.

1.3. Principles of molecular design to modulate TADF properties of organic emitters

In order to overcome the limitation of triplet exciton quenching in fully organic molecules, TADF emitters require a minimal energy separation between S_1 and T_1 states (ΔE_{ST}) along with long-living triplet excitons to prevent radiationless deactivation and high values (10^4 - 10^6 s⁻¹) of rISC rate constant (k_{rISC}). The tiny value of the energy splitting allows triplets to thermally up-convert to a singlet state efficiently, followed by fast ($k_r \sim 10^9$ - 10^{11} s⁻¹) radiative relaxation to the ground state, eventually permitting IQE of unity. Moreover the tiny energy gap is essential to boost rISC according to Arrhenius equation for rISC rate constant (k_{rISC}) (1) and the first-order perturbation theory (2)⁴², suggesting the increase of first-order mixing coefficient (λ) with decreasing ΔE_{ST} , even with tiny finite spin-orbit interaction (H_{SO}) in molecules without any heavy atom:

$$k_{rISC} = Ae^{-\frac{\Delta E_{ST}}{kT}} \quad (1)$$

$$\lambda \propto \frac{H_{SO}}{\Delta E_{ST}} \quad (2)$$

where A is a preexponential factor, k is Boltzmann constant and T is temperature. Energies of the lowest-lying singlet and triplet states are defined through orbital energy (E_{orb}) of one-electron system in excited state, Coulomb term (C) and the exchange energy term (J), according to the equations 3-5:

$$E_{S_1} = E_{orb} + C + J \quad (3)$$

$$E_{T_1} = E_{orb} + C - J \quad (4)$$

$$\Delta E_{ST} = |E_S - E_T| = 2J \quad (5)$$

Hence, the excited state energies differ only due to spin arrangement of the singlet (destabilized) and triplet (stabilized) excited states, whilst the entire electron arrangement is identical for both excited states and gives equivalent values of each energy term for both excited states. Therefore, minimization of the ΔE_{ST} splitting implies minimization of exchange integral:

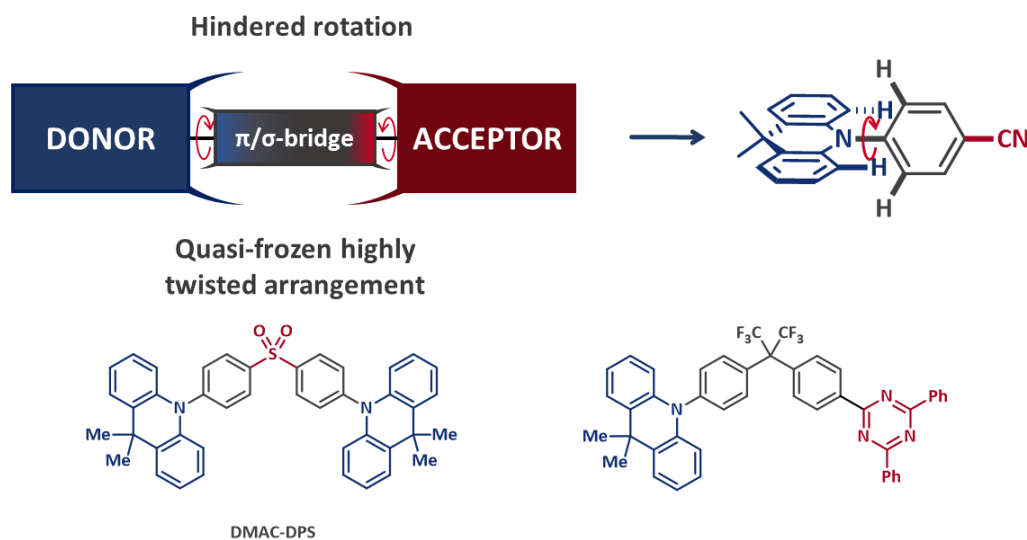
$$J = \iint \varphi(r_1)\psi(r_2) \left(\frac{e^2}{4\pi\epsilon_0|r_1 - r_2|} \right) \varphi(r_2)\psi(r_1) dr_1 dr_2 \quad (6)$$

where ψ and φ stand for the highest occupied (HOMO) and the lowest unoccupied (LUMO) molecular orbital wave functions respectively, e is elementary electric charge, ϵ_0 is the vacuum permittivity and r_n are the positions of the electrons. Thus, minimization of J can be achieved by decreasing the overlap between the wave functions, in other words by spatial separation of HOMO and LUMO.

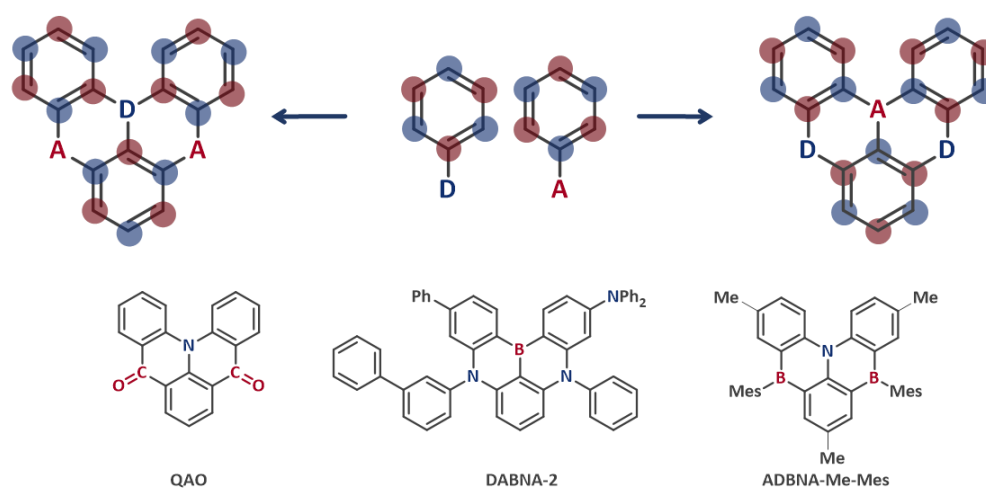
Though minimization of ΔE_{ST} through frontier molecular orbitals (FMO) segregation is an essential prerequisite to impart rISC to an emitter, many other factors may strongly affect efficiency of the back-population as well as emission parameters and ultimate performance in OLEDs: prompt (τ_P) and delayed (τ_D) emission lifetimes, PLQY, full-width at half-maximum (FWHM) etc. The normal conditions provide only 26meV of thermal energy, being nearly the only suitable for operation of consumer electronics. However some efficient TADF emitters were reported to have large splitting values ranging from 300 meV up to 600 meV⁴³, thus, in the latter case, being closer to the conventional fluorescent materials without substantial FMO segregation⁴⁴. Moreover, different nature of excited states⁴⁵, vibronic (nonadiabatic) coupling⁴⁶⁻⁴⁸, multiple intermediate states^{49,50} and/or S_1 - T_1 pairs⁵¹, SOC and possible metastable conformations of the emitters have to be equally considered as efficient ways to facilitate rISC.

In terms of molecular design, the most common and feasible way to impart rISC and TADF properties to an emitter is spatial segregation of FMOs. It is usually achieved in highly twisted molecules composed of distinct electron excessive (donors, D) and electron accepting (A) units that accommodate HOMO and LUMO apart (**Figure 5a**). One of the approaches for physical separation of the frontier orbitals relies on quasi-perpendicular or other highly twisted rigid arrangements of the D-A that effectively minimize π -interaction between them. Introduction of a π -bridge can improve the partition of FMOs, however it inevitably expands the overall electronic system, resulting in a narrower bandgap and consequently longer emission wavelengths

(a) Conventional FMO separation:



(b) "Multiple resonance" effect:



(c) Excited-state intramolecular proton transfer:

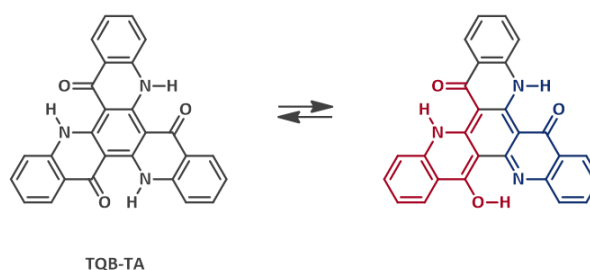


Figure 5. Approaches for FMOs separation through (a) reduced overlap of HOMO and LUMO in highly twisted conformations^{52,53}, (b) multiple resonance effect and (c) photoisomerisation. Blue and red colors represent localisation of HOMO and LUMO or D and A units.

(lower color purity for blue emitters)⁵⁴. Alternatively, sp³-hybridized electronically inert bridges (alkyl chains, spiro-atoms etc.) can significantly break (up to complete isolation) any electronic communication between D and A⁴⁴. This strategy, yet reported, still relied on various through-space interactions to ensure practical PLQYs⁵³. The absolute interruption of the conjugation significantly decreases luminescence efficiency, as k_r is proportional to the oscillator strength (f) between S_i and S₀:

$$k_r \propto f\nu \quad (7)$$

where ν is emission wavelength.

Other molecular engineering strategies to minimize ΔE_{ST} , while retaining high f values, proposed separation of HOMO and LUMO within one molecule even without evident D and A units. They relied on so called “multiple resonance effect” (**Figure 5b**)⁵⁵⁻⁵⁷ or excited-state intramolecular proton transfer (**Figure 5c**)⁵⁸, allowing to alternately relocate HOMO and LUMO over separate parts of one flat molecule. However, materials based on these strategies of FMO separation remain to be rather scarce and difficult to design: even small alternations in the structures may be critical for ΔE_{ST} and therefore TADF emission^{59,60}.

1.4. D and A units to construct TADF materials

The vast majority of TADF emitters are still designed using the most synthetically feasible approach involving combination of sterically demanding D and A entities. Despite the plethora of TADF materials have been developed and reported to date, they are usually composed of limited number of donor entities, while the structural synthetic development mainly focuses on molecular engineering of the acceptor part⁶¹⁻⁶³.

The donors are usually represented by N-containing aromatic compounds: triarylaminines, carbazoles, acridanes, phenoxazines, phenothiazines and azasilines that are connected to A either directly through N-atom or via one of C-atoms of the molecular periphery of the D framework (**Figure 6**). The molecular configuration, isomerism strongly affect the emission parameters, ΔE_{ST} splitting and k_{TISC} ⁶⁴⁻⁶⁶. The acceptors are usually based on conventional electron withdrawing groups (nitriles,

carbonyl compounds, halogens and haloalkyls), electron deficient N-heterocycles (triazine, pyrimidine, azoles, heptazine etc.), structures incorporating other heteroatoms (B: boranes, borates, borinates, boron-fluorine complexes etc.; P: phosphineoxides; S: sulfoxides and sulfones) in various oxidation states, π -systems^{67,68} and their infinite combinations (**Figure 6**). The electron withdrawing properties of an acceptor define energy level of LUMO, thus judicious choice of both D and A is paramount to obtain a desired bandgap energy, which is emission wavelength.

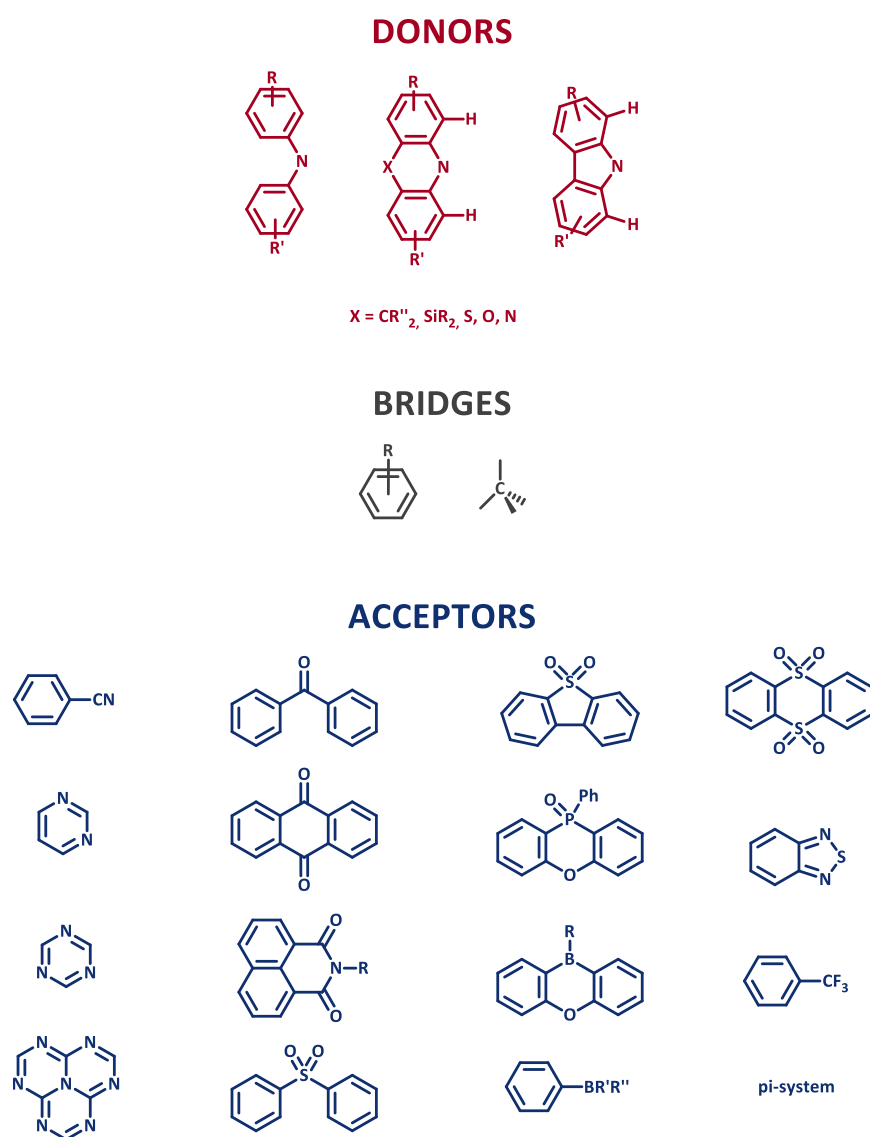


Figure 6. Selected donors, acceptors and bridges widely employed to construct TADF emitters.

The substituents furnishing a donor part of a molecule are known to affect HOMO energy and tune electronic properties of an entire emitter⁶⁹. For example, the donor strength can be substantially increased upon attaching alkyls, -OR, -SR, carbazole, arylamines, alkyls etc. at *para*- or *ortho*- positions in relation to the N, on the contrary, aromatic fragments, like phenyl, can stabilize HOMO thanks to the extension of the conjugation system and its weak electron-withdrawing properties⁶². However, care should be taken when introducing any substituents (even “electronically inert”), as this inevitably increases complexity of a system and can lead to appearance of new excited states, SOC, new conformations interfering in the emission⁷⁰⁻⁷⁶.

The bridges between D and A units are optional and are usually used to impart certain geometric arrangement and/or molecular shape, to better separate FMOs, thus increasing amount of the delayed component in the emission⁷⁷. They are usually represented by phenyl linkers or sp^3 -hybridized C-atoms (short alkyls or spiro-atoms) that break π -conjugation. The choice of a linker is however also important, as it may affect ΔE_{ST} splitting⁷⁸ and the bandgap width.

1.5. Perovskite solar cells – brief overview

Perovskites are inorganic compounds with a general formula ABX_3 and the crystal structure similar to naturally-occurring mineral $CaTiO_3$ that gave the name to the whole family of hybrid materials (**Figure 7a**). Organic-inorganic hybrid absorbers used in PSCs are usually represented by lead or tin organo-halide compounds, where $A = MA$ ($CH_3NH_3^+$), FA ($NH_2=CHNH_2^+$), Rb^+ or Cs^+ ; $B = Pb^{2+}$ or Sn^{2+} and $X = I^-$, Br^- or Cl^- . These light-harvesters combine many appealing optoelectronic properties placing them at the very frontline of the PV research: strong panchromatic absorption (**Figure 7b**)^{79,80}, tunable bandgap⁸¹⁻⁸³, efficient generation and ambipolar transport of charge carriers⁸⁴, low (<50 meV) exciton binding energy^{85,86}, long (~175 μm) carrier diffusion lengths⁸⁷, excellent processability and material affordability.

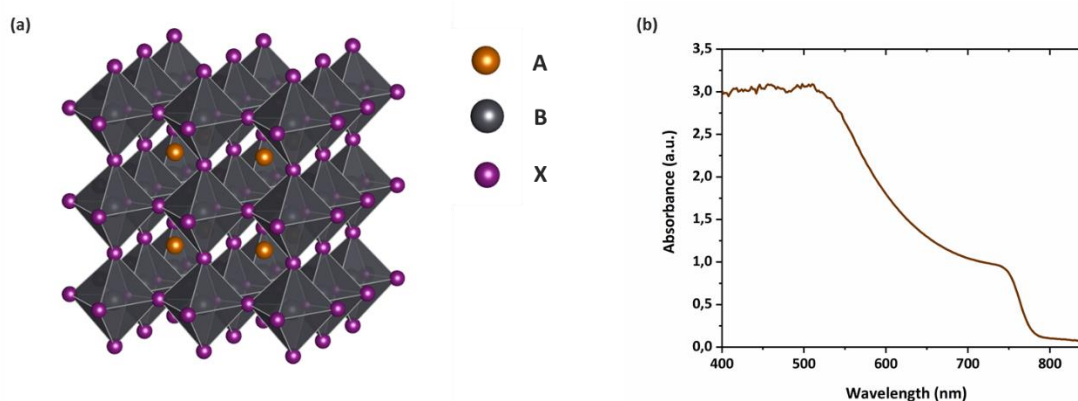


Figure 7. (a) The crystal structure of a typical ABX_3 perovskite. (b) Absorption spectrum of $[(FAPbI_3)_{0.87}(MAPbBr_3)_{0.13}]_{0.92}(CsPbI_3)_{0.08}$ thin film.

Even though the optoelectronic properties of the hybrid perovskites were disclosed and studied decades ago, its application for photovoltaics was reported only in 2009. Kojima A. et al. the first reported the use of $MAPbI_3$ and $MAPbBr_3$ as sensitizers for liquid-electrolyte dye-sensitized solar cells (DSSCs), however power conversion efficiencies (PCE) were of only 3.81% and 3.13% respectively⁸⁸. These solar cells were not durable due to fast hydrolysis of methylammonium haloplumbites. The subsequent investigation in 2011 described an optimization for the sensitized PSCs fabrication resulting in doubled PCE, but the stability issue has not been resolved yet⁸⁹.

The significant step forward, towards the nowadays-used technology was made in 2012 by Kim et al. when the architecture of solid state dye-sensitized solar cells (ssDSSC) was adopted. Replacement of a liquid electrolyte with solid 2,2',7,7',-tetrakis-(N,N-dimethoxyphenyl-amine)-9,9'-spirobifluorine (spiro-MeOTAD) HTM eventually increased PCE up to 9.7% and extended the lifetime of perovskite-based devices to 500h stable device operation^{90,91}. Many other improvement regarding *n*-type^{92,93} and *p*-type materials⁹⁴⁻⁹⁷, perovskite composition, morphology^{98,99} and dimensionality¹⁰⁰, deposition methods¹⁰¹, interfacial engineering¹⁰², surface passivation techniques¹⁰³ and layer doping were undertaken to skyrocket the PSC efficiencies beyond 25% nowadays¹⁰⁴, thus already exceeding average metrics of the commercialized Si-congeners over only 10 years of tsunami-intense research.

1.6. PSC architectures and materials

PSCs are usually composed of few (typically – 5) functional layers that facilitate exciton dissociation in a perovskite absorber, charge carrier injection and transport followed by charge extraction at cathode and anode. The entire solar cell is commonly supported by a glass or plastic substrate, covered with transparent conductive oxide (TCO) working electrode: indium-tin oxide (ITO) or fluorine-doped tin oxide (FTO). The transparent electrode props a three-layer stack composed of two charge-selective semiconducting layers embedding a perovskite absorber. The order and the constituting materials of these layers depends on PSC architecture (*vide infra*). A selective metal (Au, Ag, C or Al etc.) back contact caps up the layer stack. The electrode material (i.e. its work function) is chosen according to materials used and the device architecture.

Perovskite intrinsic (*i*) layer can be sandwiched between two semiconducting layers (*n*-type and *p*-type materials), thus following conventional (*n-i-p*) or inverted (*p-i-n*) structures, and resulting in the architectures where incident light comes through ETL or HTL respectively (**Figure 8**). Depending on the microstructure of *n*-type transporting material, PSCs can be further categorized into mesoscopic and planar

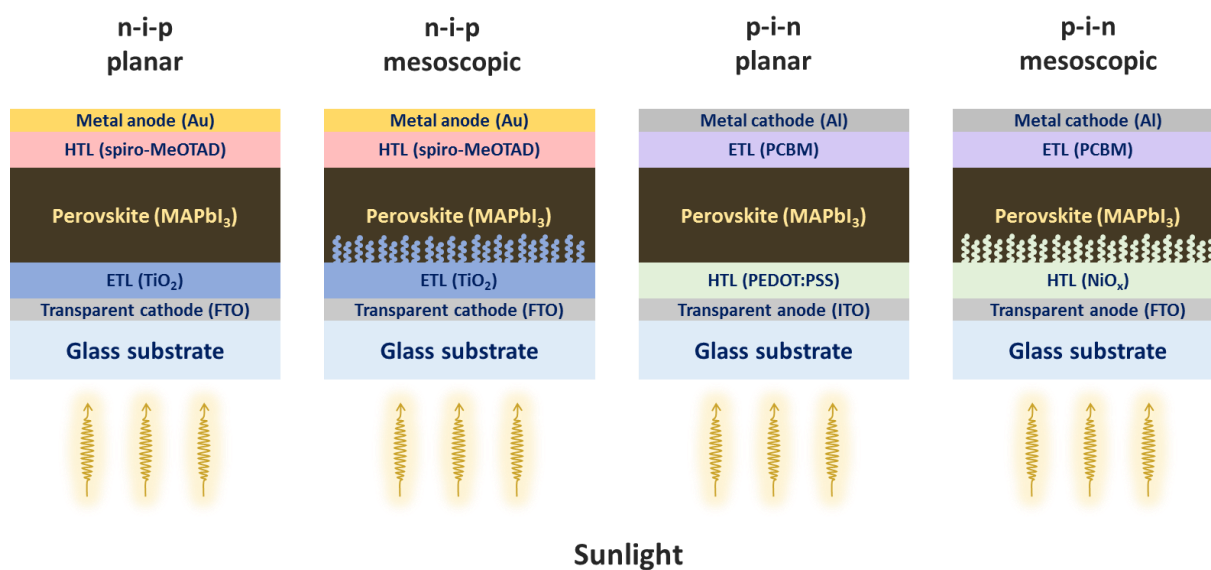


Figure 8. Schematic representation of four typical PSC architectures

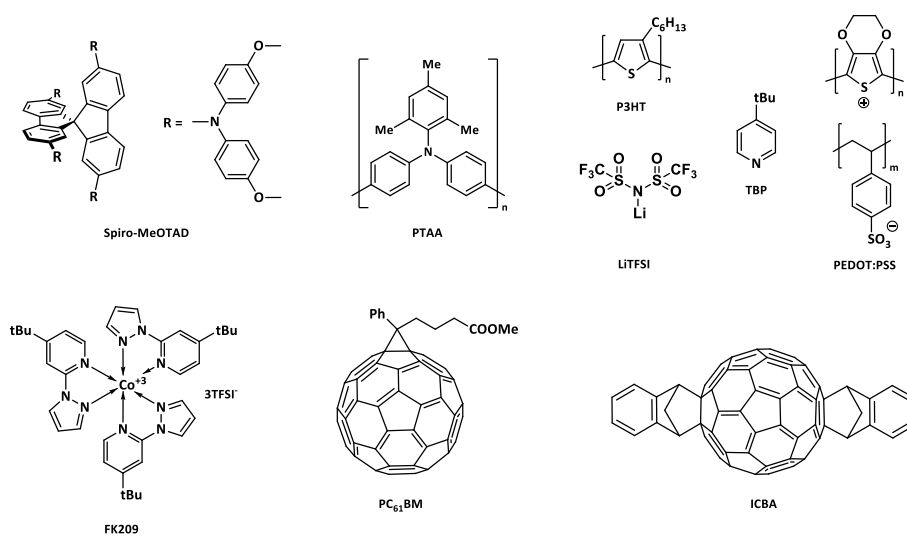
structures. Specifically, mesoscopic architectures utilize mesoscopic layer of nanostructured metal oxides (TiO₂, SnO₂, Al₂O₃, ZrO₂, NiO etc.) as a functional scaffold to support better formation of a perovskite film or for charge carrier extraction. Simplified planar heterojunction structure exclude the mesoscopic interlayer and utilize only a compact metal oxide film. Architectures without HTL or ETL have been equally reported, however devices inevitably displayed poorer performances due to stronger parasitic recombination at the interfaces.

The paramount requirements for the charge-selective layers are (i) the proper band alignment with the perovskite absorber that allow efficient charge carrier extraction to the interfaces, while preventing harmful charge recombination; (ii) smooth continuous interfaces ensuring tight contact with perovskite and selective electrodes; (iii) high charge carrier mobilities and (iv) good processability and affordability to maintain the cost advantages of PSC technology.

ETM, or *n*-type, materials permit extraction of photogenerated electrons from the perovskite absorber. The ETL's conduction band (CB) or LUMO is supposed to be more stabilized (~100-300 meV) than that of the intrinsic perovskite layer, while the valence band (VB) or HOMO should be significantly deeper to block the holes transfer and prevent charge recombination. Moreover, in *n-i-p* architectures, ETM should be transparent in the entire visible light region to ensure no parasitic light absorption.

Thereby, metal oxides (TiO_2 , ZnO , SnO_2 etc) are usually used for *n-i-p* device structures, while the organic ETMs (organic small molecules and polymers with strong electron acceptors, fullerenes and fullerene derivatives: C_{60} , PC_{61}BM or PC_{71}BM , ICBA etc.) are used in inverted *p-i-n* structures.

HTM, or *p*-type material, assists the extraction of photogenerated holes from the perovskite absorber. As opposed to ETMs, HTMs should possess VB or HOMO level 100-300 meV destabilized relative to the perovskite, thus ensuring barrierless hole injection, while strongly destabilized CB or LUMO (very low electron affinity) can be beneficial for blocking electron transfer. In addition, *p-i-n* architectures require minimal parasitic light absorption from the HTL at the front side of a device. Thus, the materials used in the inverted architectures are usually NiO_x , Cu-group materials (CuI , CuSCN , CuO_x etc.), PEDOT:PSS, while the most frequently employed regular structure vastly relies on electron-rich small molecules, conductive polymers and inorganic materials.



Since the best efficiencies achieved for ssDSSC and the very first stable results for PSC, spiro-MeOTAD became the benchmark molecule for all newly developed hole-selective materials. Spiro-MeOTAD is composed of a 9,9'-spirobi[fluorene] molecular scaffold furnished with 4 DMPA (4,4'-dimethoxydiphenylamine) redox-active entities on the molecular periphery. The molecular core is made of two orthogonal fluorene units providing bulky globular arrangement of the DMPA substituents, thus giving rise to ample solubility, high T_g values, i.e. stability of amorphous state of fabricated thin

films, thermal stability and charge carrier mobilities in the range of 10^{-5} - 10^{-4} $\text{cm}^2/(\text{V}\cdot\text{s})$. On the other hand, the reversible redox properties, energy level value (IP \sim -5.1 eV), and interaction with the perovskite absorber are defined mostly by DMPA entities.

Spiro-MeOTAD has, however, few critical drawbacks: (i) extremely high cost of the material (\sim 350 \$/g) due to multistep synthesis and requirements of sublimation-grade purity; (ii) innate low hole mobility and conductivity, that require heavy doping with deliquescent ionic additives (LiTFSI, FK209) and tert-butylpyridine (TBP), believed to cause (iii) poor long-term stability.

Conducting polymers as poly(triaryl amine) (PTAA) or poly(3-hexylthiophene-2,5-diyl) (P3HT) are often used as alternatives to low molecular weight organic materials. Macromolecules are considered to overcome the spiro-MeOTAD disadvantages thanks to their ultrafast on-chain charge carrier mobility and excellent film formation properties. However, polymers still require doping to induce high conductivity, and there is strong batch-to-batch deviation in molecular weights or even in regularity of a polymer. Moreover many conducting polyconjugated polymers strongly absorb visible light, causing optical losses which, together with tedious polymer purification, make its use cost-inefficient.

Inorganic HTMs are considered to overcome low charge carrier mobilities, high material cost and poor long-term stability inherent to organic semiconductors. Nonetheless, the choice of materials is limited, and fine tuning of electronic and morphological properties is not as feasible as for organic counterparts. In addition, the deposition process of inorganic materials may be energy-inefficient (vacuum deposition) or may break the integrity of a perovskite film due to the use of non-orthogonal solvents for subsequent deposition of the absorber and a desired inorganic *p*-type semiconductor.

1.7. Molecular design of low-molecular-weight HTMs

Small organic HTMs constitutes an extensive research topic aimed to find relationships between HTM molecular structure, physico-chemical properties and photovoltaic performance in solar cells. Organic chemistry toolbox allow facile molecule tailoring to specifically address the weaknesses of the parental reference material: low charge carrier mobility, cost inefficiency and poor long-term stability. In general, an

efficient new HTM should impart few important features: (i) proper energy levels, (ii) good charge carrier mobility and conductivity, (iii) good solubility and processability, (iv) chemical and morphological stability, (v) protecting properties (hydrophobicity/operation in pristine form) to prevent perovskite degradation and (iv) cost-efficiency.

The most widespread building blocks for the construction of HTMs for optoelectronics are still represented by electron-rich triarylamines thanks to their reversible and fast redox processes at N atom, high-lying ionization potential (IP), rather good charge-carrier transport properties, film-formation ability and thermal stability¹⁰⁵. The 3D arrangement of triarylamine entities strongly affects molecular packing in solid state, thus affecting morphological stability of amorphous glassy state of thin films desirable for devices^{106,107}. The most usual structural motifs of triarylamine-based low molecular weight materials are rod-shaped, star-shaped (or discotic) and spiro-arranged frameworks (**Figure 9**). The linear arrangement has been well known since early development of HTLs for OLEDs. These simple structures combine feasible synthesis, scalability and therefore – cost-efficiency. However, small rod-shaped molecules usually have low T_g and, as a result, they are prone to crystallize un operating devices¹⁰⁸. The elongation of the molecules partially overcomes the morphology instability, but significantly decreases solubility and processability of the materials. Most of “1D” HTMs require ionic dopants for good performance in devices.

The next structural group of HTMs is starburst and/or discotic molecules that often originates from innate arrangement of a parental triphenylamine (TPA) and/or fused polyaromatic heterocycles as well as polycyclic aromatic hydrocarbons (PAHs) as a supporting scaffold. As “1D” congeners, these materials have been extensively employed since OLEDs and were often found to exhibit superior morphological stability, while displaying preferential face-on organization at surfaces that facilitate intermolecular π -interaction and interlayer charge transport^{109,110}. These improved interactions allowed to use HTMs in pristine form, but they may result in significant lack of solubility. Simple starburst molecules can

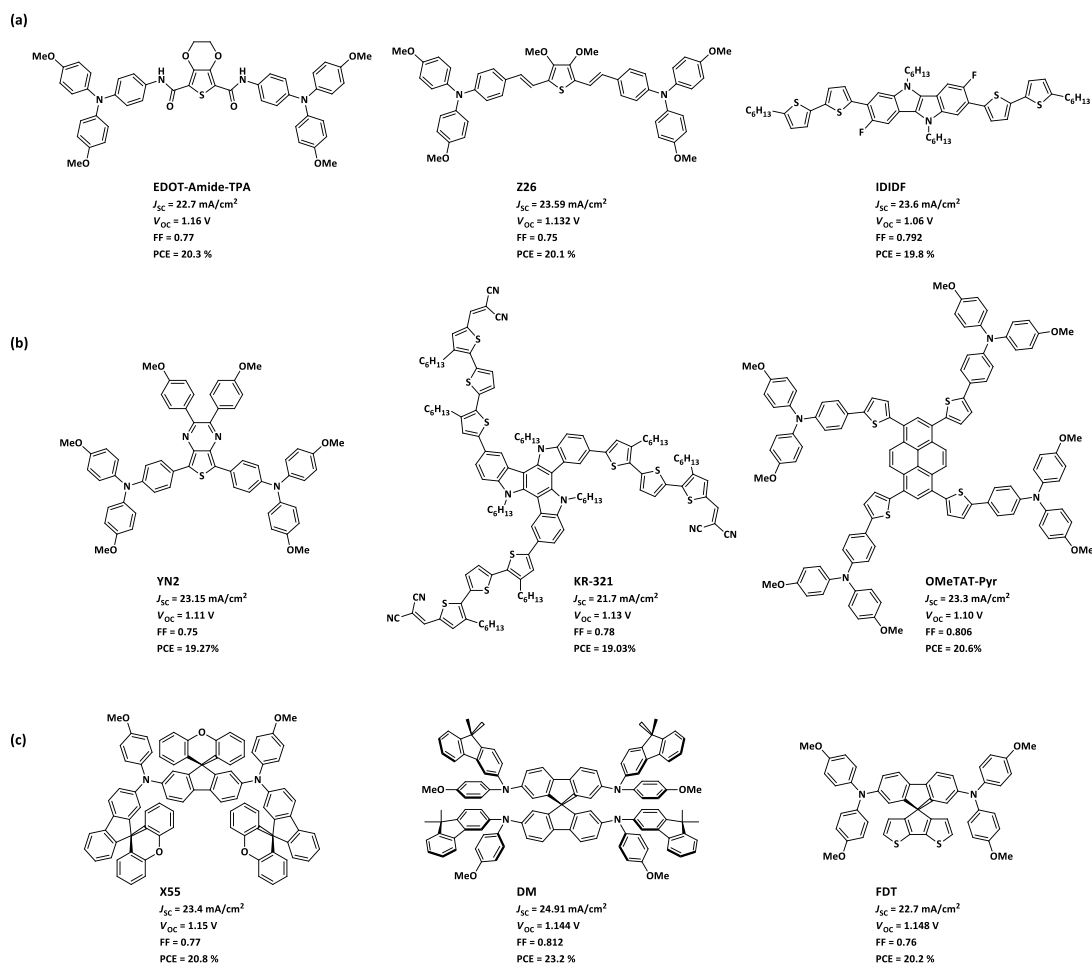


Figure 9. Selected representative HTMs with (a) linear^{111–113}, (b) starburst^{114–116} geometry and (c) spiro-arranged^{117–119} molecules for highly efficient PSCs.

be usually afforded through few-step synthetic procedures, however TPA planarization and extensive functionalization of the molecular periphery can dramatically increase the final costs.

Spiro-arranged molecules easily overcome morphological instability. They innately display high T_g , good solubility and film formation properties as opposed to the simpler “monomer” building blocks¹²⁰. The parental spiro-MeOTAD has been widely deployed since OLEDs and ssDSSCs, commercialized and become a flagship HTM for PSC¹²¹. However, the globular shape of spiro-arranged molecules brings about more intermolecular voids because of structural bulkiness and distant packing in solids, eventually resulting in inferior charge transport and need in deliquescent ionic dopants. Moreover, preparation of a primary spiro-aromatic core requires few steps and costly starting materials, while further furnishing of a periphery leads to cost-inefficiency.

Besides triarylaminines, other electron excessive molecular motifs became a subject of extensive research: 5-member heteroaromatic rings (pyrrole, azoles, furan, thio- and selenophene), related conjugated, fused and spiro-systems. Introduction of heteroatoms and polycyclic heteroaromatic compounds (PHAs), as well as electron-deficient motifs to the HTM scaffold were demonstrated to result in new interesting and advanced properties^{94,122}.

In conclusion, design and synthetic guidelines for judicious molecular tailoring of functional materials with advanced properties are still in high demand and are subject of ongoing research. New molecularly engineered scaffolds are to be further designed and better studied to address the urgent need in innovative functional materials for light-energy conversion devices.

1.8. Motivation and outline of the thesis

The field of light-energy conversion electronics is booming and ready to face up the energy-security challenges of the upcoming future. The advances in the domain of organic optoelectronics are inextricably linked to the development of new organic materials and better understanding (i) how the structural architecture and physico-chemical properties at molecular level translate into the performance of the corresponding bulk “macroscopic” material in an operating device; (ii) how one can judiciously engineer new molecules to specifically address the requirements for advanced performance and (iii) what the synthetic guidelines to prepare the materials in the most efficient and high-yielding manner are.

With these ideas in mind I have performed a thorough literature search and further data analysis to investigate potential advantages of introduction of a spiro-(hetero)atom to an acridane scaffold for preparation of functional materials for light-energy conversion devices. First, I describe synthetic approaches towards spiro-acridane materials, including special cases of acridanes with a spiro-heteroatom; second, I analyze spiro(heteroatom)-acridane materials developed for TADF OLEDs deriving and grouping the cases where a spiro-node brings a certain property or a function; third, I survey and report published data on spiro-acridane HTMs for PSCs, highlighting a great potential to further explore the capacity and use the spiro-acridane molecular motif for light-energy conversion devices. The findings are presented in chapter 2.

In the next parts of our work I introduce SBA molecular platform and ullazine PHA for molecular engineering of functional materials for optoelectronics. In chapter 3, after optimization of a synthetic approach towards SBA-scaffold, I prepared a compact deep-blue TADF emitter **SBABz4** composed of so far poorly studied twinned SBA acridane donor and conventional 4-benzonitrile acceptor. TADF properties were studied in solutions and solid films, demonstrating superior color purity in relation to the “monomer” analogue **DMABz4**. OLEDs employing **SBABz4** emitter attained maximum EQE of 6.8% close to the theoretically possible 7.1% – based on the assumption of 30% light outcoupling efficiency.

In chapter 4, I further explored the capacity of SBA-molecular platform, preparing and studying materials for PSCs. Endowed with various alkyl chains at the in-plane N-

atoms and DMPA-substituents at the molecular periphery, 4 new HTMs were employed in PSCs in doped form. The new materials were as efficient as the benchmark spiro-MeOTAD, but displayed significantly reduced *J-V* hysteresis and excellent stability after 1000 h light stability test. Me-substituted HTM, displayed the highest PCE of 18.05% for the champion device and demonstrated the best stability, retaining 88% of the initial PCE, thus being among the most stable doped HTMs reported to date.

In chapter 5, I explored chemistry of electron excessive polyheteroaromatic compounds – ullazines. In order to prepare ullazine functional materials, I have optimized synthetic procedures to get a feasible and high-yielding access to the unsubstituted ullazine core and reactive 6-bromoullazine. Furthermore, selective approaches towards all possible monocarboxaldehydes were examined and used to prepare D-A conjugates with dihexylmalonate acceptors to probe and study the effect of regioisomerism on the photophysical and electrochemical properties of the new dyes. One of the D-A conjugates displayed suitable HOMO level and was used as an HTM for PSC without any dopant, attaining PCE of 13.07%.

Chapter 6 presents a general conclusion of this thesis. The supplementary information for chapters 3-5 is reported in chapter 7. Chapters 3-5 are based on published articles with minor modifications.

CHAPTER 2

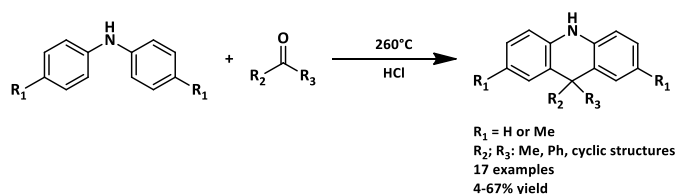
SPIROACRIDANS AS LIGHT EMITTERS AND HOLE TRANSPORTERS

In this chapter I summarize and analyze the reported information on preparation and use of acridane spirocyclic compounds as functional materials for light-energy conversion devices. The main scope of this literature minireview is spiroacridane emitters for OLEDs and HTMs for PSCs. Spirobiphenazasilines and spirocoordinated boron complexes are also included to discuss an effect of spiroheteroatom inclusion. Where possible, performance of spirocyclic compounds is compared with their “monomeric” aridine congeners with Me- or Ph- substituents at 9 position to find out (dis)advantages of a use of the bulky orthogonal spiro-arrangement.

2.1. Synthesis of spiro-fused arylamine compounds*

To the best of my knowledge the first synthesis of 9,9-spiroacridane scaffolds dates back to 1978, when E. Sturm et al. reported preparation and electrochemical investigation of N,N'-bismethylated SBA from ortho-magnesiated N-methyldiphenylamine and N-methylacridone followed by intramolecular condensation of the intermediate carbinol¹²³. In 1984, W. Tritschler et al. reported condensation of diphenylamines with ketones affording 9,9-disubstituted acridanes, including spirocyclic compounds when cyclic ketones were used. However, the reactions were performed in extreme conditions and generally resulted in very low yields¹²⁴.

Scheme 1. Acid-catalyzed condensation of diphenylamines with ketones

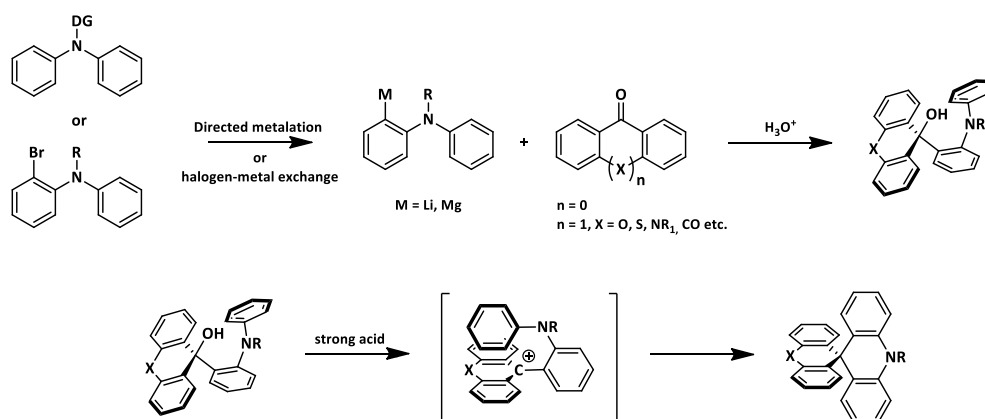


Basically, as for the other aromatic carbon-spirocyclic compounds, the principal and the most high-yielding preparation method for spiroacridanes requires a cyclic carbonyl (ketone) component and a strong nucleophile, as it was first reported by E. Sturm et al. The nucleophile is a carbanion generated either from 2-

*The numeration of structures is independent in each chapter.

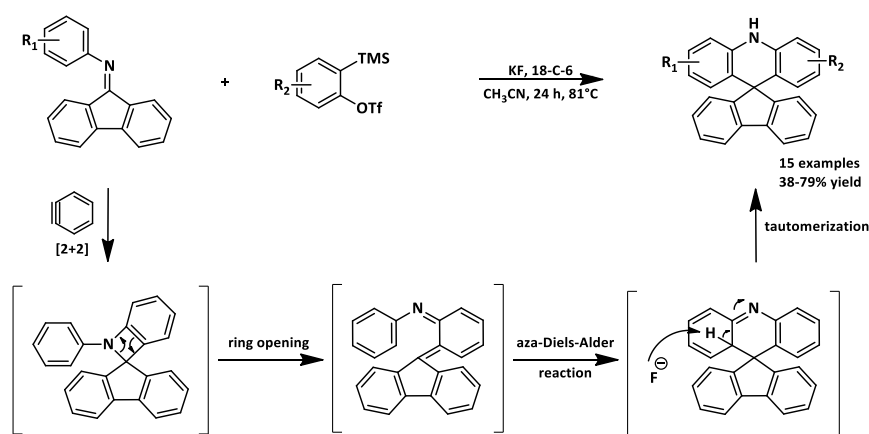
bromodiphenylamine entity or using a directed metalation. The opposite approach – nucleophilic addition to a protected acridone derivative – has been only used for preparation of spirobisacridane core. The nucleophilic addition results in an intermediate triarylcarbinol that is used further in intramolecular electrophilic cyclisation in acidic media, finally providing with the desired spiroaromatic molecular platform (**Scheme 2**). The latter step performed for the synthesis of the SBA core unsubstituted at in-plane N-atoms usually suffers from the aromatization of 9-dihydroacridinole to 9-substituted acridine. This reaction requires milder conditions: diluted acids, lower temperatures and rational use of the different protecting groups, enabling stepwise deprotection in acidic media¹²⁵.

Scheme 2. General synthetic approach towards spiroacridane compounds.



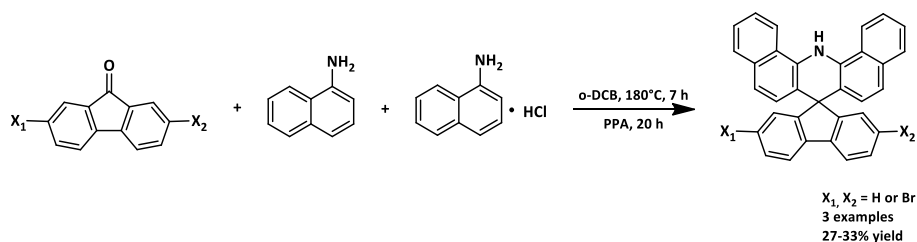
An alternative method for preparation of spiroacridane compounds has been recently reported by W.Wang et al¹²⁶. The authors describe a tandem [2+2] cycloaddition-ring-opening cascade using in situ generated benzyne and easily accessible fluorene-N-arylimines, thus demonstrating a facile synthetic approach towards a number of substituted 10H-spiro[acridine-9,9'-fluorenes] in moderate to good yields (**Scheme 3**).

Scheme 3. Tandem [2+2] cycloaddition-ring-opening reaction yielding spiroacridanes.



Y. Wei et al. reported a condensation of 1-naphthylamine and 1-naphthylamine hydrochloride with unsubstituted fluorenone and bromofluorenones at high temperature in acidic media (**Scheme 4**)¹²⁷. The desired spirocyclic acridane compounds were obtained in low yield and the procedure was not discussed in detail. The reported results strongly contrasted to the oxygen substituted congeners prepared similarly in high yields^{128,129}.

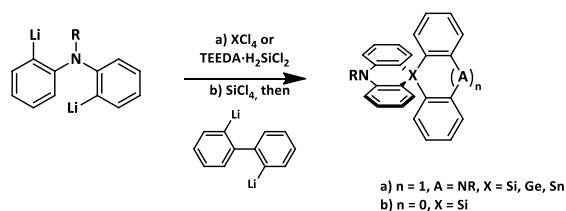
Scheme 4. Synthesis of 14H-spiro[dibenzo[c,h]acridine-7,9'-fluorene] from 1-naphthylammonium and fluorenone.



To the best of my knowledge, the first preparation of a number of spirocyclic acridane compounds with spiro-heteroatom connections has been reported in early 1960s by the group of J. D. Gabers. Synthesis of symmetric Si-spiro-fused arylamines requires treatment of 2 equivalents of bis-metalated arylamines with 1.0 equivalent of SiCl_4 to achieve better yields (**Scheme 5**)¹³⁰⁻¹³², the inversed addition of the reagents¹³³ or use of $\text{TEEDA} \cdot \text{H}_2\text{SiCl}_2$ complex¹³⁴ resulted in poorer formation of the desired spirobiphenazasiline. The addition of 1.0 equivalent of SiCl_4 to bismetalated diphenylamine followed by 1.0 equivalent of bis-lithiated biphenyl was demonstrated to

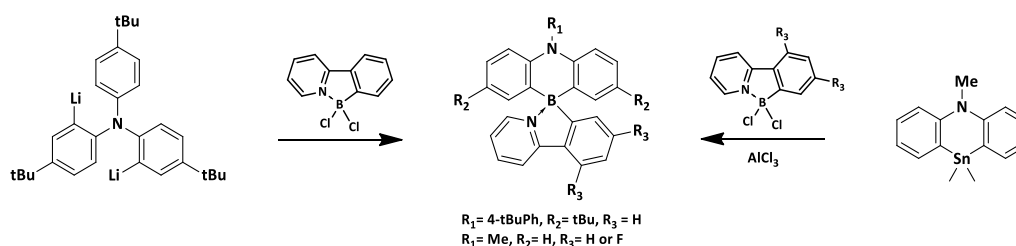
be an efficient synthetic route for centrally-asymmetric spiro-silafluorene-phenazasiline (**Scheme 5**)¹³⁵. Centrally-symmetric spiroacridanes with Ge (spirobiphenazagermines) or Sn (spirobiphenazastannines) spiro-node can be prepared analogously to spirodibenzoazasilines from bismetalated arylamines and the corresponding tetrahalides (**Scheme 5**)^{136,137}.

Scheme 5. General synthetic routes towards spiro-heteroatom acridanes.



Though I could not find any information, that spirobiphenazastannines had been utilized to prepare functional materials yet, their “monomeric” analogues phenazastannines were employed as reactants to synthesize boron-based spiro compounds (spiro-coordinated B complexes), using boro-destannylation followed by double arylation tandem reaction (**Scheme 6**)^{138,139}. Similar results can be achieved using a simplified protocol with bislithiated phenylamines. Both methods were reported to deliver the desired spiro-N-coordinated borane complex in modest yields of 30-50% (**Scheme 6**).

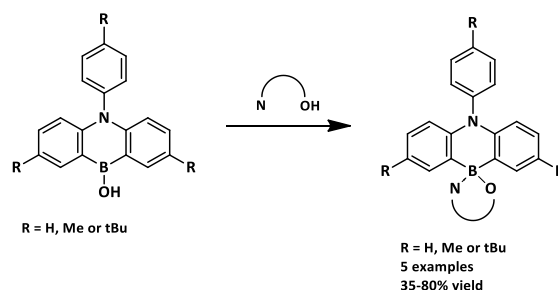
Scheme 6. Synthetic approaches yielding spiro-N-coordinated borane complexes.



Synthesis of spiro-N-coordinated borinate complexes was effectuated via cycloborinic acid intermediates followed by a condensation with a desired N-chelating phenolic reagent (**Scheme 7**)¹⁴⁰. The reaction occurred readily, delivering the spiro-

boron compounds in good to excellent yield, however the final products were reported to be sensitive to moisture.

Scheme 7. Synthetic route towards spiro-N-coordinated borinate complexes from cycloborinic acids.

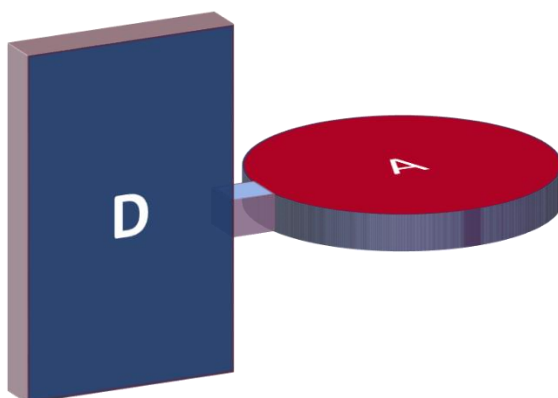


In this section I summarized methodologies for preparation of aromatic spirocyclic-acridane compounds that have been utilized as functional materials. Many other heterocyclic spiroacridanes reported to possess bioactivity as well as some *d*-block metal complexes, that can be formally considered as acridane spirocyclic compounds, are out of the scope of our research.

2.2. TADF materials based on spiro-acridane compounds

A number of exhaustive reviews on TADF materials and spirobifluorenes¹²⁰ for organic optoelectronics have been published. As opposed to these reports ranging the emitters according to the nature of acceptors or emission color^{63,141–143}, summarizing recent progress⁶¹, in this section I aim to discuss organic functional materials employing spiroacridane molecular motif. In addition, where possible, I describe how introduction of a spiro-connection affects the properties of the materials in relation to the widely employed congeners without the spiro-bridge: 9,9-dimethyl-9,10-dihydroacridine (DMA or DMAC) and 9,9-diphenyl-9,10-dihydroacridine (DPAC).

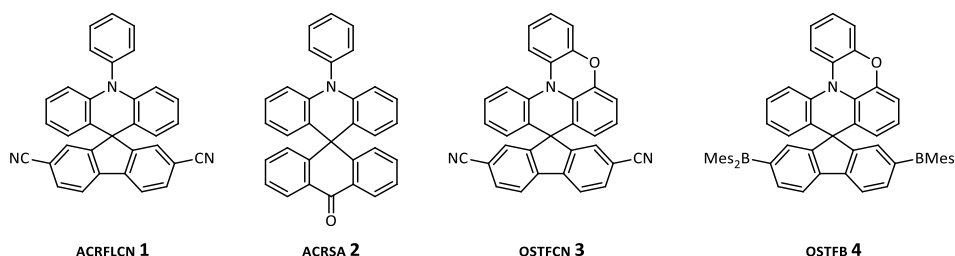
2.2.1. Separation of FMOs via spiro-atom



A spiro-connection of an acridane with another cyclic aromatic core with pronounced electron accepting properties allows efficient segregation of FMOs: in this case acridane accommodates HOMO, while the LUMO is located on the counterpart. Thus, the sp^3 -hybridized “insulating” σ -linkage efficiently breaks an orbital overlap and minimizes splitting between S_1 and T_1 according to the **Equation 5**.

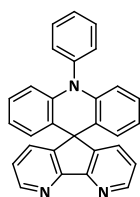
To the best of my knowledge, the very first TADF material ACRFLCN employing spiro-connection was reported by G. Méhes et al in 2012¹⁴⁴. The authors described the molecule composed of a donor N-phenyl acridane connected to a dicyanofluorene acceptor via spiro-carbon atom (D- σ -A structure). The electronically inert spiro-bridge lead to a spatial segregation of FMOs, leading to minimization of ΔE_{ST} . As a result, greenish-yellow fluorescence with strong delayed component and PLQY of 67.3% was

observed for a TPsi-F film doped with **ACRFLCN**. The OLED device employing **ACRFLCN** emitting dopant attained maximum η_{ext} of 10.1%. Moreover authors proposed oxygen sensing, demonstrating reversible quenching of the emission upon exposure to atmosphere with O₂.

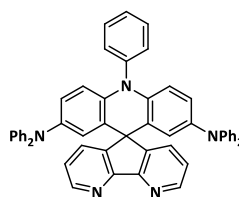


K. Nasu et al. have further reported the approach of FMOs segregation via sp³-hybridized C-spiroatom, describing a TADF emitter **ACRSA**, composed of the similar N-phenyl acridane donor and anthracenone acceptor¹⁴⁵. The new material demonstrated increased PLQY of 81%, blueish-green electroluminescence with the pronounced delayed component attributed to TADF. Maximum η_{ext} of 16.5% was attained in OLED device, clearly indicating an efficient utilization of “dark” electrogenerated triplet excitons. I. Lyskov et al. rationalized the enhancement of rISC and improvement of TADF properties by presence of low-lying intermediate $n\pi^*$ triplet states as well as strong vibronic and spin-orbit forces that promote faster back up-conversion⁴⁹.

Y.-K. Wang et al. have further developed the strategy with the separation of FMOs via spiro- σ -linkage¹⁴⁶. The authors described benefits of rigidification of the donor, introducing a bridging O-atom, and exploited an alternative B(Mes)₂ acceptor on the periphery of the fluorene unit. The tilted planes of D and A allowed better through-space-interactions of FMOs, facilitating RISC, but still retaining low ΔE_{ST} . High maximum EQE of 20.4% for **OSTFCN** was achieved in the OLED device. The boron-substituted congener **OSTFB** demonstrated maximum EQE of 18.8% and more red-shifted spectrum. The **OSTFCN**-based device demonstrated long LT₅₀ of 18000 h at practical luminance of 100 cd/m².

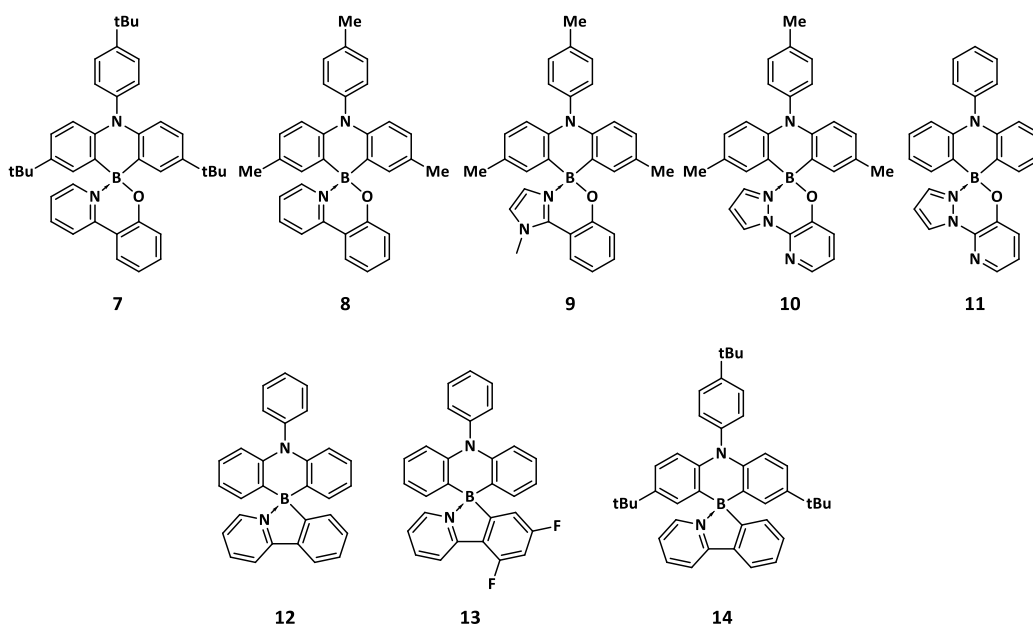


A-AF 5



DPAA-AF 6

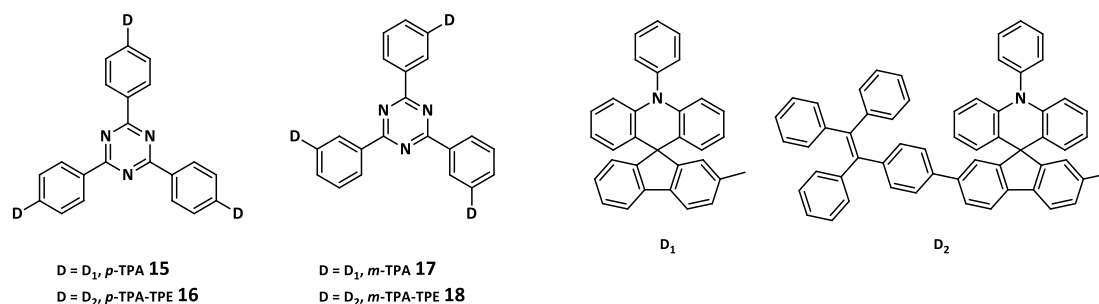
Substitution of the fluorene unit with 4,5-diazafluorene acceptor and combining it with N-phenyl acridane donor in **A-AF** resulted a fluorescent molecule with a sole fast ns component in trPL¹⁴⁷. The authors ascribe absence of the delayed component to a significant overlap of the frontier orbitals due to spiroconjugation, thus bringing about large ΔE_{ST} of 0.594 eV. Better localization/dispersion of HOMO over the electron donating pendant phenylamine groups lead to minimization of ΔE_{ST} splitting up to 0.021 eV for **DPAA-AF**. The substituted emitter displayed blue-greenish emission with a distinct TADF component. However, **DPAA-AF** employed in an OLED device attained maximum EQE of 9.6%.



Finally, another group of emitters is represented by four-coordinate B-complexes **7-14**, where boron atom not only connects aromatic entities in perpendicular arrangement but also serves as a node, not participating in either FMOs but allowing to tune them independently. Spiro-B-atom was claimed to provide structural rigidity to the

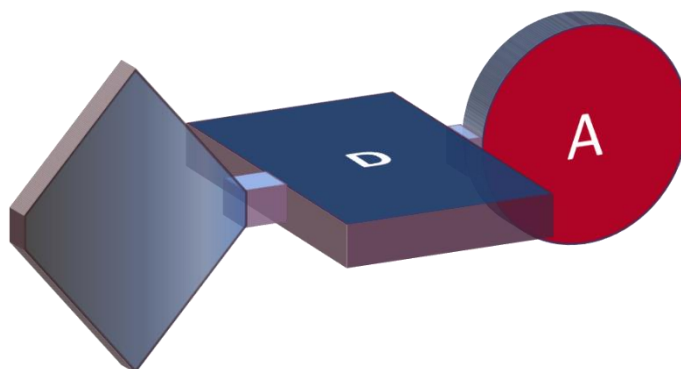
molecules and to increase acceptor strength, stabilizing and localizing LUMO over the N-heterocyclic aromatic plane. Series of these charge-transfer complexes exhibiting TADF have been reported by B.M. Bell et al.¹⁴⁰ and M. Stanoppi et al.¹³⁸ The former authors reported the spiro-oxazaborolo-compounds **7-11** (spiro-N-coordinated borinate complexes) to have tunable TADF emission across a wide range of colors and good PLQY in pristine films. However, only few selected materials have been utilized to fabricate TADF OLEDs. Spiro emitter **8** exhibited yellow emission and have attained maximum EQE of 8.3% with low luminance loss. The compound **9** showed very low luminance efficiency in the employed device stack to be measured and fully characterized.

M. Stanoppi et al. reported preparation and photophysical properties of the spiro-azaborolo-compounds **12-14** (spiro-N-coordinated borane complexes)¹³⁸. The TADF B-complexes were investigated in solid PMMA films: green to yellow TADF emission was detected with low PLQY in the range 25-33%. Degassed solutions exhibited emission with sole fast PL component. The authors rationalize TADF loss to conformational flexibility of the molecules causing strong radiationless relaxation of the excited molecules in solution (in contrast to the structural rigidity or spiro-oxazaborolo-compounds proposed by Bell et al.¹⁴⁰).

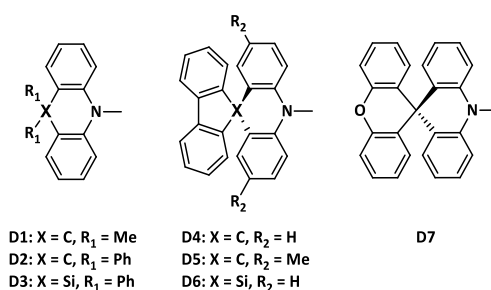


Y. Wang et al reported 4 star-shaped fluorescent molecules composed of a central triazine acceptor and spiroacridane periphery¹⁴⁸. Though HOMO and LUMO were calculated to be well segregated over the spiroacridane and triazine respectively, TADF properties of the materials have not been reported. The D-A starburst cores were further endowed with TPA-substituent to study aggregation-induced emission (AIE) properties and to fabricate conventional non-doped FOLEDs emitting bluish-green light with maximum EQE of 1.8%, when *m*-TPA-TPE was employed as the emitter.

2.2.2. Use of a spiro-pendant for construction of donor units



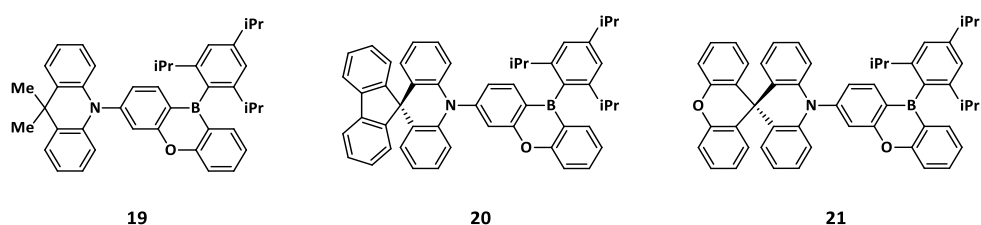
In this section I discuss spiroacridane-based emitters comprising an acceptor linked to the donor's in-plane N-atom directly or via π -bridge, while the spiro-pendant is utilized as a quasi-inert part of an acridane donor. I tackle to elucidate the impact of the introduction of the spiro-linkage to the donor motif comparing the reported properties of the spiroacridane emitters (**D4-D7**) to the simpler congeners (**D1-D3**) with acyclic methyl- or phenyl- substituents.



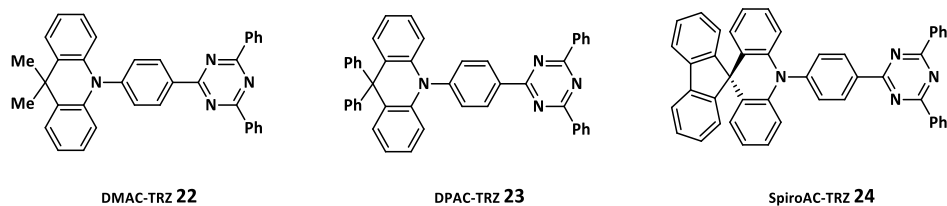
I try to group the characteristics that were induced thanks to the rigid spiro-cyclic entities and to figure out principles allowing to judiciously design an emitter with predetermined advanced properties. Also I sum up the properties of the rest of reported TADF emitters utilizing spiroacridane donors where a comparison with the “simpler” emitters is not possible due to a lack of the data reported.

2.2.3. Fine tuning of the electronic and emission properties: HOMO level tuning and introduction of new excited states

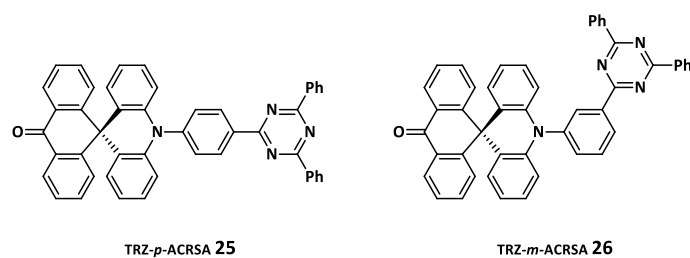
The substituents at 9-position of 9,10-dihydroacridine mainly do not participate in the π -system of the heterocycle. The sp^3 -hybridised carbon atom effectively breaks the conjugation spanning over the whole acridane system. However, depending on the substituents attached to the saturated node, it can affect the energy levels of acridane via inductive effect, hyper-/spiro-conjugation or accommodating additional energy levels that may affect emissive properties, allowing to finely tune electronic properties of a donor or of the entire emitter¹⁴⁹.



To the best of my knowledge the very first spiroacridane donors **D₄** and **D₇** for TADF materials have been introduced by M. Numata et al¹⁵⁰. The authors report a family of high efficiency pure blue emitters with a bulky 10H-phenoxaborin acceptor. The compounds demonstrated strong emission in toluene solutions with high PLQY up to unity. Introduction of the spiro-substituent to the emitters **20** and **21** was shown to blueshift the emission peak by *ca.* 20 nm as opposed to **19**; in the same time Stokes shift was substantially reduced. The authors point out that absorption and electrochemical properties of the TADF emitters were similar, associating the hypsochromic shift to the restriction of the Frank-Condon factor. However, differences in IP for the **D₁**, **D₄** and **D₇**-based compounds are noticeable and might be also associated to the blue shift observed for the emission of the spiro-based emitters **20** and **21**. The emitters **19-21** exhibited very high maximum η_{ext} in the range of 20%, being far beyond the efficiencies typical for conventional FOLEDS. The record of 21.7% efficiency was attained for **D₁**-based compound, however spiro-compounds **20** and **21** showed significantly purer blue color, closer to CIE requirements.

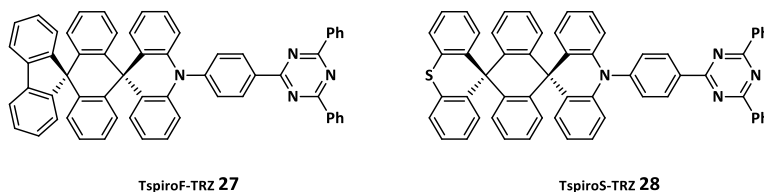


To the best of my knowledge, T.-A. Lin et al. the first discussed the noticeable inductive effect of the Me, Ph and spiro-fluorene pendants at 9 position of the acridane donor, reporting TADF molecules made of **D1**, **D2**, **D4** and triazine acceptor: **DMAC-TRZ**, **DPAC-TRZ** and **SpiroAc-TRZ** respectively. Expectedly, the substituents display an inductive effect altering the position of HOMO level of emitters and affecting the emission wavelength¹⁵¹, fully consistent with difference in oxidation potentials for unsubstituted acridanes **D1** and **D2** and related compounds, as reported by E. Sturm et al¹²³. The emitters with **D1** donor tend to display energy levels about 100 meV higher when assessed from the first oxidation potential in CV or UPS experiments, compared to the diphenyl-substituted acridane **D2** or spirocyclic **D4** or **D7**. Thus, even a small difference in energy levels affects the emission wavelength. Ceteris paribus, emission from materials comprising **D1** are ca. 10-20 nm bathochromically shifted as opposed to the aryl-substituted **D2** and spirocyclic acridanes **D4** and **D7**, whereas the differences in emission properties between the latter two are usually negligible, rendering these donors to be more suitable for the design of deep-blue TADF emitters.

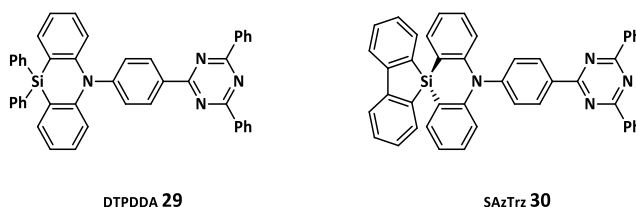


A stronger stabilization effect for the HOMO was proposed by L. Gan et al. for the TADF emitters **TRZ-p-ACRSA** and **TRZ-m-ACRSA** employing acridane donor with electron-accepting spiro-anthracenone substituent at 9 position¹⁵². The authors point out that introduction of the spiro-anthracenone does not participate in the π -conjugation spanning over acridane, as sp^3 -hybridized C-atom breaks the orbital overlap efficiently.

Moreover, the LUMO is fully located on the triazine acceptors and does not reside on **ACRSA**-donor. However, the electron-deficient spiro-pendant brings about multiple ^3LE and ^3CT states, fully consistent with a previous report⁴⁹. Different nature of these triplet states allows efficient SOC⁷⁶ and non-adiabatic VC^{47,48}, eventually increasing k_{rISC} up to 10^{-6} s^{-1} . **TRZ-p-ACRSA** utilized as an emitter in a TADF OLED demonstrated very high maximum EQE of 28% with reduced efficiency roll-off.



W. Li et al. claimed an acceleration of rISC process ($k_{\text{rISC}} \sim 10^{-5} \text{ s}^{-1}$) and simultaneous decrease of τ_{TADF} lifetime for the tri-spiral emitters **TspiroS-TRZ** terminating with spiro[anthracene-9,9'-thioxanthene] elongated pendant⁵³. The authors assumed that fast rISC might be caused with the presence of S-atom in the substituent that induced internal “heavy-atom effect” resulting in improved SOC and rISC acceleration. However the similar k_{rISC} were reported for **TspiroF-TRZ**, **SpiroAC-TRZ** and **DMAC-TRZ** that do not contain S-atoms. On the other hand, spiro[anthracene-9,9'-fluorene] substituent of the **TspiroF-TRZ** emitter was reported to accommodate a ^3LE state that is nearly degenerate to ^3CT of the acridane-triazine luminophore, eventually acting as an intrinsic non-radiative trap. The authors also emphasize that ^3LE levels of spiro[anthracene-9,9'-thioxanthene] unit lie about 200 meV higher than ^3CT of the luminophore and do not interfere with the emission.

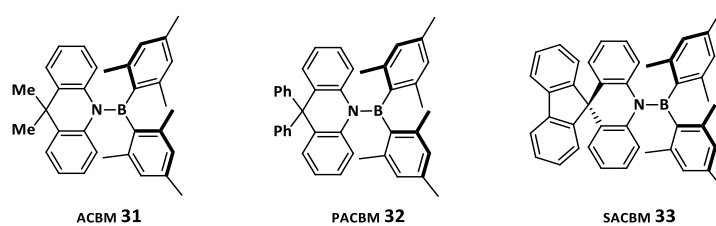


S.-J. Woo et al. reported the TADF emitter **SAzTRZ** made from spiro-silafluorene-phenazasiline donor **D6** and triazine acceptor. Introduction of spiro-Si atom lead to the

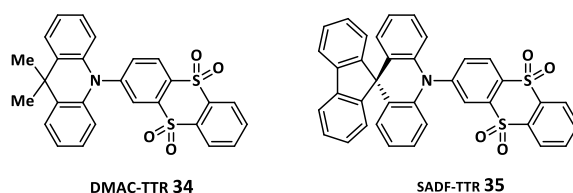
widening of the bandgap and significantly blueshifted emission, as compared to carbon-spirocyclic analogues^{135,151}. The bandgap for the deep-blue TADF emitter **DTPDDA** with diphenyl-substituted donor **D3** was almost similar to the spirocyclic **SAzTRZ** with **D6**¹⁵⁴. The authors also emphasized the importance of the judicious molecular design of azasiline based emitters for fine tuning of excited states as they strongly affect rISC mechanism and emission efficiency. While **DTPDDA** displays broad structureless CT-like radiative transition regardless the medium and temperature, the low-temperature phosphorescence and fluorescence emission spectra of **SAzTrz** in cyclohexane solution were structured, indicating the radiative transitions from the lowest lying ³LE state of the spiro-Si donor. The authors assume, that this order of excited states may imply energy losses associated with multiple transitions required for the up-conversion from the lowest lying ³LE to ³CT followed by rISC-assisted back-population of ¹CT. The single thermally-assisted transition in **DTPDDA** resulted in superior PLQY of $74 \pm 2\%$ (vs. 65% for **SAzTRZ**) in doped mCP:TSP0₁ solid films¹⁵⁴. Maximum EQE reported for the Si-containing emitters in operating OLEDs differ significantly (22.3% for **DTPDDA** vs. 20.6% for **SAzTRZ**), however the direct comparison is hardly possible due to different architectures utilized to fabricate the devices.

2.2.4. Rigidification and stabilization of a donor conformation

To the best of my knowledge, T.-A. Lin et al. the first reported the possible beneficial rigidification effect of spiro-jointed donor **D4** that may stabilize particular conformation of an emitter and thus improve its photophysical properties as opposed to more flexible **D1** and **D2** without spirocyclic entity¹⁵¹. The authors pointed out the correlation between bending angles of the acridane planes determined in single crystal XRD experiments (**SpiroAC-TRZ** < **DMAC-TRZ** < **DPAC-TRZ**) and PLQYs, suggesting that restriction of torsional and vibrational motions of a donor results in suppression of radiationless relaxation channels. Spiro-acridane **D4** coupled with triazine acceptor had the least folded acridane plane and demonstrated the highest PLQY of 100% in a host mCPCN matrix, while Me-endowed **D1** showed lower bending angle and higher PLQY (90%) compared to the emitter **D2** bearing bulky Ph (82%).



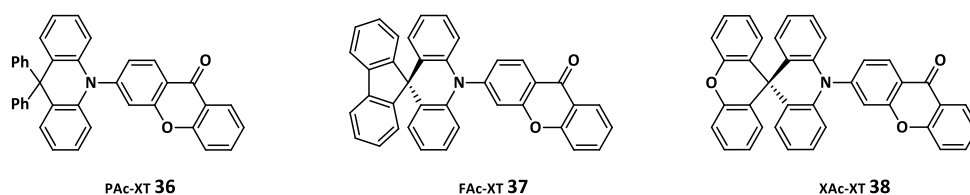
A family of B-endowed D-A conjugates with a direct N-B linkage and no common π -bridge, as a phenyl entity, was described by Lien Y.-J. et al to possess TADF properties¹⁵⁵. The authors demonstrate, that in order to achieve sufficient HOMO-LUMO separation, a molecule has to adopt a highly twisted conformation with quasi-equatorial arrangement of acridane donor and B(Mes)₂ acceptor. The substituents at 9,9-position of acridane appeared to have a paramount effect on the molecular geometry, thus favoring or disfavoring the emission via TADF channel. The spiro-endowed donor **D₄** (**SACBM**) preferably adopted the desired “quasi-equatorial” conformation with flattened acridane plane featuring strong TADF, whereas methyls (**ACBM**) and phenyls (**PACBM**) at the distal position were reported to force the molecule to adopt a conformation with quasi-axial arrangement of B(Mes)₂ unit. This arrangement lead to a shortening of B-N bond length due to enhancement of N \rightarrow B dative interaction at the ground state, and, as a result, poor HOMO and LUMO separation with reduced charge transfer (CT). In addition, in certain conditions, **SACBM** was possible to crystallize in two forms providing crystals with “quasi-equatorial” conformation and decreased delayed component in the emission (single crystal PLQY = 48.1% vs. 99.7%). The OLEDs fabricated using the **SACBM** demonstrated green emission and the highest, among other conjugates, maximum EQE of 19.1% (11.2% for **ACBM** and 4.1% for **PACBM**).



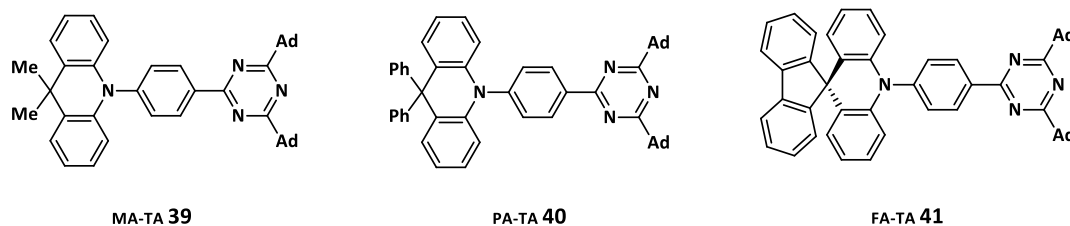
Soon after, K. Wang et al. reported thianthrene 5,5,10,10-tetraoxide-based emitters (**DMAC-TTR** and **SADF-TTR**), investigating energy losses associated with the

use of emitters comprising flexible 9,9-dimethyl-9,10-dihydroacridine **D1** donor moiety, widely employed to construct TADF materials⁷⁴. The authors emphasized that conformational lability of **D1** can lead to multiple semi-stable conformations with strikingly different photophysical properties due to widening of ΔE_{ST} gap. As a result, structural flexibility can lead to conformations with extended conjugation and poor FMOs segregation. This results in suppression of TADF radiation channel, severe energy losses and low performance of conformationally-flexible emitters in operating TADF devices. One of the strategies, proposed by the group, was the rigidification of the donor by employing spiro-junction. The use of **D4** instead of **D1** brought about the sole stable conformation with single TADF emission band and substantially improved maximum η_{ext} of 20.2% for **SADF-TTR** (vs. 13.9% for **DMAC-TTR**) in yellow-green part of the spectrum.

2.2.5. Avoiding the concentration quenching



Importance of donor bulkiness was demonstrated by J. Lee et al. investigating TADF concentration quenching mechanisms and the ways to suppress it¹⁵⁶. The authors pointed out, that non-radiative deactivation of TADF molecules prevailed via electron-exchange interaction for triplet excitons according to Dexter energy-transfer model. Thus, molecular structure of a donor can have a paramount effect to prevent concentration quenching, due to the short-range nature of Dexter energy transfer. The authors demonstrated, that the emitters comprising xanthone acceptors coupled with acridanes bearing bulky phenyls (**PAc-XT**), spiro-xanthene (**XAc-XT**) or spiro-fluorene (**FAc-XT**) pendants at 9,9-position, delivered high PLQYs in PPF films studied in wide range of concentrations. Minimal concentration quenching for the bulky emitters allowed to fabricate non-doped OLEDs attaining maximum η_{ext} of 11.2%, 14.1% and 12.6% for **PAc-XT**, **XAc-XT**, **FAc-XT** respectively.



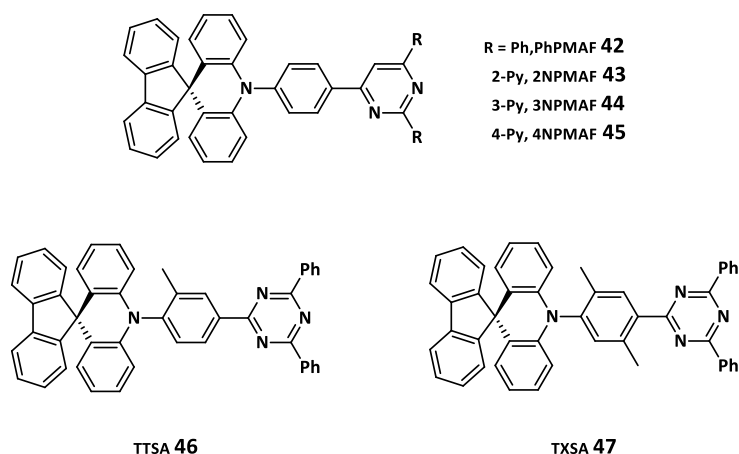
Y. Wada et al. reported TADF emitters **MA-TA**, **PA-TA** and **FA-TA** composed of adamantyl-substituted triazine acceptors attached to **D1**, **D2** and **D4** respectively designed for solution-processable OLEDs⁵⁷. The emission properties of the TADF conjugates were studied in a big variety of hosts with different doping ratio. The authors also reported improved solubility (for the **D2**-based molecule), significantly alleviated concentration quenching for the developed materials and emission blue-shift detected for the pristine thin films compared to the diluted toluene solutions. However, authors ascribe all these properties to the bulky electron donating adamantyl substituents that suppress interaction and Dexter energy transfer among emitter molecules in solid films. Interestingly, the similar emitter composed of **D4** and Ph-substituted triazines (**SpiroAC-TRZ**) were even less sensitive to the concentration PLQY quenching that suggests an importance of balanced acceptor design⁵¹. The solution processed TADF OLEDs exhibited maximum η_{ext} of 22.1%, 11.2% and 6.7% for **MA-TA**, **FA-TA** and **PA-TA**. The low efficiency for phenyl- and spiro-furnished emitter is strongly contrasting with the TADF emitters discussed above, however the authors point out, that OLEDs were optimized only for **MA-TA**.

Further elongation of the spiro-pendant as an “inert” substituent attached to the acridane donor also resulted in significantly suppressed aggregation-caused emission quenching, as described by W. Li et al⁵³. The authors report fabrication of non-doped devices employing the tri-spiral emitters **TspiroF-TRZ**, **TspiroS-TRZ** and **DMAC-TRZ**, **SpiroAC-TRZ** as references with simpler structures. The TADF materials with elongated spiro-pendants demonstrated excellent and, to date, the best performance for non-doped TADF OLEDs, achieving maximum η_{ext} of 16.5% and 20.0% respectively. Tested in similar conditions, the “shorter” and more compact emitters **SpiroAC-TRZ** and **DMAC-TRZ** demonstrated lower maximum EQE of 15.4% and 14.7%. Importantly, the similar trends for η_{ext} for the non-doped OLEDs were preserved for luminance of

100 cd/m², while **SpiroAC-TRZ** displayed inferior to **DMAC-TRZ** (EQE = 8.2% vs. 9.8% respectively) performance at very high luminance of 1000 cd/m².

The reported phenomenon, consisting on suppression of the concentration quenching using a spiro-endowed donors, was demonstrated in few other publications studying thin film PLQYs and/or optimal emitter doping concentration for OLEDs fabrication and demonstrated the advantage for emitters with **D₄** over **D₁** in all cases^{150,158}. However, geometry and bulkiness of an acceptor should be taken into account too, as the employment of different acceptors may induce significantly different PLQY drop in a function of emitter doping concentrations even upon use of structurally similar donors^{151,157,159,160}.

2.2.6. Tuning the proportion of horizontally oriented emitting dipoles



Isotropic emission from EML in OLEDs without preferential orientation of emitting dipoles and without light-outcoupling enhancement results in maximum EQEs (η_{ext}) limited by about 25% according to the **Equation 8**:

$$\eta_{\text{ext}} = \eta_{\text{int}}\eta_{\text{out}} \quad (8)$$

where η_{out} is light outcoupling efficiency and η_{int} is internal quantum efficiency.

Nevertheless, outcoupling efficiency can be enhanced by managing the distribution of the emitting dipoles orientation in the device EML. Anisotropic distribution of the emissive dipoles with the preferential perpendicular alignment in

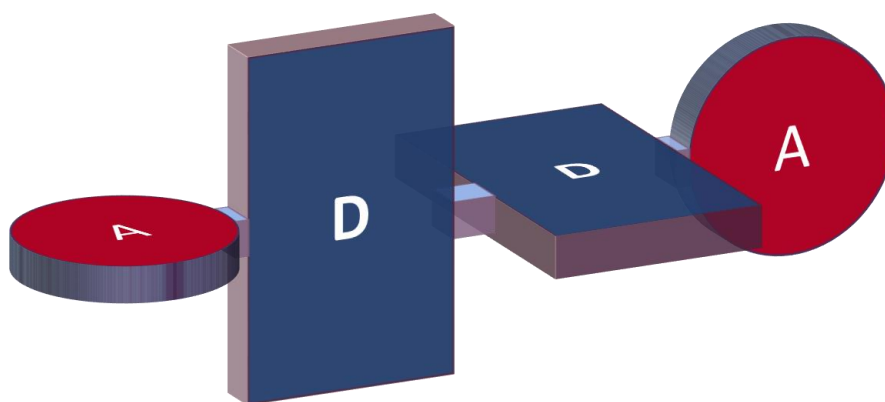
relation to the outcoupling vector can boost the EQE of the OLEDs up to 30% and beyond^{39-41,151}. The judicious molecular design was proven to be an efficient method to design molecules that are prone to have a high proportion of horizontally oriented emitting dipoles.

Very high maximum EQE of 37% has been reported by T.-A. Lin et al. for **SpiroAC-TRZ**¹⁵¹. The unusually value was associated to the strong tendency of the emitting dipoles of the spiro-endowed emitter to adopt horizontal orientation up to $\Theta_{||} = 83\%$, as opposed to the analogues **DMAC-TRZ** (72%) and **DPAC-TRZ** (78%) without spirocyclic substituent. The authors render this property to be intrinsic for the emitters, as it is hardly affected by host or/and the doping concentration. Moreover, Lin T.-A. et al. proposed that **SpiroAC-TRZ** is exhibiting the strongest anisotropy thanks to symmetrically balanced structure of the emitter with nearly coplanar phenyl-substituted triazine acceptor and structurally similar pendant fluorene that favors anchoring to a surface with the preferred orientation. The similar trends with very high ratio of horizontally-oriented dipoles (up to 86-91%) was reported for a family of structurally similar TADF emitters (41-45) composed of **D4** and pyrimidine acceptors¹⁶¹. Interestingly, **FA-TA** with bulkier adamantyl substituent was estimated to achieve maximum EQE only up to 20%, while a non-optimized OLED employing **FA-TA** attained maximum η_{ext} of 11.2%, thus suggesting that “balanced” structure might be beneficial for the preferred horizontal arrangement and increased light-outcoupling¹⁵⁷. In addition, **SpiroAC-TRZ** analogues **TTSA** and **TXCA** with Me-substituted π -bridge were shown to be isotopically distributed ($\Theta_{||} = 65\%$ for both emitters) when co-deposited with mCP/TSPO₁ matrix that might indicate that even a subtle structural change in a TADF emitter could strongly affect the emitting dipole orientation¹⁶². Importantly, in the same work significantly lower values of $\Theta_{||} = 71\%$ were reported for **SpiroAC-TRZ**, in contrast to the data reported by Lin T.-A. et al¹⁵¹.

An extension of the spiro-pendant for acridane donor was also proven to be advantageous to increase the ratio of horizontally oriented dipoles¹⁵³. The rod-shaped bulky tri-spiral TADF emitters **TspiroS-TRZ** and **TspiroF-TRZ** displayed exceptionally high horizontal orientation dipole ratio up to 90% and 88% respectively, allowing to achieve maximum EQE of 33.3% and 28.1% respectively for the doped OLEDs.

Finally, introduction of the Si-spiro-connection (**SAzTrz**) was also proven to favor the horizontal orientation of the emitting dipoles as well as for carbon-jointed analogues. Acyclic analogue **DTPDDA** was isotropically distributed ($\Theta_{||} = 66\%$) in a matrix^{154,162}, while its spiro-cyclic congener exhibited higher $\Theta_{||}$ of 70% when codeposited with mCPT:SPO₁ and 79% in DPEPO, thus demonstrating a clear dependence of $\Theta_{||}$ from medium used¹³⁵, in contrast to the report by T.-A. Lin et al¹⁵¹.

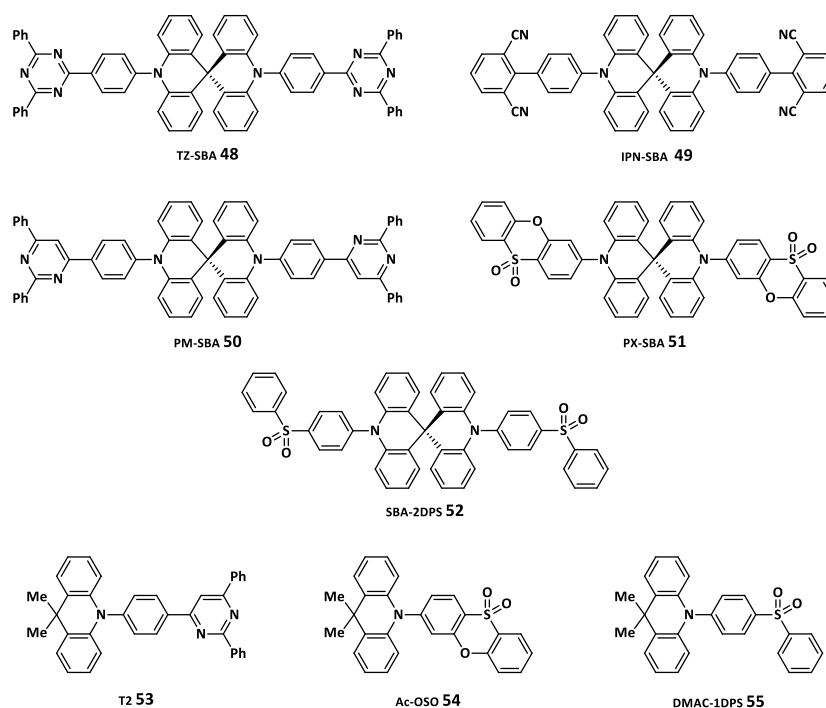
2.2.7. TADF materials based on spiro-bisacridane core



In this section, I discuss so far the least presented and employed structure of a twinned spiro-bisacridane donor. The spiro-node holds the acridane planes in a quasi-perpendicular arrangement and blocks their electronic communication via π -conjugation, thus allowing to consider them as two electronically independent donors. In the same time, SBA molecular platform is very versatile for a facile chemical modification at in-plane N atom as well as at the molecular periphery. Moreover, the complex 3D-platform allows to devise a final molecule with a predetermined stick-like or a globular shape.

M. Liu et al. the first reported employment of SBA-donor for a construction of a number (48-51) of symmetric stick-like TADF emitters¹⁵⁹. The authors demonstrated a family of highly efficient materials that can simultaneously benefit from a significant blue-shift, reduced aggregation quenching, and maintain reasonably high PLQYs in doped and neat films as opposed to the TADF materials employing Me-substituted **D1**, such as **DMAC-TRZ**¹⁵¹, **T2**¹⁶³ and **Ac-OSO**¹⁶⁴. On the other hand, the symmetric SBA-

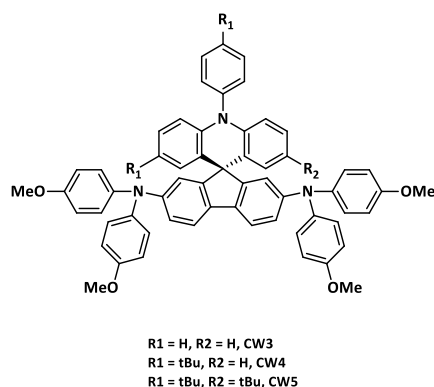
based emitters displayed slightly red-shifted PL emission compared the emitters with **D2** or **D4** donors, while the PLQYs reported for thin pristine and doped films are not consistent and scarce, thus not allowing to detect any correlation so far^{151,161}. However, the SBA-based TADF emitters adopted preferential horizontal alignment when vacuum co-deposited with DPEPO matrix ($\Theta_{||} = 86\text{-}93\%$), thus going beyond the previously reported records. As a result, the OLEDs employing the SBA-emitters attained excellent η_{ext} ranging from 21% for blue emission to 35% for green.



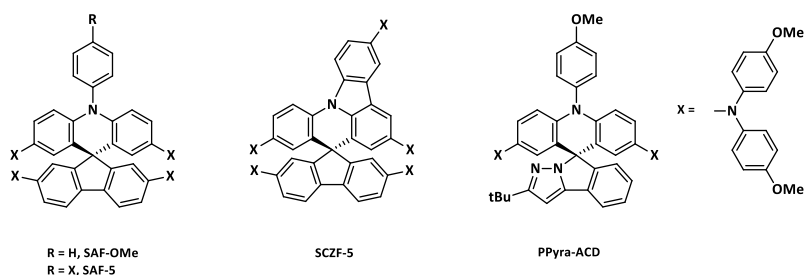
Recently, Zeng et al. reported a comparative study of two TADF emitters based on SBA twinned donor and the monomeric congener **D1**¹⁶⁵. The authors also reported a significant blue-shift for the spiro-twinned emitter **SBA-2DPS** and very high $\Theta_{||}$ of 87%, indicating strong tendency of the SBA-based emitting dipoles to orient horizontally, while the **D1**-based congener **DMAC-1DPS** was distributed isotropically even with slight vertical orientation in the DPEPO host matrix ($\Theta_{||} = 59\%$). As a result, OLEDs with **SBA-2DPS** were fabricated and demonstrated high maximum EQE of 25.5% and light outcoupling efficiency η_{out} of 38.2% (maximum $\eta_{\text{ext}} = 17.4\%$, $\eta_{\text{out}} = 24.7\%$ for **D1**-analogue).

2.3. Hole transporting materials for PSCs

Charge transporting layers are indispensable components for state-of-the-art PSCs. Spiro-based HTMs remain to be one of the most used organic charge selective layers for perovskite photovoltaics thanks to their excellent solubility and processability properties allowing to spin-cast smooth and morphologically stable amorphous thin layer. Many reviews have been published summarizing recent progress and scrutinizing structure-performance relationship for state-of-the-art HTMs, including spiro-core based materials. Surprisingly, despite the ease to construct spiro-acridane structure or to incorporate it into the final HTM, only few examples were found in literature, nonetheless reporting very promising properties of spiro-acridane based HTMs.



To the best of my knowledge, Li M.-H. et al. the first reported spiro-acridane based hole-transporting materials for PSCs¹⁶⁶. The HTMs **CW₃**, **CW₄** and **CW₅** were constructed from two different fragments: TPAs and DMPA-substituted biphenyl held together orthogonally via spiro sp^3 -hybridized carbon atom. Thus the structure was mimicking spiro-MeOTAD from only one side, while the orthogonal counter-unit was different and appeared to increase T_g . On the contrary, the HOMO levels were almost unaffected and reported to be ~ -4.9 eV. The spiro-acridane HTMs were used to fabricate *n-i-p* mesoscopic PSCs. The materials were doped only with *t*BP and LiTFSI and no Co-oxidant: the cells containing **CW₄** outperformed other spiro-acridane HTMs as well as the benchmark spiro-MeOTAD (**Table 1**).



Wang Y.-K. et al. reported the further use of spiro-fluorene-acridine platform to construct advanced HTM **SAF-OMe** that can operate in PSCs without dopants, comparing it with the etalon spiro-MeOTAD¹⁶⁷. In contrast to **CW-HTMs**, **SAF-OMe** bears two extra DMPA substituents attached to the acridane fragment, thus combining spiro-MeOTAD and PTAA monomer units in one molecule. The authors also report slight destabilization of HOMO (-5.07 eV) in relation to the reference spiro-MeOTAD (-5.22 eV), that can be associated to the presence of DMPA donors attached to the electron-rich acridane fragment. Moreover, doped **SAF-OMe** exhibited three times higher hole mobility, thus opening an avenue to the superior performance in PSCs. Importantly, the spiro-acridane HTM was proven to operate even without dopants, attaining high PCE of 12.39%, while the spiro-bifluorene-based reference could demonstrate only modest PCE of 5.91%. In addition, dopant-free **SAF-OMe** HTLs demonstrated improved hydrophobic properties and eventually better storage stability at RH \approx 30%.

Zhu X.-D. et al. have reported analogous HTMs **SAF-5** and **SCZF-5** bearing five DMPA units¹⁶⁸. Additional DMPA donors attached to the Ph-substituent have further increased electron density on the acridane core and further destabilized HOMO of **SAF-5** (-5.02 eV) in relation to **SAF-OMe**. The ligation of the Ph-pendant to the acridane unit, on the contrary, expanded the π -conjugation and lead to a deeper HOMO level for **SCZF-5** (-5.22 eV), better aligned to the valence band of MAPbI₃ perovskite (-5.34 eV). Hole mobility of the doped **SCZF-5** was almost twice higher compared to **SAF-5**, and might be associated with more rigid structure and better charge delocalization over the carbazole-comprising HTM. As a result, PSCs fabricated with **SCZF-5** HTL attained the highest PCE of 20.10%. Similarly to **SAF-OMe**, **SAF-5** and **SCZF-5** demonstrated bigger water contact angles than spiro-MeOTAD, resulting in better storage stability without any encapsulation at RH \approx 30%.

Wang Y. et al. reported a family of spiro-phenylpyrazole-based HTMs¹⁶⁹. The hole-selective material **PPyro-ACD** comprising spiroacridane unit displayed the highest HOMO level (-4.96 eV) compared to spiro-xanthene (-5.24 eV) and spiro-thioxanthene (-5.24 eV) congeners. Poor alignment of the acridane HTM and MAPbI₃ energy levels in a planar PSC lead to the worst performance among the new materials studied and spiro-MeOTAD reference, thus emphasizing the importance of careful molecular design for electron excessive spiro-acridane materials.

Table 1. Photovoltaic performance of PSCs employing spiro-acridane HTMs.

HTM	Perovskite	V _{OC} , V	J _{SC} , mA/cm ²	FF	PCE, %	PCE _{ref} , %	Ref.
CW₃		0.989	16.49	0.67	10.94		
CW₄	MAPbI ₃	1.05	21.75	0.72	16.56	14.32	¹⁶⁶
CW₅		1.01	15.39	0.7	10.76		
SAF-OMe (undoped)	MAPbI _{3-x} Cl _x	1.05 (0.97)	21.07 (20.59)	0.76 (0.62)	16.73 (12.39)	14.84 (5.91)	¹⁶⁷
SAF-5	MAPbI ₃	1.07	20.41	0.63	13.93	18.11	¹⁶⁸
SCZ-F		1.11	24.40	0.74	19.16		
PPyra-ACD (undoped)	MAPbI ₃	0.77 (0.46)	11.28 (3.25)	0.58 (0.32)	5.01 (0.48)	16.15 (8.51)	¹⁶⁹

CHAPTER 3

PHOTOPHYSICAL PROPERTIES OF SPIROBISACRIDANE-BENZONITRILE TADF EMITTERS

We designed and synthesized a new organic light-emitting diode emitter, **SBABz4**, containing spiro-biacridane donor (D) in the core surrounded by two benzonitrile acceptors (A). The dual A–DxD–A structure is shown to provide pure-blue emission in relation to its single A–D counterpart. Time-resolved photoluminescence (TRPL) recorded in the broad dynamic range from solutions and solid films revealed three emission components: prompt fluorescence, phosphorescence, and efficient thermally activated delayed fluorescence (TADF). The last is independently proven by temperature-dependent TRPL and oxygen-quenching PL experiment. From the PL lifetimes and quantum yield, we estimated maximum external quantum efficiency of 7.1% in **SBABz4**-based OLEDs and demonstrated 6.8% in a working device..

This chapter is based on the published work: *J. Phys. Chem. C* **2018**, *122*, 22796–22801.

DOI:10.1021/acs.jpcc.8b08716

(Equal contribution with Liudmila G. Kudriashova)

Authors: Nikita A. Drigo, Liudmila G. Kudriashova, Sebastian Weissenseel, Andreas Sperlich, Aron Joel Huckaba, Mohammad Khaja Nazeeruddin and Vladimir Dyakonov

In this work I conceptualized, synthesized and characterized all organic materials, performed data analysis and partly wrote the manuscript.

3.1. Introduction

Thermally activated delayed fluorescence (TADF) changed the field of organic optoelectronics since the first reports by Adachi and co-authors in 2011^{37,38}. Internal electroluminescence quantum efficiencies close to 100% and outstanding external quantum efficiencies (EQE) above 30% were achieved in the number of organic light-emitting diodes (OLEDs) employing metal-free TADF emitters^{151,159,170-173}. This tremendous research progress was caused by high application potential of the new OLED generation, as well as by fascinating TADF photophysics.

Electrical injection of carriers produces singlet and triplet excitons with 1:3 branching ratio, reducing the emission probability to 25% of the entire excited population in organic semiconductors. Therefore, maximum internal electroluminescence efficiency of conventional OLED emitters does not exceed 25%, imposing a theoretical limit of 5-7.5% on EQE of the devices with 20-30% light outcoupling. Along with the triplet-triplet annihilation^{174,175} and heavy-metal-complex phosphorescence^{19,20,176,177}, TADF was shown to take advantage of dark triplet states, subsequently improving internal electroluminescence efficiency. TADF opened the way to fully overcome the efficiency-limiting spin statistics by thermally activated triplet-to-singlet up-conversion.

The efficiency of the triplet up-conversion, which occurs via reverse intersystem crossing (rISC), increases with decreasing singlet-triplet energy splitting, ΔE_{ST} .¹⁷⁸ ΔE_{ST} is commonly rendered low by a large dihedral angle between donor (D) and acceptor (A) moieties and consequently small HOMO-LUMO spatial overlap. This conformational requirement significantly limits the variety of possible donor-acceptor pairs for intramolecular TADF. On the other hand, energies of the HOMO and LUMO, together with the spatial overlap of the orbitals, define the optical properties essential for applications, emission color in particular. Molecular design of pure blue emitters is especially challenging since they should combine wide optical gap, narrow luminescence spectrum, and sufficient radiative efficiency. Therefore, despite the vast demand of organic optoelectronics, deep blue TADF emitters remain scarce^{69,150,159,172,179}

The majority of intramolecular TADF emitters currently presented in literature have a D-A-D structure with one or several donor moieties attached to a single acceptor in the core. Alternatively, molecules with dual emissive cores were shown to be superior in performance to their single-core analogs^{180,181}. Moreover, several spiro-linked donors were developed to provide rigid stick-like structure and partial self-orientation of the molecules^{151,182}. This approach enhanced light outcoupling, resulting in an efficiency breakthrough in the blue TADF-based OLEDs. However, photophysics of TADF emitters with a double donor in the core, as well as the role of spiro-linkage is yet to be revealed.

Herein we present a novel compact deep-blue TADF emitter with a spiro-bisacridane double donor core surrounded by two benzonitrile acceptors. We determine the correlation between structure and luminescence properties of this dual A-DxD-A compound in relation to its single A-D counterpart. The spiro-bi-donor shifts the emission to the deep blue region. The blue emitter combines phosphorescence at low temperature with TADF at room temperature. We show that the emitter is applicable for OLEDs and demonstrates $EQE_{\text{max}} = 6.8\%$ in a test device. We also compared photophysical properties of the neat emitters with those dispersed in (bis[2-(diphenylphosphino)-phenyl]ether oxide) (DPEPO) matrix¹⁸³ in order to study the luminescence quenching effects and the influence of molecular environment.

3.2. Results and discussion

Figure 10a shows the molecular structures of 4,4'-(10H,10'H-9,9'-spirobi[acridine]-10,10'-diyl)dibenzonitrile (**SBABz₄**) and its monomer counterpart, 4-(9,9-dimethylacridin-10(9H)-yl)benzonitrile (**DMABz₄**). The deep HOMO of SBA or DMA donor was combined with shallow LUMO of benzonitrile acceptor to provide a wide optical gap sufficient for emission in the blue-green region^{52,159,184}. Mutual arrangement of H-atoms at the peri-position of the acridane and at *o*-position of the acceptor's phenyl ring impedes D-A rotation, resulting in a semi-frozen conformation with a large dihedral angle between the acridane and benzonitrile planes⁵². This nearly orthogonal D-A orientation is expected to break the HOMO-LUMO spatial overlap, thus decreasing the ΔE_{ST} and giving rise to TADF.

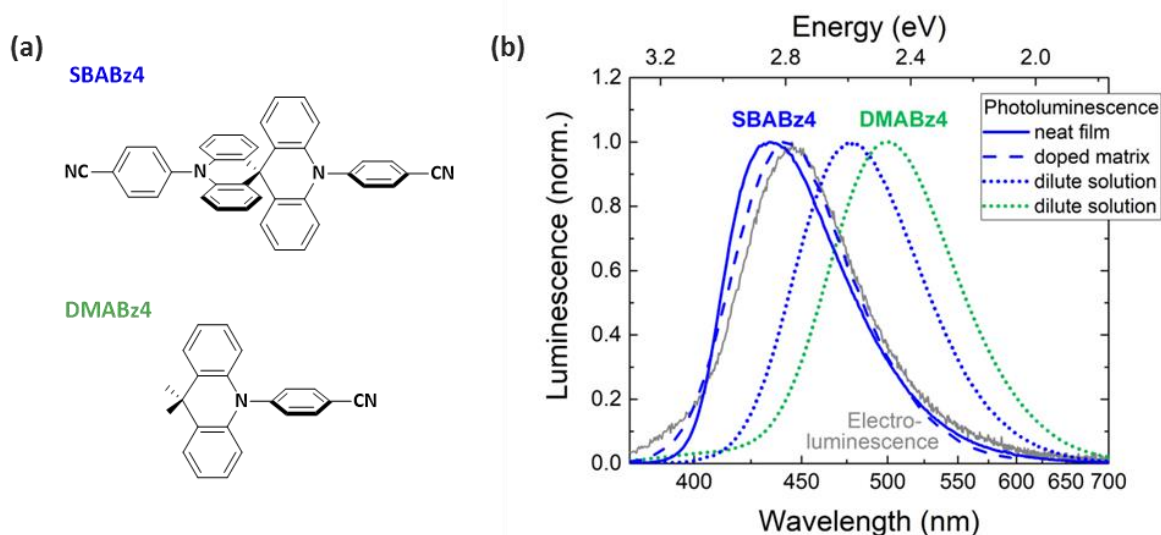


Figure 10. (a) Structural formulas of **SBABz4** and **DMABz4** emitters. (b) Normalized PL spectra of **SBABz4** (blue) and **DMABz4** (green). Solid, dashed, and dotted colored lines represent neat film, doped 5wt% **SBABz4**:DPEPO matrix, and dilute solutions in dichloromethane (DCM), respectively. Grey solid line shows electroluminescence from **SBABz4**-based OLED.

We prepared the SBA core using a modified procedure by Ooishi et al¹²⁵. We used *sec*BuLi for ortho-directed lithiation and milder (diluted HCl) conditions for the intramolecular cyclization. The optimized synthesis was carried out on a milligram-to-gram-scale with shortened reaction times and improved total yield. DMA core was synthesized according to the published protocol¹⁸⁵. Buchwald-Hartwig amination with 4-bromobenzonitrile concluded the preparation of the desired emitters (**Scheme 8**).

Scheme 8. Synthetic scheme for preparation of SBA-platform, SBA- and DMA-based TADF emitter.

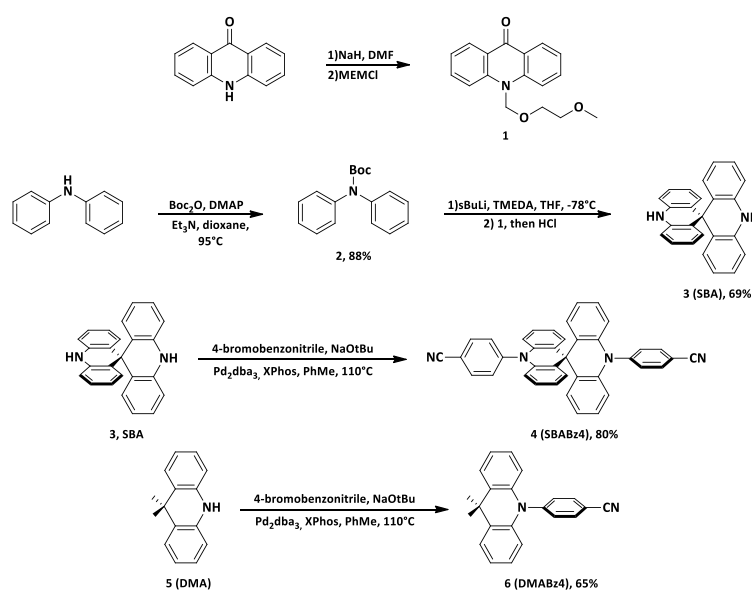


Table 2. Thermal, electrochemical and photophysical properties of **DMABz₄** and **SBABz₄**.

Parameter	DMABz₄	SBABz₄
T _d , °C	270	440
HOMO, eV ^[a]	-5.75 eV	-5.79 eV
LUMO, eV ^[a]	-2.50 eV	-2.49 eV
λ _{abs} , nm	280, 363	280, 302, 363
λ _{em} , nm ^[b]	411, 468, 517, 532	407, 453, 493, 509
PLQY, w/o O ₂	(83.8 ± 2.0)%	(55.7 ± 1.3)%
PLQY, with O ₂	(3.3 ± 0.5)%	(8.2 ± 0.2)%

[a] Converted to the NHE by adding +0.69V and converted to vacuum scale by adding +4.44 eV.

[b] Emission peak values for the dilute solutions in cyclohexane, tetrahydrofuran (THF), acetonitrile, and methanol respectively.

Figure 10b displays normalized photoluminescence (PL) and electroluminescence (EL) spectra of **SBABz₄**, recorded in a neat film, a doped 5wt% **SBABz₄**:DPEPO matrix, dilute dichloromethane (DCM) solution, and **SBABz₄**-based OLED. **SBABz₄** has pure blue emission peaking at 435 nm for the neat film. EL from the **SBABz₄**-based device is in excellent agreement with the PL from the corresponding doped matrix. The structureless luminescence spectra with significant positive solvatochromism (**Figure 11a,b**; **Table 2**) indicate the emission from CT state¹⁸⁶.

Figure 10b compares PL spectra of **DMABz₄** and **SBABz₄** dilute solutions in DCM. Whereas **SBABz₄** shows blue emission ($\lambda_{max} = 470 \text{ nm}$), emission from the **DMABz₄** is blue-green ($\lambda_{max} = 500 \text{ nm}$). Photoluminescence quantum yields (PLQYs) of the deoxygenated **SBABz₄** and **DMABz₄** solutions are 55.7% and 83.8% respectively (**Table 2**). Altogether, spiro-linkage in the **SBABz₄** core provides blue shift of the emission, while preserving reasonably high PLQY.

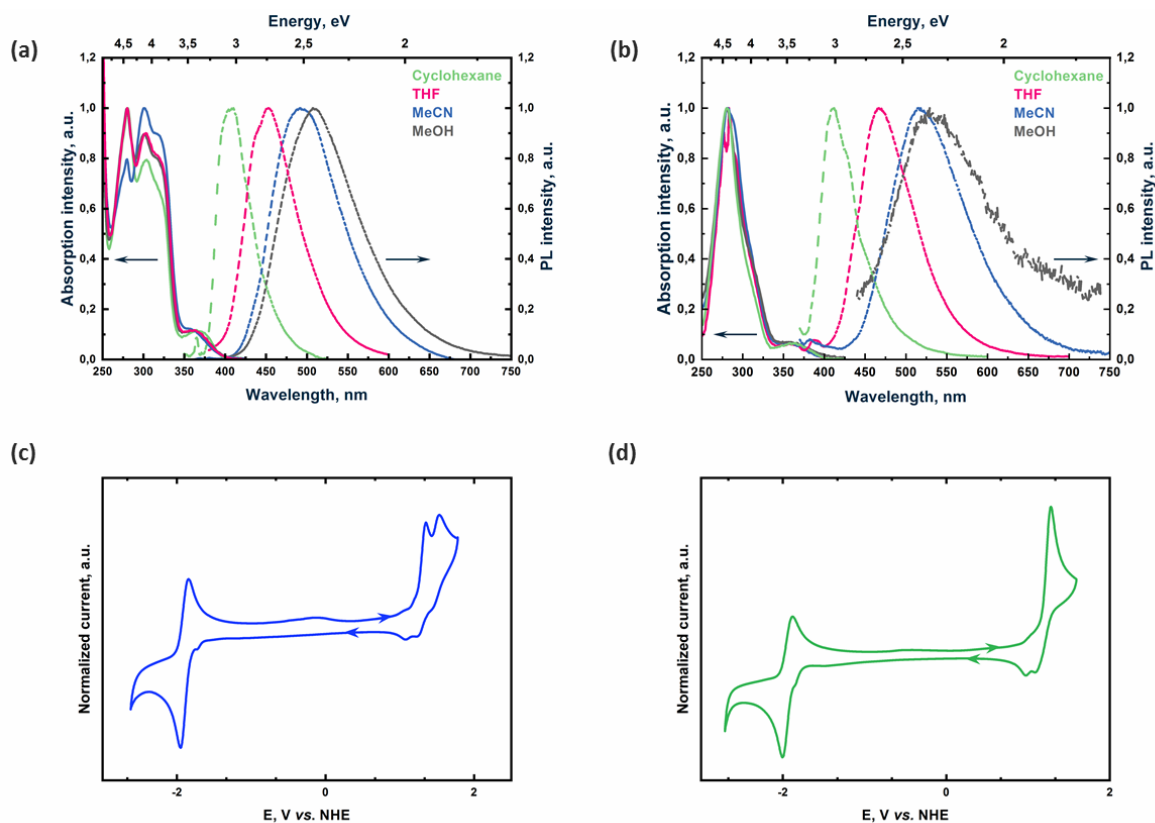


Figure 11. Ultraviolet-visible absorption and PL spectra of (a) **SBABz₄** and (b) **DMABz₄** in different solvents. Voltammograms of (c) **SBABz₄** and (d) **DMABz₄** in a 0.1 M solution of Bu₄NPF₆ in dry deoxygenated DMF at room temperature under N₂ atmosphere, measured with glassy carbon working electrode, Pt wire reference and counter electrodes, ferrocene/ferrocenium (Fc/Fc⁺) as internal standard.

Currently prevailing TADF design with core-acceptor allows PLQY improvement via an increase in the number of donor units or the donor conjugation length^{38,69,184,187}. The resulting bulky donor inevitably causes a red shift of luminescence, because of less localized and/or less stabilized HOMO. Alternatively, the rigid spiro-linkage maintains a large dihedral angle between the acridane subunits in the **SBABz₄** core, thus breaking the overlap between donor parts and introducing the desired blue shift into the emission. At the same time, the doubled number of emissive units still allows to maintain high luminescence efficiency. Therefore, **SBABz₄** was chosen for further study and fabrication of pure blue OLEDs.

Figure 12 demonstrates transient PL and normalized PL spectra at different stages of decay for a solid 5wt% **SBABz₄**:DPEPO film at room (298 K) and low (77 K) temperatures. Transient PL at both temperatures contains fast and slow components.

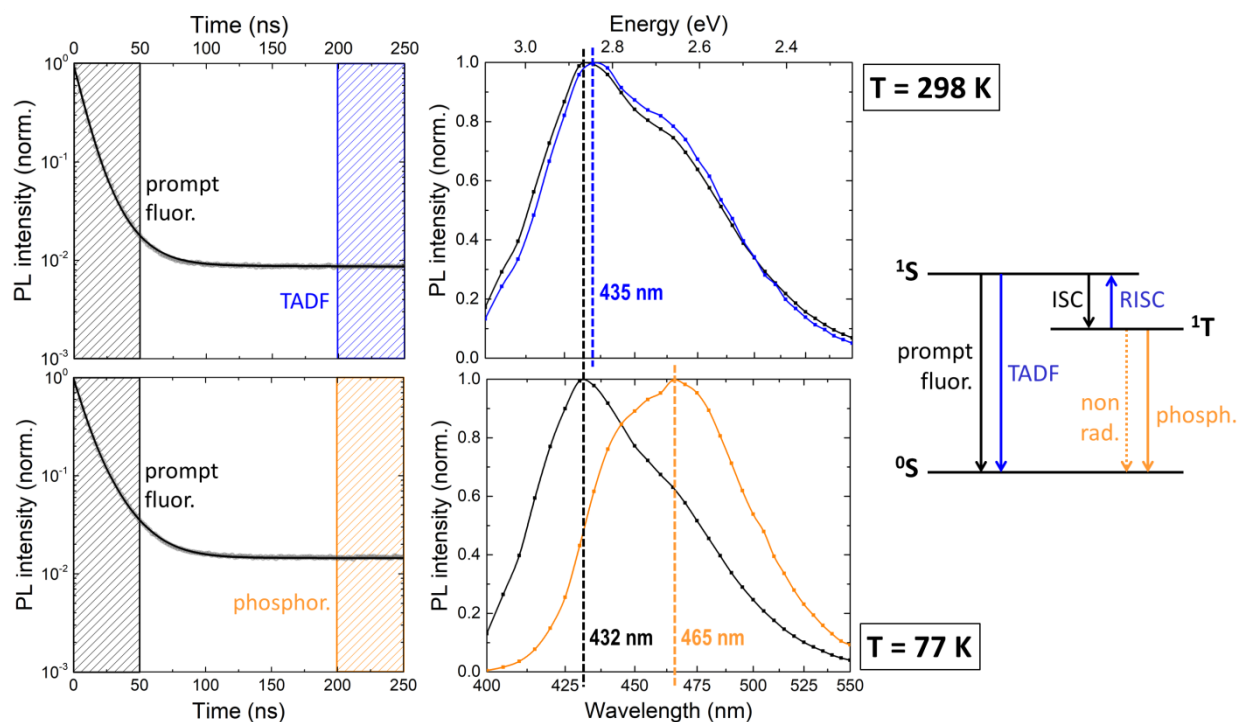


Figure 12. PL decay curves and the corresponding normalized PL spectra at different stages of decay in 5wt% **SBABz4**:DPEPO film at 298 K (upper plots) and 77 K (lower plots). Prompt components were integrated within 0-50 ns, delayed within 200-250 ns. Right: proposed energy diagram of the respective processes.

The fast component, peaking at 435 nm, dominates within the first 100 ns of decay regardless of the temperature. We ascribe this component to the prompt fluorescence from the ^1CT level. PL spectrum of the slow component at 77 K has noticeable red shift relative to the prompt one. Therefore, we assume that the slow component at low temperature is phosphorescence from lower-lying triplet. In contrast, the spectrum of the slow PL component at room temperature practically coincides with the prompt fluorescence. Thus, the delayed emission at room temperature originates from the same ^1CT level as the prompt fluorescence. Therefore, we assign it to TADF, mediated by slow reverse intersystem crossing. The corresponding energy diagram is depicted in the **Figure 12**. Neat **SBABz4** film qualitatively showed the same behavior (**Figure 29**).

Figure 13 shows steady-state and time-resolved emission from a dilute solution of **SBABz4** in DCM before and after oxygen exposure. Whereas the shape and position of PL spectrum remained unchanged under oxygen exposure, PLQY decreased sevenfold (from 55.7 to 8.2%, **Figure 13a** and **Table 2**). The transient PL contains prompt and

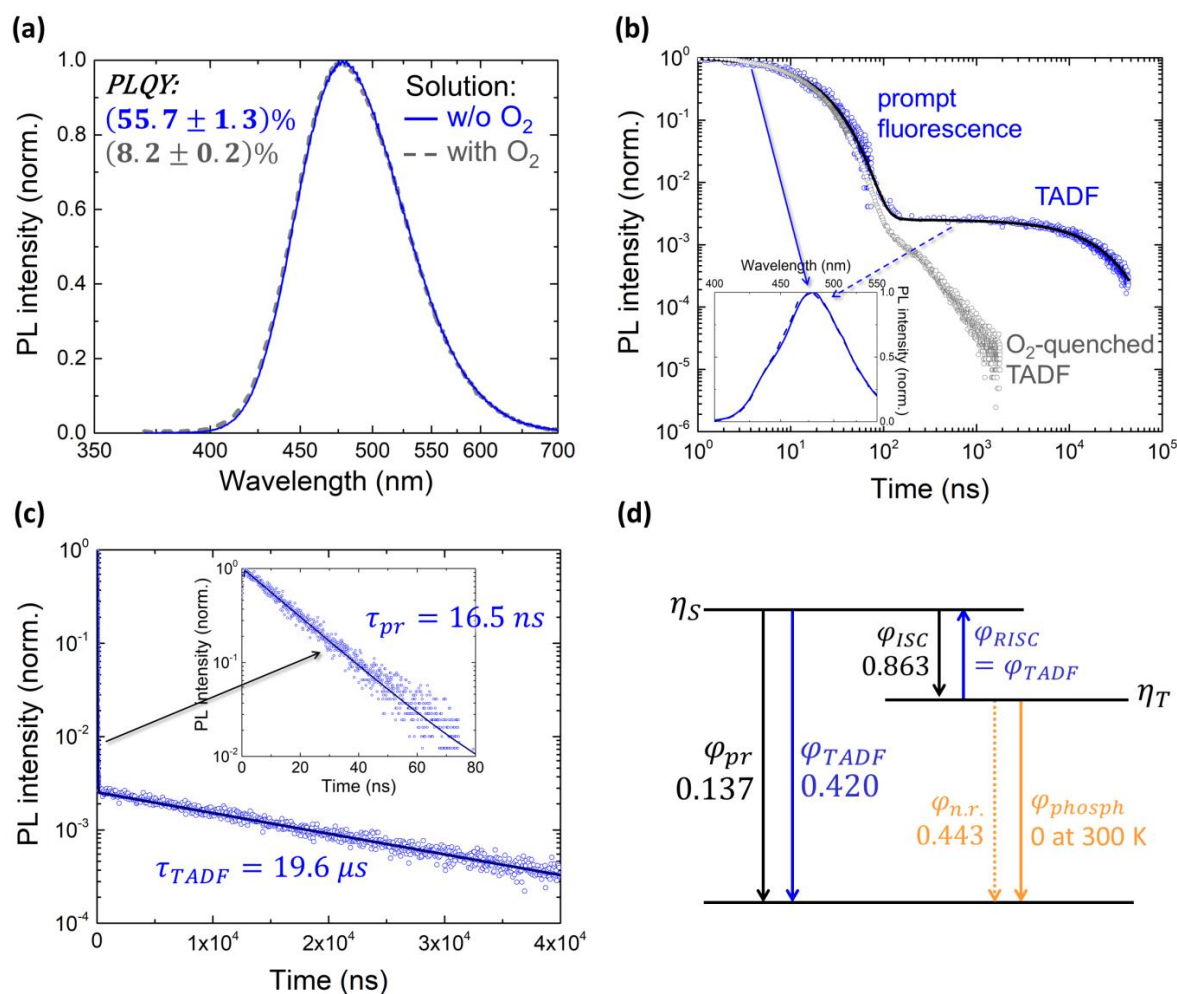


Figure 13. Steady-state and transient PL of dilute ($10^{-5} \text{ mol L}^{-1}$) oxygenated (grey) and deoxygenated (blue) solutions of **SBABz4** in DCM at room temperature. (a) PL spectra normalized at the peak value. (b) Transient PL detected at 475 nm. The inset: normalized PL spectra recorded within 0-25 ns (solid) and 150-1500 ns (dashed) of the decay. (c) Transient PL of the deoxygenated solution on a semi-logarithmic scale. Inset: the prompt component. (d) Energy diagram depicting quantum efficiencies of the involved processes.

delayed components (**Figure 13b**) with identical spectra (**Figure 13b**, inset). The fast component remains unaltered in the presence of oxygen. Therefore, we ascribe it to prompt fluorescence from ¹CT. In contrast, the slow component is substantially quenched by oxygen. Therefore, we assign it to TADF from ¹CT level populated via rISC. **Figure 13c** shows the same PL decay curve from the deoxygenated solution on a semi-logarithmic scale, where the straight lines indicate the purely monoexponential character of both decay processes. Characteristic time constants (16.5 ns for the prompt fluorescence and 19.6 μs for TADF), were extracted from the double-exponential fit, fully

consistent with luminescence from simple three-level system with triplet up-conversion (**Figure 13c**).

Contribution of the prompt and delayed components in the total PLQY can be calculated numerically as the area under the decay curve or, in the simple case of monoexponential fit, expressed through the magnitudes and lifetimes of the components:

$$\varphi_{pr} = \frac{A_{pr}\tau_{pr}}{A_{pr}\tau_{pr} + A_{TADF}\tau_{TADF}} \cdot PLQY \quad (9)$$

$$\varphi_{TADF} = \frac{A_{TADF}\tau_{TADF}}{A_{pr}\tau_{pr} + A_{TADF}\tau_{TADF}} \cdot PLQY \quad (10)$$

Here φ_{pr} and φ_{TADF} are quantum efficiencies of the prompt fluorescence and TADF; A_{pr} and A_{TADF} are magnitudes of the decaying exponents; τ_{pr} and τ_{TADF} are respective lifetimes; $PLQY$ is the measured total photoluminescence quantum yield. According to the Equations (9-10) and fitting parameters, quantum efficiency of TADF in the **SBABz4** ($\varphi_{TADF} = 0.420$) significantly exceeds that of prompt fluorescence ($\varphi_{pr} = 0.137$). Now, under the assumption that phosphorescence is not present at room temperature, quantum efficiencies of ISC, rISC, and non-radiative triplet decay can be expressed via φ_{pr} and φ_{TADF} : $\varphi_{ISC} = 1 - \varphi_{pr}$, $\varphi_{RISC} = \varphi_{TADF}$, and $\varphi_{n.r.} = \varphi_{ISC} - \varphi_{TADF}$ (**Figure 13d**). With that, maximum internal electroluminescence efficiency of the emitter in OLED can be expressed as:

$$\Phi_{EL,int} = \eta_S\varphi_{pr} + \eta_S\varphi_{ISC}\varphi_{RISC} + \eta_T\varphi_{RISC} \quad (11)$$

Here η_S and η_T are portions of singlets and triplets produced via electrical injection (0.25 and 0.75, respectively). We obtained $\Phi_{EL,int} = 44\%$ for **SBABz4**, which results in the estimation of $EQE_{max} = 8.8\%$ in the devices with assumed 20% light outcoupling. The estimation exceeds the 5% limit for first generation OLEDs. A fabricated **SBABz4**-based device with non-optimized layer thicknesses and doping concentration showed $EQE_{max} = 6.8\%$ close to the estimation (**Figure 14b**).

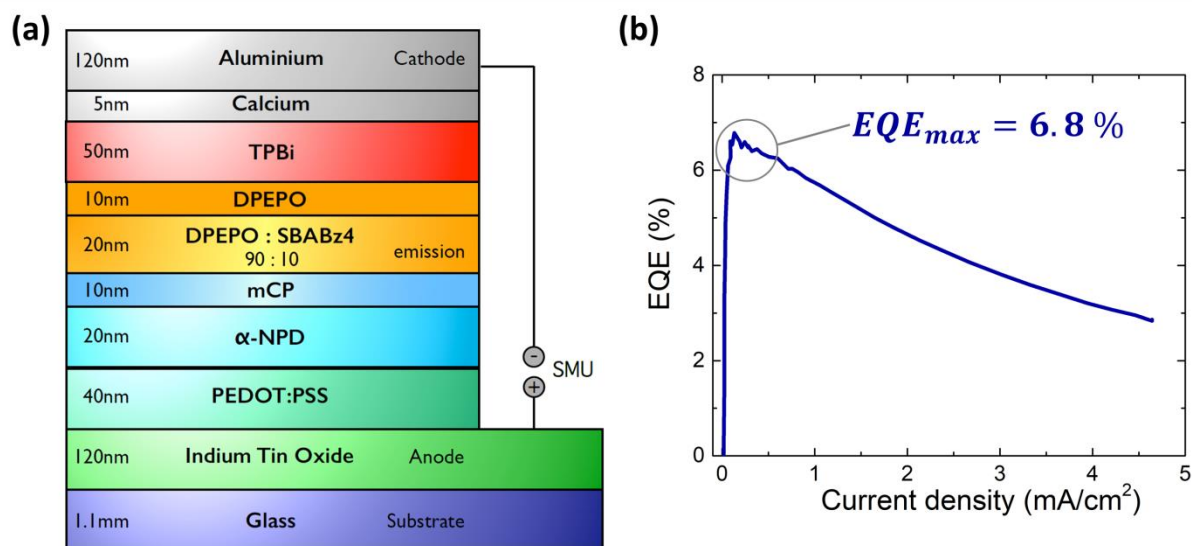


Figure 14. (a) OLED layout. Emitting 10wt% **SBABz4**:DPEPO layer was co-evaporated. (b) EQE of the **SBABz4**-based OLED operating at 5 V.

Figure 15 demonstrates PL decay curves of the neat **SBABz4** film and 5wt% **SBABz4**:DPEPO film. Transient PL in both films clearly shows two distinctive components: prompt fluorescence and TADF. Both components deviate from the purely exponential decay behavior observed previously in the dilute solution (**Figure 13c**). We found out that a stretched exponent provided an excellent fit for both prompt and delayed components. Hence, the decay curves were fitted with a sum of two stretched exponents, and characteristic lifetimes were extracted as their average decay times (**Table 6**). These lifetimes are not directly comparable to the lifetime of single-exponential PL decay in the solution; therefore, we denoted them as $\langle\tau_{pr}\rangle$ and $\langle\tau_{TADF}\rangle$.

Notably, delayed fluorescence in the neat film decays two orders of magnitude faster than in the host matrix (0.13 μs and 9.8 μs , respectively). We assign the increased decay rate in the neat **SBABz4** film to molecular aggregation with subsequent increase of non-radiative decay rate. For the same reason, PLQY of the doped matrix is higher than this of the neat film (40% and 27%, respectively; **Figure 15** and **Table 2**).

The ratio between quantum efficiencies of the prompt and delayed components $\varphi_{pr}/\varphi_{TADF}$ in the films was calculated as the ratio of the areas under the corresponding curves (**Table 6**). Remarkably, prompt fluorescence in the neat film outperforms TADF ($\varphi_{pr}/\varphi_{TADF} \approx 5.83$), whereas both components equally contribute to the emission of

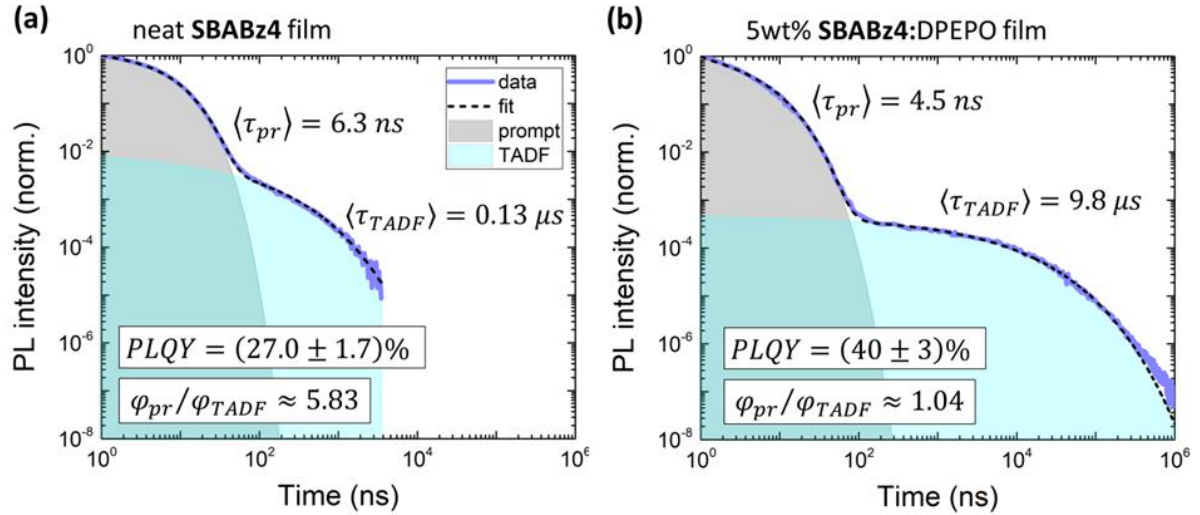


Figure 15. PL decay curves of the neat **SBABz4** (a) and 5wt% **SBABz4**:DPEPO (b) films detected at 435 nm at room temperature. Fit (dashed) is the sum of two stretched decaying exponents.

the doped matrix ($\varphi_{pr}/\varphi_{TADF} \approx 1.04$). Now, using the measured values for PLQY, one can extract absolute quantum efficiencies of the involved processes for thin films (Figure 30). Indeed, TADF efficiency drops dramatically in the neat film ($\varphi_{TADF} \approx 0.040$) in comparison to the doped matrix ($\varphi_{TADF} \approx 0.196$). All in all, isolating and immobilizing the emitter molecules in the host matrix significantly improve TADF lifetime and efficiency, which is essential for OLED performance.

We applied Equation (11) in order to obtain performance estimates for **SBABz4**-based OLEDs from photophysical constants of thin films (Table 7). Resulting maximum internal EL efficiency of 5wt% **SBABz4**:DPEPO film exceeds that of the neat film more than twice (0.237 and 0.095, respectively). Interestingly, the estimated EQE for the OLED based on the doped matrix ($EQE_{max} = 7.1\%$) is in excellent agreement with the corresponding experimental value ($EQE_{max} = 6.8\%$), as long as the light outcoupling of 30% is assumed (Table 7). Therefore, we propose that the light outcoupling of **SBABz4**-based OLEDs exceeds conventional 20%, as it was shown earlier for other stick-like emitters^{151,182,188}.

Temperature-dependent trPL in combination with absolute PLQY measurements allows calculation of the energy splitting ΔE_{ST} for the singlet and triplet levels involved in TADF process (Figure 30)¹⁸⁹. We obtained $\Delta E_{ST} \approx 70$ meV for 5wt% **SBABz4**:DPEPO film. This energy difference is sufficiently low ($\Delta E_{ST} \sim k_B T$) to provide efficient TADF.

ΔE_{ST} can be further decreased via judicious variation of acceptor units. On the other hand, stronger acceptors were shown to cause red shift of emission in similar systems¹⁸², whereas the emission from **SBABz4** is deep blue.

3.3. Conclusion

In conclusion, we designed and synthesized a novel compact deep-blue OLED emitter, **SBABz4**, containing SBA and benzonitrile units, and its monomer counterpart **DMABz4**. We showed that the spiro-linkage in the double-donor core of **SBABz4** renders its luminescence pure-blue relative to the single-donor **DMABz4**, while preserving efficient TADF. Therefore, core-donor provides desirable for applications color tuning in the deep blue region, as opposed to the commonly used TADF molecular design with core-acceptor. The **SBABz4** emitter combines prompt fluorescence, phosphorescence at low temperature, and TADF at room temperature. The latter was independently proven by temperature-dependent transient PL measurements and oxygen-quenching of the delayed PL component. We estimated $EQE_{max} = 7.1\%$ in **SBABz4**-based OLEDs from the PL lifetimes and efficiencies, and obtained $EQE_{max} = 6.8\%$ in an operating test device. The stretched exponent is shown to fit the transient PL in the films very well, whereas PL decay in dilute solution is found to be purely exponential. Immobilization and isolation of the emitter molecules in the DPEPO host matrix maintain the efficient TADF. Finally, we show that **SBABz4** emitter doped in the host matrix demonstrates superior photophysical properties over the neat film.

CHAPTER 4

SPIROBISACRIDANE HOLE TRANSPORTING MATERIALS FOR PEROVSKITE SOLAR CELLS

Four spirobisacridane hole-transporting materials were synthesized and employed in perovskite solar cells. The molecules bear electronically inert alkyl chains of different length and bulkiness, attached to in-plane N-atoms of nearly orthogonal spiro-connected acridanes. Di-*p*-methoxyphenylamine substituents tailored to the central SBA-platform define electronic properties of the materials mimicking the structure of the benchmark spiro-MeOTAD, while the alkyl pending groups affect molecular packing in thin film and affect long-term performance of PSCs. Devices with SBA-based hole transporting layers attain efficiencies on par with spiro-MeOTAD. More importantly, solar cells with the new HTMs are hysteresis-free and demonstrate good operational stability, despite being doped as spiro-MeOTAD. The best performing MeSBA-DMPA retained 88% of the initial efficiency after 1000 h ageing test under a constant illumination. The results clearly demonstrate: SBA-based compounds are potent candidates for a design of new HTMs for PSCs with improved longevity.

This chapter is based on the published work: *J. Am. Chem. Soc.* **2019**. (Just accepted manuscript)
DOI: 10.1021/jacs.9b07166

Authors: Nikita Drigo, Cristina Roldan-Carmona, Marius Franckevičius, Kun-Han Lin, Rokas Gegevičius, Hobeom Kim, Pascal A. Schouwink, Albertus A. Sutanto, Selina Olthof, Muhammad Sohail, Klaus Meerholz, Vidmantas Gulbinas, Clémence Corminboeuf, Sanghyun Paek and Mohammad Khaja Nazeeruddin

In this work I synthesized and characterized all materials, performed data analysis and wrote the manuscript.

4.1. Introduction

Lead organic-inorganic hybrid perovskite solar cells have attracted significant attention over the past years thanks to their low cost processing and high power conversion efficiencies (PCEs). Despite their extraordinary improvement in device performance, from the first reported 3.8%⁸⁸ to a certified 25.2% efficiency nowadays¹⁰⁴, their long-term stability, i.e. product lifetime, remains one of the most challenging obstacles to fully come out from academia to the market¹⁹⁰⁻¹⁹².

High efficiency PSCs consist typically of a multilayer structure in which the perovskite absorber is sandwiched between charge transporting layers, selective either for electrons (ETL) or holes (HTL). Many efforts have been aimed to diminish the inherent vulnerability of these constituent materials. For example, the perovskite absorber is intrinsically assailable to moisture, oxidative atmosphere, heat and ultraviolet radiation¹⁹³⁻¹⁹⁵. However, recent investigations have partially addressed this weakness through rational compositional engineering, as a result allowing a stabilized 3D structure with improved long-term stability and reproducible efficiencies.¹⁹⁶⁻¹⁹⁹ On the other side, charge injection/extraction layers are considered equally important to ensure device durability²⁰⁰⁻²⁰². Yet, induced metal^{203,204} and ion²⁰⁵⁻²⁰⁷ migrations from the adjacent layers can cause fast chemical modification of the perovskite, causing current-voltage hysteresis loop and shrinking initial PCE within the first hours of operation.

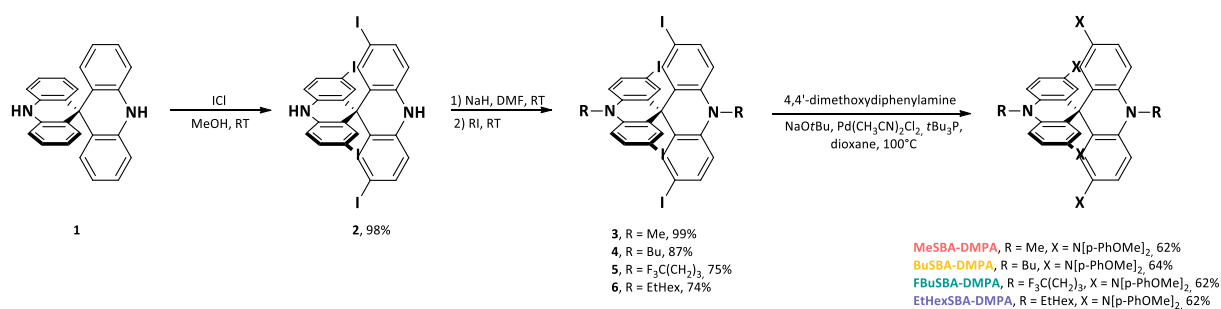
Despite stable and affordable ETLs (e.g. TiO₂ or SnO₂) have successfully been reported in high performance devices, similar alternatives for HTL are still challenging. Spiro-MeOTAD and poly-(triarylamine) (PTAA) remain to be the benchmark hole-selective materials for state-of-the-art PSCs. However, they require the addition of hydrophilic dopants like lithium bis(trifluoromethanesulfonyl)imide (LiTFSI), tris(2-(1*H*-pyrazol-1-yl)-4-*tert*-butylpyridine)cobalt(III) tri[hexafluorophosphate] (FK209) and 4-*tert*-butylpyridine (TBP). Unfortunately, their presence aggravates long-term solar cell metrics and can cause chemical modification of HTM, e.g. pyridination,²⁰⁸ dimerization²⁰⁹ or, possibly, iodination²¹⁰.

Though many attempts have been made to find universal guidelines for efficient hole-selective materials²¹¹, a unified theory for HTM molecular design has not yet been elaborated. Numerous systematic studies focused on structure-performance relationships, providing with some practical and theoretical insights. For instance, judicious selection of isomers^{212–214}, introduction of multiple spiro-conjunctions^{215–217} and alkyl pending groups^{218,219}, planarization of molecules^{218–221} or its subparts^{119,222}, as well as incorporation of heteroatoms into molecular scaffolds^{223–225} are reliable approaches to get withstanding efficient HTMs with elevated glass transition temperature, improved conductivity and high carrier mobility. However, vital data on operational stability of novel HTMs remain non-uniform and quite scarce. Better understanding of structure-long term performance relationship as well as clearer synthetic guidelines for molecular design of efficient and stable HTMs are still in high demand, thus urging deeper investigations of new molecular architectures.

Inspired with the elegant molecular architecture and excellent performance of the spiro-MeOTAD, in this study we demonstrate that a “fusion” of the champion HTM concepts (spiro-MeOTAD and PTAA) provides with a new SBA family of molecules which not only perform on par with spiro-MeOTAD, but also prevent severe degradation of PSCs under constant AM 1.5G one sun illumination, operating with negligible hysteresis.

4.2. Results and discussion

In relation to the conventional spiro-MeOTAD, the SBA platform provides additional easily modifiable sites at in-plane N atoms for molecular design. We devised and synthesized 4 novel HTMs that structurally mimic spiro-MeOTAD. These molecules contain saturated inert alkyl chains of varying length and bulkiness attached to the acridanes' N-atoms, thus allowing to study their possible impact on device performance and stability. Alkyl chains were considered to be the simplest structural “variable” for disclosing structure-performance relationships. Though electronically inert, they have been reported to affect perovskite crystallizability²²⁶ and HTL hydrophobicity, thus improving device longevity^{222,227}.

Scheme 9. Synthetic procedure for the SBA-based HTMs.

Scheme 9 depicts the synthetic approach for obtaining the SBA-based family of HTMs. The synthesis of the SBA-core was carried out according to the optimized procedure²²⁸. The spiro-bisamine **1** was treated with ICl in methanol to provide with tetraiodide **2** in excellent yield. The SBA core was further endowed with alkyl chains of different length and bulkiness. Buchwald-Hartwig amination with DMPA concluded the preparation of the target HTMs. All final compounds were well-soluble in common organic solvents, including chlorobenzene and toluene, typically used for HTM processing on perovskite absorbers.

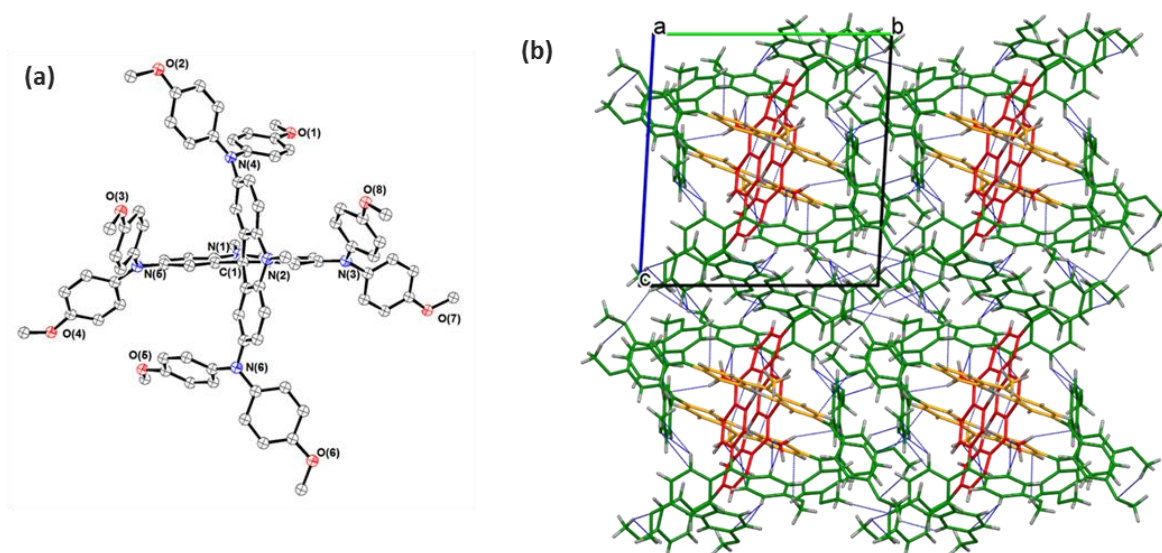


Figure 16. (a) ORTEP representation of **MeSBA-DMPA** crystal structure and perspective view along one of the acridane units showing distorted from orthogonality arrangement of the acridane planes (hydrogen atoms omitted for clarity). (b) Perspective views along *a* crystallographic axis for an expanded unit cell of **MeSBA-DMPA**. Few unit cells are displayed to show packing motif of **MeSBA-DMPA** and short contacts. Colors are used to distinguish orthogonal acridane planes of the SBA core (red and orange), DMPA pending groups (green) and short contacts (blue dotted lines).

The molecular structure of **MeSBA-DMPA** was independently confirmed using single-crystal X-ray diffraction analysis (**Figure 16a**). The distorted tetrahedral sp^3 -hybridised spiro-carbon atom connects two acridane planes of the SBA-core in quasi-orthogonal arrangement. The dihedral angle between mean planes traced through acridane parts of the SBA core is 88.39° , smaller compared to almost orthogonal fluorene planes in spiro-MeOTAD (89.94°)²²⁹. Note that the acridane units of SBA core are not equivalent: one adopts a nearly planar conformation, with a small deviation of 5.22° for one of the phenyl rings from fully planar acridane entity. The second acridane is more folded along C_1-N_2 axis, due to the boat-like conformation of the central heteroatom ring. The corresponding deviation from the planarity is 14.72° . The methyl substituents are slightly displaced of the acridane planes. Notably, $N_1-C_1-N_2$ atoms do not lie on the same line, but form a bent structure with $N_1-C_1-N_2$ angle of 159° . These distortions might be associated with the intermolecular π - π , CH/π and NCH_3/π contacts between the acridane units of the neighboring SBA cores. The more folded acridanes realize intermolecular contacts between each phenyl ring with mean distances of 3.3\AA , while the quasi-coplanar acridanes form NCH_3/π interactions of 2.89\AA . Consequently, despite the bulkiness of the molecule and orthogonality of acridane planes in SBA-platform, such intermolecular interactions build a continuous orthogonal network of liaised SBA-units, forming channels of densely stacked self-embedded spiro-cores (**Figure 16b**).

Table 3. Optoelectronic and thermal properties of SBA-based HTMs.

HTM	λ_{abs} , nm	λ_{em} , nm	E_g , eV	$E_{S+/S}$, eV	IP, eV	T_{dec} , °C	T_g , °C	μ^* , $\text{cm}^2/(\text{V s})$
MeSBA-DMPA	312, 348	422	3.1	-4.94	-4.95	423	–	4.98×10^{-5} (2.3×10^{-3})
BuSBA-DMPA	310, 362	428	3.1	-4.95	-4.98	414	93	1.53×10^{-5} (2.6×10^{-3})
FBuSBA-DMPA	311, 359	425	3.1	-4.92	-5.02	396	89	2.02×10^{-6} (2.8×10^{-3})
EtHexSBA-DMPA	312, 366	422	3.1	-4.94	-5.04	389	55	6.27×10^{-6} (1.6×10^{-3})

*Values in parentheses referred to the HTMs doped with LiTFSI, FK209 and TBP

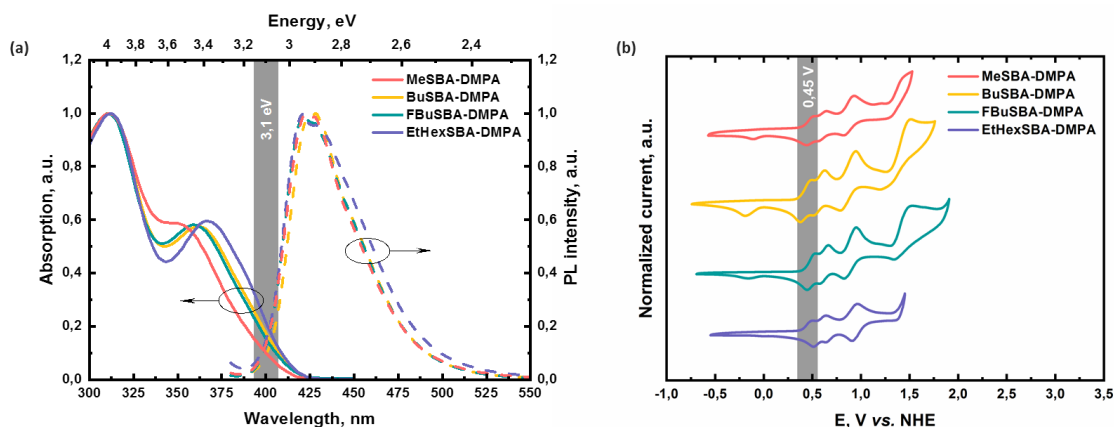


Figure 17. (a) Ultraviolet-visible absorption and PL spectra of SBA-based HTMs THF solution. (b) Voltammograms of SBA-HTMs in a 0.1 M solution of Bu_4NPF_6 in dry deoxygenated DMF at room temperature under N_2 atmosphere, measured with glassy carbon working electrode, Pt wire reference and counter electrodes, ferrocene/ferrocenium (Fc/Fc^+) as internal standard.

These acridane “wells” are surrounded with redox-active DMPA-entities, which form highly branched 3D network of CH/π , π - π and $\text{CH}\cdots\text{O}$ contacts with SBA cores and DMPA groups of the nearby molecules. In contrast with spiro-MeOTAD and other unsubstituted SBA-based compounds^{125,229}, **MeSBA-DMPA** expels all solvent molecules and forms non-solvated crystals with no significant voids and multiple continuous networks of short contacts among parts of the neighboring molecules.

Figure 17a displays the normalized absorption and photoluminescence (PL) spectra of **MeSBA-DMPA**, **BuSBA-DMPA**, **FBuSBA-DMPA** and **EtHexSBA-DMPA** solutions in THF. The absorption and PL profiles of the HTMs demonstrate qualitatively similar behavior. Photoabsorption curves show two intense bands peak in the region between 300 nm and 425 nm. While the high-energy band remains insensitive to the alkyl substituent attached to the in-plane N-atom, the low-energy peak is a little affected. In particular, the short and rigid methyl substituent shifts the low-energy absorption band maximum to the blue region, while longer substituents shift it to the red. The PL spectra display alike patterns with a maximum at about 425 nm, mostly insensitive to the alkyl substituents. Such observations suggest that the geometrical conformations in ground and excited states, as well as their photophysical properties, are vastly determined by the SBA-core with diphenylamine groups, rather than alkyl

substituents. The optical band gaps (E_g) of *ca.* 3.1 eV were estimated from the corresponding intersections of absorption and emission onsets (**Table 3**).

The experimental energy levels of the SBA-based HTMs were estimated using cyclic voltammetry (CV) and ultraviolet photoemission spectroscopy (UPS) experiments. In agreement with the photophysical data, the HTMs demonstrate consonant electrochemical properties ascribed to reversible redox processes on the phenylamine substituents without regard to the various alkyl “tails” at acridanes’ N-atoms (**Figure 17b**). Several reversible oxidation waves indicate an excellent electrochemical stability and good capacity of the compounds to carry multiple charges. In addition, no cathodic waves were detected, indicating, along with wide E_g , a potential capacity to block electrons. The experimental energies for HOMO levels were assessed to be *ca.* -4.95 eV vs vacuum, which were further confirmed with the solid state ionization potential (IP) measurements (**Table 3, Figure 32**). This finding also agrees well with ionization potential computed using density-functional theory at B₃LYP/6-31G(d,p) level (**Table 3, Table 11**).

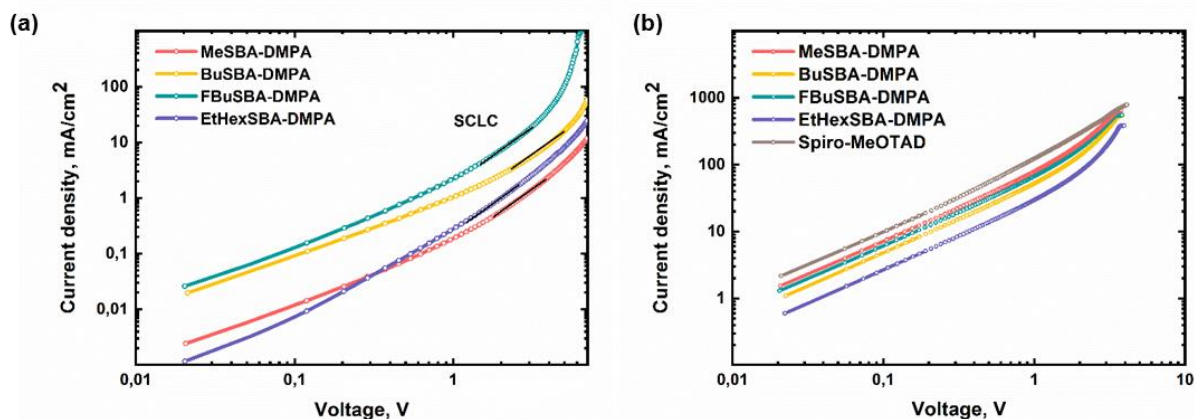


Figure 18. (a) Hole mobility measurements in hole only devices using pristine SBA-based HTMs. The space charge limited current (SCLC) regions used for mobility estimation are traced with black solid lines. (b) Hole mobility measurements in hole only devices using pristine doped SBA-based HTMs and spiro-MeOTAD.

The charge transporting properties of the SBA-based HTMs were also investigated in hole-only devices. We fabricated cells with a structure based on indium-tin oxide (ITO) / poly(3,4-ethylenedioxythiophene)-poly(styrenesulfonate)

(PEDOT:PSS) / SBA-based HTL / Au and extracted the hole mobilities of HTMs from the space-charge limited current (SCLC) regime of J - V curves based on the Mott-Gurney law, $J = (9/8)\epsilon_0\epsilon_r\mu V^2/d^3$ where J is the current density, ϵ_0 is the vacuum permittivity, ϵ_r is the relative dielectric constant of the organic semiconductor (here, we used 3), μ is the hole mobility, V is the applied voltage and d is the thickness of the HTM which was estimated to be around 190 nm. As observed in the **Table 3** and **Figure 18a**, pristine **MeSBA-DMPA** demonstrated the highest hole mobility of $4.98 \times 10^{-5} \text{ cm}^2/\text{Vs}$ among the SBA-based compounds. The gradual drop of the mobility might be rationalized with lower packing density in the solid state, which impedes charge transfer process. However, **BuSBA-DMPA** and **FBuSBA-DMPA**, with similar lengths of the alkyl substituents, exhibited significant differences in their charge transporting properties. Further investigation through multi-scale simulations²³⁰ suggests that the larger energetic disorder present in **FBuSBA-DMPA** film may be the main factor for its lower hole mobility (**Figure 38**). Upon doping with LiTFSI, FK209 and TBP, SBA-based HTLs demonstrated enhancement of hole mobility (**Table 3**, **Figure 18b**).

The thermal properties of the SBA-based HTMs were investigated using thermogravimetric analysis (TGA) and differential scanning calorimetry (DSC). TGA results revealed high thermal stability in all molecules with 5% weight loss temperature (T_{dec}) decrease upon elongation of the pending alkyl substituents (**Figure 19**). Except for **MeSBA-DMPA**, the similar trend was observed for glass transition temperature (T_g) obtained from DSC experiments with no melting or recrystallization detected (**Figure 20**). The DSC curve for the methyl-substituted HTM exhibit only a broad shallow exotherm that might be associated to relaxation processes in the solid. No glass transition was detected at the investigated temperature range. All optical, electrochemical and thermal parameters of the investigated compounds are summarized in **Table 3**.

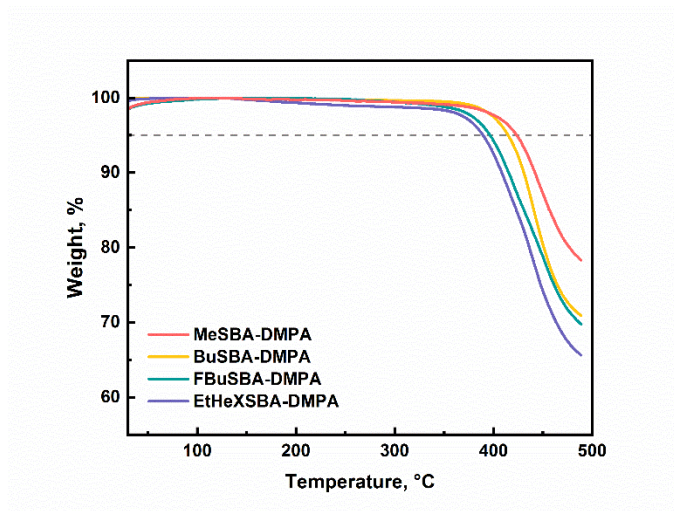


Figure 19. Thermogravimetric analysis data the SBA-based HTMs. The data were obtained for the compounds heated under N_2 atmosphere at the heating rate $10^\circ C/min$.

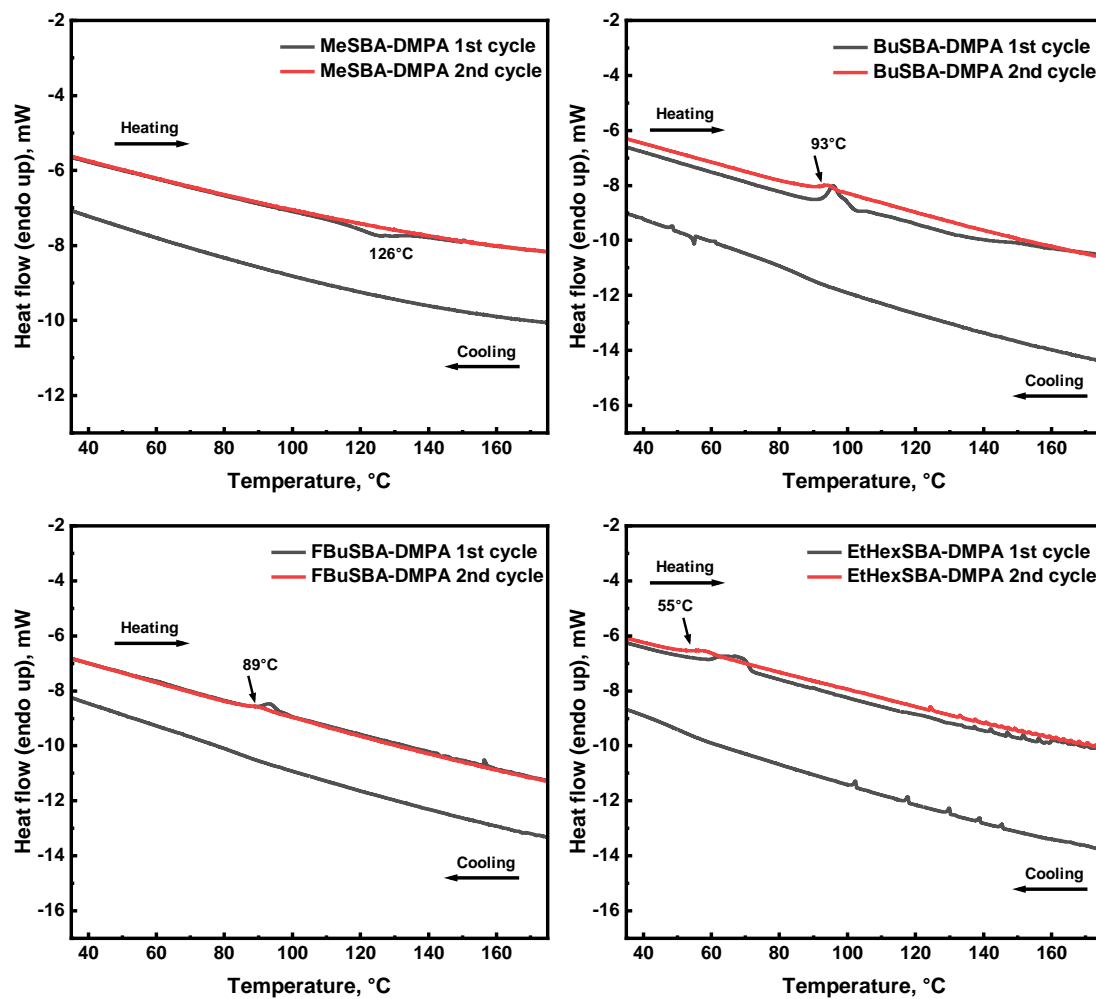


Figure 20. Differential scanning calorimetry thermograms for the SBA-based HTMs. The data were obtained for the compounds heated under N_2 atmosphere at the heating rate $10^\circ C/min$.

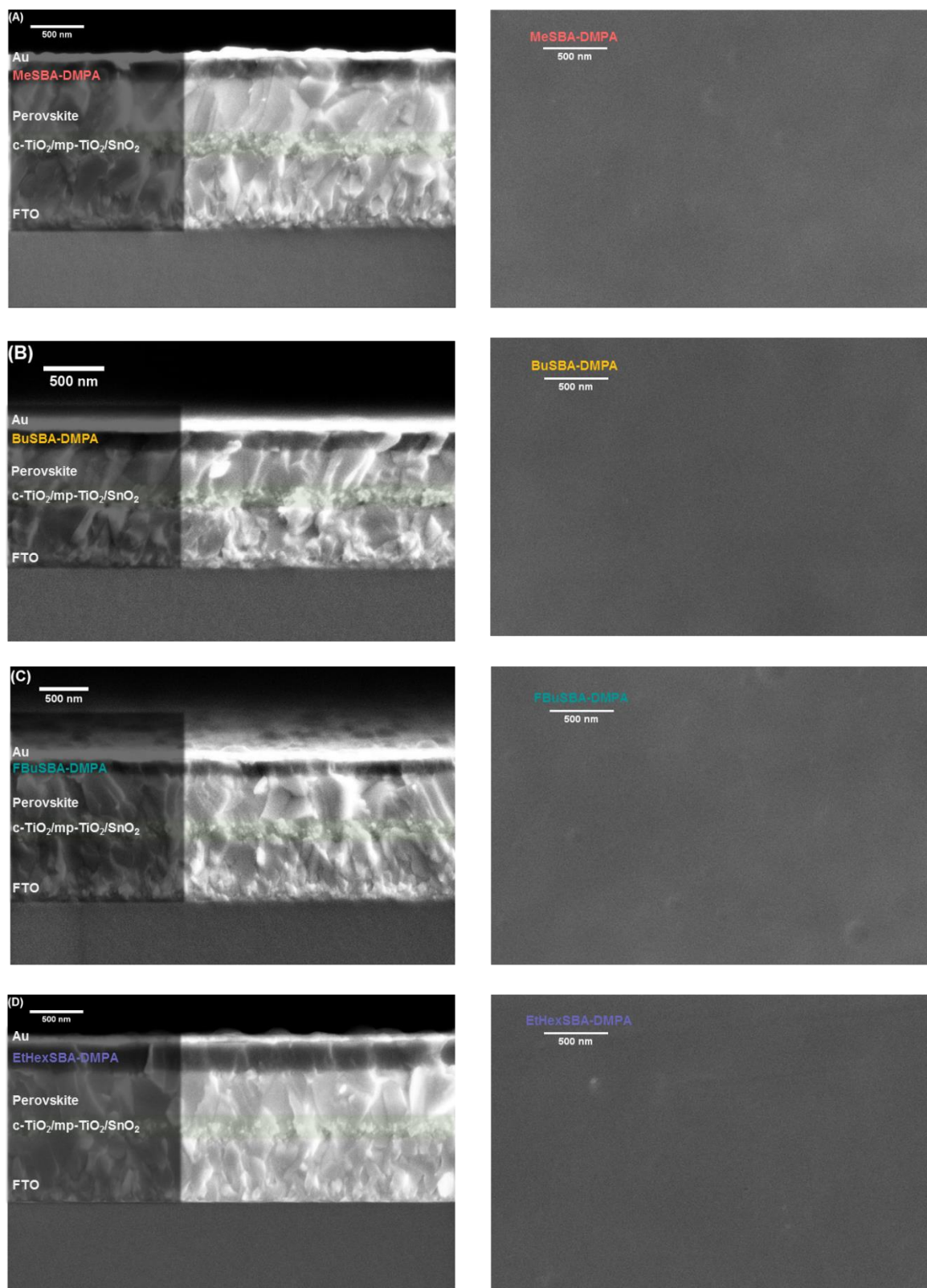


Figure 21. Cross-sectional (left) and surface (right) microphotographs of PSCs employing SBA-based HTMs. SEM images were recorded by in-lens detector of FEI Teneo scanning electron microscope at high tension of 3 and 5 kV.

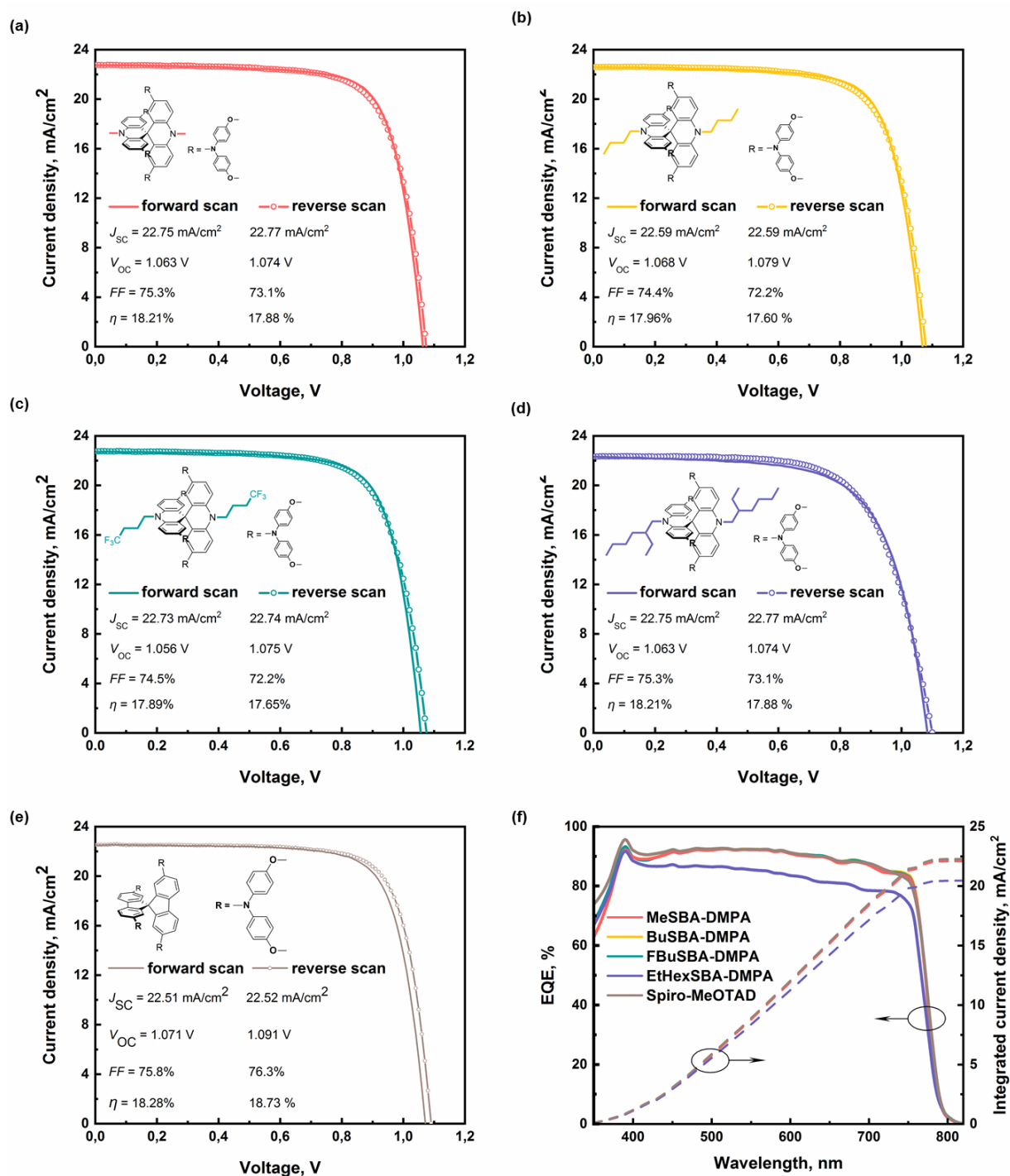


Figure 22. (a-e) J - V curves of PCSs employing different SBA-based HTMs and spiro-MeOTAD reference. The corresponding molecular structures and device metrics are shown as intersections. (f) EQE spectra and integrated current for the devices with SBA-based HTMs

We fabricated solar cells based on a triple-cation perovskite absorber to demonstrate the capability of SBA-based compounds to perform as HTMs in photovoltaic devices. **Figure 21** show the cross-sectional scanning electron microscopy

(SEM) images of a typical *n-i-p* device consisting of fluorine-doped tin oxide (FTO) / compact-TiO₂ (c-TiO₂, ~50 nm) / mesoporous-TiO₂(mp-TiO₂, ~100 nm) covered with SnO₂ (~40 nm) / perovskite absorber (~500 nm) / HTM (~200 nm) / Au (~70 nm). SBA-based HTMs formed smooth and homogeneous thin films with good coverage of the perovskite layer (**Figure 21**). The current density-voltage (*J-V*) curves collected from the champion devices under simulated solar illumination (AM 1.5 G, 100 mW/cm²) are presented in **Figure 22a-e**. Spiro-MeOTAD is also included for comparison.

Interestingly, the alkyl fragments tailored to the SBA core have a strong influence on the HTM performance though SBA derivatives display almost identical photophysical and electrochemical properties. The average PCEs obtained for these devices ranged from 16.4% to 18.05%, with **MeSBA-DMPA** demonstrating the highest short-circuit currents (*J_{sc}*) and PCEs. This provides additional support to the calculated mobilities, further indicating that the shortest methyl substituent could contribute to the densest packing of the molecules, leading to improved charge extracting and transporting properties. Gradual increase of length and bulkiness of the alkyl substituents results in consonant deterioration in performance, as observed for **BuSBA-DMPA** and **FBuSBA-DMPA** (bearing “arms” of 4 carbon atoms show similar PCEs that are *ca.* 0.27% below that of **MeSBA-DMPA**). In addition, fluorine-substituted **FBuSBA-DMPA** demonstrated subtle decrease in open circuit voltages (*V_{oc}*) and higher *J_{sc}* compared to twin **BuSBA-DMPA** with aliphatic substituents. The simultaneous increase of length and bulkiness of the pendant group from 4 to 8 carbon atoms in **EtHexSBA-DMPA** proved to be detrimental for PSC metrics: PCEs and FFs appeared to be lower by about 1.65% and 0.08 correspondingly. Device metrics and *J-V* curves of the champion devices are represented in **Table 4**. In addition, since *J-V* curves often display hysteretic behavior and render real PCE ambiguous to estimate, we collected data scanning the applied voltage at 0.05 V/s from forward bias (FB) to short circuit (SC) and then inversely.

Table 4. Performance of the champion PSCs with SBA-based HTMs and spiro-MeOTAD reference.

HTM	Scan direction	J_{sc} , mA/cm ²	V_{oc} , V	FF	PCE, %	Average PCE, %
MeSBA-DMPA	Forward	22.75	1.063	0.753	18.21	18.05
	Reverse	22.77	1.074	0.731	17.88	
BuSBA-DMPA	Forward	22.59	1.068	0.744	17.96	17.78
	Reverse	22.59	1.079	0.722	17.6	
FBuSBA-DMPA	Forward	22.73	1.056	0.745	17.89	17.77
	Reverse	22.74	1.075	0.722	17.65	
EtHexSBA-DMPA	Forward	22.31	1.084	0.676	16.34	16.40
	Reverse	22.33	1.100	0.670	16.46	
Spiro-MeOTAD	Forward	22.51	1.071	0.758	18.22	18.50
	Reverse	22.52	1.091	0.763	18.73	

All devices using the SBA-based HTMs demonstrated J - V loops without noticeable hysteresis (**Figure 22**, **Figure 33**), indicating that the SBA-DMPA structure can form continuous intimate contact with the absorber, thus extracting holes efficiently and preventing parasitic ion accumulation at the interface²⁰⁰. **Figure 22e** shows external quantum efficiency (EQE) for PSCs with the SBA-based HTMs, including spiro-MeOTAD as reference. All devices with the SBA HTMs, except **EtHexSBA-DMPA**, demonstrate EQEs on par with spiro-MeOTAD. A negligible deviation in the high-energy part of the spectra hardly affects integrated J_{sc} . The calculated J_{sc} values are lower but consistent with the ones assessed from J - V curves. Note that the significantly lower IPCE in **EtHexSBA-DMPA** could be attributed to the hampered charge extraction at the perovskite/HTM interface (vide infra). As previously asserted, the electronically inert bulky and chiral ethylhexyl substituents can be responsible for more distant and less ordered packing of the molecules in the solid film, hindering the carrier transport and therefore decreasing the overall performance. Stabilized photocurrent measurements, power output and device statistics are reported in **Figure 34** and **Figure 35**.

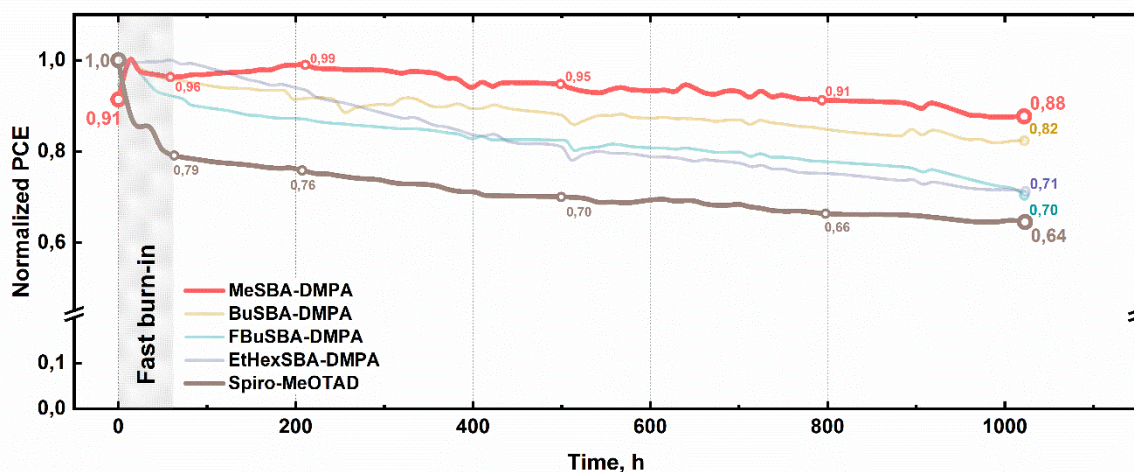


Figure 23. Normalized MPPT for PCEs with SBA-based HTMs and spiro-MeOTAD as reference, recorded at 25°C under a constant simulated AM 1.5G sun light illumination and Ar atmosphere.

We additionally performed maximum power point tracking (MPPT) measurements using devices with doped SBA-based HTMs and spiro-MeOTAD as a reference. The unsealed cells were exposed to a constant simulated AM 1.5G sun light illumination of 100 mW/cm² in argon atmosphere at 25 °C for more than 1000 h. The devices were kept at MPP during stability measurements and *J-V* curves were automatically recorded every 1 h. Results, summarized in **Figure 23**, revealed significant differences one from another and from spiro-MeOTAD, though structural differences of the new HTMs were only the variation of electronically inert substituents at acridanes' N-atoms. As appreciated in the **Figure 23**, after the first 60 h of operation, the device performance for spiro-MeOTAD decreased significantly to 80% of the initial PCE, retaining the lowest efficiency after 1000 h of ageing. On the contrary, the performance decay in SBA-based HTMs was substantially delayed in all cases. Solar cells fabricated with the new materials demonstrated increase of PCE during the first 12-24 h of operation followed by slow performance dwindle: **BuSBA-DMPA** and **FBuSBA-DMPA** displayed qualitatively similar trends to spiro-MeOTAD. Notably, the aliphatic **BuSBA-DMPA** and fluorinated **FBuSBA-DMPA** showed overall better stabilities, retaining respectively 82% and 70% of the initial efficiency at the end of the test. Moreover, **BuSBA-DMPA** demonstrated a substantial reduction in the burn-in drop of the efficiency during the first ~100 h of operation. **EtHexSBA-DMPA** did not display any

abrupt efficiency drop during the initial period of the measurements, but gradually decayed down to 71% after 1000 h of ageing. The best durability amongst the SBA-based HTMs was exhibited by **MeSBA-DMPA**, retaining 88% of the initial efficiency after more than 1000h of the ageing test, thus rendering **MeSBA-DMPA** to be one among the most stable HTMs so far reported^{119,220,227}. Interestingly, after a short burn-in period with a local efficiency minimum of 96%, **MeSBA-DMPA** regained nearly its maximum efficiency followed by a slow decay. The origin of the observed fluctuation remains unclear, but might be associated to slow relaxation processes in the thin organic film.

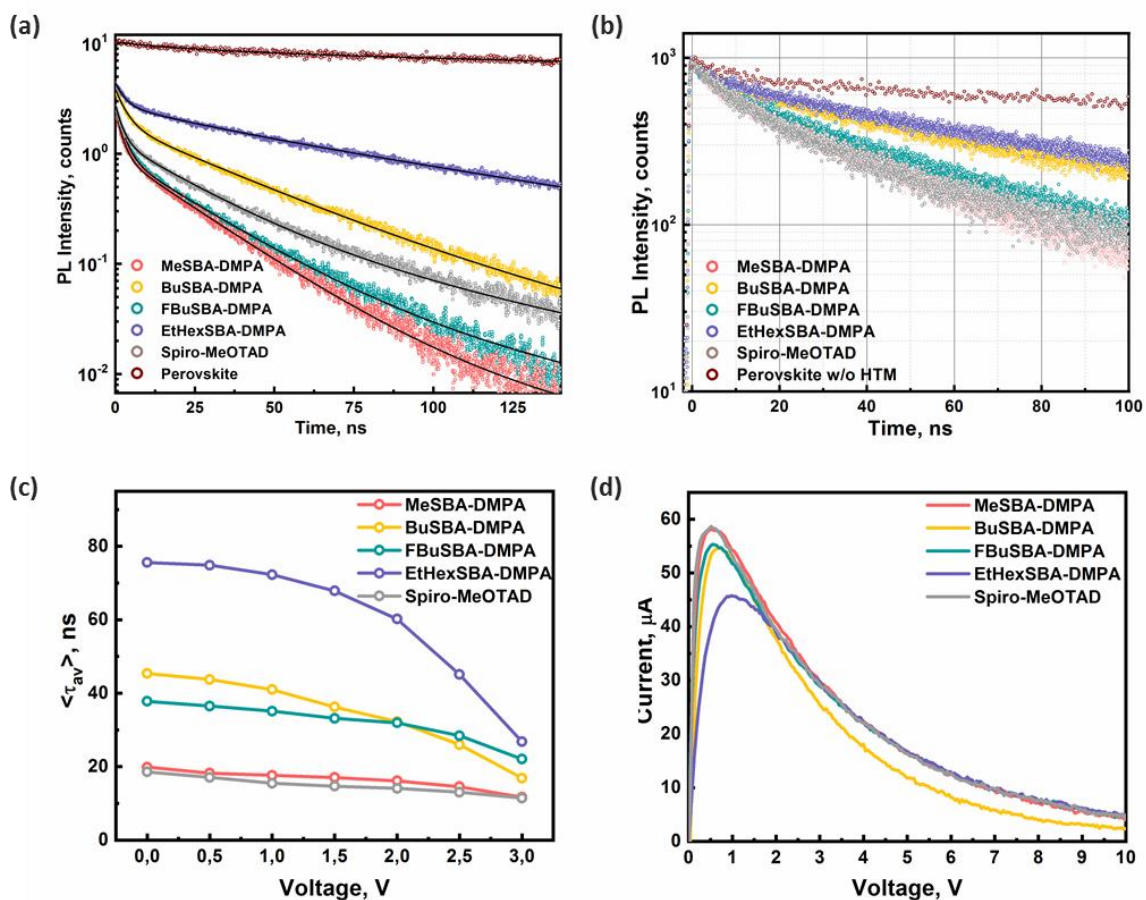


Figure 24. (a) Photoluminescence decay kinetics of the perovskite films comprising spiro-MeOTAD and four different SBA-based HTMs and reference perovskite film. (b) Photoluminescence decay kinetics of the perovskite films comprising spiro-MeOTAD, four different SBA-based HTMs and a reference perovskite film under excitation and PL detection from the glass side. (c) Electric field-dependent average photoluminescence lifetimes. (d) Photocurrent transients in fresh perovskite solar cells covered with different HTMs.

Thus, according to our results, all SBA-based HTMs demonstrated enhanced stability and significantly mitigated burn-in during the first hundred hours of operation indicating that the molecular structure of the HTM, its packing at the interface or bulk could be paramount to prevent severe degradation of the HTL in PSC devices.

To get more insight into the interface charge extraction properties of the materials, we combined time-resolved photoluminescence (trPL), voltage-dependent trPL and transient photocurrent decay (TPCD) experiments on the freshly-prepared and aged perovskite films and solar cells.

Figure 24a shows the photoluminescence decay kinetics of the as-prepared perovskite film on glass and identical films covered with spiro-MeOTAD and the SBA-based HTMs. Sample excitation and PL detection were performed from the HTM layer side, and the obtained decay kinetics were fit with biexponential functions. The obtained fitting parameters are provided in **Table 8**. Perovskite film without HTM exhibits a fast 27 ns decay component, typically attributed to the initial electron trapping process occurring immediately after charge carrier generation²³¹, whereas a 609 ns component should be associated with the Shockley Read Hall (SHR) recombination²³². The obtained long-lived PL decay of pure perovskite film implies a high material quality with a low defect concentration and long charge carrier diffusion lengths. When the perovskite films are covered with the HTMs, the photoluminescence is quenched, and its decay becomes faster with clear fast component lasting for several ns. This fast component is almost absent under excitation and PL detection from the glass side (**Figure 24b**). Therefore we attribute it to a decrease of hole population generated close to the perovskite/HTM interface. While the slower decay component should be associated with the holes created in the bulk of the perovskite. The relative amplitude of the fast component correlates with the slow decay rate. Apparently, both of them are determined by the hole extraction rate indicating that HTMs do not act as ideal hole acceptors and hole transfer to HTM competes with its diffusion out of the interface. The extraction of holes generated in bulk is determined by their diffusion towards interface and efficiency of transfer to HTM. In the case of HTMs causing fast PL decay (**MeSBA-DMPA** and **FBuSBA-DMPA**) the majority of holes generated close to the interface are

likely transferred to HTMs, and lifetime of holes created in bulk is mainly determined by their diffusion rate towards the interface. As hole transfer to **EtHexSBA-DMPA** and **BuSBA-DMPA** is apparently slower, a certain portion of holes diffuse out of the interface, and a total hole extraction rate from the perovskite layer becomes limited by transfer rate through the interface rather than by diffusion. These results imply that the electron extraction to mp-TiO₂ is also slower, which is in agreement with the higher hole mobility²³³. It should be noted, that the two best SBA-based hole acceptors ensure faster hole transfer than the classical spiro-OMeTAD hole transporter.

We performed electric-field-dependent time-resolved photoluminescence experiments to gain additional insight about the hole extraction properties, in complete PSCs. As the TiO₂/perovskite contact is identical in all cells, the dependence of the PL relaxation on the electric field will be mainly determined by the quality of the perovskite/HTMs interface. **Figure 24c** shows the average photoluminescence lifetimes of the perovskite solar cells covered with different HTM materials under the applied external voltages ranging from 0 to 3.0 V. Only a weak voltage induced PL quenching was observed for the best hole acceptors, namely **MeSBA-DMPA** and spiro-MeOeTAD, suggesting that: a) electric field is effectively screened in perovskite layer so that the hole transport towards interface with HTM is mainly determined by diffusion rather than their drift, b) hole transfer rate to HTM is fast enough to be sensitive to beneficial field induced energy level shifts at perovskite/HTM interface. In the case of **EtHexSBA-DMPA** and **BuSBA-DMPA**, the field-induced hole transfer acceleration causes their faster extraction. Noteworthy, these dependences are also in good correlation with the device efficiencies, where the highest performance was achieved for spiro-MeOTAD, **MeSBA-DMPA** and **FBuSBA-DMPA**.

To investigate the influence of different HTMs on the total charge carrier extraction dynamics in the solar cells, we have performed transient photocurrent measurements upon photoexcitation of the device with short ns laser pulses. **Figure 24c** shows transient photocurrent kinetics on the microsecond time scale for working perovskite solar cells with HTMs measured under pulsed laser illumination under applied 0.6 V forward voltage, i.e. close to maximal power point. The photocurrent

kinetics reveals two major processes: photocurrent rise and its decay. The relatively slow photocurrent rise, which also depends on the HTM, is obviously determined by the time required to transfer hole to HTM. This is because the electric field in perovskite layer is screened, and charge carrier motion is diffusional without preferential direction, creating no current in solar cell. Current appears when the charge carriers are transferred to transport layers. The photocurrent peak delay perfectly correlates with the hole extraction times from devices with different HTMs. Meanwhile, the current decay is almost independent of the HTMs type, thus it apparently corresponds to the electron transfer to mp-TiO₂, which is slower as concluded from PL investigations.

We note that significant differences in the hole transfer rates at interfaces can hardly be explained by differences in HOMO levels of HTMs, which according to **Table 3** are very similar. More likely those differences are determined by different packing of HTM molecules at interface with perovskite causing different effective hole transfer distances. In particular, we observe the fastest hole transfer for **MeSBA-DMPA** containing small methyl groups, while the slowest transfer rate is for **EtHexSBA-DMPA** with large ethylhexyl groups.

Despite the obtained hole extraction rates correlate with the solar cell efficiencies, the differences in performance are surprisingly small, suggesting that the hole extraction rate alone plays only a marginal role. This apparently occurs because the hole extraction rates are still significantly faster than the carrier recombination rate at operating cell illumination intensity. On the other hand, the extraction time determines the hole density in the perovskite layer during device operation, which may influence the cell stability. Indeed the highest stability was obtained using the best hole acceptor **MeSBA-DMPA**, while the lowest corresponds to the worst hole acceptor **EtHexSBA-DMPA**. However, the hole extraction rate is not the decisive parameter determining stability, as deduced from the cell performance evolution containing spiro-MeOTAD.

We have additionally measured the PL decay kinetics in perovskite films covered with different HTMs after aging in N₂ atmosphere for 900 hours (**Figure 37, Table 9**). While the hole extraction rates become slower and almost identical for all SBA-based HTMs, spiro-MeOTAD experienced the most significant changes: the hole extraction

time increased more than twice, which agrees with the most significant efficiency decay of the solar cell with spiro-MeOTAD.

Previous works have demonstrated that metal/ion migration through HTM can lead to degradation of PSCs²⁰³⁻²⁰⁷. To address this aspect, we computed the free-volume present in amorphous HTMs performing molecular dynamics (MD) simulations²¹⁹. The free-volume of amorphous HTMs increases with the substituted chain length, which may imply a higher permeability to metal/ion for long-chain analogues (**Table 10**). Apart from spiro-MeOTAD, the computed free-volume correlates well with the experimental observed long-term PCE decay, assuming that a smaller free-volume leads to a slower efficiency decay.

4.3. Conclusions

In conclusion, we have synthesized four new SBA-based HTMs with different alkyl substituents attached to the in-plane N-atoms of the spiro-connected acridanes. The SBA cores were endowed with DMPA entities to structurally mimic spiro-MeOTAD and to investigate how introduction of the heteroatom and alkyl chains into the molecular scaffold of HTM affect the device performance and long-term stability.

The SBA HTMs employed in PSCs, attained efficiencies on par with the benchmark spiro-MeOTAD and negligible *J-V* hysteresis. Importantly, the results suggest that even minor differences in chemical structure can significantly change the rates of hole extraction from perovskite, which, however, only weakly influence the device efficiency, but strongly affect long term stability and evolution of devices in the course of time. In particular, the best results were achieved using **MeSBA-DMPA** with the shortest C₁-substituent, while elongation of the side arms lead to the gradual deterioration of device metrics and poorer stability. We associate the excellent stability of the devices employing **MeSBA-DMPA** with its dense packing of the molecules and uniform interfaces that may not only prevent mass transfer at the interface, but also facilitate charge extraction from the active perovskite layer.

CHAPTER 5

APPROACHES FOR SELECTIVE SYNTHESIS OF ULLAZINE DONOR–ACCEPTOR SYSTEMS

Methods for effective synthesis for the four possible isomeric 3,9-diphenylullazine carboxaldehydes and reactive halogen intermediates are described. Ullazine donor–acceptor (D–A) dyes were studied using UV/Vis, photoluminescence (PL) spectroscopy and cyclic voltammetry. X-ray single crystal diffraction analysis independently confirmed the structures of two key intermediates. A D–A dye based on ullazine with dihexylmalonate acceptor was tested as a dopant-free hole-transporting material (HTM) in a perovskite solar cell, exhibiting promising power conversion efficiency (PCE) reaching 13.07 %.

This chapter is based on the published work: *Chem. Eur.J.* **2017**, *23*,17209 –17212
DOI:10.1002/chem.201704694

Authors: Nikita A. Drigo, Sanghyun Paek, Aron J. Huckaba, Pascal A. Schouwink, Nouar Tabet and MohammadK.Nazeeruddin

In this work I synthesized and characterized all materials, performed data analysis and wrote the manuscript.

5.1. Introduction

Due to their intriguing properties, research into polycyclic heteroaromatic compounds (PHAs) have gained tremendous momentum, especially towards organic electronics applications. PHAs are numerous and vary in shapes and sizes from simple structures to complex 3d-motifs with B, N, O, S, P or other heteroatoms that can modulate key properties.^{234–236} Ullazine, a PHA exhibiting a fused aza-polycyclic core, is isoelectronic to pyrene but combines the extended π -system of the latter with the electron-rich nature of indolizine-like heterocycles. Ullazine's in-plane N-atom is able to donate electron density to the periphery to form a 14- π annulene perimeter with central positive iminium moiety and electron rich periphery, thus promoting intramolecular charge transfer (ICT) (**Figure 25**).²³⁷

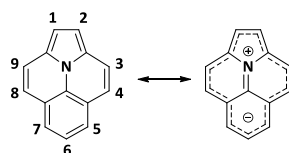


Figure 25. Numbering and resonance structures of Ullazine.

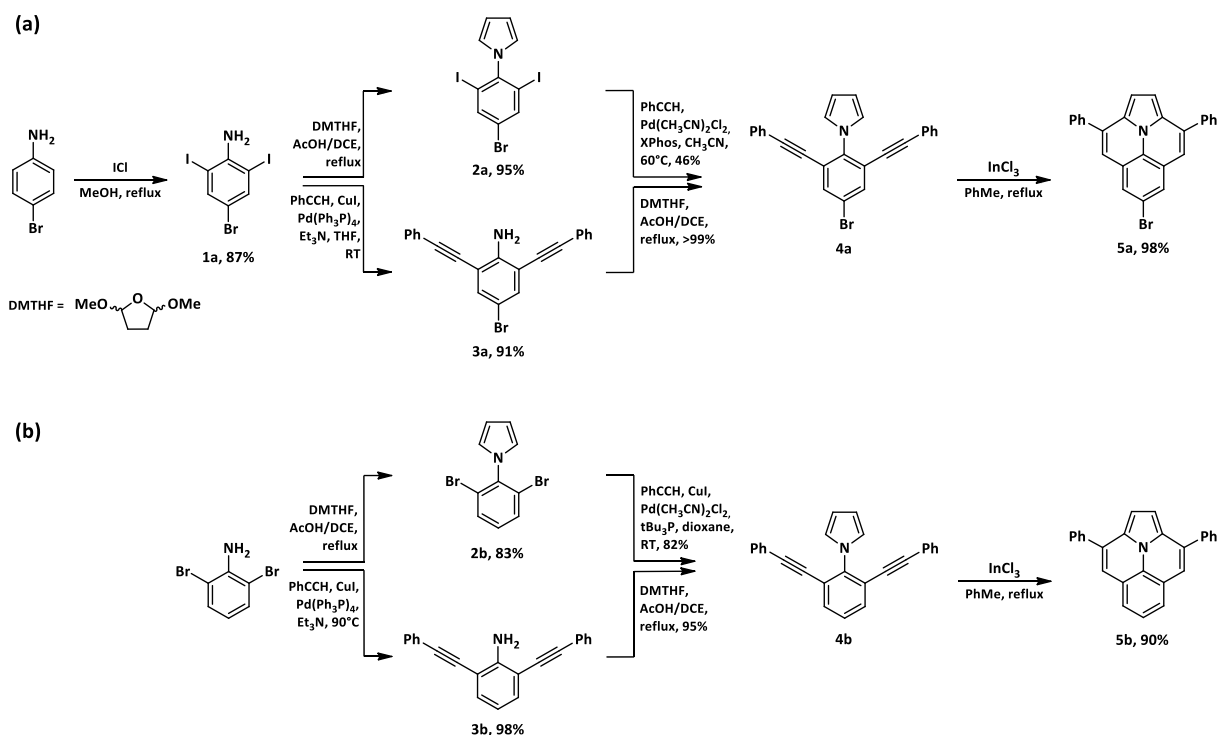
Ullazines, have been known since 1983 with the first reports on preparation by Balli²³⁸ and ion stability studies by Gerson appeared.²³⁷ However, tedious synthesis and lack of application disfavored further investigation of the polycycle's capabilities. Almost 30 years later, seminal reports on the first feasible synthesis of the ullazine scaffold and applying ullazine sensitizers for dye-sensitized solar cells spurred significant interest in the heteropolyaromatic system.^{239–246} Even so, methods for selective and effective modification of ullazine periphery remain scarce, though publications claiming facile construction of ullazine scaffolds still appear regularly.^{247–258} Herein, we report approaches for effective regioselective functionalization of 3,9-disubstituted ullazines, which were used as π -extended and electron-rich modular units for functional materials.

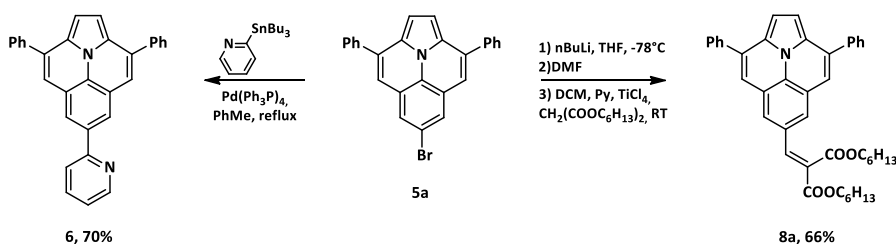
5.2. Results and discussion

Since published procedures describe the effective and high-yielding preparation of ullazine-5-carboxaldehydes as the major product in Vilsmeier–Haack carbonylation and 6-chloroullazines as the only accessible reactant for cross-coupling reactions²⁴⁰, we focused on exploring routes towards the other possible core-substituted ullazine isomers containing carbonyl or reactive halogen functionalities. The synthesis devised in this work enables simple derivatization of the ullazine core or key intermediates to enable further selective functional group installation and further transformation. Owing to the strong electron-donating character of the ullazine periphery, we synthesized donor-acceptor (D-A) systems to gain deeper insight into photophysical and electrochemical properties of each regioisomer. We chose phenyl moieties as substituents at the 3 and 9 positions to impart stability²³⁷ to the polycyclic scaffold and to simplify synthesis and characterization. Dihexylmalonate served as the solubilizing acceptor moiety.

Our study began with the preparation of 6-bromo-substituted ullazine (**Scheme 10a**). Electrophilic iodination of 4-bromoaniline with 2.0 eq of. ICl yielded diiodide **1a**²⁵⁹.

Scheme 10. Synthetic routes for (a) 6-bromo-3,9-diphenylullazine **5a** and (b) 3,9-diphenylullazine **5b**.



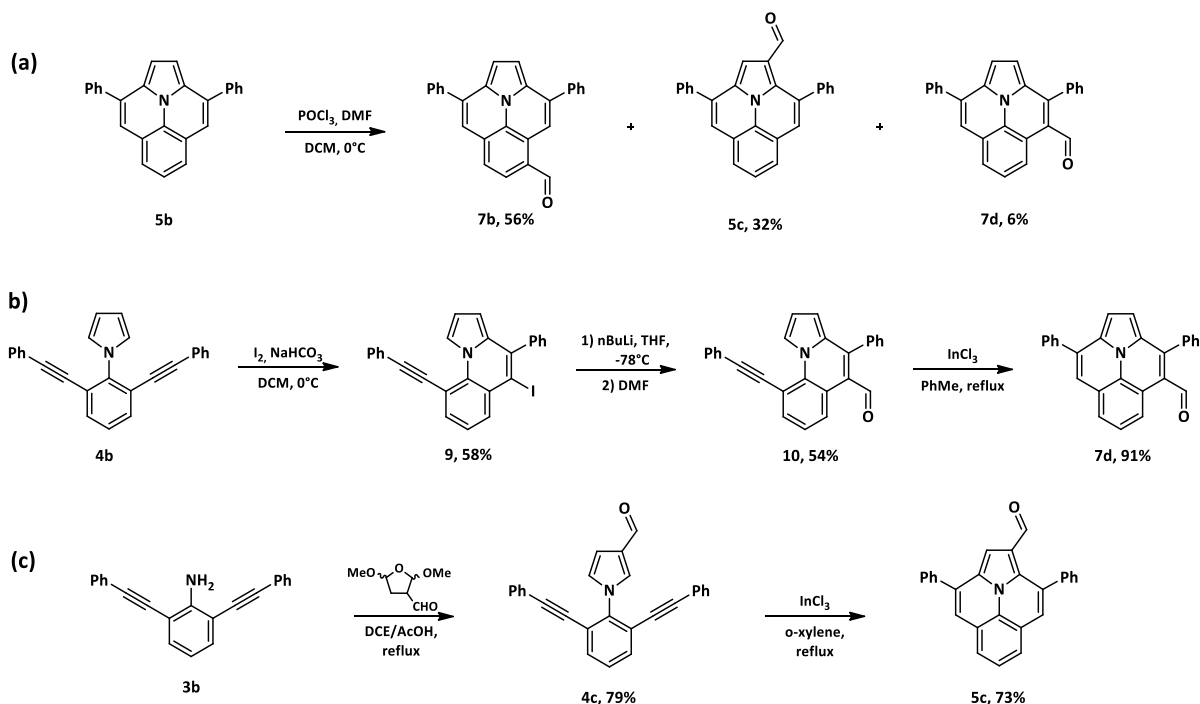
Scheme 11. Synthesis of ullazine dye **8a** and model cross-coupling reaction towards **6**.

Following the published route for 3,9-disubstituted ullazines²⁴⁰ we firstly prepared the pyrrole **2a**, but found the subsequent Sonogashira coupling was ineffective despite the well-known reactivity of aryl iodides: **2a** reacted sluggishly and non-selectively (**Table 12**, appendix). Swapping the order of reaction resulted in an increased yield: direct preparation of the bisalkyne **3a** from 4-bromo-2,6-diiodoaniline **1a** utilizing milder reaction conditions and cheaper catalytic system, followed by Clauson-Kaas ring rearrangement provided pyrrole **4a**. Finally, InCl_3 -catalyzed cyclization completed the synthesis of 6-bromosubstituted ullazine **5a** (**Scheme 11**). Particularly noteworthy in the optimized procedure are the high-yielding conditions tolerant to the halogen atom placed in the ullazine's 6-position throughout all stages of the synthesis. Overall yield of the desired 6-bromoullazine **5a** starting from 4-bromoaniline was 77% over four steps.

One-pot combination of Bouveault aldehyde synthesis and Knoevenagel condensation afforded desired dye **8a** from **5a** in 66% yield (**Scheme 11**). Unfortunately, we could not isolate the corresponding ullazine-6-carboxaldehyde, as it appeared to be sensitive to air and oxidized readily being exposed to it, which was due to the lack of electron donation in the 6 position.²⁴⁰ However, **5a** proved to be an effective cross-coupling partner with 2-(tributylstannyl)pyridine delivering the product **6** in 70% yield. (**Scheme 11**).

Next, we sought the ullazine functionalized with the acceptor at 5 position. After optimization of Sonogashira coupling we employed the same procedure as above to obtain the unsubstituted ullazine with an increased overall yield of 84% (**Scheme 10b**). Interestingly, Vilsmeier–Haack formylation of **5b** also provided **5c** in decent yield (32%) along with the reported minor product **7d** (6%). The structure of **5c** was confirmed with

Scheme 12. (a) Vilsmeier–Haack formylation of **5b**. (b) Direct preparation of ullazine-4-carbaldehyde **7d**. (c) Direct preparation of ullazine-1-carbaldehyde **5c**.

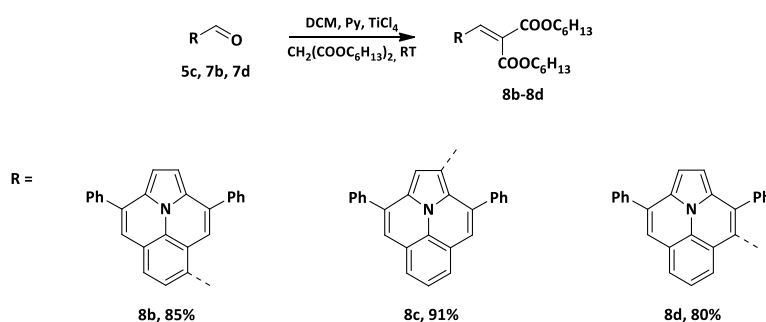


single crystal x-ray diffraction (**Figure 26a,b**). To the best of our knowledge, formation of the pyrrole carboxaldehyde regioisomer moiety has not been reported in literature so far.

Unfortunately, other attempts to synthesize 5-substituted ullazines directly were unsuccessful: treatment of **5b** with halogen or boron electrophiles in various conditions did not yield the desired products. Thus, modification of the 5 position in ullazine core still remains a challenging issue due to strong electron donation at this position.^{240,260}

The reaction of the bisalkyne **4b** with molecular iodine at 0°C delivered monoiodoindolizine **9**, a useful precursor for 4-derivatized ullazines (**Scheme 12b**), and the structure was confirmed by single crystal X-ray diffraction (**Figure 26c,d**).²⁶¹ We utilized **9** to obtain corresponding dye **8d** stepwise but in selective manner and with improved total yield. Interestingly, InCl_3 -catalyzed cyclization of the iodoindolizine **9** selectively yielded **5b** albeit in low yield ($\sim 30\%$). Installation of a deactivating carbonyl group did not hinder the cyclisation, providing **7d** in excellent yield.

Scheme 13. Synthesis of the ullazine dyes **8a–8d** in TiCl_4 -catalysed Knoevenagel condensation.



Lastly, the final InCl_3 -catalysed cyclisation of the alkyne **10** did not require elevated temperatures as it was the case for **4c**. To reach the final isomer **5c**, commercially available 2,5-dimethoxy-3-oxotetrahydrofuran smoothly formed **4c**, a precursor for the dye **8c**. The installed carbonyl group was observed to deactivate the pyrrole ring towards electrophiles. Thus cyclization required higher temperatures (**Scheme 12c**).

Finally, the ullazine monocarbaldehydes **5c**, **7b** and **7d** were condensed with dihexylmalonate in the presence of TiCl_4 , providing with the desired dyes **8b–c** in excellent yields (**Scheme 13**).

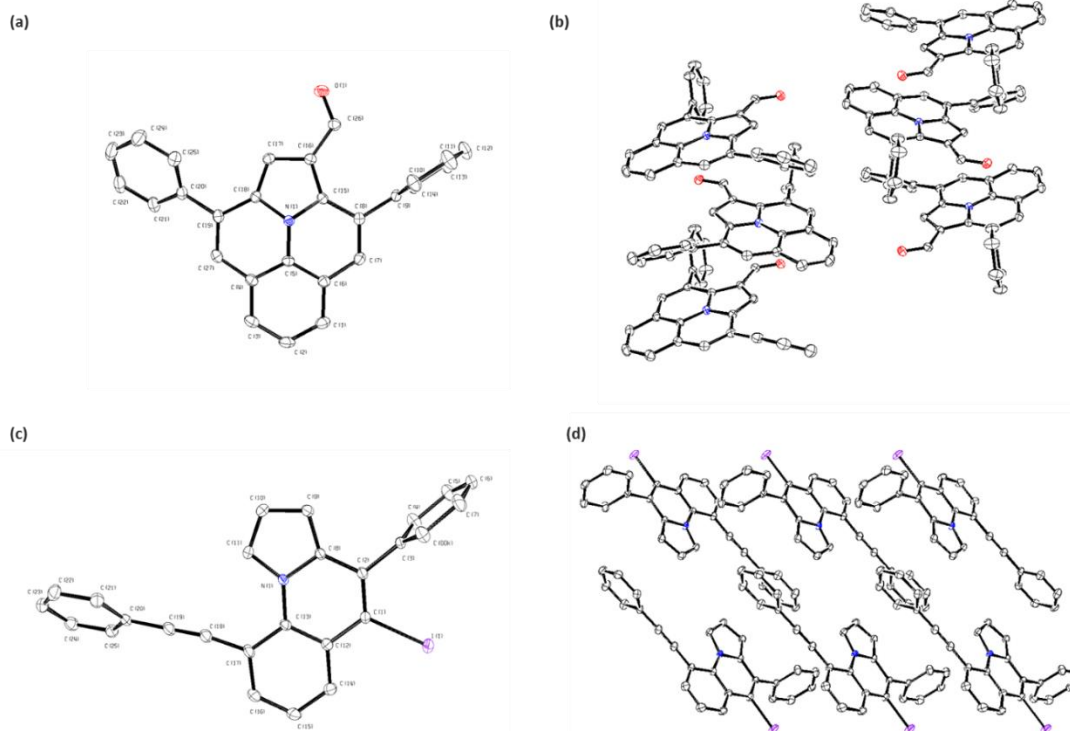


Figure 26. ORTEP representation and packing motif in crystals of (a, b) **5c** and (c, d) **9** crystal structures.

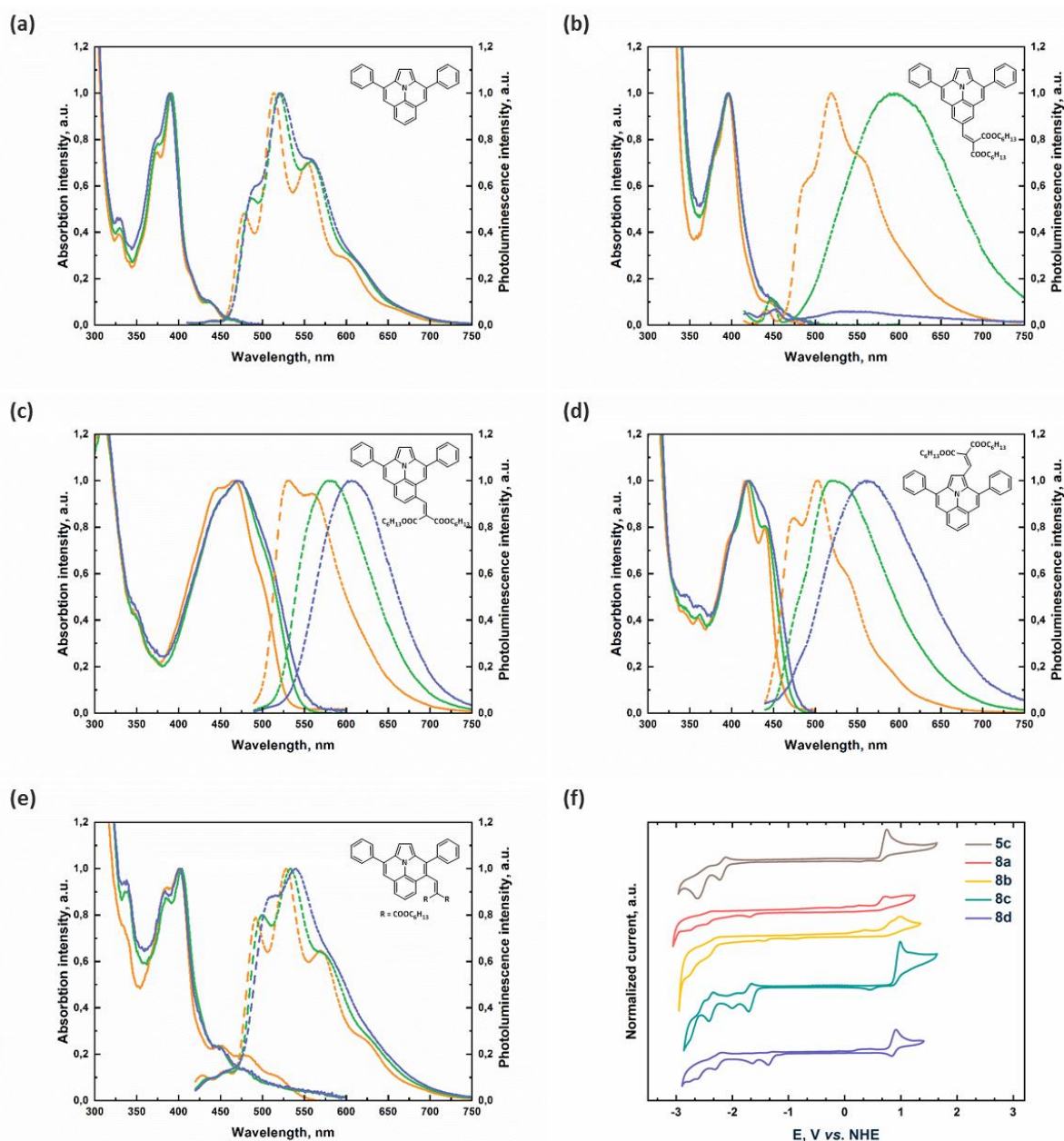


Figure 27. (a)-(e) UV-vis (solid) and PL (dashed) spectra normalized at peak value recorded for unsubstituted ullazine **5b** and dyes **8a-d** in cyclohexane (orange), THF (green) and acetonitrile (blue); (f) voltammograms of **5b** and dyes **8a-d** in a 0.1M Bu₄NPF₆ solution in dry deoxygenated DMF.

UV-Visible and PL spectroscopy was performed in solvents of differing polarities: cyclohexane, tetrahydrofuran and acetonitrile. Photophysical properties of the unsubstituted ullazine **5b** and the dyes **8a-8d** (Figure 27a-e, Table 5) were studied.

Table 5. Photophysical and electrochemical properties of **5b** and dyes **8a-d**.

Compound	λ_{abs} , nm ^[a]	λ_{em} , nm ^[a]	E_{red} , V	E_{ox} , V	ΔE , eV	$E_{\text{o-o}}$, eV ^[b]	HOMO, eV ^[c]	LUMO, eV ^[c]
5b	374, 391 ^[b]	478, 513 , 553	-2.22	0,75	2.97	2.71, (2.61)	-5.43	-2.46
8a	395	519	-1.68	0,77	2.45	2.61, (2.48)	-5.45	-3.00
8b	446, 466	530 , 560	-1.43	0,84	2.27	2.30, (2.23)	-5.52	-3.25
8c	416 , 439	474, 502	-1.70	0,99	2.69	2.63, (2.59)	-5.67	-2.98
8d	386, 401	492, 529 , 570	-1.36	0,91	2.27	2.64, (2.08)	-5.59	-3.32

[a] Measured in cyclohexane. Bold corresponds to the highest intensity in a band; [b] estimated from the intersection of the normalized absorbance and emission spectra in acetonitrile or low-energy onset of absorption spectra in acetonitrile (values in parentheses); [c] converted to the NHE by adding +0.69V and converted to vacuum scale by adding +4.44 eV.

Except for **8a** and **8b**, each dye exhibited vibronically-structured absorption bands in cyclohexane. Upon increasing solvent polarity to THF and acetonitrile, structural features were lost, apart from the spectra of **8d**, which remained unchanged regardless the solvent polarity. Nonetheless, all high-energy absorption bands were largely insensitive to changes in solvent polarities. Ullazine **5b** displays strong absorption bands in the high energy region (250-330) nm that were ascribed to $\pi \rightarrow \pi^*$ transitions. Weaker absorbance was observed between 350-450 nm and assigned to ICT.

Ullazine dyes **8a** and **8d** exhibit similarly structured absorption bands with slight bathochromic shift in ICT onset, while **8b** and **8c** display weaker $\pi \rightarrow \pi^*$ transition and a stronger ICT band, both of which are broadened and red-shifted by 30 and 80 nm correspondingly. The ICT band energy thus follows the expected trend for electron donation strength at different ullazine periphery sites (5>2>4>7).²⁴⁰

Similarly, vibronic structure was observed in the PL spectra recorded in cyclohexane for ullazine **5b** and dyes **8a**, **8c**, **8d**, while **8b** is broadened. Upon increasing solvent polarities from cyclohexane to acetonitrile, emission of **5b** and **8d** experienced nearly no change bathochromic shifts by 5-10 nm were observed with nearly no vibronic

structure difference. However, **8a-c** exhibited: solvatochromism, displaying red-shifts ranging from 20 to 70 nm. Interestingly, PL maximum of **8c** is blue shifted by 10nm in cyclohexane compared to the emission of **5b** that presumably indicates destabilization of an excited state of **8c** in nonpolar medium (Table 14).

The electrochemical properties of **5b** and **8a-d** were then investigated by cyclic voltammetry. The ground-state oxidation potential E^{s+}/E^s for the parental unsubstituted ullazine **5b** was observed to be -5.43 eV against vacuum level. Attachment of the acceptor stabilized the HOMO level of the dyes **8a-d** by 20-200 mV, which agreed well with photophysical data (Table 5).

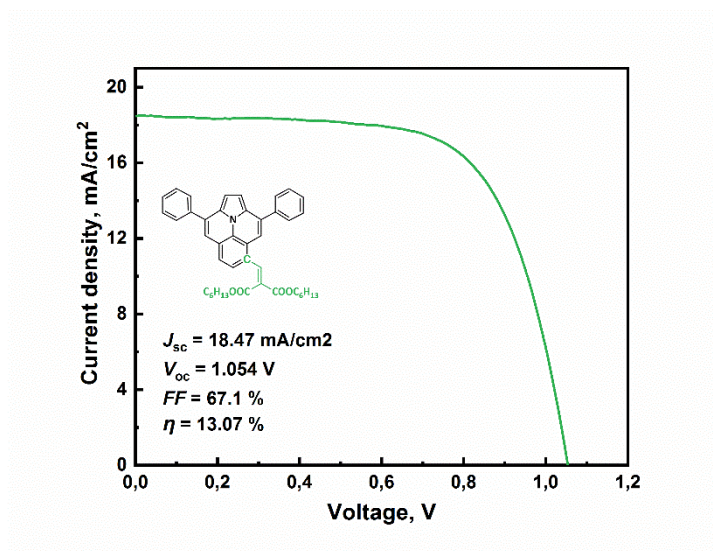


Figure 28. *J-V* curve of a champion PCSs employing the ullazine dye **8b**.

Dye **8b** was deemed a possible candidate for use as a dopant free hole-transporting material (HTM) for perovskite solar cells because of strongest ICT characteristics and suitable HOMO level. Under 1 Sun illumination, the champion devices containing **8b** as an HTM attained a modest PCE of 13.08%, with $J_{sc} = 18.47 \text{ mAcm}^{-2}$, $V_{oc} = 1.054 \text{ V}$, and $FF = 0.671$ (Figure 28).

5.3. Conclusion

In conclusion, we have developed procedures for the regioselective synthesis of all possible 3,9-diphenylullazine-monocarboxalhexydes, as well as reactive halogen-containing precursors for straightforward modification of the ullazine periphery. Ullazine D-A dyes were found to have strong CT bands and were applied as dopant-free HTMs in Perovskite solar cells. With an easily modifiable substitution pattern that enables fine tuning of energy levels, ullazine-based materials are believed to be promising candidates for application in organic electronics.

CHAPTER 6

CONCLUSIONS AND FUTURE PERSPECTIVE

The focal point of this thesis is positioned on the development of novel organic materials for optoelectronic applications. I have chosen two conceptually different molecular motifs to investigate their structures and physico-chemical properties in relation to their “macroscopic performance” as bulk materials in operating thin-film light-energy conversion devices. The materials I have been investigating during the period of my PhD studies are ullaizines, electron-excessive flat PHAs with the pronounced intramolecular CT, and SBA-based bulky globular spiro-conjugates either with sole benzonitrile acceptors at their in-plane N-atom, or electronically inert alkyl chains while the periphery was furnished with electron-donating DMPA substituents. The SBA-based compounds have been employed as emitting dopants in TADF OLEDs, and as HTMs in PSC. Preliminary data concerning the use of ullazine derivatives as HTM in PSC have been also obtained.

Firstly, in the Chapter 2 I surveyed, summarized and analyzed the reported data on the organic materials for optoelectronics that comprise spiro-acridane motif in their structure, mainly considering emitting TADF dopants for OLEDs and HTMs used as HTLs for PSCs. I analyzed and structured the physico-chemical parameters and performance in the devices associated with the introduction of the spiro-node in the acridane-based materials, making a comparative study with non-spirocyclic congeners. In the context of TADF emitters for OLEDs, I categorized the molecules into three groups: i) D- σ -A emitters where a spiro-node segregates FMOs, ii) Ar- σ -D-A structures where a spiro-cycle is a bulky donor and iii) the least represented and exploited so far A-D- σ -D-A emitter architecture with a twinned non-conjugated SBA donor (σ stands for spiro-atom). D- σ -A TADF emitters display significant drawback relevant to this molecular structures: strong segregation of FMOs often results in low PLQYs and bad performances in OLEDs due to low f . Moreover, structural versatility of these conjugates might be more limited due to complexity of synthetic routes towards D- σ -A motifs. On the other hand, the introduction of quasi-inert spiro-cyclic pendants (Ar- σ -D-A structures) at the 9 position of acridane can bring about multiple properties compared to widely used DMA-based emitters: 1) spiro-aromatic junction stabilizes HOMO (similarly to DPAC-based materials) widening the bandgap and blueshifting the

emission; 2) spiro-aromatic junctions usually improves solubility (in relation to DPAC-based materials that often lack this property); 3) a spiro-aromatic pendant can accommodate multiple fine energy states that facilitate rISC, enhanced by stronger SOC eventually boosting TADF efficiency; 4) spiro-endowed donors are more rigid and prone to adopt the only highly twisted conformation favorable for TADF and suppressing the parasitic dual emission; 5) bulkiness of the spiro-acridane donors mitigates significantly strong concentration quenching in films made of pristine TADF emitters, thus paving the way to non-doped and/or solution processable OLEDs; 6) spiro-comprising acridane donors are usually stick-like molecules with high anisotropy: molecules are prone to adopt horizontal orientation (high $\Theta_{||}$ values up to 90%) during vacuum deposition, eventually increasing light-outcoupling and maximum η_{ext} . Moreover, introduction of the spirocyclic pendant usually does not complicate the synthetic procedures.

As a result, this minireview clearly pointed out the benefits of use of spirocyclic acridane materials as opposed to simpler DMA and DPAC comprising TADF emitters. Furthermore, among the limited data reported regarding the use of spiroacridane-based HTMs for PSCs, I discovered the signs of good material stability in operating PSCs. Moreover, the spiro-acridane materials demonstrated promising performance when employed even in non-doped forms. The great potential of spirocyclic donors demonstrated of TADF emitters and the evident lack of the data on twinned non-conjugated SBA-based materials spurred our interest to investigate and exploit the capacity of this structure to create advanced materials for light-energy conversion devices.

In chapter 3 I introduced a compact TADF emitter **SBABz₄** composed of SBA dual non-conjugated donor and 4-benzonitrile acceptor. The use of the twinned donor with the spiro-junction brought about strong blue shift in the emission in relation to its “monomer” counterpart **DMABz₄**, as expected. The photophysical properties of the new emitters were studied in solutions and thin films. The TADF character of the emission was confirmed in temperature-dependent trPL measurements and oxygen quenching experiments. The OLEDs employing **SBABz₄** as an emitting dopant demonstrated maximum EQE of 6.8% close to the estimated value of 7.1%, calculated with the

assumption of 30% light out coupling efficiency. These experimental results support the hypothesis that SBA twinned donor can be used for preparation of stick-like TADF emitters with pronounced hypsochromic shift and increased horizontal orientation.

In chapter 4 I further exploit the capacity of SBA molecular platform to create 4 new HTMs for highly efficient and stable PSCs. The in-plane N-atoms of the main SBA core were substituted with electronically inert alkyl chains of different length and bulkiness, while the periphery of the SBA-core was endowed with DMPA entities to properly adjust the energy levels of the new materials to VB of perovskite absorber. The final globular molecules simultaneously mimicked the structure of two benchmark HTMs: spiro-MeOTAD and a monomeric fragment of PTAA. The new materials demonstrated efficiencies on par with the etalon spiro-MeOTAD, while the *J-V* hysteresis was significantly reduced. Among other SBA-based HTMs, Me-substituted **MeSBA-DMPA** exhibited the highest PCE of 18.05% and superior stability retaining 88% of the initial PCE after more than 1000 h of ageing under the constant 1 sun illumination, even though all HTMs were doped as spiro-MeOTAD. Worth noting, that all SBA-based HTMs were more stable in contrast to spiro-MeOTAD, while the champion **MeSBA-DMPA** is among the most stable doped HTMs so far reported. This work demonstrated a significant advance in molecular design of operationally-stable HTMs for durable PSCs.

In chapter 5 I introduce a new electron excessive structural motif – ullazine, as a candidate to be used for the design of HTMs for PSCs. This electron-rich PHA combines energy level of commonly employed DMPA, while having an extended π -conjugation with the flat pyrene-like structure and the pronounced intramolecular CT. This work is focused on synthesis optimization aiming to feasibly prepare ullazine derivatives functionalized at different ring positions. In particular, a 6-bromoullazine derivative was obtained in high yields, and its further functionalization at the 6-position was demonstrated. The access to the four possible 3,9-diphenylullazinecarboxaldehyde regioisomers, so far unavailable or available only as side products, was also made possible. The elaborated procedures allowed to synthesize 4 D-A conjugates starting from the corresponding ullazine-carboxaldehydes and condensing with

dihexylmalononitrile. The materials were subjects to study the relationship between regioisomerism and their photophysical/ electrochemical properties. Only one of the ullazine D-A conjugates displayed the energy level suitable to get tested as an HTL for PSCs, attaining PCE of 13.07% without any doping. The results of this work demonstrate the potential of the ullazine fragment to get used as a donor motif for materials featuring intramolecular CT, however further investigation is required to optimize the energy levels and redox reversibility.

Summarizing, I have demonstrated the potential and versatility of SBA-and ullazine molecular platforms for preparation of organic materials for applications in light-energy conversion devices. The judicious choice of substituents, including electronically inert ones, molecular shape, regioisomerism are paramount when devising materials with advanced and/or predetermined properties. I hope that this work will contribute not only to a better understanding of the relationships between molecular structure and performance of organic materials in operating devices, but also to the further motivation and development of new materials with superior properties, approaching the ultimate goal of commercialization of the last generation thin-film organic and hybrid electronics.

CHAPTER 7

APPENDIX

6.1. Synthesis and Characterization of Organic Products – General Information

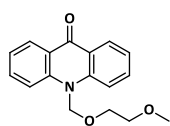
All commercially obtained chemicals were used without further purification, unless otherwise noted. Unless otherwise noted, all reactions were performed under the dry N₂ atmosphere, all reaction requiring air-free technique were performed in oven-dried glassware or in glassware that was heated with a heat gun under vacuum for 5-10 minutes. Thin-layer chromatography (TLC) was conducted with pre-coated TLC-sheets ALUGRAM® SIL G/UV₂₅₄ and visualized with UV. Flash column chromatography was performed using Sili-cycle P60, 40-63 μm (230-400 mesh). ¹H and ¹³C NMR spectra were recorded on a Bruker AVIII-HD (400 MHz) and are reported in ppm using solvents as an internal standards (CDCl₃ at 7.26 ppm and 77.16 ppm, acetone-*d*₆ at 2.05 ppm and 29.84 ppm, CD₂Cl₂ at 5.32 ppm and 53.84 ppm, C₆D₆ at 7.16 ppm and 128.06 ppm for ¹H and ¹³C NMR spectra respectively).²⁶² Data reported as: s = singlet, d = doublet, t = triplet, m = multiplet, br = broad, coupling constant(s) in Hz; integration. UV-Vis spectra were measured with a PerkinElmer Lambda 900 UV/VIS/NIR. PL experiments were performed using a FluoroSENS Gilden Photonics spectrophotometer. Cyclic voltammetry was measured with a Biologic S-200 cyclic voltammeter. Electrochemical measurements were performed in a 0.1M solution of Bu₄NPF₆ in dry DMF²⁶³ using Fc/Fc⁺ as an internal reference, Pt wire as a reference and counter electrodes and a glassy carbon disk as the working electrode. Mass spectra were recorded with a Bruker AutoFlex mass spectrometer using electrospray ionization (ESI), nanospray ionization (NSI), atmospheric pressure chemical ionization (APCI) or matrix-assisted laser desorption/ionization (MALDI) techniques.

Triethylamine used for Sonogashira reactions was dried in prior to use,²⁶⁴ 2,6-diiodo-4-bromoaniline was prepared according to the procedure published in literature²⁵⁹. TMEDA used for the synthesis of 10H,10'H-9,9'-spirobi[acridine] was dried prior to use.²⁶⁴ 10-((2-methoxyethoxy)methyl)acridin-9(10H)-one, methyl 2-(phenylamino)benzoate and 9,9-dimethyl-9,10-dihydroacridine were synthesized according to the published procedures.^{185,265,266} 10H,10'H-9,9'-spirobi[acridine] (**3**) was prepared with the modified procedure by M. Ooishi et al.¹²⁵

6.2. Appendix to chapter 3

6.2.1. Synthetic details

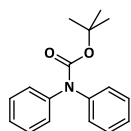
10-((2-methoxyethoxy)methyl)acridin-9(10H)-one, 1



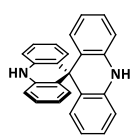
10-((2-methoxyethoxy)methyl)acridin-9(10H)-one is a known compound.

It was synthesized and purified according to the procedure by Y. Aoyama with comparable yield.¹⁸⁵ ¹H NMR spectrum was in a good agreement to those already published. To the best of our knowledge, ¹³C NMR has not been reported yet. ¹H NMR (400 MHz, Chloroform-*d*) δ 8.53 (dd, $J = 8.2, 1.8$ Hz, 2H), 7.79 – 7.67 (m, 4H), 7.33 (ddd, $J = 8.0, 6.0, 1.9$ Hz, 2H), 5.82 (s, 2H), 3.93 – 3.77 (m, 2H), 3.70 – 3.60 (m, 2H), 3.44 (s, 3H). ¹³C NMR (101 MHz, Chloroform-*d*) δ 178.60, 142.60, 134.13, 127.76, 122.60, 122.24, 115.42, 77.24, 72.37, 67.45, 59.34.

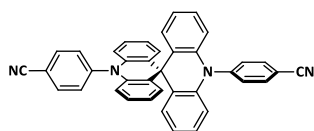
tert-butyl diphenylcarbamate, 2



A 250 mL round-bottomed flask was charged with diphenylamine (5.08 g, 30.0 mmol), DMAP (0.37 g, 3.0 mmol), Et₃N (5.0 mL, 36.0 mmol) and 1,4-dioxane (60 mL). The mixture was heated up to 95°C and Boc₂O (14.1 mL, 66.0 mmol) was added dropwise to the preheated solution. The mixture was kept stirring at 95°C until gas evolution ceased. The formation of the protected amine was monitored by TLC, if necessary, a small portion of Boc₂O was added to complete the reaction. Afterwards, all volatiles were removed under reduced pressure. DCM was added and the organic phase was washed with plenty of water, dried over MgSO₄ and concentrated. The residue was purified by passing through a short silica gel column using a mixture hexane/DCM (1:2) as the eluent ($R_f \approx 0.35$) to give **2** as a white solid (7.08 g, 88% yield). ¹H NMR (400 MHz, Chloroform-*d*) δ 7.34 – 7.27 (m, 4H), 7.24 – 7.14 (m, 6H), 1.45 (s, 9H). ¹³C NMR (101 MHz, Chloroform-*d*) δ 153.95, 143.17, 128.81, 127.10, 125.73, 81.23, 28.35. (ESI-MS): calcd. for [M+H]⁺ C₁₇H₂₀NO₂: 270.1494; found 270.1491.

10H,10'H-9,9'-spirobi[acridine], **3**

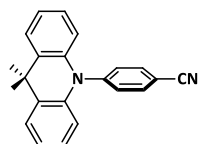
A heat-gun-dried N₂-filled 250 mL round-bottomed Schlenk-flask was charged with the carbamate **2** (4.7 g, 17.5 mmol), TMEDA (3.15 mL, 21.0 mmol), dry THF (35 mL) and cooled down to -78°C. *sec*-BuLi (13.8 mL, 19.3 mmol, 1.4M solution in cyclohexane) was added to the solution dropwise resulting a yellow-orange mixture that was stirred at -78°C for 2 hours. Afterwards a solution of the acridone **1** (4.1 g, 14.6 mmol) in THF (45 mL) was added dropwise to the solution of the organolithium reagent and kept stirring at -78°C for 1h, then allowed to reach RT gradually. Excess of 0.5M aqueous HCl was added to the reaction mixture carefully and stirred for 10 min. Afterwards DCM was added and the resulting organic phase was washed with plenty of water and an aqueous solution of Na₂CO₃ until gas evolution ceased, dried over MgSO₄ and concentrated. The residue was purified by silica gel column chromatography using a mixture hexane/DCM (1:1) as the eluent (*R_f* ≈ 0.4) to give **3** as an off-white solid (3.5 g, 69% yield). ¹H NMR (400 MHz, Acetone-*d*₆) δ 8.26 (brs, 2H), 6.97 (ddd, *J* = 7.8, 7.1, 1.6 Hz, 4H), 6.92 – 6.82 (m, 8H), 6.66 – 6.57 (m, 4H). ¹³C NMR (101 MHz, Acetone-*d*₆) δ 137.43, 132.99, 131.61, 127.58, 120.74, 114.16, 47.94. (FTMS-APCI): calcd. for [M]⁺ C₂₅H₁₈N₂: 346.1470; found 346.1473.

4,4'-(10H,10'H-9,9'-spirobi[acridine]-10,10'-diyl)dibenzonitrile, **4** (SBABz4)

A heat-gun-dried N₂-filled 25 mL Schlenk-tube was charged with **3** (0.173 g, 0.5 mmol), 4-bromobenzonitrile (0.346 g, 2.0 mmol), NaOtBu (0.240 g, 2.5 mmol), Pd₂dba₃ (0.017 g, 0.019 mmol), XPhos (0.022 g, 0.045 mmol) and dry toluene (5 mL). The mixture was stirred at 110°C overnight, cooled down to ambient temperature, diluted with EtOAc and washed with aqueous NH₄Cl and water. The organic phase was dried over MgSO₄, concentrated under reduced pressure and purified by silica gel column chromatography using a mixture hexane/DCM (2:3) as the eluent (*R_f* ≈ 0.3). The product was precipitated from DCM-MeOH and then from DCM-hexane to give pure **4** as a white solid (0.220 g, 80%). ¹H NMR (400 MHz, Chloroform-*d*) δ 8.09 – 7.97 (m, 4H), 7.68 – 7.60 (m, 4H), 7.12 (dd, *J* = 7.8, 1.6 Hz, 4H), 6.91 (ddd, *J* = 8.5, 7.2, 1.6 Hz, 4H), 6.78 (ddd, *J* = 7.8, 7.2, 1.2 Hz,

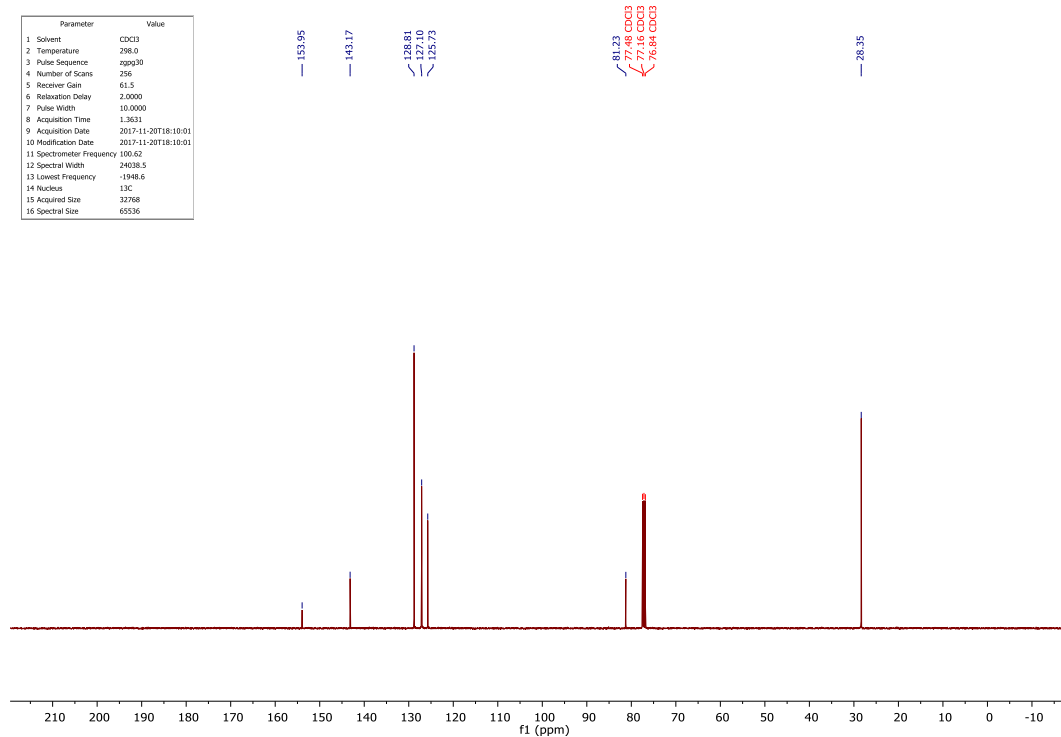
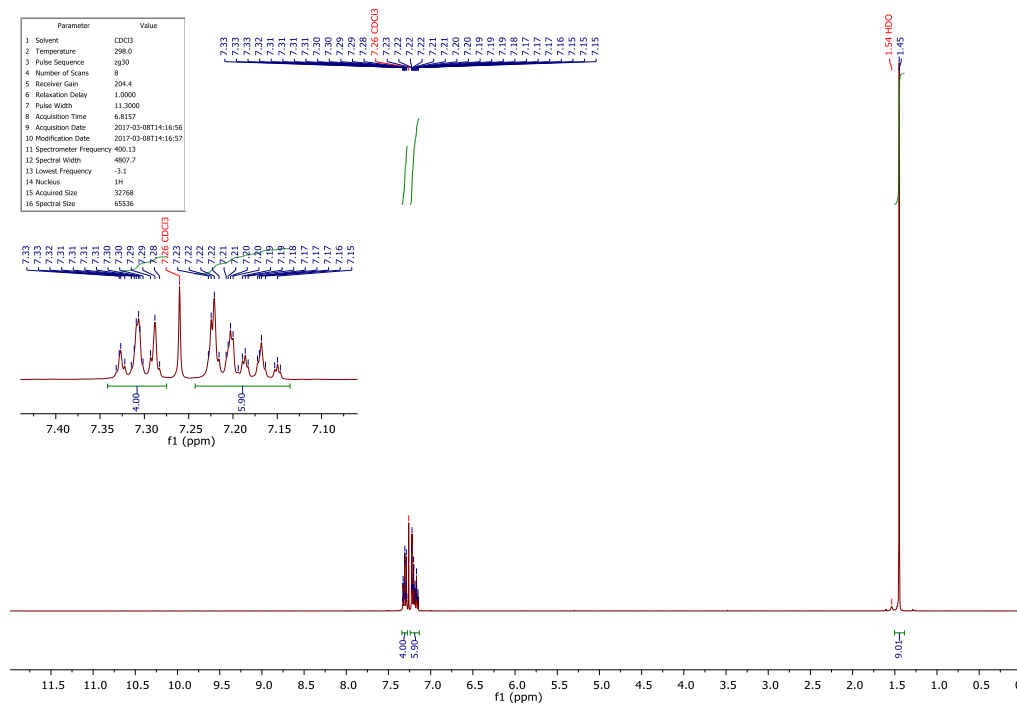
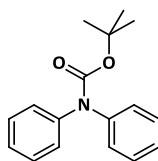
4H), 6.19 (dd, $J = 8.3, 1.2$ Hz, 4H). ^{13}C NMR (101 MHz, Chloroform-*d*) δ 145.72, 137.73, 135.16, 132.90, 132.87, 131.73, 126.92, 121.59, 118.16, 113.73, 112.66, 46.92. (FTMS-APCI): calcd. for $[\text{M}]^+$ $\text{C}_{39}\text{H}_{24}\text{N}_4$: 548.2001; found 548.2015.

4-(9,9-dimethylacridin-10(9H)-yl)benzonitrile, 7 (DMABz4)

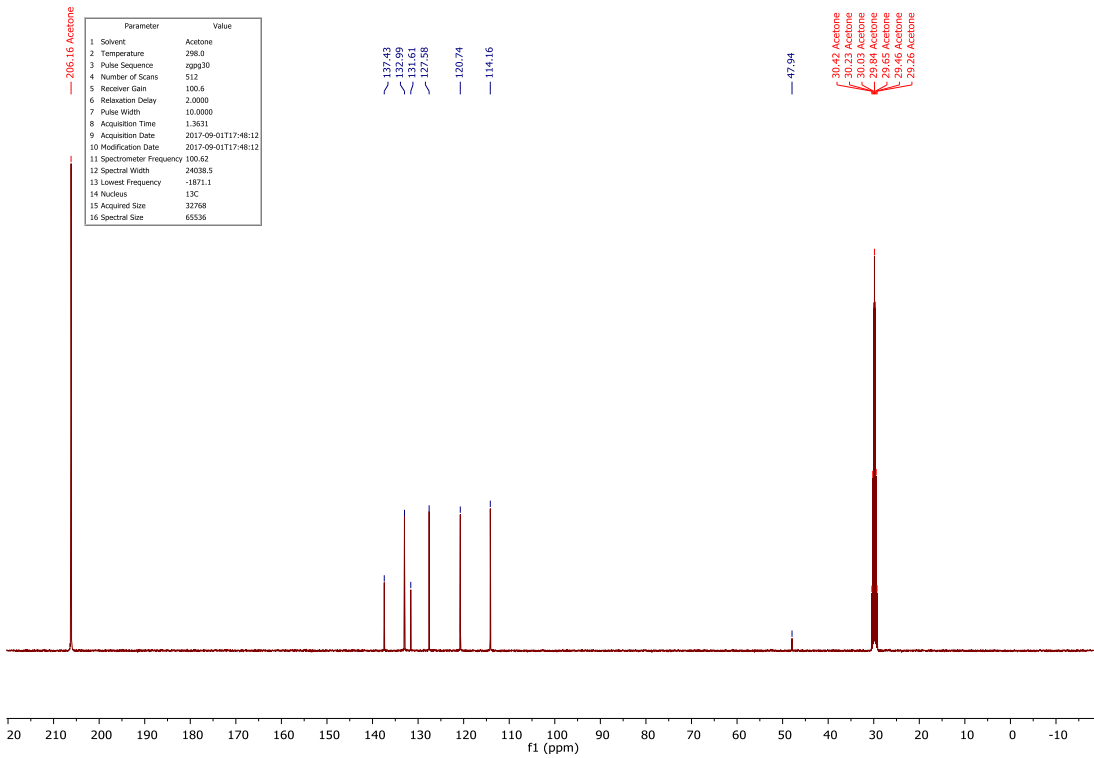
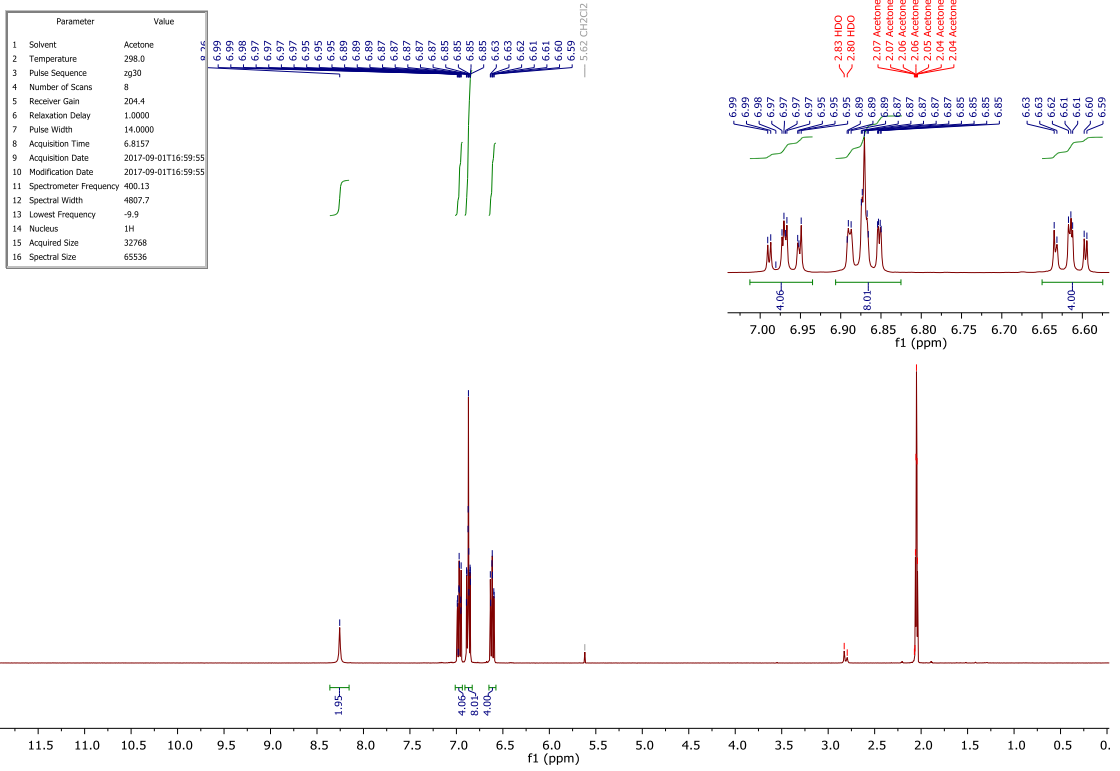
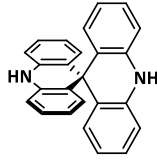


A heat-gun-dried N_2 -filled 50 mL Schlenk-tube was charged with DMA (0.314 g, 1.5 mmol), 4-bromobenzonitrile (0.409 g, 2.25 mmol), NaOtBu (0.360 g, 3.75 mmol), Pd_2dba_3 (0.034 g, 0.038 mmol), XPhos (0.054 g, 0.113 mmol) and dry toluene (10 mL). The mixture was stirred at 110°C overnight, cooled down to ambient temperature, diluted with EtOAc and washed with aqueous NH_4Cl and water. The organic phase was dried over MgSO_4 , concentrated under reduced pressure and purified by silica gel column chromatography using a mixture hexane/DCM (1:1) as the eluent ($R_f \approx 0.25$). The product was precipitated from DCM-MeOH and then from DCM-hexane to give pure **4** as a white solid (0.302 g, 65%). ^1H NMR (400 MHz, Chloroform-*d*) δ 7.94 – 7.86 (m, 2H), 7.52 – 7.45 (m, 4H), 7.05 – 6.95 (m, 4H), 6.33 – 6.24 (m, 2H), 1.67 (s, 6H). ^{13}C NMR (101 MHz, Chloroform-*d*) δ 146.23, 140.29, 134.88, 131.65, 131.17, 126.60, 125.56, 121.81, 118.51, 114.93, 111.49, 36.31, 30.96. (FTMS-NSI): calcd. for $[\text{M}]^+$ $\text{C}_{22}\text{H}_{18}\text{N}_2$: 310.1470; found 310.1543.

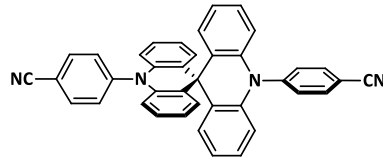
6.2.2. ¹H- and ¹³C- NMR spectra of the final compounds



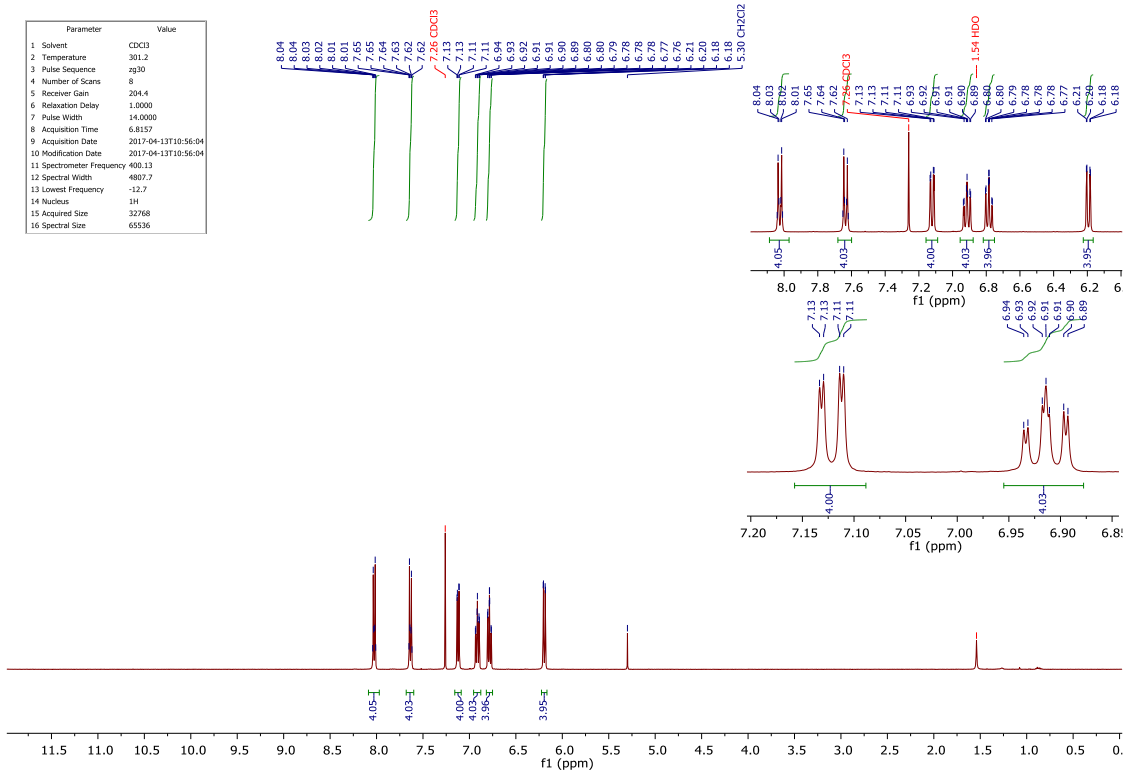
APPENDIX



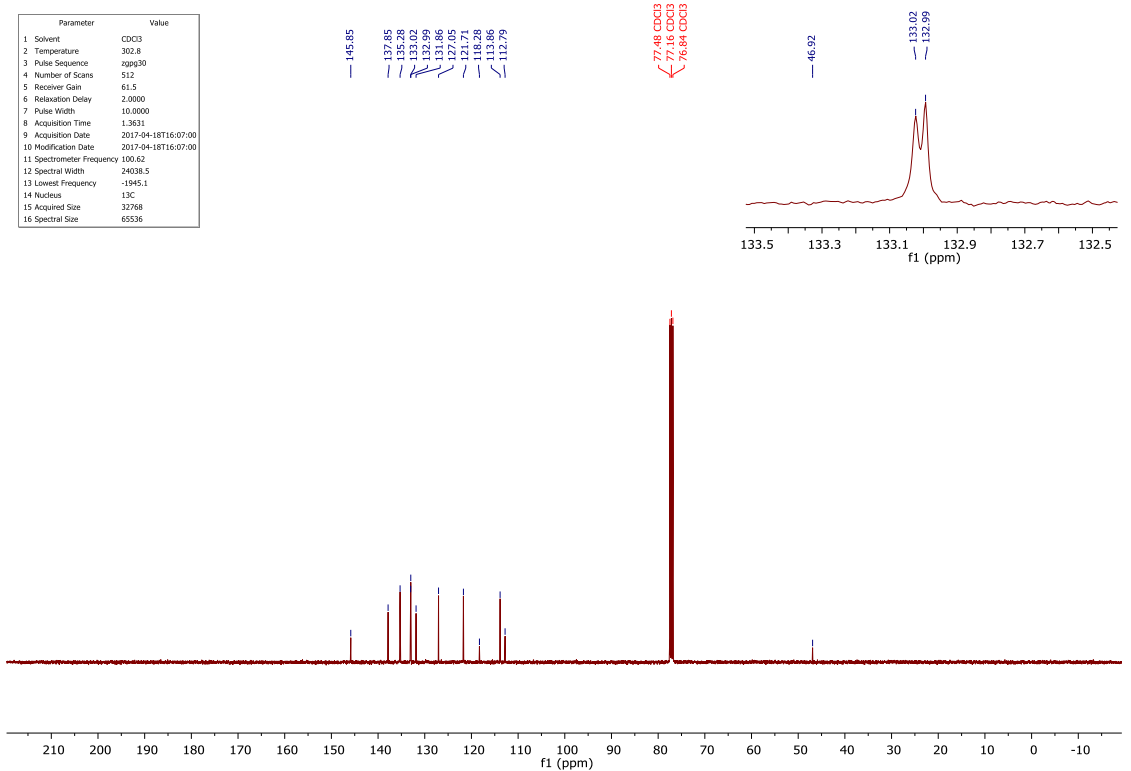
APPENDIX



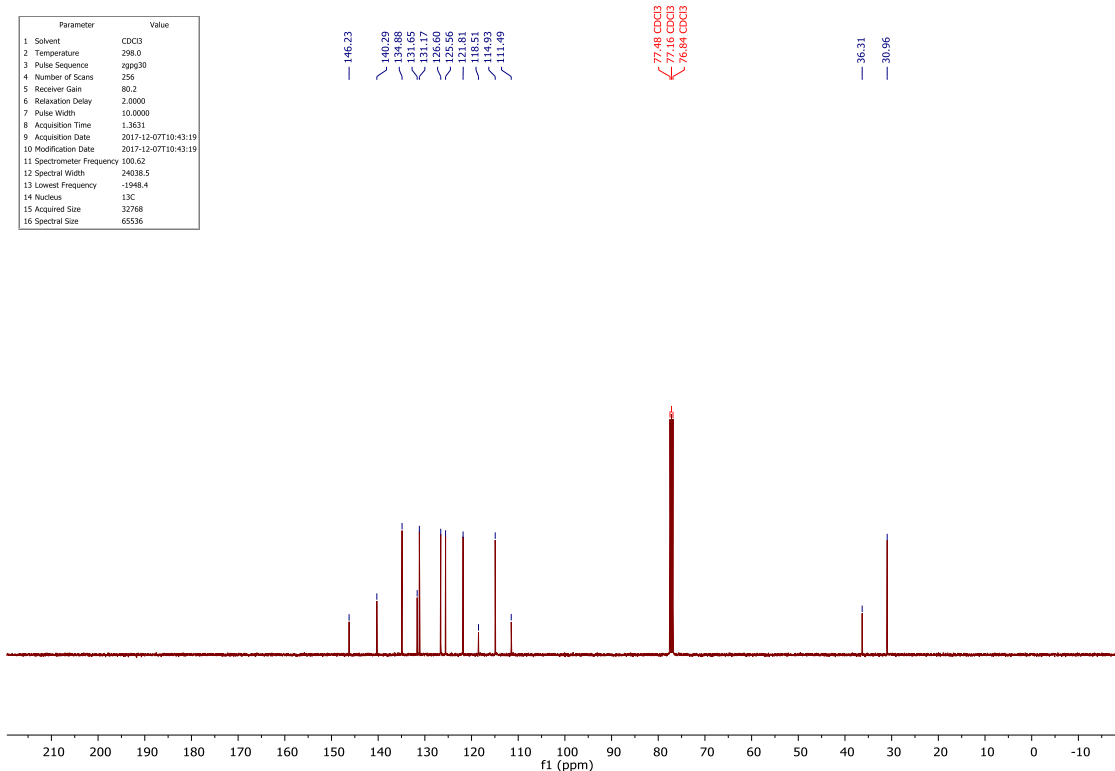
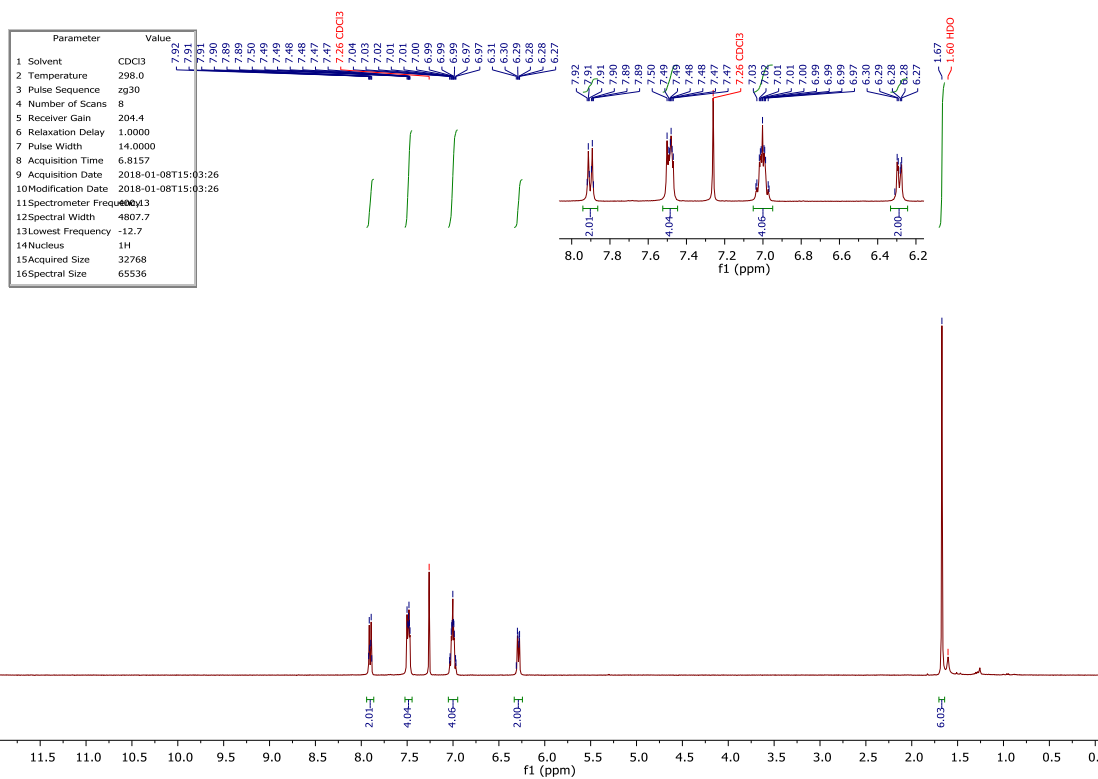
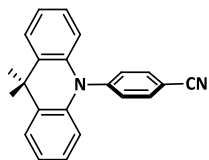
Parameter	Value
1 Solvent	CDCl3
2 Temperature	301.2
3 Pulse Sequence	zg30
4 Number of Scans	8
5 Receiver Gain	204.4
6 Relaxation Delay	1.0000
7 Pulse Width	14.0000
8 Acquisition Time	6.8157
9 Acquisition Date	2017-04-13T10:56:04
10 Modification Date	2017-04-13T10:56:04
11 Spectrometer Frequency	400.13
12 Spectral Width	4607.7
13 Lowest Frequency	-12.7
14 Nucleus	1H
15 Acquired Size	32768
16 Spectral Size	65536



Parameter	Value
1 Solvent	CDCl3
2 Temperature	302.8
3 Pulse Sequence	zgpg30
4 Number of Scans	512
5 Receiver Gain	61.5
6 Relaxation Delay	2.0000
7 Pulse Width	10.0000
8 Acquisition Time	1.3631
9 Acquisition Date	2017-04-18T16:07:00
10 Modification Date	2017-04-18T16:07:00
11 Spectrometer Frequency	100.62
12 Spectral Width	24038.5
13 Lowest Frequency	-1945.1
14 Nucleus	13C
15 Acquired Size	32768
16 Spectral Size	65536



APPENDIX



6.2.3. Materials Preparation and Measurements Results

Solution preparation

Deoxygenated solutions of **SBABz₄** and **DMABz₄** in dichloromethane (DCM) with concentration 10^{-5} mol L⁻¹ were prepared in a glove box under nitrogen atmosphere. Deoxygenated solutions of **SBABz₄** for UV-vis absorption and luminescence measurements in different solvents were obtained by bubbling nitrogen and sealing with a JYoung valve. Spectroscopic grade solvents were used without further purification.

Film preparation

Films for optical measurements were prepared in a glove box with nitrogen atmosphere. Neat **SBABz₄** and **SBABz₄:DPEPO** films were processed on a 0.5x0.5 sq.-inches glass substrates without modification. The substrates were sequentially cleaned with deionized water, acetone, and isopropanol for 10 min each in an ultrasonic bath and plasma-edged for 30 s before use. Solutions of **SBABz₄** (or **SBABz₄:DPEPO** with the desired weight ratio) in DCM with concentration 5 mg mL⁻¹ were spin-coated at 3000 rpm during 1 min. After spin-coating, the substrates were annealed on a hot plate at 100°C for 10 minutes.

PL measurements

PL spectra and transients of solutions and films were recorded with calibrated Fluorescence Spectrometer FLS980 (Edinburgh Instruments), equipped with three excitation sources: continuous broad-spectrum xenon lamp Xe1, pulsed violet diode laser EPL-375 (wavelength 375.0 nm, pulse width 80 ps), and microsecond xenon flash lamp μ F920. Laser repetition rate was tunable with discrete steps in the range from 2.5 kHz to 20 MHz. Spectral resolution of the system was 0.1 nm. Temporal resolution for time-resolved measurements varied from 2 to 50 ns, depending on the recorded time range.

All measurements for solid films at room and low temperatures were carried out in active vacuum (10^{-5} mbar) in Janis ST-100 cryostat. Measurements at room temperature were performed beforehand for every sample. Emission recorded at

different time scales was merged to improve temporal resolution for the prompt component.

PLQYs were measured with the calibrated integrating sphere F-Mo1 in FLS980 spectrometer. All measurements for solutions were conducted in a standard (10x10 mm) quartz cuvette with a tight screw cap. Solid films for PLQY measurements were sealed in a quartz cuvette under nitrogen atmosphere.

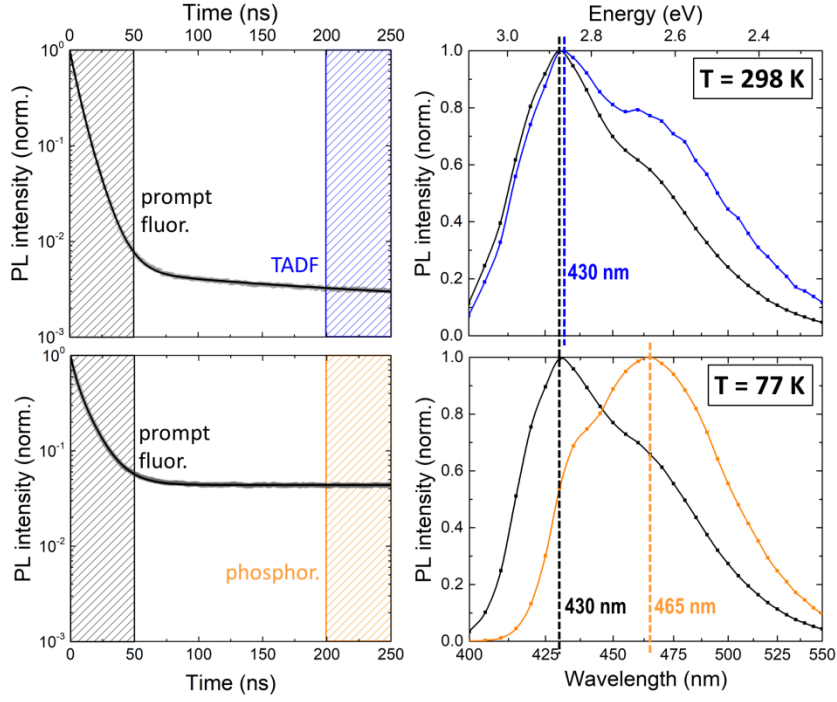


Figure 29. PL decay curves and the corresponding normalized PL spectra at different stages of decay of a neat **SBABz4** film at 298 K (upper plots) and 77 K (lower plots). Prompt components were integrated within 0-50 ns, delayed within 200-250 ns (integration regions are shown at the PL decays with corresponding colours). Right: energy diagram of the corresponding processes.

6.2.4. Quantum efficiencies of components in PL decay

Double-exponential fit for normalized PL decay curve:

$$PL_{norm}(t) = A_{pr} \exp\left(-\frac{t}{\tau_{pr}}\right) + A_{TADF} \exp\left(-\frac{t}{\tau_{TADF}}\right);$$

Contribution of the prompt fluorescence to the total PLQY:

$$\varphi_{pr} = \frac{\int_0^{\infty} A_{pr} \exp(-t/\tau_{pr}) dt}{\int_0^{\infty} A_{pr} \exp(-t/\tau_{pr}) dt + \int_0^{\infty} A_{TADF} \exp(-t/\tau_{TADF}) dt} \cdot PLQY = \frac{A_{pr} \tau_{pr}}{A_{pr} \tau_{pr} + A_{TADF} \tau_{TADF}} \cdot PLQY;$$

Contribution of the delayed fluorescence to the total PLQY:

$$\varphi_{TADF} = \frac{\int_0^{\infty} A_{TADF} \exp(-t/\tau_{TADF}) dt}{\int_0^{\infty} A_{pr} \exp(-t/\tau_{pr}) dt + \int_0^{\infty} A_{TADF} \exp(-t/\tau_{TADF}) dt} \cdot PLQY = \frac{A_{TADF} \tau_{TADF}}{A_{pr} \tau_{pr} + A_{TADF} \tau_{TADF}} \cdot PLQY;$$

6.2.5. Stretched exponential fit for transient PL

Fit with two decaying stretched exponents for normalized PL decay curve:

$$PL_{norm}(t) = A_{pr} \exp\left(-\left(\frac{t}{\tau_{pr}}\right)^{\beta_1}\right) + A_{TADF} \exp\left(-\left(\frac{t}{\tau_{TADF}}\right)^{\beta_2}\right);$$

Then average decay time is expressed as:

$$\langle \tau_{pr} \rangle = \int_0^{\infty} t \cdot PL_{norm}(t) dt = \tau_{pr} \cdot \frac{1}{\beta_1} \Gamma\left(\frac{1}{\beta_1}\right),$$

$$\langle \tau_{TADF} \rangle = \tau_{TADF} \cdot \frac{1}{\beta_2} \Gamma\left(\frac{1}{\beta_2}\right);$$

Here $\Gamma(x)$ is gamma-function.

Ratio $\varphi_{pr}/\varphi_{TADF}$ between quantum efficiencies of the prompt and delayed components was calculated as a quotient of the areas under the corresponding stretched exponents, S_{pr}/S_{TADF} .

Table 6. Fit parameters for the normalized PL decay curves of **SBABz4** thin films.

Parameter	neat SBABz4 film		5wt% SBABz4 :DPEPO film	
	prompt	TADF	prompt	TADF
A , a.u.	1.01	0.0085	1.02	0.00046
τ , ns	5.8	46	3.45	2750
β	0.85	0.42	0.67	0.39
$\langle \tau \rangle$, ns	6.3	134.4	4.6	9815
S , a.u.	6.47	1.11	4.71	4.51
$\varphi_{pr}/\varphi_{TADF}$	5.83		1.04	

6.2.6. Performance estimates for SBABz4-based OLEDs

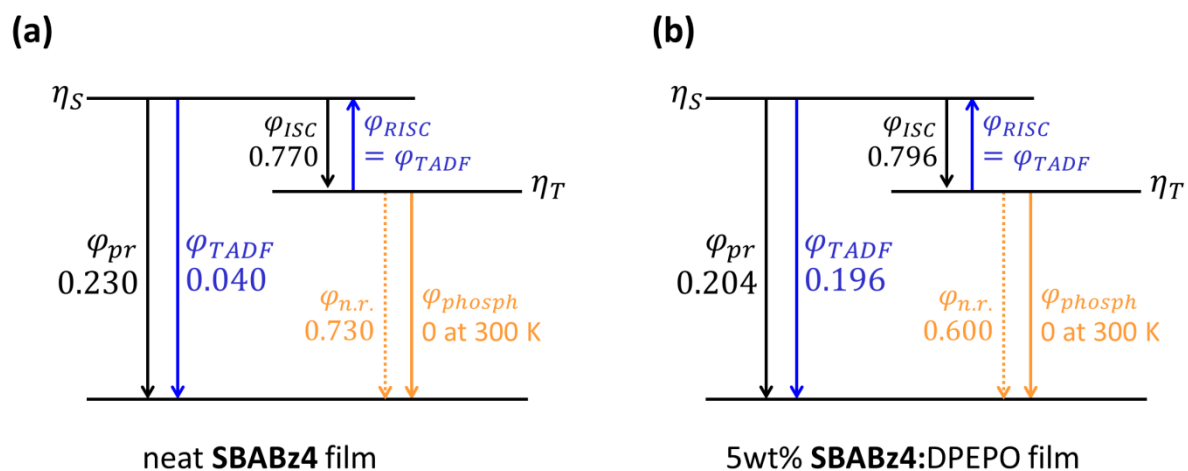


Figure 30. Energy diagram depicting quantum efficiencies of various processes in the neat **SBABz4** (a) and 5wt% **SBABz4:DPEPO** (b) films.

Table 7. Maximum external electroluminescence efficiencies and external quantum efficiencies estimated from photophysical parameters for **SBABz4**-based OLEDs.

Parameter	neat SBABz4 film	5wt% SBABz4:DPEPO film
$\Phi_{EL,int}$	0.095	0.237
$EQE_{max20\%}$ ^[a]	1.9%	4.7%
$EQE_{max30\%}$ ^[b]	2.9%	7.1%

[a] EQE of corresponding OLED estimated for 20% light outcoupling.
 [b] EQE of corresponding OLED estimated for 30% light outcoupling.

6.2.7. RISC activation energy

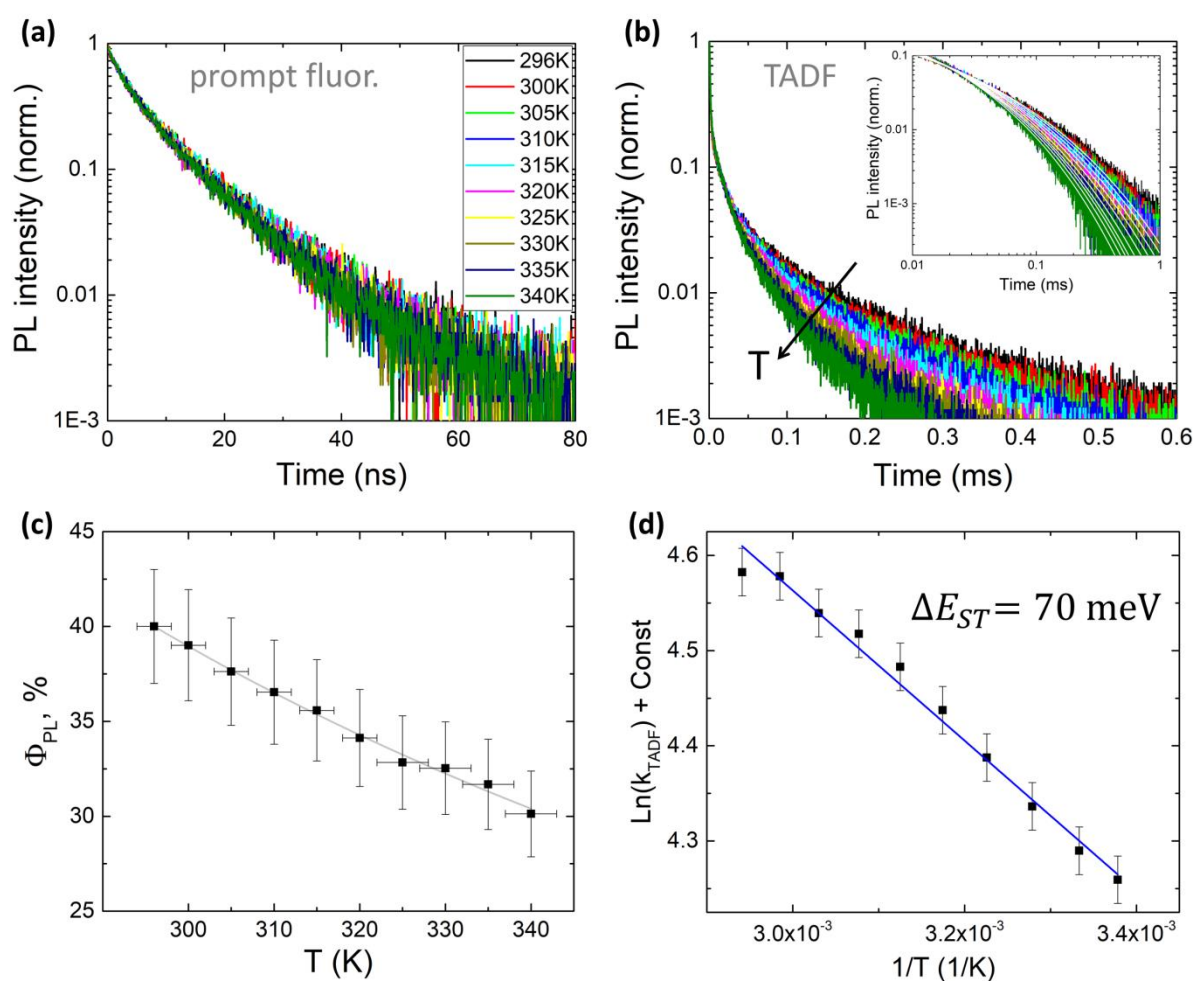
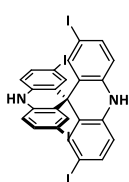


Figure 31. TRPL from 5wt% SBABz₄:DPEPO film above the room temperature. (a) Prompt fluorescence. (b) Delayed fluorescence. The inset shows stretched exponential fit (white lines) in double logarithmic scale. (c) Absolute PLQY measured at growing temperature in the inert atmosphere. (d) Arrhenius-like plot for k_{TADF} .

6.3. Appendix to chapter 4

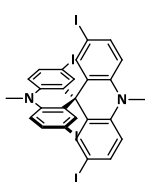
6.3.1. Synthetic details

2,2',7,7'-tetraiodo-10*H*,10'*H*-9,9'-spirobi[acridine], 2

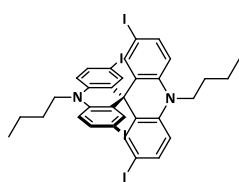


A 25 mL round-bottomed flask was charged with SBA 1 (0.103 g, 0.3 mmol) and MeOH (6 mL). ICl (0.205 g, 1.26 mmol) in MeOH (3 mL) was added to the suspension dropwise at RT upon stirring. The mixture was kept stirring at RT overnight. The precipitate was filtered off, washed with plenty of methanol and dried to give 2 as a brownish-grey solid (0.25 g, 98% yield). The reaction was performed on multigram scale resulting the similar yield. The tetraiodinated amine 2 is poorly soluble in common organic solvents except diethyl ether. ^1H NMR (400 MHz, Acetone- d_6) δ 8.72 (brs, 2H), 7.37 (dd, $J = 8.5, 2.0$ Hz, 4H), 7.14 (d, $J = 2.4$ Hz, 4H), 6.80 (d, $J = 8.5$ Hz, 4H). ^{13}C NMR (101 MHz, Acetone- d_6) δ 141.01, 137.40, 136.42, 132.84, 117.44, 82.30, 46.55. HRMS (MALDI-TOF-MS): calcd. for $[\text{M}]^+$ $\text{C}_{25}\text{H}_{14}\text{I}_4\text{N}_2$: 849.7336; found 849.732.

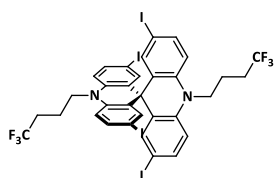
2,2',7,7'-tetraiodo-10,10'-dimethyl-10*H*,10'*H*-9,9'-spirobi[acridine], 3



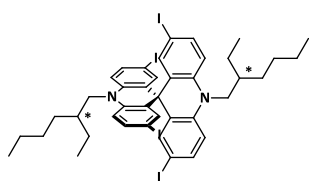
A 25 mL round-bottomed flask was charged with 2 (0.255 g, 0.3 mmol) and DMF (5 mL). NaH (0.027 g, 0.66 mmol, 60% dispersion in mineral oil) was added to the suspension portionwise at RT upon stirring. The mixture was left to react for 30 min resulting an orange-brown solution. Afterwards MeI (0.19 mL, 3.0 mmol) was added to the mixture at RT. White precipitated formed immediately. The mixture was stirred overnight and then it was diluted with plenty of water. The precipitate was filtered off, washed thoroughly with water and methanol and dried up giving 3 as a white powder. (0.26 g, 99%) ^1H NMR (400 MHz, Chloroform- d) δ 7.44 (dd, $J = 9.0, 2.2$ Hz, 4H), 7.02 (d, $J = 2.1$ Hz, 4H), 6.74 (d, $J = 8.4$ Hz, 4H), 3.47 (s, 6H). The compound was only sparingly soluble to obtain ^{13}C NMR spectrum. HRMS (MALDI-TOF-MS): calcd. for $[\text{M}]^+$ $\text{C}_{27}\text{H}_{18}\text{I}_4\text{N}_2$: 877.7649; found 877.768.

10,10'-dibutyl-2,2',7,7'-tetraiodo-10*H*,10'*H*-9,9'-spirobi[acridine], 4

The titled compound was synthesized and worked-up according to the similar procedure as for 3, starting with 2 (0.255 g, 0.3 mmol) in DMF (5 mL), NaH (0.027 g, 0.66 mmol, 60% dispersion in mineral oil) and *n*BuI (0.34 mL, 3.0 mmol). The desired product 4 was isolated as an off-white powder. (0.25 g, 87%) ¹H NMR (400 MHz, Chloroform-*d*) δ 7.39 (dd, *J* = 8.8, 2.2 Hz, 4H), 6.99 (d, *J* = 2.2 Hz, 4H), 6.73 (d, *J* = 8.9 Hz, 4H), 3.94 – 3.85 (m, 4H), 1.84 (p, *J* = 8.0 Hz, 4H), 1.62 – 1.46 (m, 4H), 1.09 (t, *J* = 7.3 Hz, 6H). ¹³C NMR (101 MHz, Methylene Chloride-*d*₂) δ = 140.81, 137.17, 137.04, 134.64, 115.36, 82.85, 46.57, 46.24, 28.40, 20.58, 14.16. HRMS (FTMS-NSI): calcd. for [M+H]⁺ C₃₃H₃₁I₄N₂: 962.8666; found 962.8660.

2,2',7,7'-tetraiodo-10,10'-bis(4,4,4-trifluorobutyl)-10*H*,10'*H*-9,9'-spirobi[acridine], 5

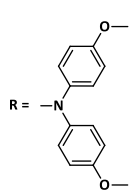
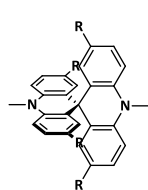
The titled compound was synthesized and worked-up according to the similar procedure as for 3, starting with 2 (0.255 g, 0.3 mmol) in DMF (5 mL), NaH (0.027 g, 0.66 mmol, 60% dispersion in mineral oil) and 1,1,1-trifluoro-4-iodobutane (0.71 mL, 3.0 mmol). The desired product 4 was isolated as an off-white powder. (0.24 g, 75%) ¹H NMR (400 MHz, Chloroform-*d*) δ 7.44 (dd, *J* = 8.8, 2.2 Hz, 4H), 6.99 (d, *J* = 2.1 Hz, 4H), 6.69 (d, *J* = 8.9 Hz, 4H), 4.06 – 3.96 (m, 4H), 2.42 – 2.26 (m, 4H), 2.14 (p, *J* = 7.6 Hz, 4H). ¹³C NMR (101 MHz, Acetone-*d*₆) δ 141.44, 137.81, 137.45, 135.30, 128.45 (q, *J* = 275.5 Hz), 116.22, 83.39, 46.97, 44.85, 31.12 (q, *J* = 29.0 Hz), 19.41 (q, *J* = 2.7 Hz). ¹⁹F NMR (376 MHz, Chloroform-*d*) δ -65.42 (t, *J* = 10.8 Hz). HRMS (MALDI-TOF-MS): calcd. for [M]⁺ C₃₃H₂₄F₆I₄N₂: 1069.8023; found 1069.801.

10,10'-bis(2-ethylhexyl)-2,2',7,7'-tetraiodo-10*H*,10'*H*-9,9'-spirobi[acridine], 6

The titled compound was synthesized and worked-up according to the similar procedure as for 3, starting with 2 (0.425 g, 0.5 mmol) in DMF (5 mL), NaH (0.044 g, 1.1 mmol, 60% dispersion in mineral oil) and 1-bromo-2-ethylhexane (0.89 mL, 5.0 mmol). The desired product 6 was isolated as an off-white powder. (0.4 g, 74%) ¹H NMR (400

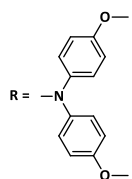
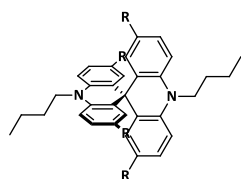
MHz, Chloroform-*d*) δ 7.35 (dd, $J = 8.9, 2.2$ Hz, 4H), 6.98 (d, $J = 2.2$ Hz, 4H), 6.78 (d, $J = 9.1$ Hz, 4H), 3.95 – 3.78 (m, 4H), 2.09 – 1.97 (m, 2H), 1.63 – 1.27 (m, 16H), 1.00 (t, $J = 7.4$ Hz, 6H), 0.92 (t, $J = 7.0$ Hz, 6H). ^{13}C NMR (101 MHz, Chloroform-*d*) δ 141.63, 136.83, 136.46, 134.58, 115.15, 82.95, 48.26, 46.32, 37.26, 30.98, 28.88, 24.29, 23.36, 14.31, 11.42. HRMS (FTMS-NSI): calcd. for $[\text{M}+\text{H}]^+$ $\text{C}_{41}\text{H}_{47}\text{I}_4\text{N}_2$: 1074.9918; found 1074.9880.

*N*²,*N*²,*N*^{2'},*N*^{2'},*N*⁷,*N*⁷,*N*^{7'},*N*^{7'}-octakis(4-methoxyphenyl)-10,10'-dimethyl-10*H*,10'*H*-9,9'-spirobi[acridine]-2,2',7,7'-tetraamine, 7 (MeSBA-DMPA)



A heat-gun-dried N_2 -filled 25 mL Schlenk-tube was charged with **3** (0.26 g, 0.3 mmol), 4,4'-dimethoxydiphenylamine (0.344 g, 1.5 mmol), NaOtBu (0.173 g, 1.8 mmol), $\text{Pd}(\text{CH}_3\text{CN})_2\text{Cl}_2$ (0.004 g, 0.015 mmol), $t\text{Bu}_3\text{P}$ (0.03 mL, 0.03 mmol, 1.0 M solution in toluene) and dry 1,4-dioxane (5 mL). The mixture was stirred at 100°C overnight, cooled down to ambient temperature, diluted with EtOAc and washed with aqueous NH_4Cl and water. The organic phase was dried over MgSO_4 , concentrated under reduced pressure and purified by silica gel column chromatography using a mixture hexane/THF (3:2) as the eluent ($R_f \approx 0.3$). The product was precipitated from THF-MeOH and THF-hexane to give pure **7** as a yellowish solid (0.24 g, 62%). A single crystal suitable for XRD analysis was grown from a chlorobenzene solution upon slow evaporation of the solvent. ^1H NMR (400 MHz, Benzene-*d*₆) δ 7.13 (d, $J = 2.6$ Hz, 4H), 7.05 – 6.97 (m, 16H), 6.92 (dd, $J = 8.8, 2.6$ Hz, 4H), 6.76 – 6.67 (m, 16H), 6.38 (d, $J = 8.8$ Hz, 4H), 3.29 (s, 24H), 2.72 (s, 6H). ^{13}C NMR (101 MHz, Benzene-*d*₆) δ 155.41, 142.50, 141.69, 136.22, 132.21, 126.53, 125.07, 123.30, 114.98, 113.37, 55.02, 48.86, 33.51. HRMS (FTMS-NSI): calcd. for $[\text{M}]^+$ $\text{C}_{83}\text{H}_{74}\text{N}_6\text{O}_8$: 1282.5568; found 1282.5576.

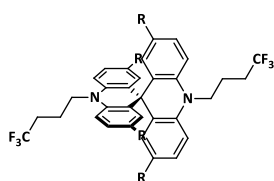
10,10'-dibutyl-*N*²,*N*²,*N*^{2'},*N*^{2'},*N*⁷,*N*⁷,*N*^{7'},*N*^{7'}-octakis(4-methoxyphenyl)-10*H*,10'*H*-9,9'-spirobi[acridine]-2,2',7,7'-tetraamine, 8 (BuSBA-DMPA)



The titled compound was synthesized and worked-up according to the similar procedure as for **7**, starting with **4** (0.18 g, 0.187 mmol), 4,4'-

dimethoxydiphenylamine (0.214 g, 0.935 mmol), NaOtBu (0.108 g, 1.12 mmol), Pd(CH₃CN)₂Cl₂ (0.003 g, 0.009 mmol), *t*Bu₃P (0.018 mL, 0.018 mmol, 1.0 M solution in toluene) and dry 1,4-dioxane (5 mL). The product was purified by silica gel column chromatography using a mixture hexane/THF (4:1) as the eluent (*R_f* ≈ 0.25). Afterwards, the isolated compound was precipitated from THF-MeOH and THF-hexane to give pure 8 as a yellowish solid (0.164 g, 64%). ¹H NMR (400 MHz, Benzene-*d*₆) δ 7.25 (d, *J* = 2.7 Hz, 4H), 7.07 – 6.98 (m, 16H), 6.87 (dd, *J* = 8.9, 2.7 Hz, 4H), 6.76 – 6.66 (m, 16H), 6.57 (d, *J* = 9.0 Hz, 4H), 3.39 – 3.32 (m, 4H), 3.30 (s, 24H), 1.48 – 1.36 (m, 4H), 1.18 (h, *J* = 7.3 Hz, 4H), 0.88 (t, *J* = 7.3 Hz, 6H). ¹³C NMR (101 MHz, Benzene-*d*₆) δ 155.45, 142.33, 141.50, 133.82, 133.52, 127.62, 125.17, 122.95, 114.94, 113.16, 55.00, 48.31, 46.13, 28.26, 20.36, 13.94. HRMS (MALDI-TOF-MS): calcd. for [M]⁺ C₈₉H₈₆N₆O₈: 1366.6507; found 1366.656.

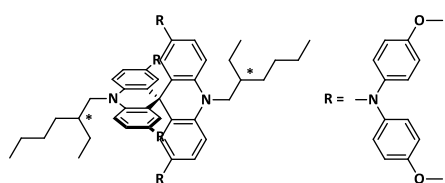
*N*²,*N*²,*N*^{2'},*N*^{2'},*N*⁷,*N*⁷,*N*^{7'},*N*^{7'}-octakis(4-methoxyphenyl)-10,10'-bis(4,4,4-trifluorobutyl)-10*H*,10'*H*-9,9'-spirobi[acridine]-2,2',7,7'-tetraamine, 9 (FBuSBA-DMPA)



The titled compound was synthesized and worked-up according to the similar procedure as for 7, starting with with 5 (0.14 g, 0.131 mmol), 4,4'-dimethoxydiphenylamine (0.15 g, 0.654 mmol),

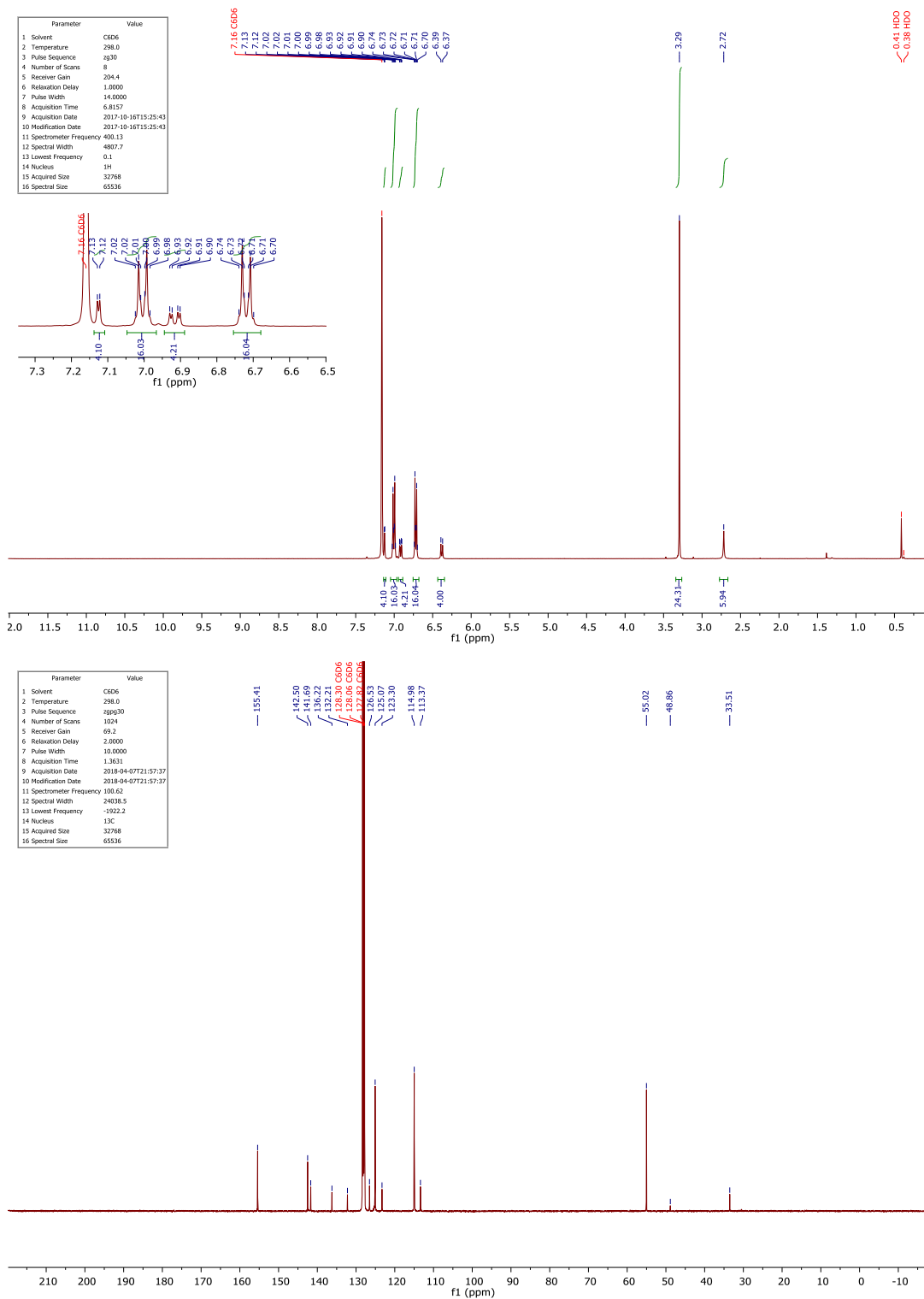
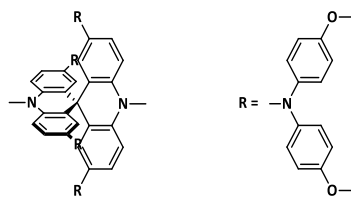
NaOtBu (0.076 g, 0.768 mmol), Pd(CH₃CN)₂Cl₂ (0.002 g, 0.007 mmol), *t*Bu₃P (0.014 mL, 0.014 mmol, 1.0 M solution in toluene) and dry 1,4-dioxane (5 mL). The product was purified by silica gel column chromatography using a mixture hexane/THF (3:1) as the eluent (*R_f* ≈ 0.25). Afterwards, the isolated compound was precipitated from THF-MeOH and THF-hexane to give pure 9 as a yellowish solid (0.12 g, 62%). ¹H NMR (400 MHz, Benzene-*d*₆) δ 7.19 (d, *J* = 2.7 Hz, 4H), 7.06 – 6.96 (m, 16H), 6.86 (dd, *J* = 8.9, 2.7 Hz, 4H), 6.76 – 6.67 (m, 16H), 6.42 (d, *J* = 9.0 Hz, 4H), 3.29 (s, 24H), 3.28 – 3.21 (m, 4H), 1.71 – 1.49 (m, 8H). ¹³C NMR (101 MHz, Benzene-*d*₆) δ 155.62, 142.11, 141.95, 133.54, 133.14, 127.63 (q, *J* = 276.7 Hz), 127.22, 125.36, 122.69, 114.98, 112.85, 55.00, 48.18, 45.25, 30.89 (q, *J* = 29.2 Hz), 18.98. ¹⁹F NMR (376 MHz, Benzene-*d*₆) δ -65.22 (t, *J* = 11.1 Hz, 6F). HRMS (MALDI-TOF-MS): calcd. for [M]⁺ C₈₉H₈₀F₆N₆O₈: 1474.5942; found 1474.600.

10,10'-bis(2-ethylhexyl)-*N*²,*N*²,*N*²,*N*²,*N*⁷,*N*⁷,*N*⁷,*N*⁷-octakis(4-methoxyphenyl)-10*H*,10'*H*-9,9'-spirobi[acridine]-2,2',7,7'-tetraamine, 10 (EtHexSBA-DMPA)

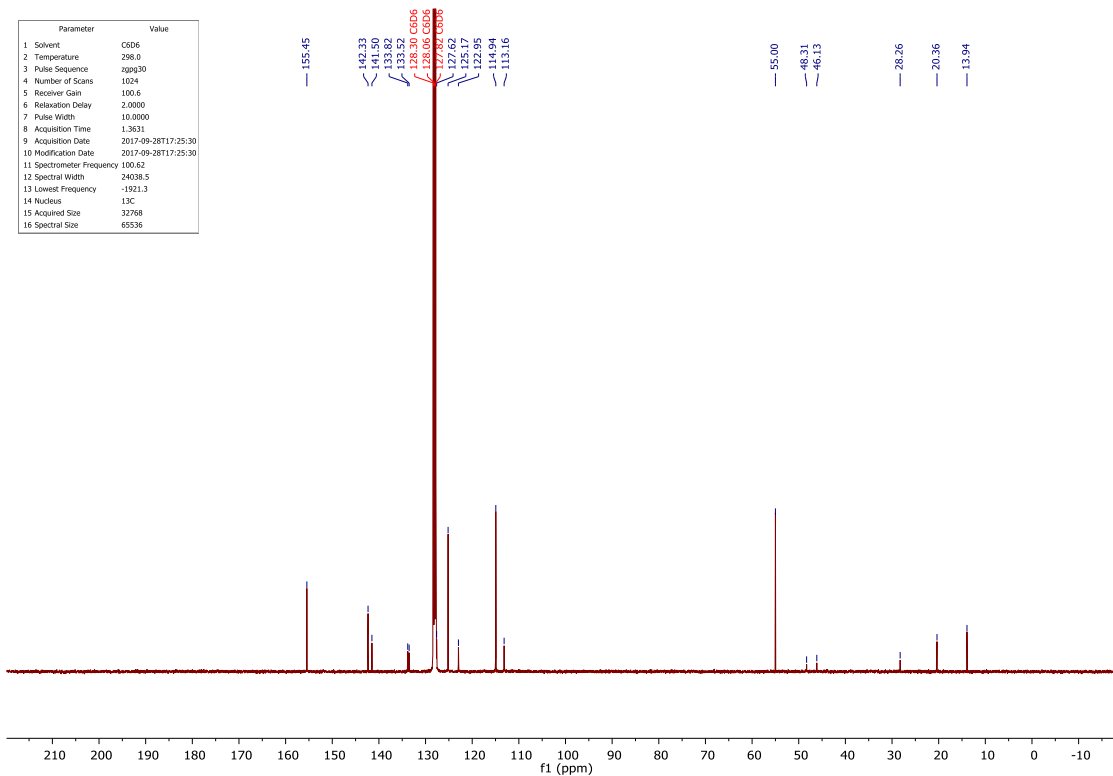
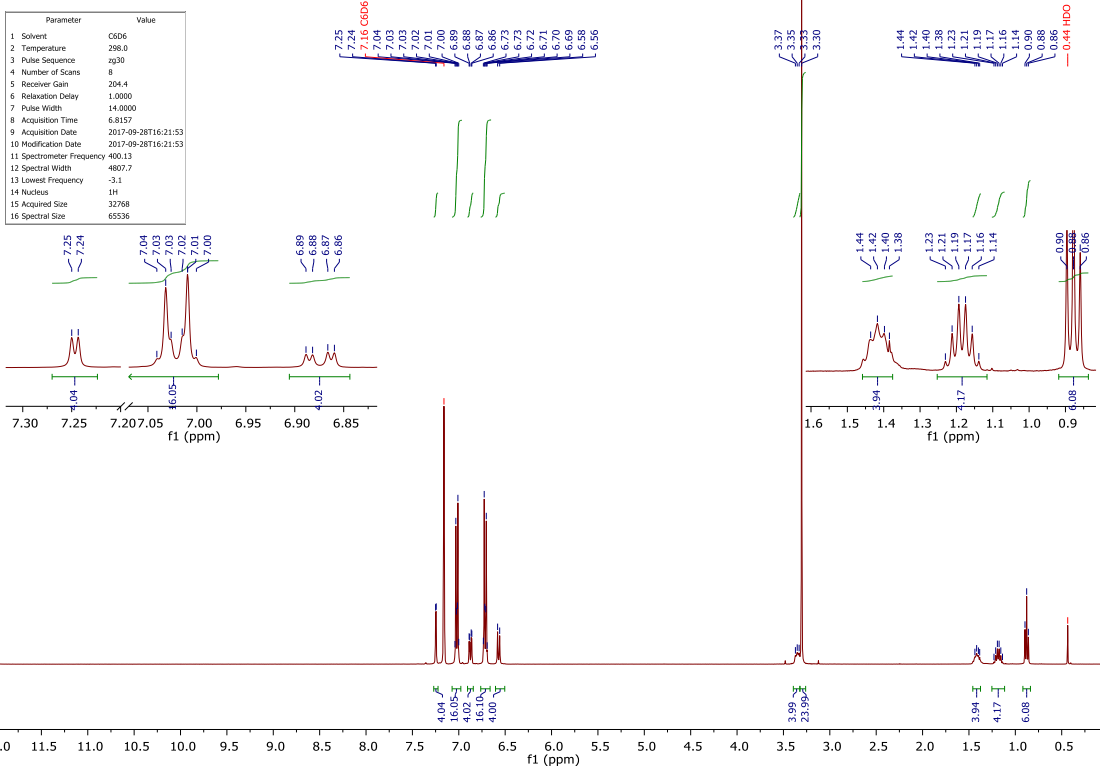
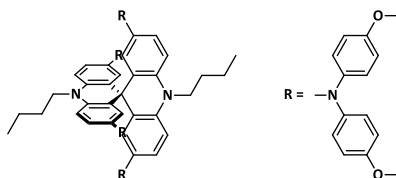


The titled compound was synthesized and worked-up according to the similar procedure as for 7, starting with with 6 (0.14 g, 0.131 mmol), 4,4'-dimethoxydiphenylamine (0.15 g, 0.654 mmol), NaOtBu (0.076 g, 0.768 mmol), Pd(CH₃CN)₂Cl₂ (0.002 g, 0.007 mmol), *t*Bu₃P (0.014 mL, 0.014 mmol, 1.0 M solution in toluene) and dry 1,4-dioxane (5 mL). The product was purified by silica gel column chromatography using a mixture hexane/THF (3:1) as the eluent (*R*_f ≈ 0.25). Afterwards, the isolated compound was precipitated from THF-MeOH and THF-hexane to give pure 10 as a yellowish solid (0.12 g, 62%). ¹H NMR (400 MHz, Benzene-*d*₆) δ 7.19 (d, *J* = 2.7 Hz, 4H), 7.06 – 6.96 (m, 16H), 6.86 (dd, *J* = 8.9, 2.7 Hz, 4H), 6.76 – 6.67 (m, 16H), 6.42 (d, *J* = 9.0 Hz, 4H), 3.47 – 3.35 (m, 4H), 3.29 (s, 24H), 1.71 – 1.49 (m, 8H). ¹³C NMR (101 MHz, Benzene-*d*₆) δ 155.46, 142.12, 141.19, 134.16, 134.13, 133.71, 125.08, 122.41, 122.38, 114.91, 113.85, 55.00, 48.94, 48.83, 48.18, 37.67, 37.63, 31.17, 28.78, 28.73, 24.35, 23.64, 14.36, 11.17. HRMS (FTMS-NSI): calcd. for [M+H]⁺ C₉₇H₁₀₃N₆O₈: 1479.7837; found 1479.7760.

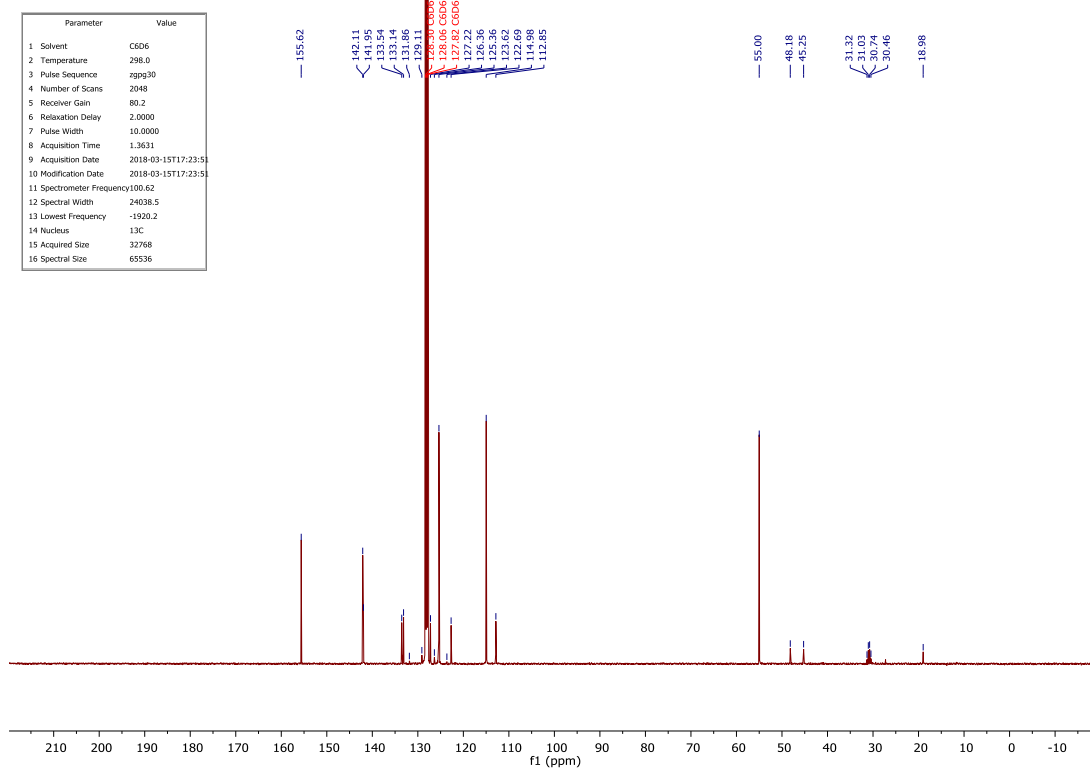
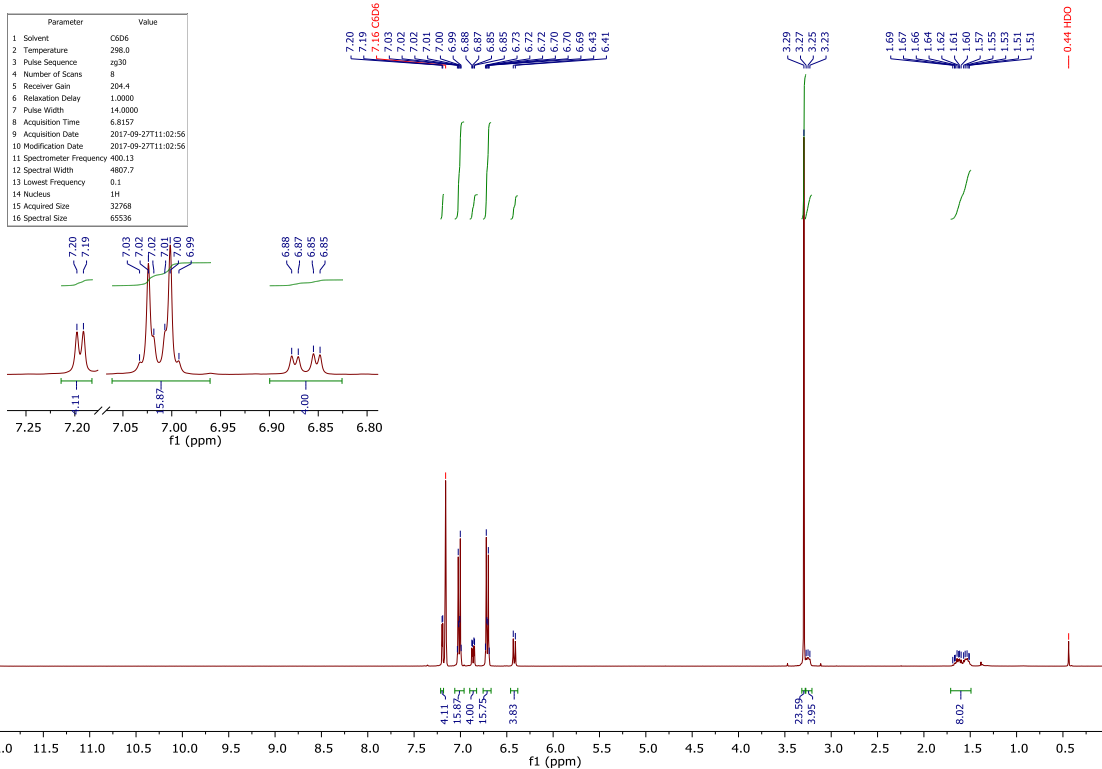
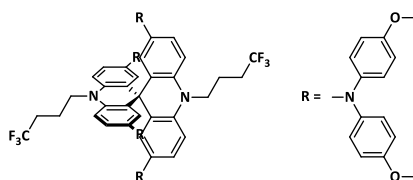
6.3.2. ¹H- and ¹³C- NMR spectra of the final compounds



APPENDIX



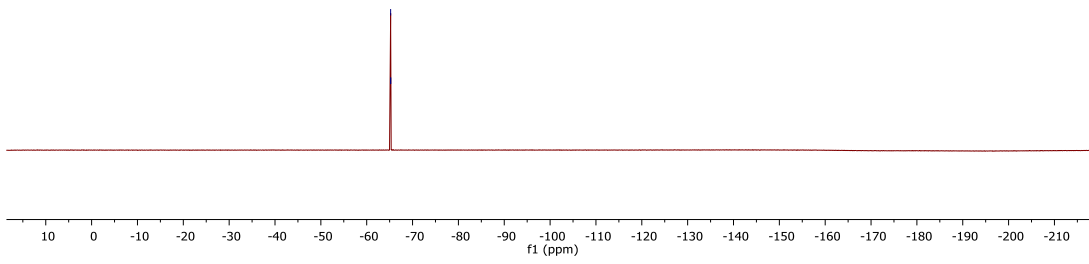
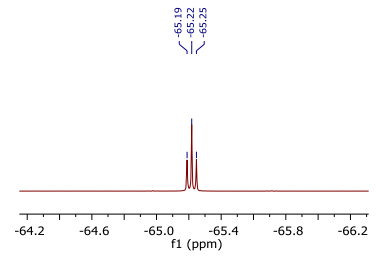
APPENDIX



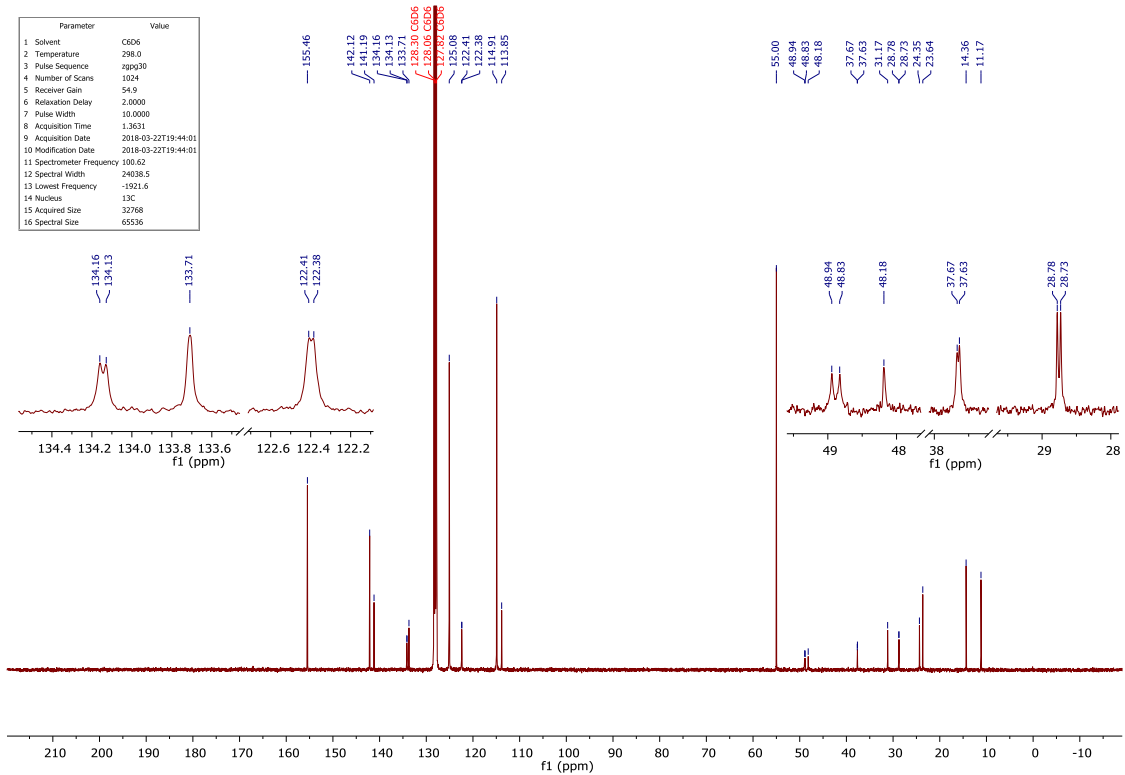
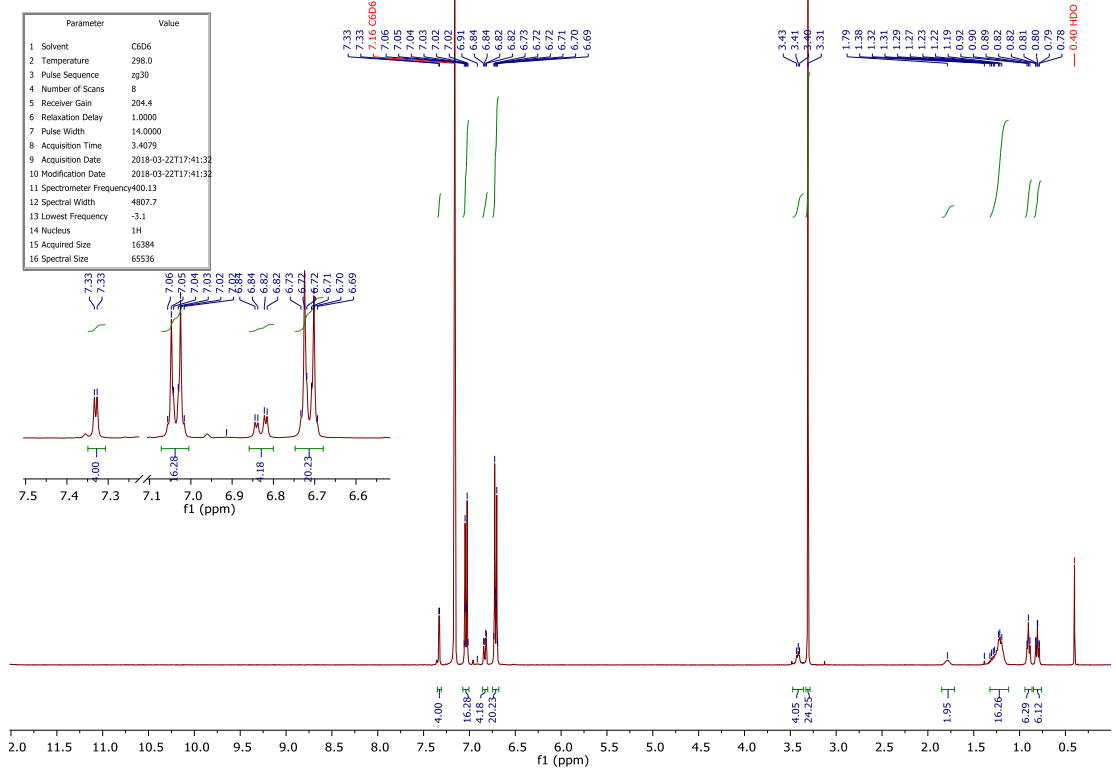
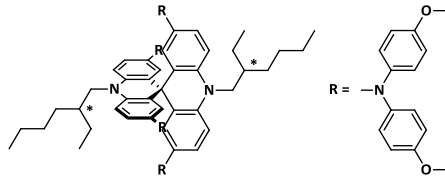
APPENDIX

Parameter	Value
1 Solvent	C6D6
2 Temperature	298.0
3 Pulse Sequence	zgpgq
4 Number of Scans	32
5 Receiver Gain	204.4
6 Relaxation Delay	1.0000
7 Pulse Width	15.0000
8 Acquisition Time	0.7340
9 Acquisition Date	2017-09-26T12:00:36
10 Modification Date	2017-09-26T12:00:36
11 Spectrometer Frequency	376.46
12 Spectral Width	89285.7
13 Lowest Frequency	-82292.9
14 Nucleus	19F
15 Acquired Size	65536
16 Spectral Size	131072

65.19
65.37
65.25



APPENDIX



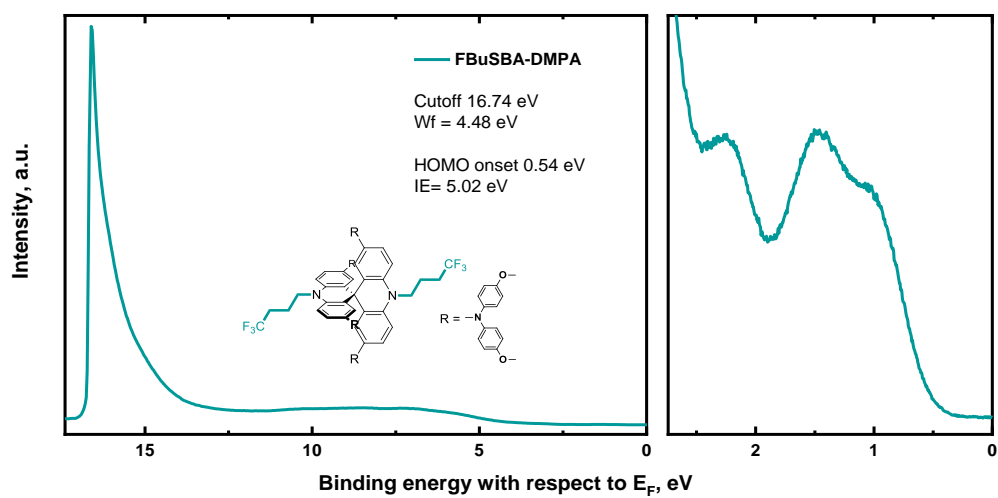
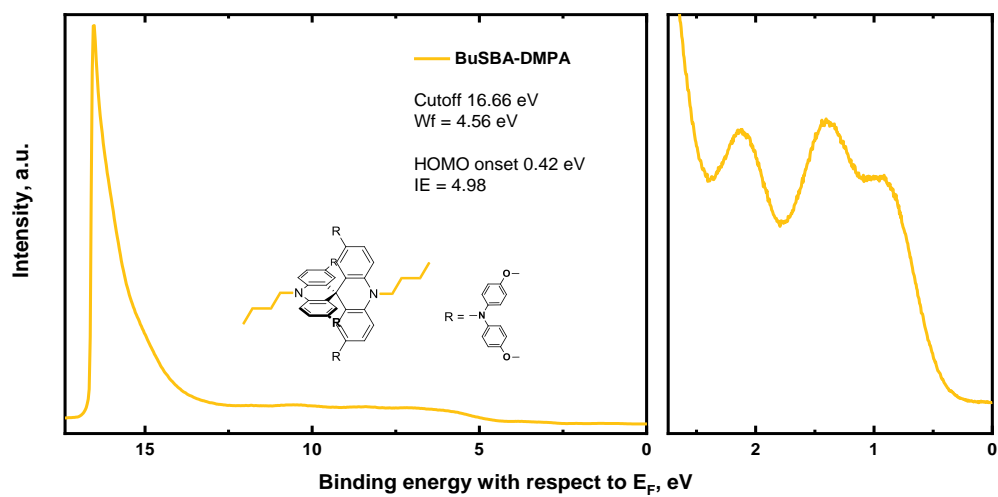
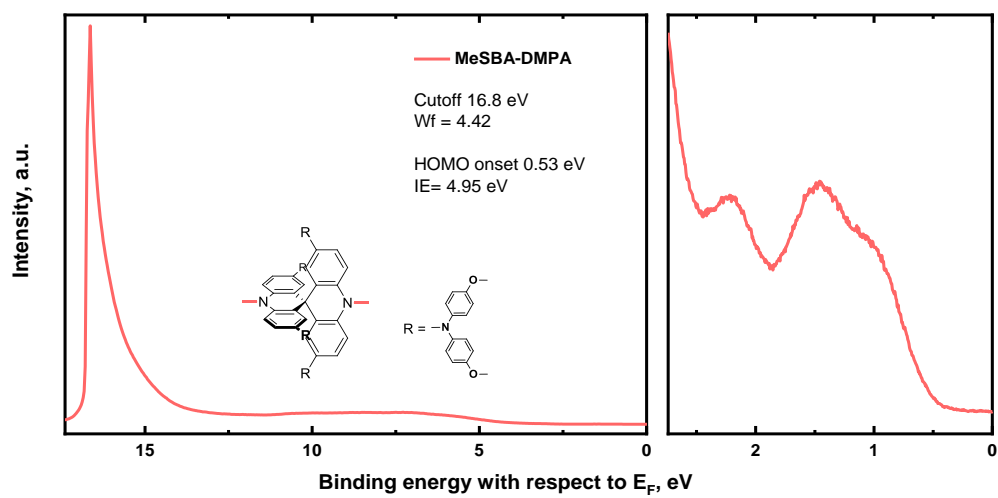
6.3.3. Single crystal X-ray diffraction data

Single crystal diffraction data were collected at 120 K on a Bruker D8 Venture diffractometer equipped with a Photon 100 detector and using a Mo micro-source (0.7107 Å). Data reduction was done with APEX3, applying semi-empirical absorption correction as implemented in SADABS²⁶⁷. The data were indexed using difference vectors and space groups were assigned with XPREP²⁶⁸. Structures were solved with SHELXT²⁶⁹ and refined with SHELXL²⁷⁰ using the full-matrix least-squares procedure (F2 based) in Olex2²⁷¹. All non-H atoms were refined anisotropically, applying restraints where necessary.

The structure is deposited at the CCDC, number CCDC 1914984.

Identification code	HTM_309_om
Empirical formula	C ₈₃ H ₇₄ N ₆ O ₈
Formula weight	1283.54
Temperature/K	120
Crystal system	triclinic
Space group	<i>P</i> -1
<i>a</i> /Å	14.7252(12)
<i>b</i> /Å	14.9165(12)
<i>c</i> /Å	16.8880(13)
α /°	88.120(2)
β /°	66.154(2)
γ /°	78.264(2)
Volume/Å ³	3316.8(5)
<i>Z</i>	2
$\rho_{\text{calc}}/\text{cm}^3$	1.278
μ/mm^{-1}	0.074
<i>F</i> (000)	1276.0
Crystal size/mm ³	0.06 × 0.05 × 0.05
Radiation	MoK α (λ = 0.71073)
2 Θ range for data collection/°	4.526 to 48.9
Index ranges	-17 ≤ <i>h</i> ≤ 17, -17 ≤ <i>k</i> ≤ 17, -19 ≤ <i>l</i> ≤ 19
Reflections collected	61770
Independent reflections	10955 [<i>R</i> _{int} = 0.0517, <i>R</i> _{sigma} = 0.0362]
Data/restraints/parameters	10955/884
Goodness-of-fit on <i>F</i> ²	1.03
Final <i>R</i> indexes [<i>I</i> ≥ 2 σ (<i>I</i>)]	<i>R</i> ₁ = 0.0437, <i>wR</i> ₂ = 0.1007
Final <i>R</i> indexes [all data]	<i>R</i> ₁ = 0.0666, <i>wR</i> ₂ = 0.1115
Largest diff. peak/hole / e Å ⁻³	0.25/-0.25

6.3.4. Ultraviolet photoelectron spectroscopy



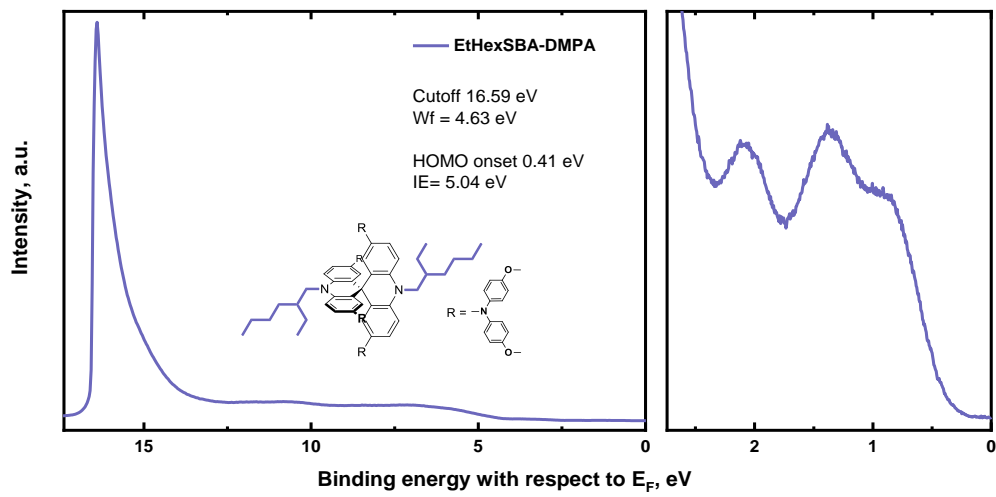


Figure 32. Ultraviolet photoemission spectra for SBA-based HTMs.

6.3.5. Device testing

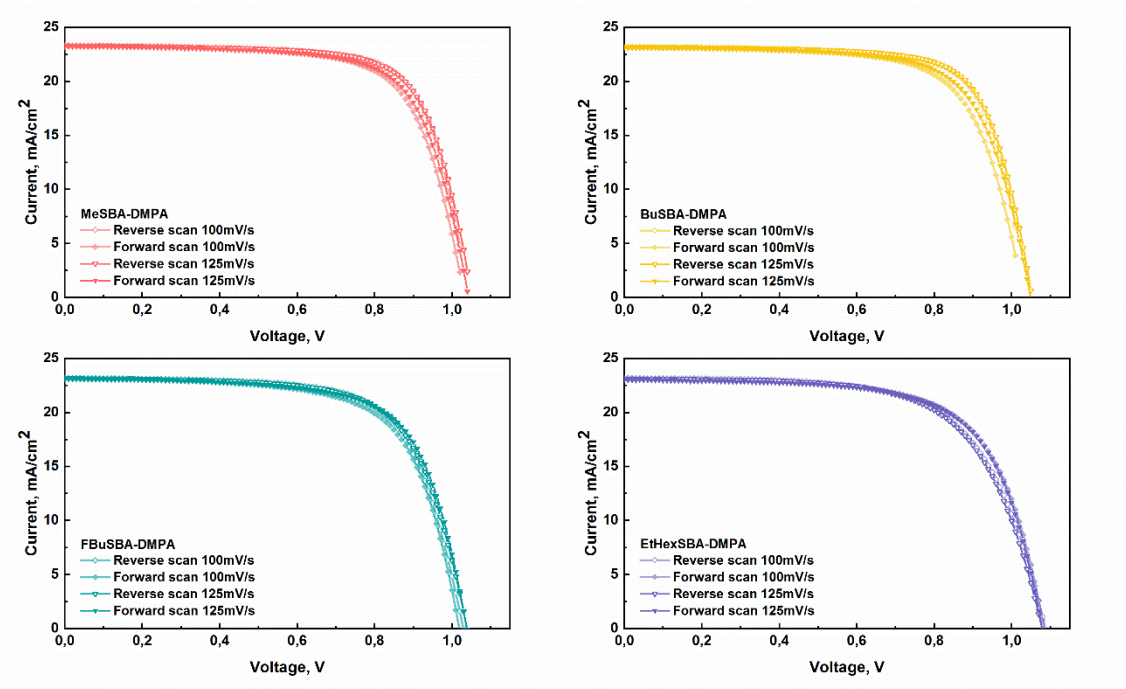


Figure 33. J - V curves of PCs employing different SBA-based HTMs recorded at different scan rates.

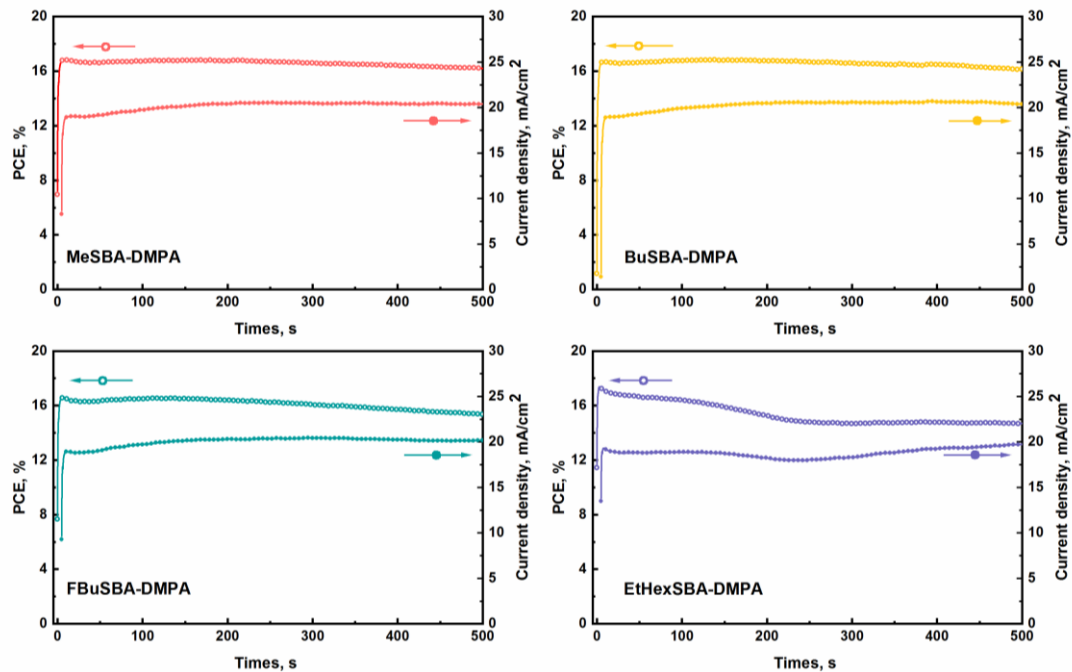


Figure 34. Stabilized photocurrent measurements for devices employing SBA-based HTMs and its power output at MPP under simulated AM 1.5 G sun illumination under ambient conditions for 500 s.

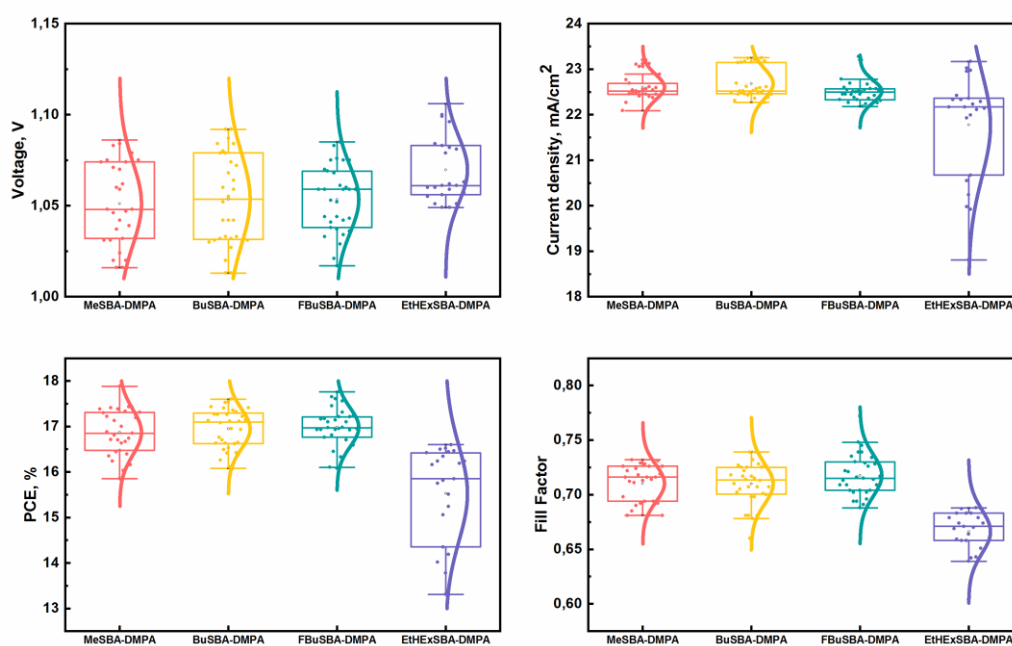


Figure 35. Metrics statistics of the PSCs with devices employing different HTMs.

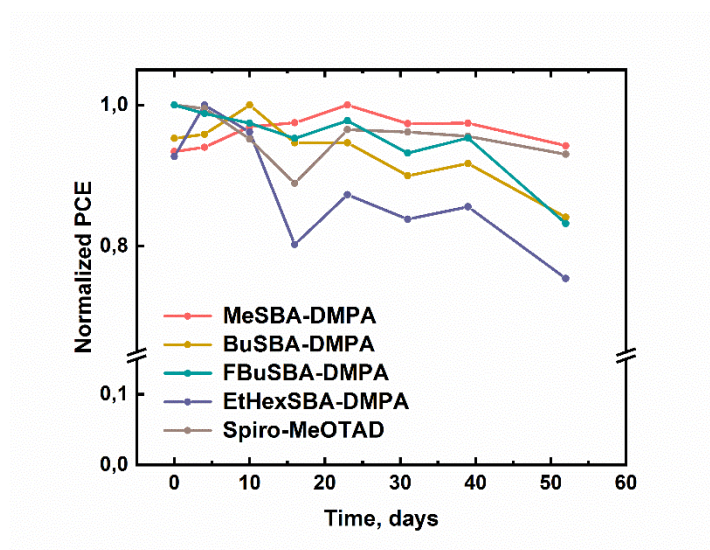


Figure 36. Storage stability (RH > 15%, dark conditions) of the devices with SBA-based HTMs and spiro-MeOTAD reference (right).

6.3.6. Transient photocurrent measurements

Transient photocurrent investigations were performed with an Agilent Technologies DSo5054A oscilloscope using 50 Ω input resistor and a Tektronix AFG 3101 function generator. Samples were excited by radiation of the optical parametric amplifier Topas-C (Light Conversion Ltd.) pumped by femtosecond Ti:sapphire laser Integra-C from Quantronix Inc.

6.3.7. Photoluminescence lifetime measurements

Fluorescence decay kinetics were measured using the Edinburgh Instruments time-correlated single photon counting fluorescence spectrometer F900. Semiconductor diode laser EPL-470 emitting 72 ps pulses at 470 nm was utilized in the transient measurements for the excitation of the samples. The pulse repetition rate was 50 MHz (200 ns) and the time resolution of the setup was about several hundreds of picoseconds by applying apparatus function deconvolution.

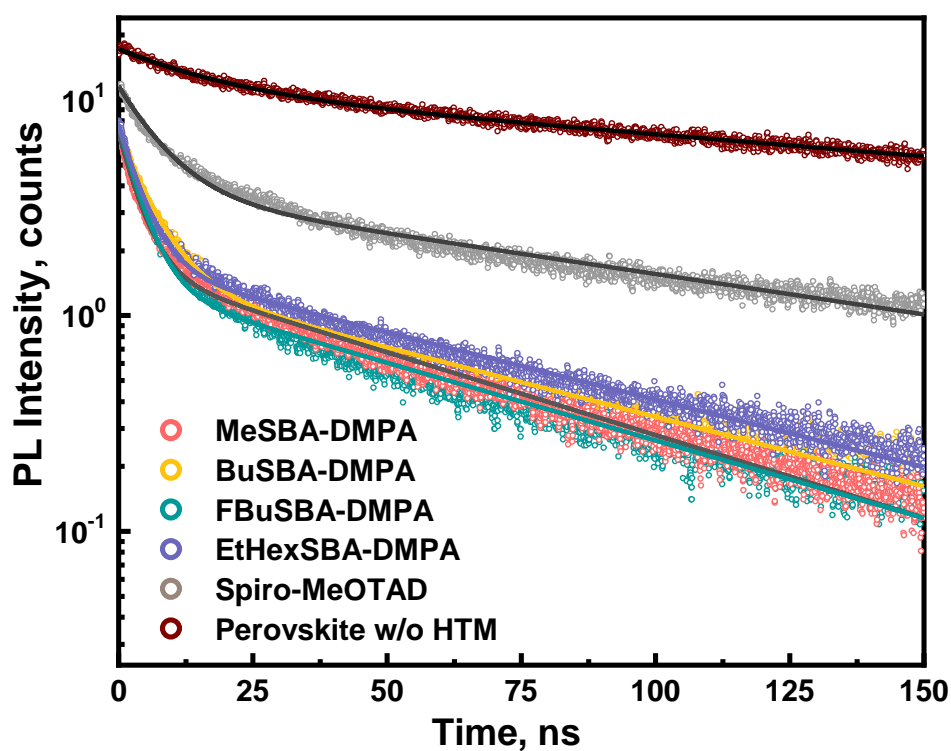
6.3.8. Electric field dependent time resolved photoluminescence and transient photocurrent measurements

Table 8. Summary of the fitting parameters of the fresh perovskite films employing SBA hole-transporting materials.

HTM	A_1	τ_1 , ns	A_2	τ_2 , ns
no HTM	1.62 (15.8%)	27.2	8.65 (84.2%)	609
MeSBA-DMPA	1.82 (67.2%)	2.5	0.89 (32.8%)	25
BuSBA-DMPA	2.31 (58.0%)	4.1	1.67 (42.0%)	40
FBuSBA-DMPA	2.06 (70.1%)	2.8	0.88 (29.9%)	29
EtHexSBA-DMPA	1.83 (42.3%)	4.6	2.5 (57.7%)	85
spiro-MeOTAD	1.88 (60.6%)	2.8	1.09 (39.4%)	35

Table 9. Summary of the fitting parameters of the aged for 900 h perovskite films employing SBA hole-transporting materials.

HTM	A_1	τ_1 , ns	A_2	τ_2 , ns
no HTM	6.5 (37.1%)	17.8	11 (62.9%)	215
BuSBA-DMPA	6.9 (82.2%)	5.2	1.5 (17.8%)	68
FBuSBA-DMPA	7.5 (83%)	4.0	1.4 (17%)	60
MeSBA-DMPA	6.5 (80%)	3.7	1.66 (20%)	57
EtHexSBA-DMPA	7.05 (76.3%)	4.1	1.74 (23.7%)	70
spiro-MeOTAD	8.64 (69.9%)	7.6	3.72 (30.1%)	116

**Figure 37.** Photoluminescence decay kinetics of the 900h aged perovskite films comprising spiro-MeOTAD, four different SBA-based HTMs and a reference triple cations perovskite film.

6.3.9. Computational Details and Theoretical Background

Ionization potential. The gas phase vertical ionization potential (IP) was computed using the Δ SCF procedure at B3LYP/6-31G(d,p) level with D3BJ²⁷² correction and Gaussian16 software²⁷³.

$$IP = \Delta SCF = E_{cN} - E_{nN} \quad (12)$$

where E_{nN}/E_{cN} is the total energy of the neutral/cationic molecule in a neutral geometry.

Model for Amorphous Morphology. The amorphous morphology was generated starting from a unit cell with 64 randomly placed molecules using Packmol.²⁷⁴ The system was minimized using the conjugate gradient algorithm and then equilibrated in the NPT ensemble (700 K, 1 bar) by performing classical molecular dynamics (MD) simulation. The equilibrated system was then extended into a $2 \times 2 \times 2$ supercell with 512 molecules followed by equilibration (700 K, 1 bar) for 5 ns. Equilibration in the NPT ensemble (300 K, 1 bar) was then performed until the density reached equilibrium (~ 50 ns). The MD simulations were performed under periodic boundary conditions with the GROMACS package^{275,276} and GAFF²⁷⁷ force field along with charge obtained by the restrained electrostatic potential (RESP) procedure based on HF/6-31G^{**}. The temperature and pressure control were accomplished using velocity rescaling with a stochastic term²⁷⁸ ($\tau_T = 1.0$ ps) and an isotropic coupling for the pressure from a Berendsen barostat ($P_o = 1$ bar, $\chi = 4.5 \times 10^{-5}$ bar⁻¹, and $\tau_P = 1.0$ ps). The time step used in all simulations was 1 fs, and bonds involving H atoms were constrained using the Linear Constraint Solver (LINCS) algorithm. A cutoff of 12 Å was applied to the van der Waals interaction through force-switch mode. As for electrostatic interactions, the particle mesh Ewald (PME) method was employed with a 0.12 nm Fourier spacing.

Charge Transport Simulations. For amorphous organic materials, charge transport is well described by the hopping model, where a charge (electron/hole) is assumed to be instantaneously localized on one molecule (or a hopping site). The charge hopping rate

between molecules can be evaluated using non-adiabatic semiclassical Marcus charge transfer theory²⁷⁹:

$$\omega_{ij} = \frac{J_{ij}^2}{\hbar} \sqrt{\frac{\pi}{\lambda k_B T}} \exp \left[-\frac{(\Delta E_{ij} - \lambda)^2}{4\lambda k_B T} \right] \quad (13)$$

where T is the temperature, J_{ij} is the transfer integral (sometimes referred to as electronic coupling) between the i and j sites, ΔE_{ij} is the site energy difference $E_i - E_j$ and λ is the reorganization energy. From the equation above, it is clear that high transfer integral and low reorganization energy lead to a high hopping rate between the two sites, which, in turn, leads to high charge mobility. In addition to J_{ij} and λ , the spread of the site energy is crucial in amorphous materials.

The reorganization energy associated with the hole transfer process is related to the local electron-phonon coupling, which is computed using adiabatic potential energy surface method (the 4-point method). The reorganization energy is expressed as:

$$\lambda = \lambda_1 + \lambda_2 = (E_{nC} - E_{nN}) + (E_{cN} - E_{cC}) \quad (14)$$

where E_{nN} (E_{cC}) is the total energy of the neutral (cationic) molecule in neutral (cationic) geometry and E_{nC} (E_{cN}) is the energy of the neutral (cationic) molecule in cationic (neutral) geometry.

Site energies are computed using the Thole model, where the correction terms resulting from the electrostatic and polarization effects from the environment (surrounding molecules and external electric field) are added to the HOMO of an isolated gas molecule²⁸⁰. The partial charges needed in this model for the neutral and cationic states were generated via CHelpG. We extract the energetic disorder present in HTMs using the Gaussian disorder model, where the energetic disorder (σ) is obtained from fitting the histogram of energy difference (ΔE_{ij}) to the Gaussian distribution.

The ZINDO-based Molecular Orbital Overlapping (MOO) method²⁸¹ was used to efficiently compute the transfer integral of every molecular pair ij in the neighbor list. The ZINDO results have been shown to be in reasonable agreement with those computed at the B3LYP/6-31G(d) level. The neighbor list was established for every molecular pair having a distance between their nearest fragments within 7 Å. After

computing all the parameters defined for each hopping site and each molecular pair appearing in Equation 13, a 10 ms kinetic Monte Carlo (kMC) simulation was performed with a 10^5 Vcm^{-1} electric field. The hole mobility was determined from an average charge velocity. The last snapshot of an MD trajectory was taken for kMC simulations and the computational hole mobility is the averaged mobility from 6 kMC simulations (each with different directions of electric field: x, y, z, -x, -y, and -z).

Free-volume in Amorphous HTMs. The Free-volume (V_{Free}) is evaluated by calculating the difference between total cell volume and the volume occupied by a molecular VDW volume (VDW radii are taken from Bondi's work²⁸²) using GROMACS (gmx freevolume).

6.3.10. Charge Transport Properties of BuSBA-DMPA and FBuSBA-DMPA

As mentioned in the main text, the hole mobility of **BuSBA-DMPA** and **FBuSBA-DMPA** are quite different in spite of their similar molecular structures. To understand the origin of such a difference, we examine the three transport parameters J_{ij} , λ and ΔE_{ij} (we use energetic disorder σ as a mobility descriptor in disordered solids) appearing in the rate equation, as shown in Equation 13. **BuSBA-DMPA** and **FBuSBA-DMPA** exhibit very similar distribution of transfer integral, which is not so surprising considering their similar molecular structures. The reorganization energy of **BuSBA-DMPA** and **FBuSBA-DMPA** are 0.181 eV and 0.203 eV. Although small reorganization energy facilitates fast charge transport, the difference in λ is alone not large enough to explain the difference in μ . Thus, we examine the energetic disorder of **BuSBA-DMPA** and **FBuSBA-DMPA**, which are 0.132 eV and 0.152 eV, respectively. From a lattice model,²⁸³ the mobility has been shown to have a relation with σ as:

$$\mu \propto \exp[-C(\beta\sigma)^2] \quad (15)$$

where C is a coefficient that depends upon the materials and models and β is the inverse of temperature ($1/kBT$). The exponential dependence of μ on $-\sigma^2$ emphasized the importance of this parameter. Therefore, we think that energetic disorder is the key factor that causes such difference in μ . Finally, our computational mobility of **BuSBA-DMPA** and **FBuSBA-DMPA** are 3.3×10^{-5} and 1.2×10^{-5} cm²/(V s), respectively, showing similar trend and order of magnitude to the experimental results.

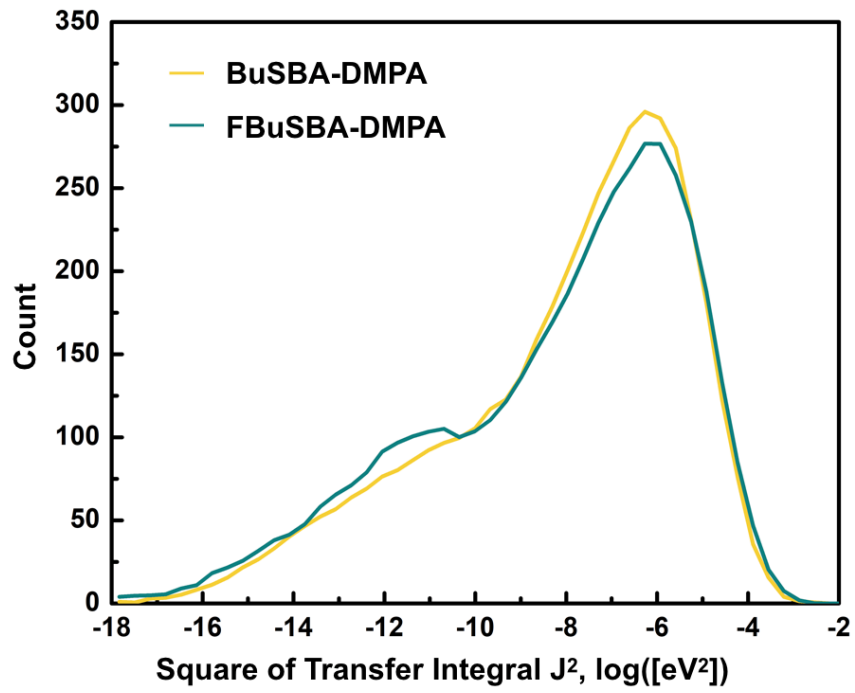


Figure 38. Distribution of transfer integral square present in BuSBA-DMPA and FBU SBA-DMPA.

6.3.11. Free-volume in Amorphous HTMs

Table 10. Free-volumes in spiro-MeOTAD and acridane-based HTMs.

HTM	V_{free} , Å ³ /molecule
MeSBA-DMPA	701
BuSBA-DMPA	782
FBuSBA-DMPA	813
EtHexSBA-DMPA	872
spiro-MeOTAD	698

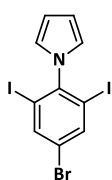
Table 11. Vertical ionization potentials of SBA-based HTMs computed using B₃LYP/6-31G(d,p) with D3BJ correction.

HTM	IP, eV
MeSBA-DMPA	5.12
BuSBA-DMPA	5.02
FBuSBA-DMPA	5.12
EtHexSBA-DMPA	4.97

6.4. Appendix to chapter 5

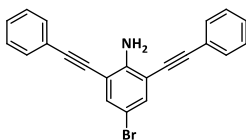
6.4.1. Synthetic details

1-(4-bromo-2,6-diiodophenyl)-1H-pyrrole, **2a**

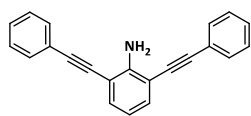


A 250 mL round-bottomed flask was charged with 2,6-diiodo-4-bromoaniline (7.0 g, 16.5 mmol), 2,5-dimethoxytetrahydrofuran (2.35 mL, 18.2 mmol), DCE (40 mL) and glacial acetic acid (40 mL). The mixture was heated to reflux for 4 h and then cooled down to RT. DCE was added and the resulting organic phase was washed with water and an aqueous solution of Na₂CO₃ until gas evolution ceased, dried over MgSO₄ and filtered through a pad of SiO₂ using DCM as eluent. Evaporation of all volatiles gave **2a** as brownish solid (7.45 g, 95% yield). ¹H NMR (400 MHz, Chloroform-*d*) δ 8.04 (s, 2H), 6.58 (t, *J* = 2.1 Hz, 2H), 6.38 (t, *J* = 2.1 Hz, 2H). ¹³C NMR (101 MHz, Chloroform-*d*) δ 145.25, 141.53, 123.44, 120.76, 110.00, 98.10. HRMS (MALDI-TOF-MS): calcd. for C₁₀H₆BrI₂N 472.7773 [M]⁺; found 472.777.

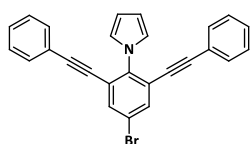
4-bromo-2,6-bis(phenylethynyl)aniline, **3a**



A flame-dried, N₂-filled, 100 mL Schlenk tube was charged with aniline **1a** (4.24 g, 10.0 mmol), CuI (0.08 g, 0.4 mmol), Pd(Ph₃P)₄ (0.46 g, 0.4 mmol), phenylacetylene (2.3 mL, 21.0 mmol), Et₃N (5.6 mL, 40.0 mmol) and THF (25 mL). The reaction mixture was stirred at room temperature overnight. Afterwards all volatiles were evaporated and water with DCM were added to the residue, the mixture was vigorously stirred to dissolve solids. The organic layer was thoroughly washed with water and dried over MgSO₄. After evaporation of volatiles the residue was purified by silica gel column chromatography using a mixture hexane/DCM (4:1) as the eluent (*R*_f ≈ 0.3) to give yellowish solid **3a** (3.40 g, 91% yield). ¹H NMR (400 MHz, Chloroform-*d*) δ 7.58 – 7.49 (m, 4H), 7.46 (s, 2H), 7.41 – 7.33 (m, 6H), 4.91 (brs, 2H). ¹³C NMR (101 MHz, Chloroform-*d*) δ 148.00, 134.55, 131.67, 128.84, 128.61, 122.69, 109.33, 107.97, 96.20, 84.22. HRMS (MALDI-TOF-MS): calcd. for C₂₂H₁₄BrN 371.0310 [M]⁺; found 371.024.

2,6-bis(phenylethynyl)aniline, **3b**

A flame-dried, N₂-filled, 250 mL Schlenk flask was charged with 2,6-dibromoaniline (5.02 g, 20.0 mmol), CuI (0.11 g, 0.6 mmol), Pd(Ph₃P)₄ (0.46 g, 0.4 mmol), phenylacetylene (6.6 mL, 60.0 mmol) and Et₃N (80 mL). The reaction mixture was stirred at 90°C overnight. After cooling to ambient temperature excess of water was added and the mixture was vigorously stirred for 30 min. The organic layer was separated, diluted with DCM, thoroughly washed with water and then dried over MgSO₄. Evaporation of volatiles gave residue that was purified by silica gel column chromatography using a mixture hexane/DCM (4:1) as the eluent (R_f ≈ 0.35) to give yellowish solid **3b** (5.74 g, 98% yield). ¹H NMR (400 MHz, Chloroform-*d*) δ 7.59 – 7.50 (m, 4H), 7.43 – 7.31 (m, 8H), 6.70 (t, *J* = 7.7 Hz, 1H), 4.83 (brs, 2H). ¹³C NMR (101 MHz, Chloroform-*d*) δ 148.99, 132.54, 131.65, 131.61, 128.58, 128.53, 128.50, 123.16, 117.41, 107.58, 95.14, 85.52. HRMS (MALDI-TOF-MS): calcd. for C₂₂H₁₅N 293.1204 [M]⁺; found 293.119.

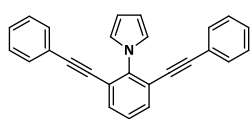
1-(4-bromo-2,6-bis(phenylethynyl)phenyl)-1H-pyrrole, **4a**

Method A. Synthesized and purified according to the similar procedure as for **2a**, starting with aniline **3a** (3.22 g, 8.65 mmol), 2,5-dimethoxytetrahydrofuran (1.23 mL, 9.51 mmol), DCE (40 mL) and glacial acetic acid (40 mL). The product appeared to be pure without passing through a pad of silica. The desired pyrrole **4b** was isolated as light yellow solid (3.64 g, >99% yield).

Method B. A flame-dried, N₂-filled, 50 mL Schlenk tube was charged with **2a** (0.237 g, 0.5 mmol), Pd(CH₃CN)₂Cl₂ (0.007 g, 0.025 mmol), XPhos (0.021 g, 0.045 mmol), Cs₂CO₃ (0.72 g, 2.2 mmol), phenylacetylene (0.12 mL, 1.1 mmol) and CH₃CN (5 mL). The reaction mixture was stirred at 60°C overnight. Afterwards all volatiles were evaporated and water with DCM were added to the residue, the mixture was vigorously stirred to dissolve solids. The organic layer was thoroughly washed with diluted HCl and water, then dried over MgSO₄. Evaporation of volatiles gave residue that was purified by silica gel column chromatography using a mixture hexane/DCM (5:1) as the eluent (R_f ≈ 0.35)

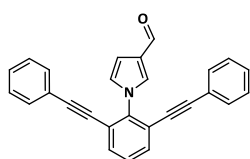
to give yellowish solid **3a** (0.098 g, 46% yield). ¹H NMR (400 MHz, Chloroform-*d*) δ 7.71 (s, 2H), 7.39 – 7.28 (m, 10H), 7.04 (t, *J* = 2.2 Hz, 2H), 6.39 (t, *J* = 2.2 Hz, 2H). ¹³C NMR (101 MHz, Chloroform-*d*) δ 142.74, 134.90, 131.82, 129.04, 128.45, 123.51, 122.69, 122.40, 120.17, 108.84, 95.25, 84.56. HRMS (MALDI-TOF-MS): calcd. for C₂₆H₁₆BrN 421.0466 [M]⁺; found 421.000.

1-(2,6-bis(phenylethynyl)phenyl)-1H-pyrrole, **4b**

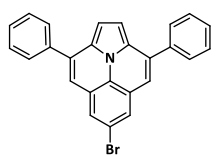


Method A. Synthesized and purified according to the similar procedure as for **2a**, starting with aniline **3b** (6.55 g, 22.4 mmol), 2,5-dimethoxytetrahydrofuran (3.2 mL, 24.6 mmol), DCE (55 mL) and glacial acetic acid (55 mL). The desired product **4b** was isolated as light yellow solid (7.32 g, 95% yield).

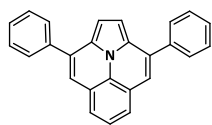
Method B. A flame-dried, N₂-filled, 100 mL Schlenk tube was charged with **2b** (3.02 g, 10.0 mmol), Pd(CH₃CN)₂Cl₂ (0.17 g, 0.6 mmol), CuI (0.08 g, 0.4 mmol) and refilled with N₂ prior to sequential addition of diisopropylamine (3.6 mL, 24.0 mmol), *t*Bu₃P (1.2 mL, 1.2 mmol, 1.0 M solution in toluene), phenylacetylene (2.6 mL, 24.0 mmol) and 1,4-dioxane (20 mL). The reaction mixture was stirred at room temperature overnight. Afterwards all volatiles were evaporated and water with DCM were added to the residue. The organic layer was thoroughly washed with diluted HCl and water, then dried over MgSO₄. Evaporation of volatiles gave residue that was purified by silica gel column chromatography using a mixture hexane/DCM (5:1) as the eluent (*R*_f ≈ 0.35) to give brownish solid **4b** (2.80 g, 82% yield). ¹H NMR (400 MHz, Chloroform-*d*) δ 7.59 (d, *J* = 7.8 Hz, 2H), 7.41 – 7.28 (m, 11H), 7.08 (t, *J* = 2.2 Hz, 2H), 6.39 (t, *J* = 2.2 Hz, 2H). ¹³C NMR (101 MHz, Chloroform-*d*) δ 143.83, 132.60, 131.75, 128.70, 128.41, 127.24, 122.89, 122.82, 121.96, 108.53, 94.04, 85.80. HRMS (APCI-MS): calcd. for C₂₆H₁₇N 343.1361 [M]⁺; found 343.1365.

1-(2,6-bis(phenylethynyl)phenyl)-1H-pyrrole-3-carbaldehyde, **4c**

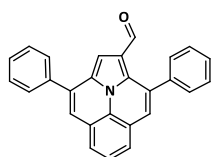
Synthesized and worked-up according to the similar procedure as for **2a**, starting with aniline **3b** (0.29 g, 1.0 mmol), 2,5-dimethoxy-3-tetrahydrofuran-carboxaldehyde (0.2 mL, 1.3 mmol), DCE (2.5 mL) and glacial acetic acid (2.5 mL). The product was purified by silica gel column chromatography using DCM as the eluent ($R_f \approx 0.3$) to give brownish solid **4c** (0.29 g, 79% yield). ^1H NMR (400 MHz, Chloroform-*d*) δ 9.91 (s, 1H), 7.70 (t, $J = 1.9$ Hz, 1H), 7.63 (d, $J = 7.8$ Hz, 2H), 7.42 (t, $J = 7.6$ Hz, 1H), 7.36 – 7.28 (m, 10H), 7.12 – 7.06 (m, 1H), 6.89 (dd, $J = 3.1, 1.6$ Hz, 1H). ^{13}C NMR (101 MHz, Chloroform-*d*) δ 185.67, 141.92, 132.55, 132.19, 131.67, 129.14, 128.57, 128.54, 127.16, 125.96, 122.17, 121.94, 107.36, 95.22, 84.57. HRMS (APCI-MS): calcd. for $\text{C}_{27}\text{H}_{17}\text{NO}$ 371.1310 $[\text{M}]^+$; found 371.1310.

6-bromo-3,9-diphenylindolizino[6,5,4,3-*ija*]quinoline, **5a**

A flame-dried, N_2 -filled, 100 mL round-bottomed flask was charged with bisalkyne **4a** (2.63 g, 6.23 mmol) and dry toluene (31 mL). InCl_3 (0.83 g, 3.74 mmol) was added rapidly in one portion and the flask was flushed with N_2 . The mixture was heated under reflux for 24 h, then cooled down to ambient temperature. Afterwards all volatiles were evaporated and a small amount of DCM was added to the residue. Resulting mixture was passed through a pad of SiO_2 using a mixture hexane/DCM (1:1) as the eluent. Evaporation of all volatiles afforded **5a** as bright yellow solid (2.57 g, 98% yield). ^1H NMR (400 MHz, Chloroform-*d*) δ 7.84 – 7.76 (m, 4H), 7.62 (s, 2H), 7.60 – 7.46 (m, 6H), 7.20 (s, 2H), 7.15 (s, 2H). ^{13}C NMR (101 MHz, Chloroform-*d*) δ 138.35, 134.53, 131.17, 128.93, 128.65, 128.36, 127.49, 126.78, 121.41, 118.20, 117.40, 107.13. HRMS (MALDI-TOF-MS): calcd. for $\text{C}_{26}\text{H}_{16}\text{BrN}$ 421.0466 $[\text{M}]^+$; found 421.060.

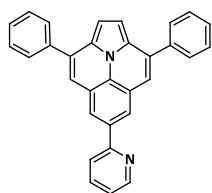
3,9-diphenylindolizino[6,5,4,3-ija]quinoline, **5b**

Synthesized and purified according to the similar procedure as for **5a**, starting with bisalkyne **4b** (1.41 g, 4.1 mmol), InCl_3 (0.54 g, 2.5 mmol) and toluene (20 mL). The desired product **5b** was isolated as yellow-orange solid (1.27 g, 90% yield). ^1H NMR (400 MHz, Chloroform-*d*) δ 7.84 – 7.77 (m, 4H), 7.58 – 7.39 (m, 9H), 7.24 (s, 2H), 7.07 (s, 2H). ^{13}C NMR (101 MHz, Chloroform-*d*) δ 138.82, 133.52, 132.68, 128.86, 128.39, 128.31, 126.84, 125.90, 123.92, 119.55, 119.44, 106.12. HRMS (MALDI-TOF-MS): calcd. for $\text{C}_{26}\text{H}_{17}\text{N}$ 343.1361 $[\text{M}]^+$; found 343.125.

3,9-diphenylindolizino[6,5,4,3-ija]quinoline-1-carbaldehyde, **5c**

Method A. Synthesized and worked-up according to the similar procedure as for **5a**, starting with bisalkyne **4c** (0.093 g, 0.25 mmol), InCl_3 (0.110 g, 0.5 mmol) and *o*-xylene (5 mL). The product was purified by silica gel column chromatography using DCM as the eluent ($R_f \approx 0.25$) to give yellow solid **4c** (0.068 g, 73% yield).

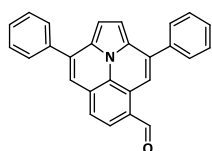
Method B. Obtained as a major byproduct in Vilmeier-Haack formylation of **5b** (vide infra, for **7b**). The carbaldehyde **5c** was isolated off as a yellow powder using silica gel column chromatography with DCM as eluent (0.25 g, 32%). ^1H NMR (400 MHz, Chloroform-*d*) δ 9.40 (s, 1H), 7.79 – 7.72 (m, 2H), 7.63 – 7.45 (m, 12H), 7.41 (s, 1H), 7.30 (s, 1H). ^{13}C NMR (101 MHz, Chloroform-*d*) δ 186.55, 138.85, 137.58, 133.99, 133.26, 131.86, 130.45, 129.31, 129.00, 128.87, 128.84, 128.15, 127.69, 126.11, 125.38, 125.19, 124.84, 121.82, 121.59, 121.23, 120.75, 105.82. HRMS (MALDI-TOF-MS): calcd. for $\text{C}_{27}\text{H}_{17}\text{NO}$ 371.1310 $[\text{M}]^+$; found 371.134.

3,9-diphenyl-6-(pyridin-2-yl)indolizino[6,5,4,3-ija]quinoline, **6**

A flame-dried N_2 -filled 10 mL Schlenk tube was charged with ullazine **5a** (0.112 g, 0.27 mmol), $\text{Pd}(\text{Ph}_3\text{P})_4$ (0.015 g, 0.013 mmol) and dry toluene (1.0 mL). Afterwards 2-(tributylstannyl)pyridine (0.11 mL, 0.345 mmol) was added dropwise via syringe. The mixture was stirred at 110°C during 24 h, cooled down to ambient temperature, diluted with DCM and washed with

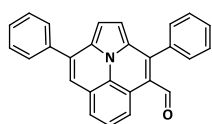
aqueous NH_4Cl and water. The organic phase was dried over MgSO_4 , concentrated under reduced pressure and purified by silica gel column chromatography using a mixture DCM/hexanes (5:1) as the eluent ($R_f \approx 0.25$). The product was precipitated from DCM-MeOH to give pure **6** as a yellow-orange solid (0.077 g, 70%). ^1H NMR (400 MHz, Chloroform-*d*) δ 8.80 – 8.73 (m, 1H), 8.16 (s, 2H), 7.93 – 7.86 (m, 1H), 7.86 – 7.77 (m, 5H), 7.59 – 7.43 (m, 6H), 7.35 (s, 2H), 7.31 – 7.26 (m, 1H), 7.10 (s, 2H). ^{13}C NMR (101 MHz, Chloroform-*d*) δ 157.75, 149.78, 138.73, 137.02, 135.07, 133.91, 132.93, 128.92, 128.49, 128.36, 126.97, 126.17, 122.13, 121.04, 119.73, 118.25, 106.61. HRMS (MALDI-TOF-MS): calcd. for $\text{C}_{31}\text{H}_{20}\text{N}_2$ 420.1626 $[\text{M}]^+$; found 420.356.

3,9-diphenylindolizino[6,5,4,3-*ija*]quinoline-5-carbaldehyde, **7b**



A flame-dried N_2 -filled 100 mL round-bottomed flask was charged with ullazine **5b** (0.73 g, 2.13 mmol), dry DMF (0.39 mL, 5.1 mmol) and DCE (21 mL). Afterwards POCl_3 was added dropwise at room temperature and the reaction mixture stirred for 2.5 hours. Concentrated solution of NaOAc was added to quench the reaction and the mixture was stirred vigorously until complete change of color from purple to orange. The organic phase was separated, washed with water, dried over MgSO_4 and concentrated under reduced pressure. The residue was chromatographed using DCM as eluent ($R_f \approx 0.3$) to afford desired carbaldehyde **7b** as a bright orange solid (0.44 g, 56%). ^1H NMR (400 MHz, Chloroform-*d*) δ 10.27 (s, 1H), 9.09 (s, 1H), 7.91 – 7.79 (m, 5H), 7.62 – 7.48 (m, 8H), 7.42 (s, 2H). ^{13}C NMR (101 MHz, Chloroform-*d*) δ 191.82, 138.38, 138.00, 136.55, 136.11, 132.19, 131.64, 130.49, 129.08, 129.02, 128.99, 128.83, 128.79, 127.76, 127.28, 125.91, 122.48, 119.24, 117.87, 117.52, 109.65, 109.09. HRMS (MALDI-TOF-MS): calcd. for $\text{C}_{27}\text{H}_{17}\text{NO}$ 371.1310 $[\text{M}]^+$; found 371.141.

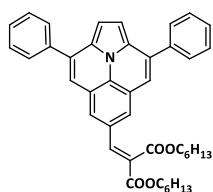
3,9-diphenylindolizino[6,5,4,3-*ija*]quinoline-4-carbaldehyde, **7d**



Method A. Synthesized and worked-up according to the similar procedure as for **5a**, starting with **10** (0.053 g, 0.143 mmol), InCl_3 (0.019 g, 0.086 mmol) and toluene (1.5 mL). The desired product **7d** was isolated as red-orange solid (0.048 g, 91% yield).

Method B. Obtained as a minor byproduct in Vilmeier-Haack formylation of **5b** (vide supra, for **7b**). The carbaldehyde **7d** was isolated off as a red-orange powder using silica gel column chromatography with DCM as eluent ($R_f \approx 0.35$, 0.047 g, 6%). ^1H NMR (400 MHz, Chloroform-*d*) δ 10.00 (s, 1H), 9.22 (dd, $J = 7.8, 1.4$ Hz, 1H), 7.80 – 7.74 (m, 2H), 7.71 – 7.45 (m, 12H), 7.12 (d, $J = 4.5$ Hz, 1H), 6.90 (d, $J = 4.5$ Hz, 1H). ^{13}C NMR (101 MHz, Chloroform-*d*) δ 192.04, 145.86, 137.95, 134.25, 132.95, 132.48, 130.62, 130.43, 129.22, 129.06, 128.70, 128.68, 128.32, 127.06, 125.41, 122.94, 122.25, 121.25, 120.63, 120.07, 113.01, 108.84. HRMS (MALDI-TOF-MS): calcd. for $\text{C}_{27}\text{H}_{17}\text{NO}$ 371.1310 $[\text{M}]^+$; found 371.138.

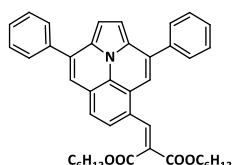
Dihexyl-2-((3,9-diphenylindolizino[6,5,4,3-*ija*]quinolin-6-yl)methylene)malonate, **8a**



A flame-dried N_2 -filled 100 mL Schlenk tube was charged with ullazine **5a** (0.211 g, 0.5 mmol), dry THF (5 mL) and dry toluene (5 mL). The mixture was stirred at room temperature until complete dissolution of solids. Afterwards the solution was brought to -40°C and *n*BuLi (0.22 mL, 0.55 mmol, 2.5M solution in hexane) was added dropwise. The reaction mixture was stirred at -40°C for 30 min followed by addition of dry DMF (77 μL , 1.0 mmol). Afterwards the solution was kept stirring at -40°C for 30 min and allowed to reach ambient temperature. Another flame-dried N_2 -filled 100 mL round-bottomed flask was charged with dry DCM (10 mL) and TiCl_4 (2.5 mL, 2.5 mmol, 1.0M solution in DCM), cooled down to 0°C . Dihexylmalonate (0.136 g, 0.5 mmol) was added to the solution of carbaldehyde at room temperature under N_2 atmosphere. The resulting mixture was transferred to the TiCl_4 -solution via syringe (with taking care to avoid heating) followed by dropwise addition of dry pyridine (0.75 mL). After stirring overnight water was added to the reaction mixture. The organic phase was separated, washed with water thoroughly, dried over MgSO_4 and concentrated under reduced pressure. The residue was purified by silica gel column chromatography using gradient elution with mixtures hexane/DCM (4:1 \rightarrow 1:1) as the eluent ($R_f \approx 0.3$, hexane/DCM \approx 1:1) to give yellow waxy solid **4b** (0.206 g, 66% yield). ^1H NMR (400 MHz, Chloroform-*d*) δ 7.94 (s, 1H), 7.82 – 7.74 (m, 4H), 7.59 (s, 2H), 7.57 – 7.44 (m, 6H), 7.22 (s, 2H), 7.12 (s, 2H), 4.31 (t, $J = 6.7$ Hz, 2H), 4.27 (t, $J = 6.7$ Hz, 2H), 1.79 – 1.60 (m, 4H), 1.46 – 1.30 (m, 6H), 1.30 – 1.04 (m, 6H),

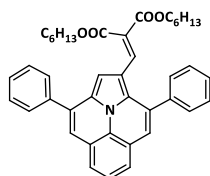
0.92 (t, $J = 6.8$ Hz, 3H), 0.71 (t, $J = 7.1$ Hz, 3H). ^{13}C NMR (101 MHz, Chloroform-*d*) δ 167.25, 164.40, 142.94, 138.36, 134.36, 133.12, 128.95, 128.65, 128.63, 128.31, 127.03, 126.18, 126.02, 120.44, 119.12, 107.21, 66.12, 65.88, 31.56, 28.69, 28.59, 25.77, 25.69, 22.70, 22.58, 14.17, 13.98. HRMS (MALDI-TOF-MS): calcd. for $\text{C}_{42}\text{H}_{43}\text{NO}_4$ 625.3192 $[\text{M}]^+$; found 625.324.

Dihexyl-2-((3,9-diphenylindolizino[6,5,4,3-*ija*]quinolin-5-yl)methylene)malonate, **8b**



A flame-dried N_2 -filled 25 mL round-bottomed flask was charged with dry DCM (3 mL) and TiCl_4 (1.5 mL, 1.5 mmol, 1.0M solution in DCM), cooled down to 0°C . Dihexylmalonate (0.081 g, 0.3 mmol) was mixed with carbaldehyde **7b** (0.110 g, 0.3 mmol) and dry DCM (2 mL). The resulting mixture was transferred to the TiCl_4 -solution via syringe (with taking care to avoid heating) followed by dropwise addition of dry pyridine (0.5 mL). After stirring overnight water was added to the reaction mixture. The organic phase was separated, washed with water thoroughly, dried over MgSO_4 and concentrated under reduced pressure. The residue was purified by precipitation from methanol to afford analytically pure dye **8b** as bright orange solid (0.16 g, 85% yield). ^1H NMR (400 MHz, Chloroform-*d*) δ 8.37 (s, 1H), 7.86 – 7.76 (m, 4H), 7.63 – 7.42 (m, 9H), 7.34 (s, 1H), 7.22 (s, 2H), 4.28 (t, $J = 6.7$ Hz, 2H), 4.21 (t, $J = 6.7$ Hz, 2H), 1.79 – 1.67 (m, 2H), 1.59 – 1.51 (m, 2H), 1.48 – 1.28 (m, 6H), 1.20 – 1.09 (m, 6H), 0.90 (t, $J = 7.2$ Hz, 3H), 0.77 (t, $J = 6.9$ Hz, 3H). ^{13}C NMR (101 MHz, Chloroform-*d*) δ 167.33, 164.80, 139.57, 138.46, 138.35, 134.79, 129.02, 128.99, 128.80, 128.74, 128.63, 128.52, 127.75, 127.52, 127.18, 126.25, 125.46, 124.36, 121.80, 119.54, 119.06, 116.09, 107.94, 107.90, 65.93, 65.83, 31.58, 31.51, 28.73, 28.47, 25.74, 25.67, 22.70, 22.59, 14.16, 14.06. HRMS (MALDI-TOF-MS): calcd. for $\text{C}_{42}\text{H}_{43}\text{NO}_4$ 625.3192 $[\text{M}]^+$; found 625.328.

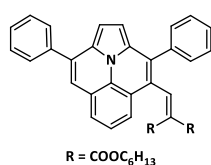
Dihexyl-2-((3,9-diphenylindolizino[6,5,4,3-*ija*]quinolin-1-yl)methylene)malonate, **8c**



Synthesized and purified according to the same procedure as for **8b**, starting with carbaldehyde **5c** (0.110 g, 0.3 mmol). After purification by silica gel column chromatography with hexane/DCM (4:1 \rightarrow 1:1) as eluent ($R_f \approx 0.35$ hexane/DCM $\approx 1:1$) the desired product **8c** was isolated as yellow viscous oil (0.171 g, 91% yield). ^1H NMR (400 MHz, Chloroform-*d*) δ 7.76 – 7.68

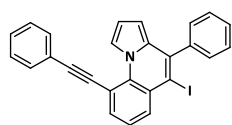
(m, 2H), 7.59 – 7.44 (m, 11H), 7.40 (s, 1H), 7.25 (s, 1H), 7.23 (s, 1H), 7.07 (s, 1H), 4.16 (t, $J = 6.9$ Hz, 2H), 4.04 (t, $J = 6.8$ Hz, 2H), 1.64 – 1.50 (m, 5H), 1.36 – 1.14 (m, 13H), 0.90 (t, $J = 6.7$ Hz, 4H), 0.83 (t, $J = 6.6$ Hz, 3H). ^{13}C NMR (101 MHz, Chloroform-*d*) δ 168.26, 164.55, 138.21, 138.00, 135.07, 134.01, 133.22, 132.13, 129.08, 129.01, 128.90, 128.77, 128.75, 128.16, 127.83, 127.79, 125.78, 125.18, 124.83, 124.43, 121.33, 121.16, 121.06, 120.59, 113.83, 105.53, 65.84, 65.12, 31.58, 31.50, 28.64, 28.37, 25.63, 22.70, 22.64, 14.19, 14.13. HRMS (MALDI-TOF-MS): calcd. for $\text{C}_{42}\text{H}_{43}\text{NO}_4$ 625.3192 $[\text{M}]^+$; found 625.318.

Dihexyl-2-((3,9-diphenylindolizino[6,5,4,3-*ija*]quinolin-4-yl)methylene)malonate, **8d**



Synthesized and purified according to the same procedure as for **8b**, starting with carbaldehyde **7d** (0.11 g, 0.3 mmol). After purification by silica gel column chromatography with hexane/DCM (4:1→1:1) as eluent ($R_f \approx 0.35$ hexane/DCM $\approx 1:1$) the desired product **8c** was isolated as dark red solid (0.15 g, 80% yield). ^1H NMR (400 MHz, Chloroform-*d*) δ 7.83 – 7.75 (m, 2H), 7.73 (s, 1H), 7.60 – 7.39 (m, 11H), 7.29 (s, 1H), 7.03 (d, $J = 4.3$ Hz, 1H), 6.79 (d, $J = 4.3$ Hz, 1H), 4.21 (t, $J = 6.7$ Hz, 2H), 3.82 (t, $J = 6.5$ Hz, 2H), 1.70 – 1.60 (m, 2H), 1.39 – 1.24 (m, 7H), 1.21 – 1.12 (m, 2H), 0.95 – 0.82 (m, 9H), 0.69 (t, $J = 6.8$ Hz, 3H). ^{13}C NMR (101 MHz, Chloroform-*d*) δ 165.13, 164.45, 143.31, 138.52, 136.24, 133.32, 132.67, 130.34, 129.97, 128.92, 128.76, 128.62, 128.51, 128.27, 127.61, 127.22, 126.10, 123.95, 123.57, 122.05, 120.29, 120.12, 118.25, 108.34, 106.77, 65.82, 65.59, 31.54, 31.36, 28.61, 28.18, 25.63, 25.54, 22.67, 22.31, 14.17, 14.09. HRMS (MALDI-TOF-MS): calcd. for $\text{C}_{42}\text{H}_{43}\text{NO}_4$ 625.3192 $[\text{M}]^+$; found 625.330.

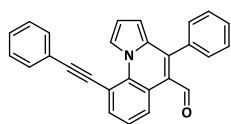
5-iodo-4-phenyl-9-(phenylethynyl)pyrrolo[1,2-*a*]quinoline, **9**



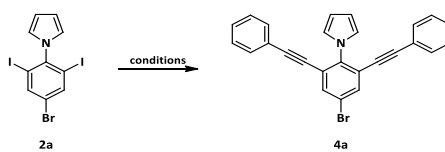
A flame-dried N_2 -filled 50 mL round-bottomed flask was charged with bisalkyne **4b** (0.45 g, 1.31 mmol), NaHCO_3 (0.24 g, 2.88 mmol) and DCM (13 mL). The mixture was cooled down to 0°C and I_2 (0.73 g, 2.88 mmol) in DCM (26 mL) was added dropwise. The reaction was kept stirring at 0°C for 10 hours, quenched with addition of concentrated solution of $\text{Na}_2\text{S}_2\text{O}_3$ and vigorously stirred until complete iodine discoloration. The organic phase was separated, dried over MgSO_4 and concentrated under reduced pressure. Silica gel column

chromatography with a hexane/DCM mixture (4:1) as the eluent ($R_f \approx 0.3$) delivered iodide **9** as yellow solid (0.36 g, 58%). ^1H NMR (400 MHz, Chloroform-*d*) δ 9.61 (dd, $J = 3.1, 1.4$ Hz, 1H), 8.24 (dd, $J = 8.2, 1.5$ Hz, 1H), 7.82 (dd, $J = 7.6, 1.5$ Hz, 1H), 7.70 – 7.59 (m, 2H), 7.59 – 7.46 (m, 3H), 7.46 – 7.31 (m, 6H), 6.68 (dd, $J = 4.0, 2.8$ Hz, 1H), 6.07 (dd, $J = 3.9, 1.1$ Hz, 1H). ^{13}C NMR (101 MHz, Chloroform-*d*) δ 142.71, 140.15, 135.59, 135.42, 133.23, 132.62, 131.44, 129.45, 128.99, 128.75, 128.55, 128.39, 126.03, 123.78, 123.08, 118.05, 112.26, 111.06, 105.68, 95.91, 93.27, 89.13. HRMS (MALDI-TOF-MS): calcd. for $\text{C}_{27}\text{H}_{17}\text{NO}$ 469.0328 $[\text{M}]^+$; found 469.033.

4-phenyl-9-(phenylethynyl)pyrrolo[1,2-a]quinoline-5-carbaldehyde, **10**

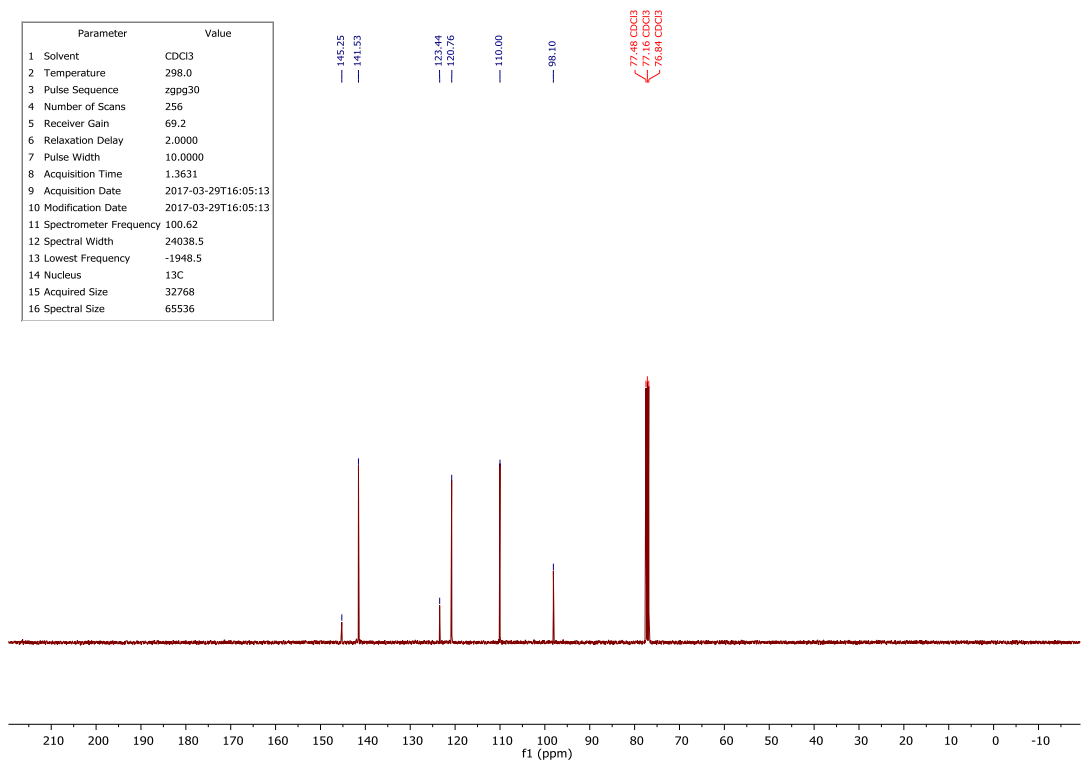
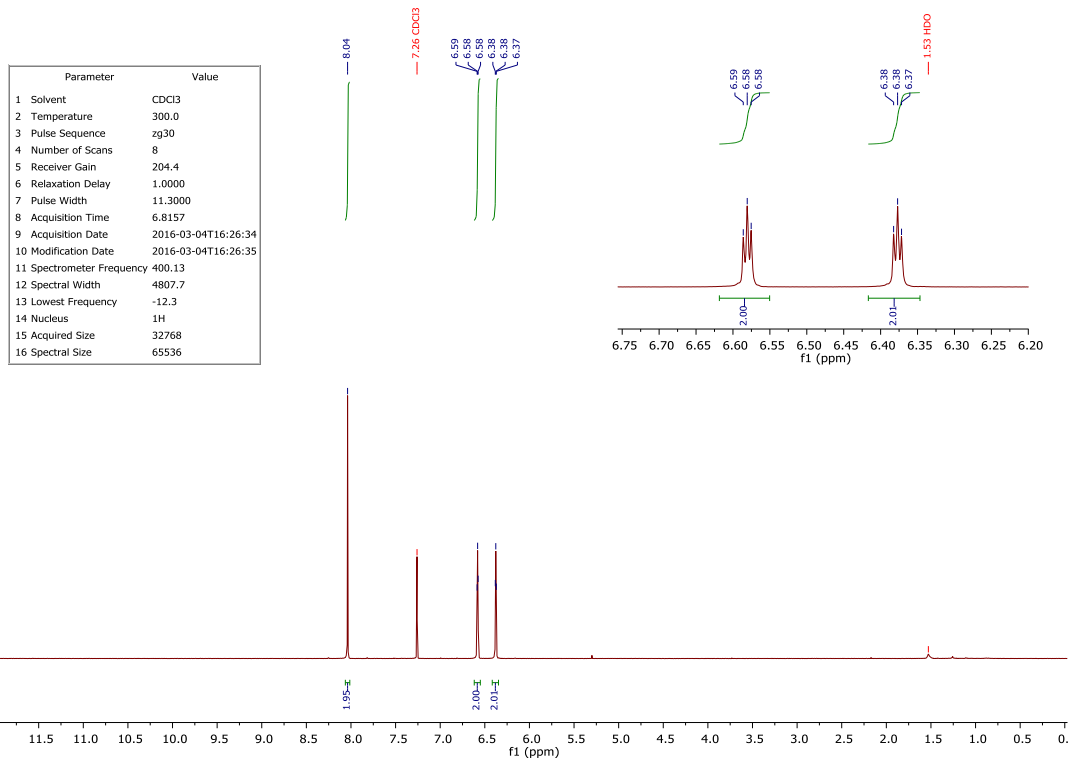
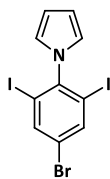


A flame-dried N_2 -filled 100 mL Schlenk tube was charged with iodide **9** (0.26 g, 0.55 mmol) and dry THF (5 mL). The solution was cooled down to -78°C and *n*BuLi (0.24 mL, 0.61 mmol, 2.5M solution in hexane) was added dropwise. The reaction mixture was stirred at -78°C for 30 min followed by addition of dry DMF (0.21 mL, 2.75 mmol). Afterwards the solution was kept stirring at -78°C for 30 min and allowed to reach ambient temperature. All volatiles were evaporated and water with DCM were added to the residue. The organic layer was washed with water, then dried over MgSO_4 and concentrated under reduced pressure to give residue that was purified by silica gel column chromatography using a mixture hexane/DCM (2:1) as the eluent ($R_f \approx 0.3$) affording orange solid **10** (0.11 g, 54% yield) ^1H NMR (400 MHz, Chloroform-*d*) δ 9.91 (s, 1H), 9.82 (dd, $J = 2.9, 1.4$ Hz, 1H), 9.44 (dd, $J = 8.3, 1.6$ Hz, 1H), 7.83 (dd, $J = 7.5, 1.5$ Hz, 1H), 7.69 – 7.59 (m, 2H), 7.57 – 7.47 (m, 5H), 7.47 – 7.37 (m, 4H), 6.83 (dd, $J = 4.1, 2.9$ Hz, 1H), 6.52 (dd, $J = 4.0, 1.3$ Hz, 1H). ^{13}C NMR (101 MHz, Chloroform-*d*) δ 192.72, 145.58, 135.20, 134.29, 131.91, 131.90, 131.39, 130.34, 129.03, 129.00, 128.74, 128.48, 128.30, 124.38, 123.00, 122.41, 122.18, 118.99, 113.99, 111.64, 110.87, 95.93, 89.42. HRMS (MALDI-TOF-MS): calcd. for $\text{C}_{26}\text{H}_{16}\text{IN}$ 371.1310 $[\text{M}]^+$; found 371.130.

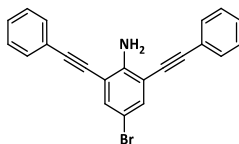
Table 12. Optimization of the Sonogashira reaction for **2a**.^[a]

Entry	Pd-source (eq.)	Ligand (eq.)	Base (eq.)	Eq. (PhCCH)	Solvent	Temperature, °C	Yield, %
1	Pd(Ph ₃ P) ₂ Cl ₂ (0.04)	-	Et ₃ N (4.0)	2.1	THF	RT	-
2	Pd(CH ₃ CN) ₂ Cl ₂ (0.06)	Cy ₃ P (0.12)	<i>i</i> Pr ₂ NH (2.1)	2.1	dioxane	RT	-
3	Pd(CH ₃ CN) ₂ Cl ₂ (0.06)	Cy ₃ P (0.12)	<i>i</i> Pr ₂ NH (2.1)	2.1	dioxane	60	-
4	Pd(Ph ₃ P) ₄ (0.06)	Cy ₃ P (0.12)	<i>i</i> Pr ₂ NH (2.1)	2.1	dioxane	60	-
5	Pd(CH ₃ CN) ₂ Cl ₂ (0.01)	<i>t</i> Bu ₃ P (0.02)	Cs ₂ CO ₃ (2.1)	2.1	CH ₃ CN	RT	-
6 ^[b]	Pd(Ph ₃ P) ₄ (0.05)	-	Cs ₂ CO ₃ (2.1)	2.1	CH ₃ CN	60	traces
7	Pd ₂ (dba) ₃ (0.05)	<i>rac</i> -BINAP (0.075)	Cs ₂ CO ₃ (2.1)	2.1	CH ₃ CN	RT	-
8	Pd(CH ₃ CN) ₂ Cl ₂ (0.06)	XPhos (0.12)	<i>i</i> Pr ₂ NH (2.1)	2.1	dioxane	60	12
9 ^[b]	Pd(CH ₃ CN) ₂ Cl ₂ (0.06)	XPhos (0.12)	Cs ₂ CO ₃ (2.1)	2.1	CH ₃ CN	60	46

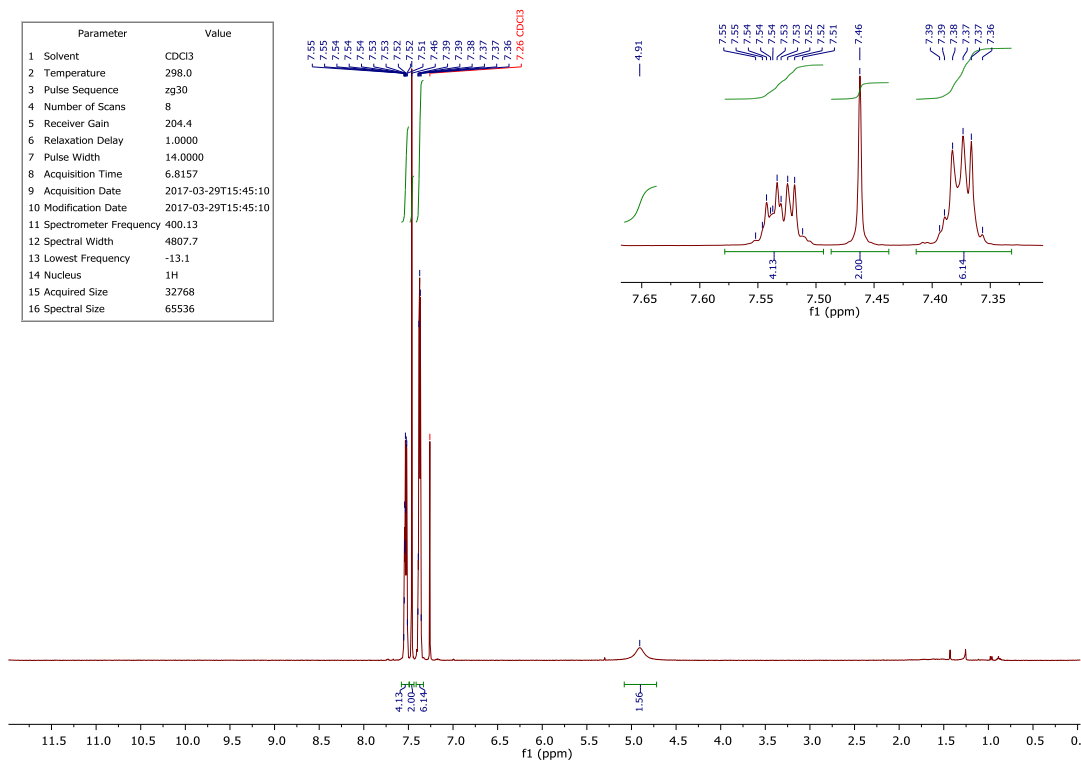
[a] unless otherwise noted reactions were carried out in presence of CuI, that was taken as ½ mol. to Pd-catalyst; [b] copper-free reaction.

6.4.2. ^1H and ^{13}C -NMR spectra of intermediate and the final compounds

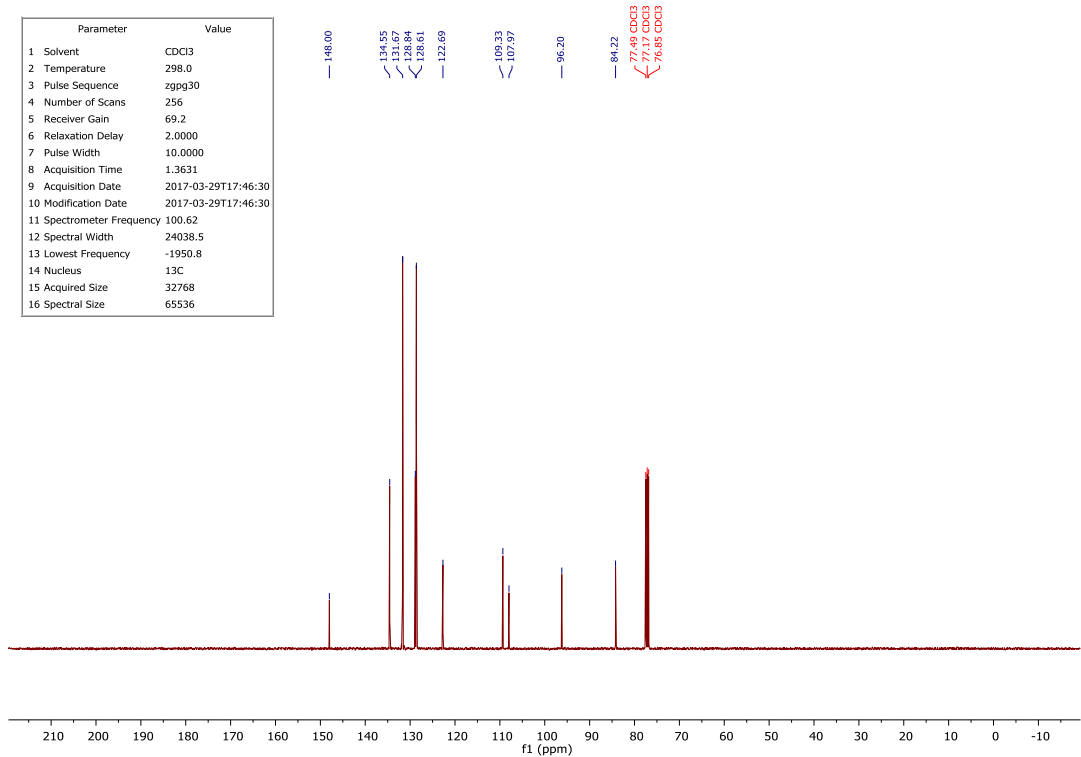
APPENDIX



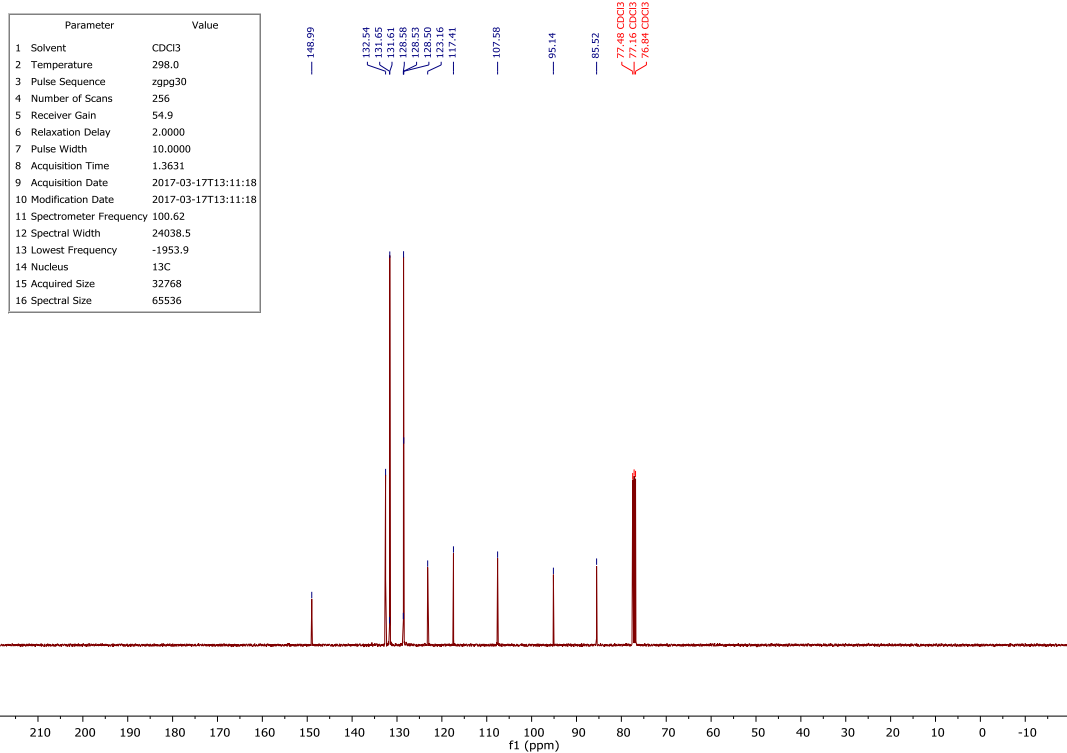
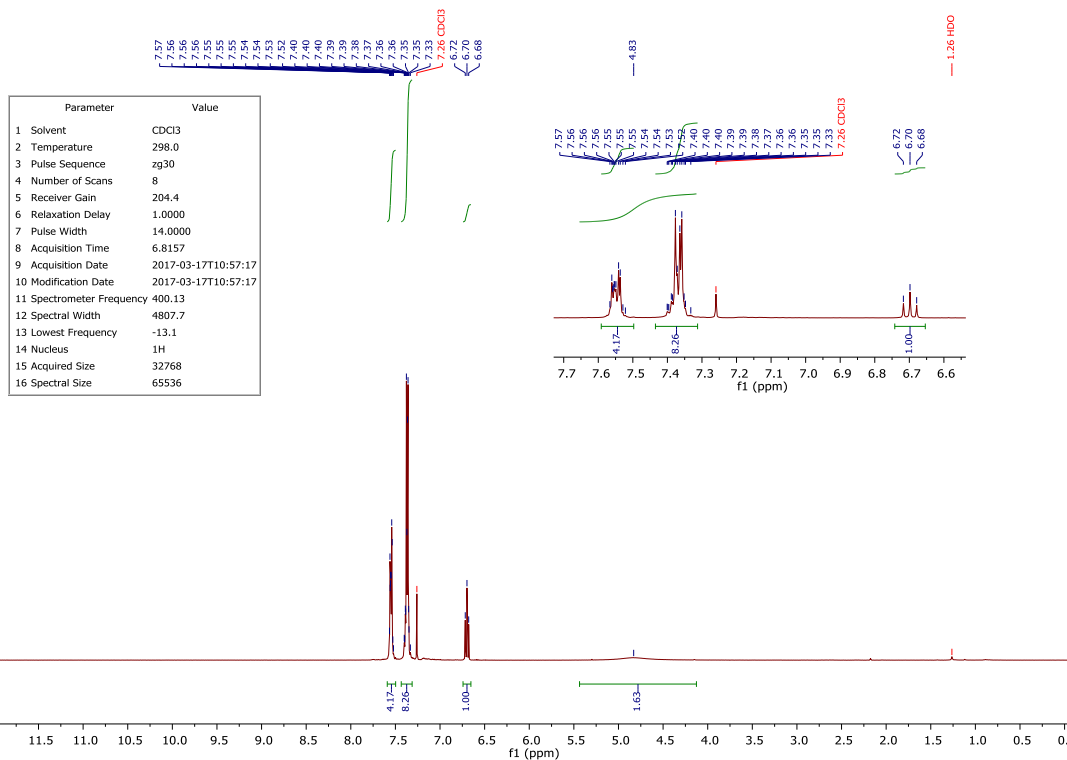
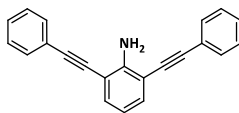
Parameter	Value
1 Solvent	CDCl3
2 Temperature	298.0
3 Pulse Sequence	zg30
4 Number of Scans	8
5 Receiver Gain	204.4
6 Relaxation Delay	1.0000
7 Pulse Width	14.0000
8 Acquisition Time	6.8157
9 Acquisition Date	2017-03-29T15:45:10
10 Modification Date	2017-03-29T15:45:10
11 Spectrometer Frequency	400.13
12 Spectral Width	4807.7
13 Lowest Frequency	-13.1
14 Nucleus	1H
15 Acquired Size	32768
16 Spectral Size	65536



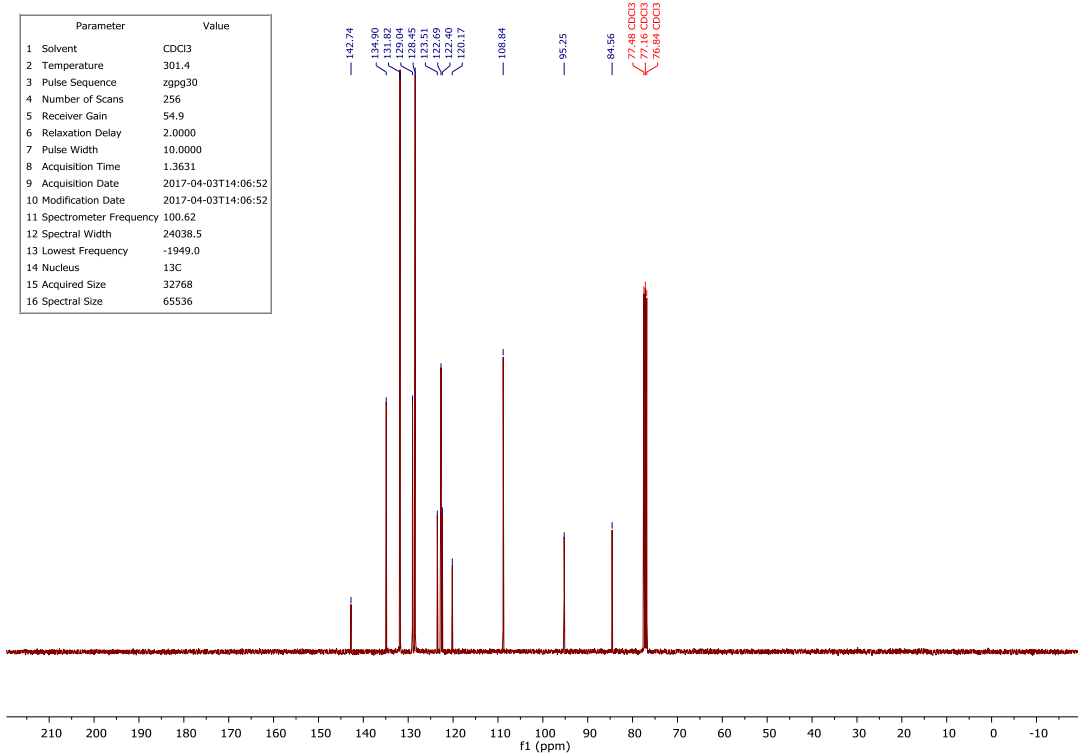
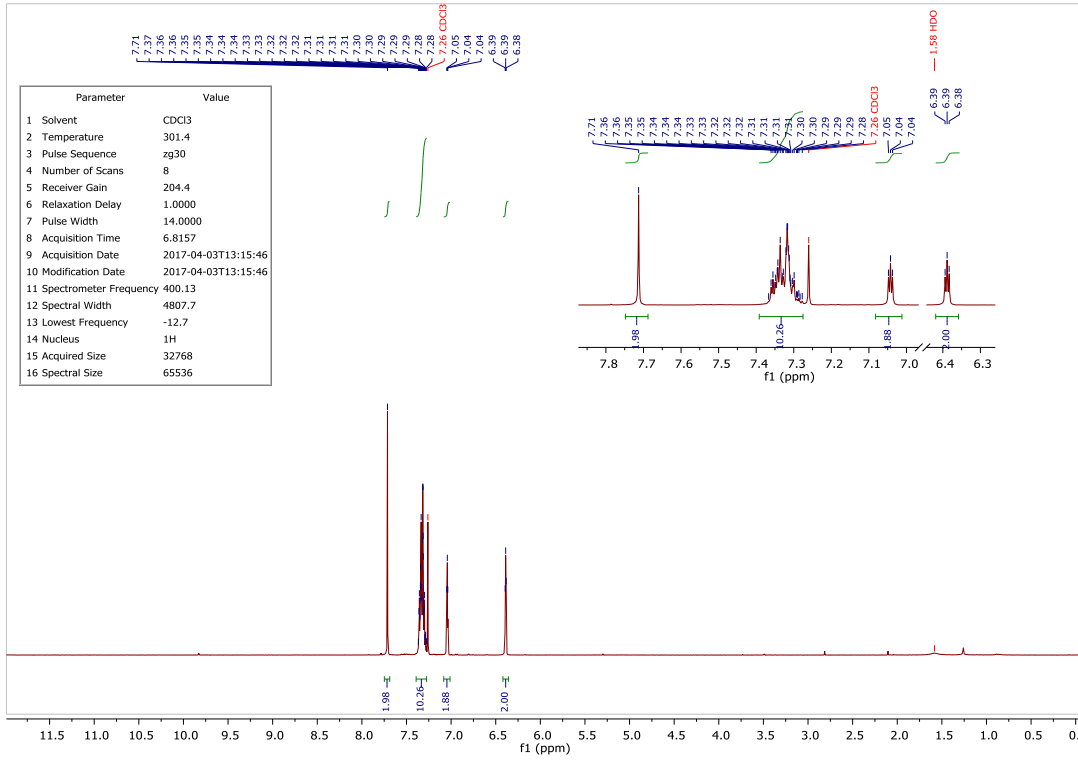
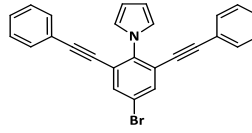
Parameter	Value
1 Solvent	CDCl3
2 Temperature	298.0
3 Pulse Sequence	zgpg30
4 Number of Scans	256
5 Receiver Gain	69.2
6 Relaxation Delay	2.0000
7 Pulse Width	10.0000
8 Acquisition Time	1.3631
9 Acquisition Date	2017-03-29T17:46:30
10 Modification Date	2017-03-29T17:46:30
11 Spectrometer Frequency	100.62
12 Spectral Width	24038.5
13 Lowest Frequency	-1950.8
14 Nucleus	13C
15 Acquired Size	32768
16 Spectral Size	65536



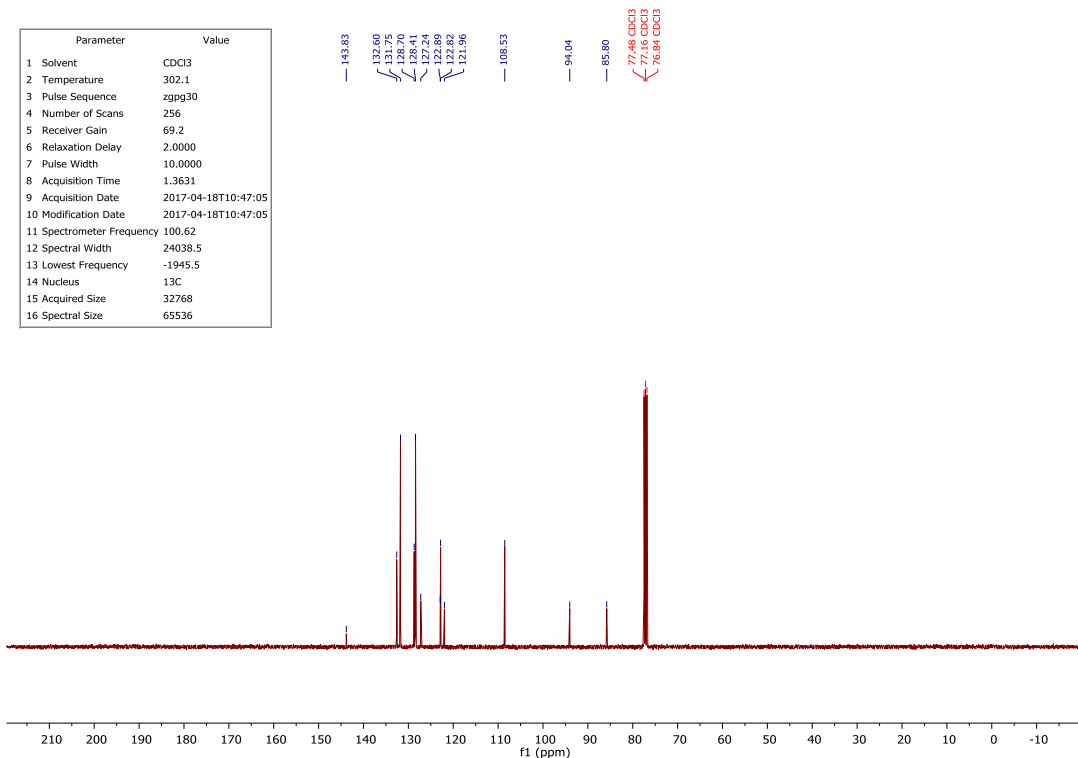
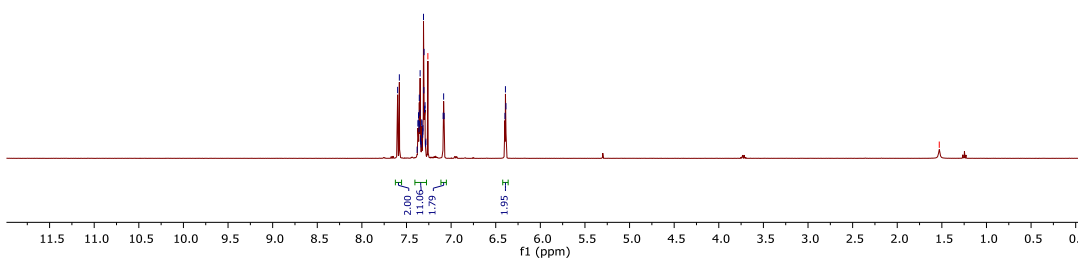
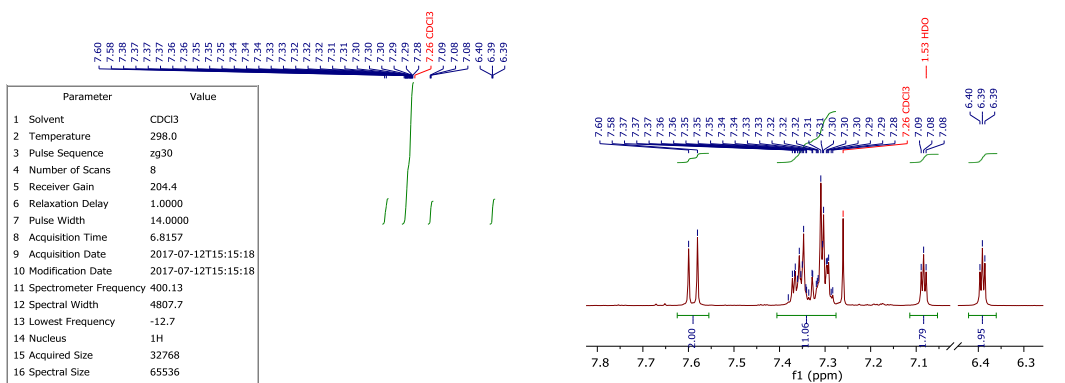
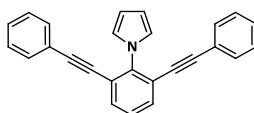
APPENDIX



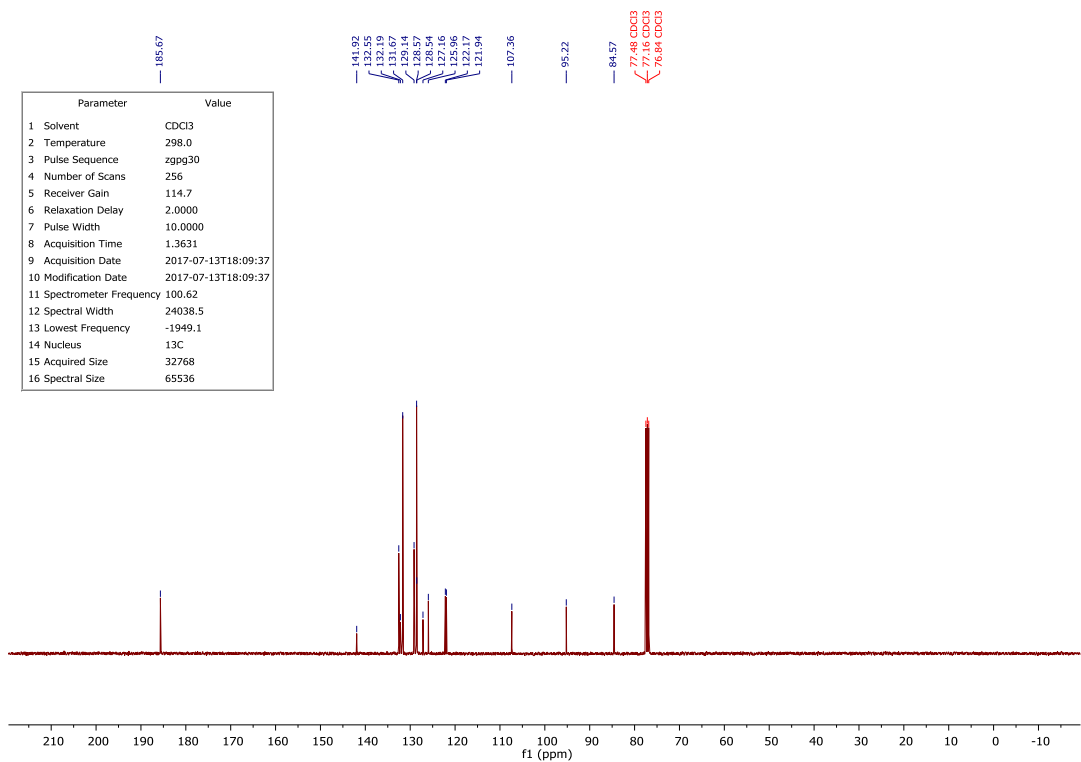
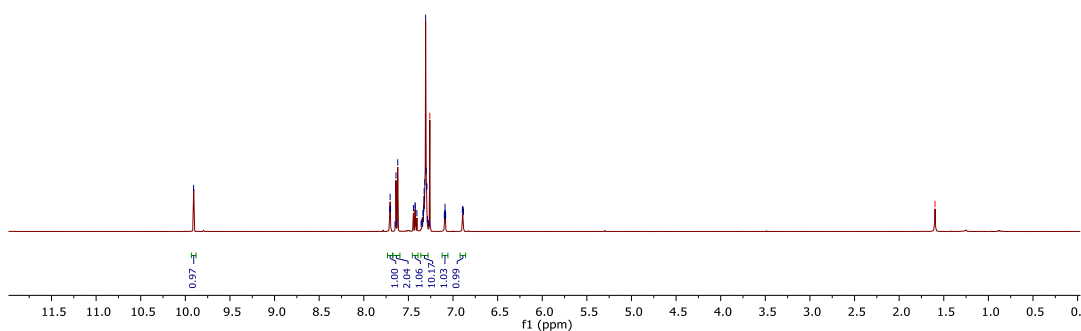
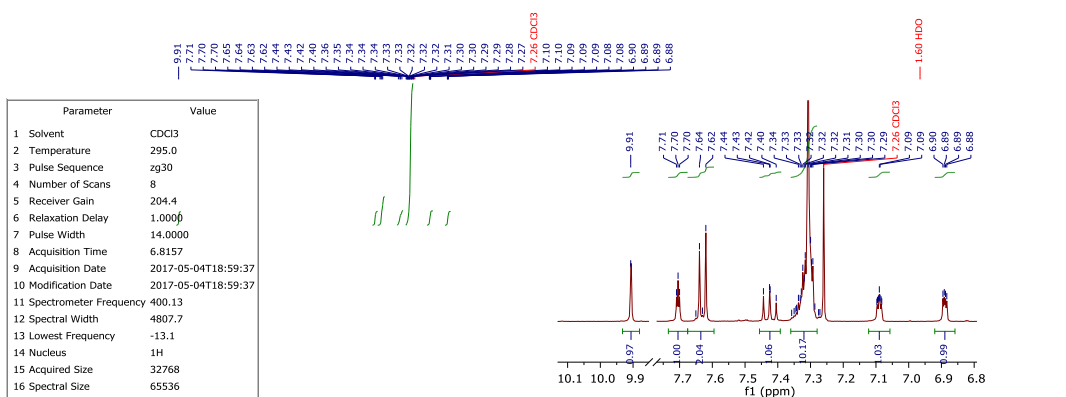
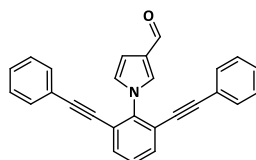
APPENDIX



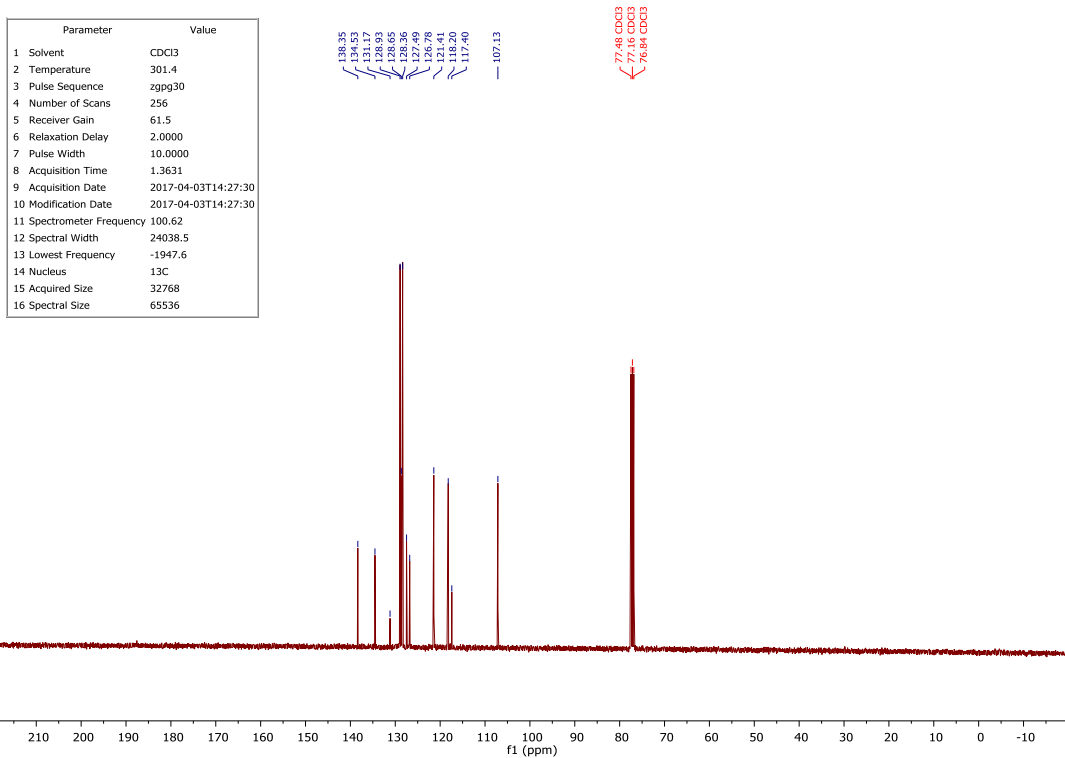
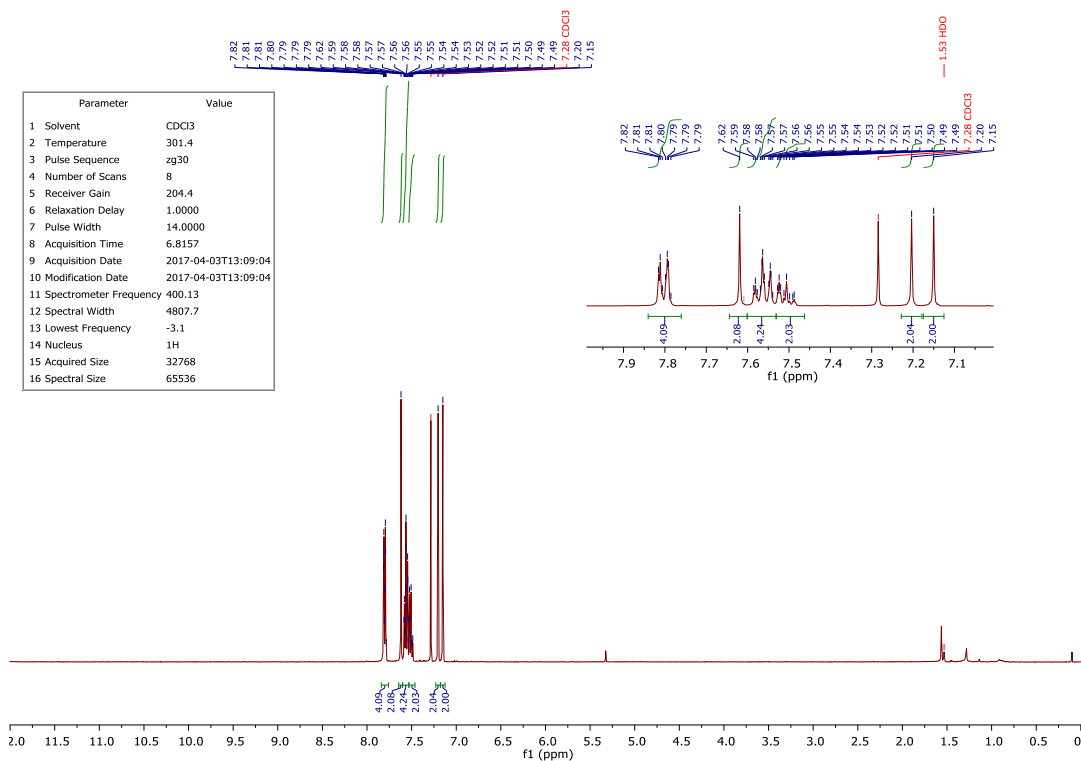
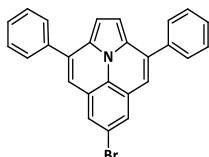
APPENDIX



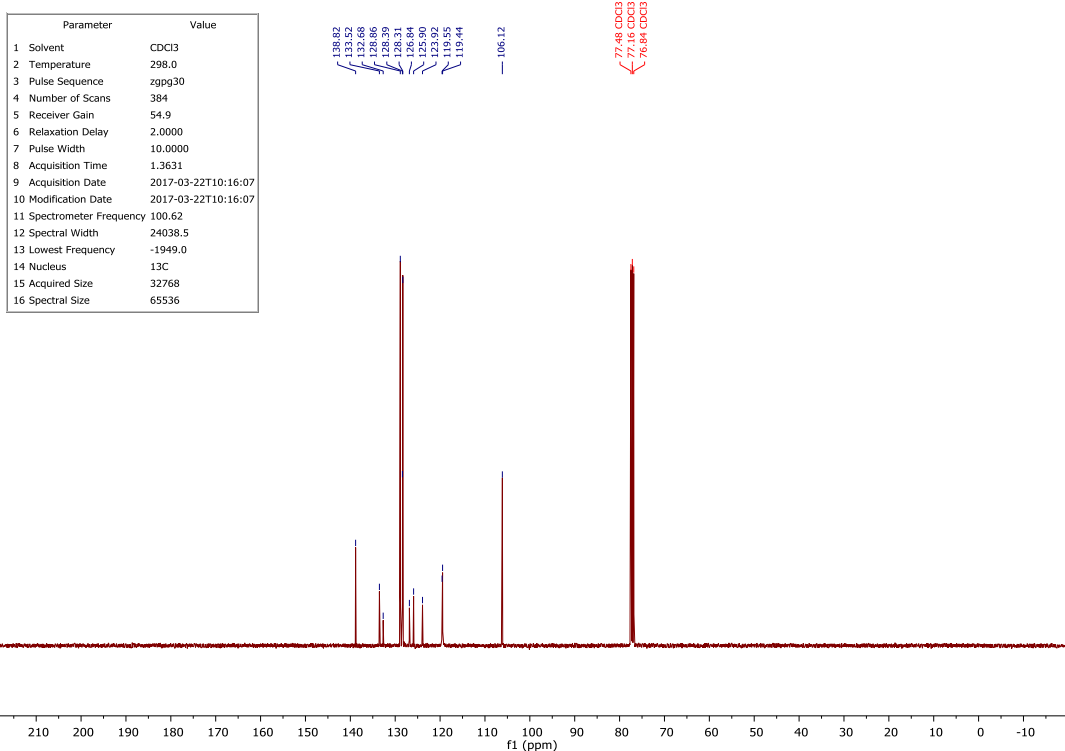
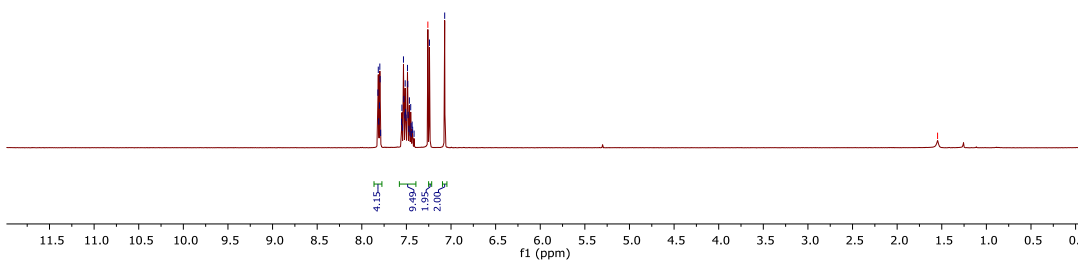
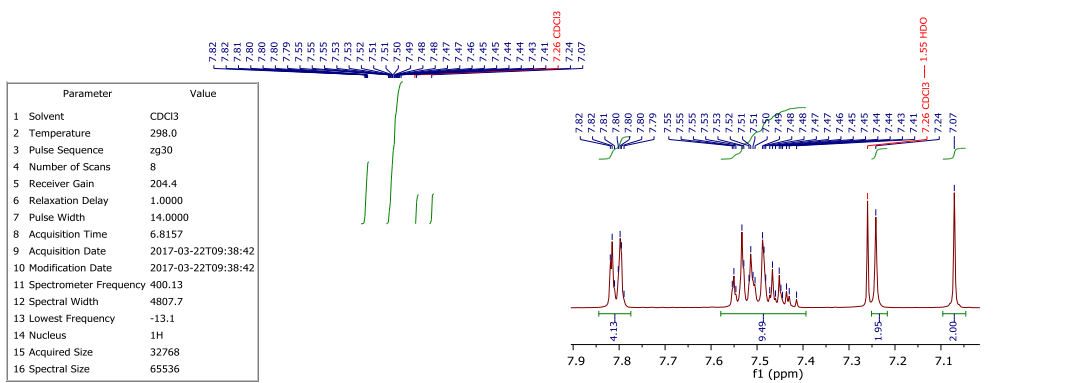
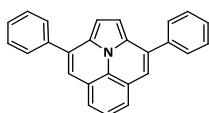
APPENDIX



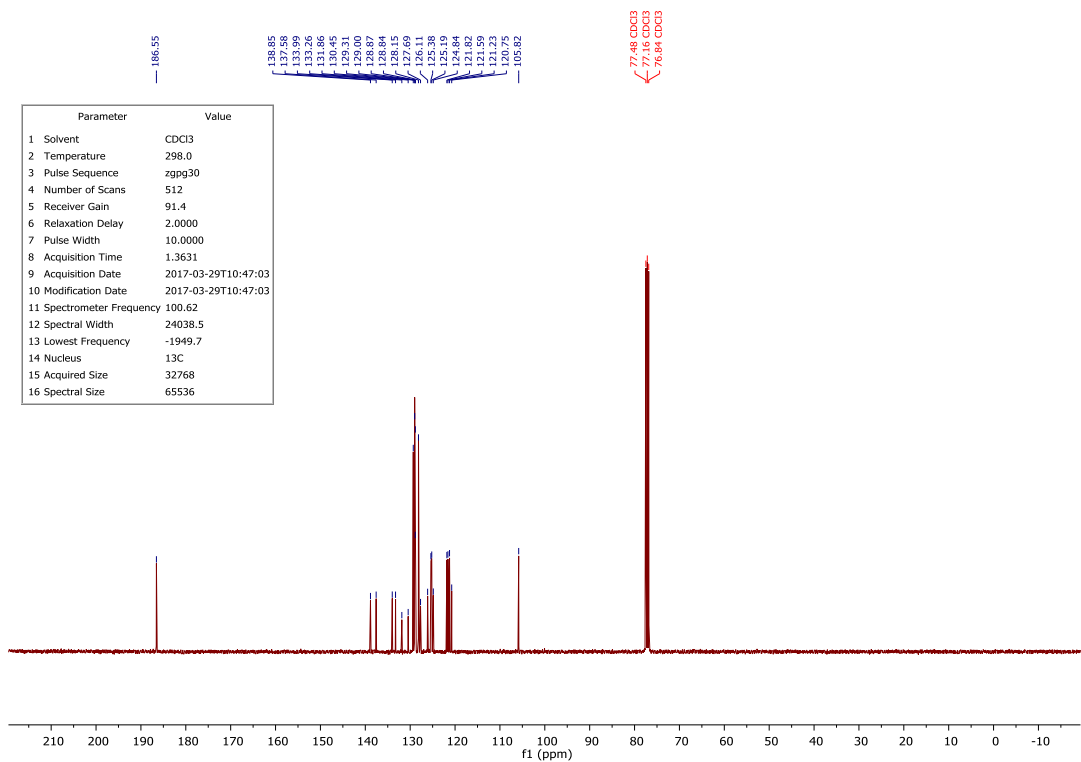
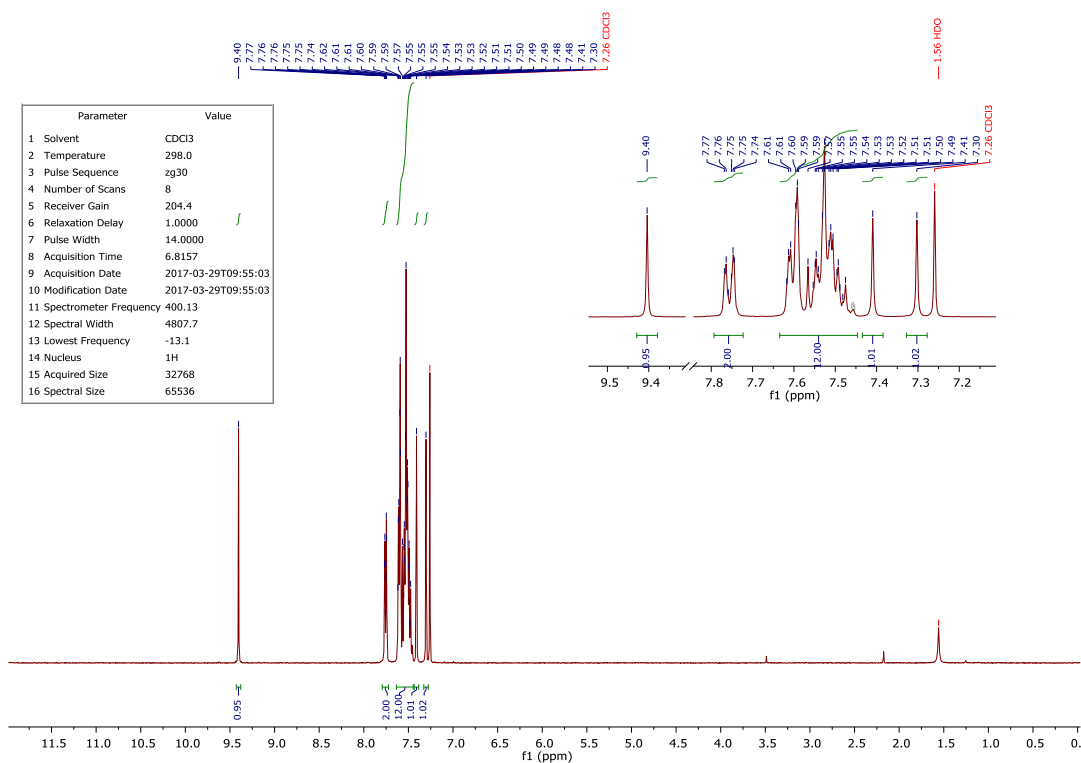
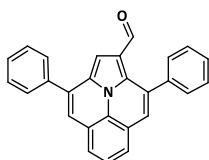
APPENDIX



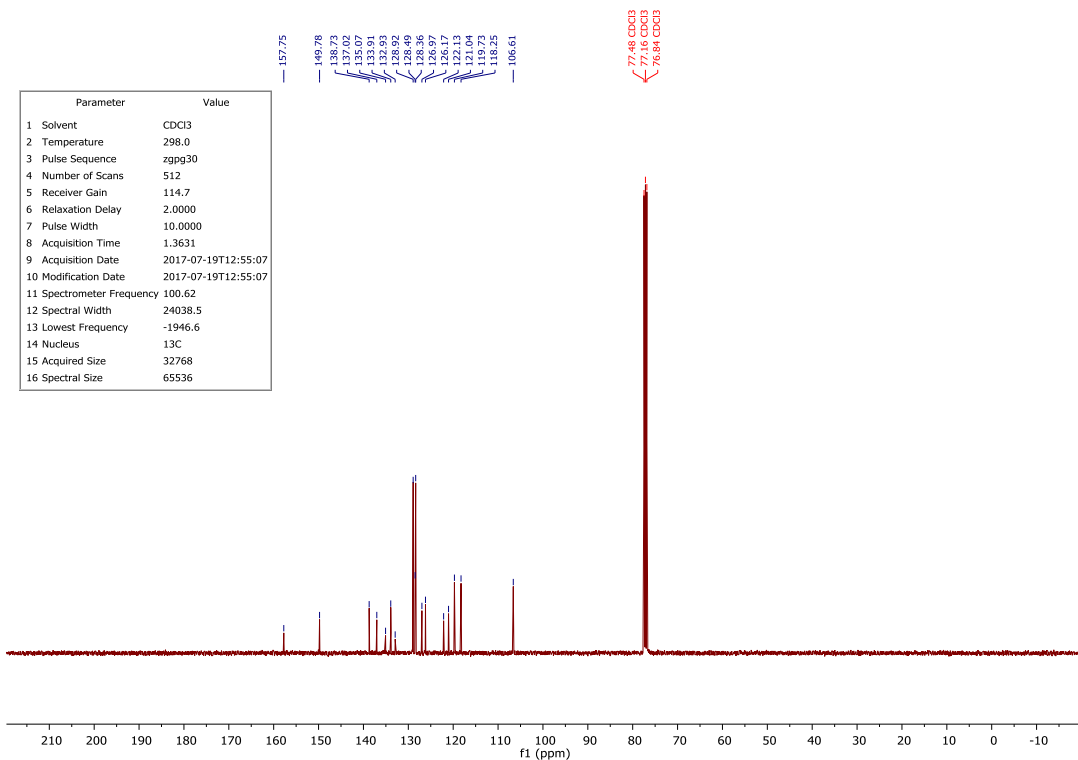
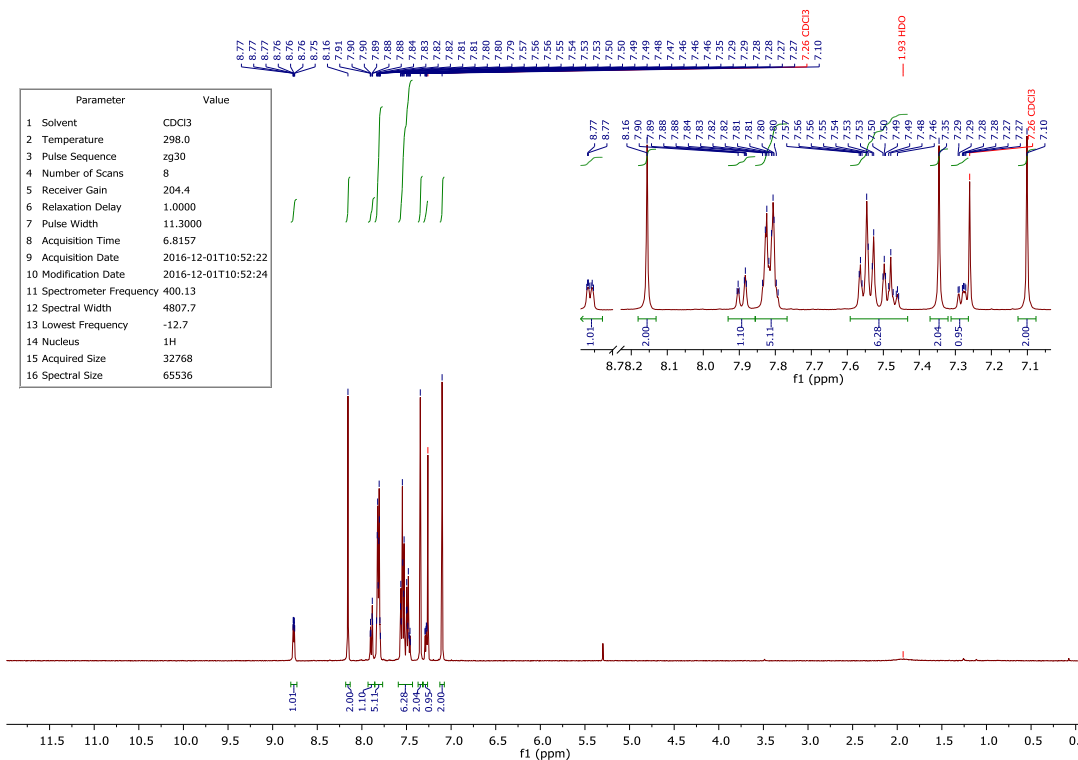
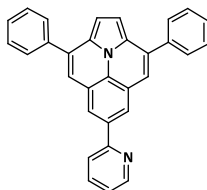
APPENDIX



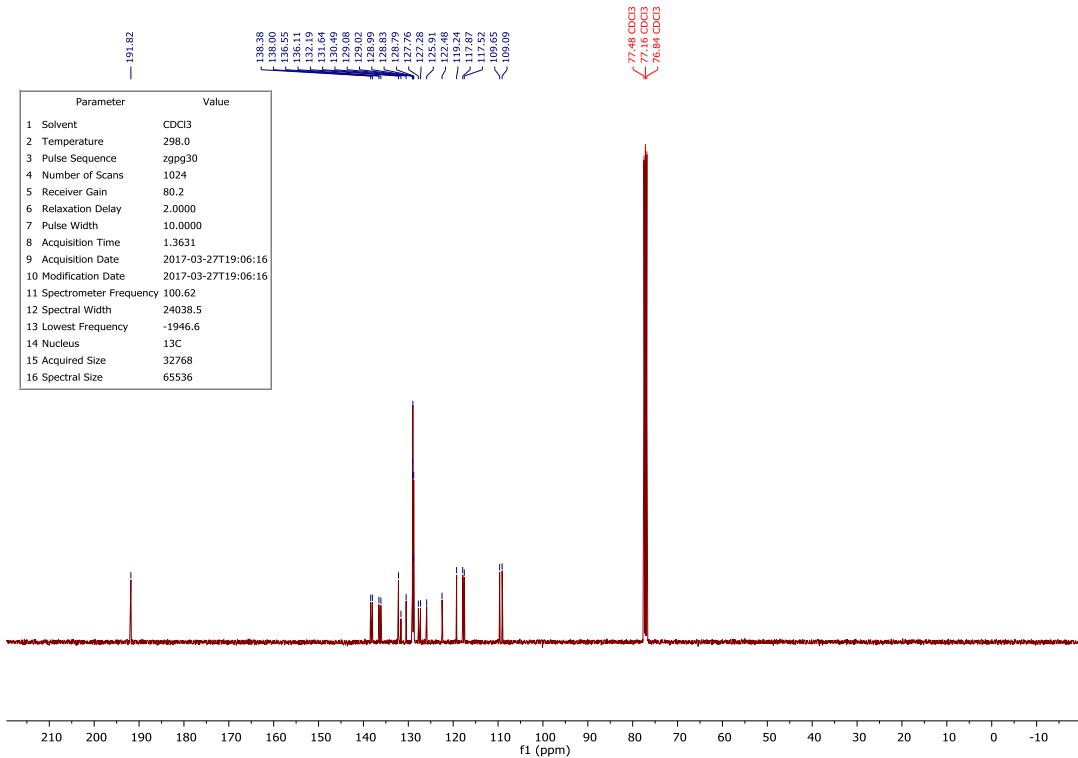
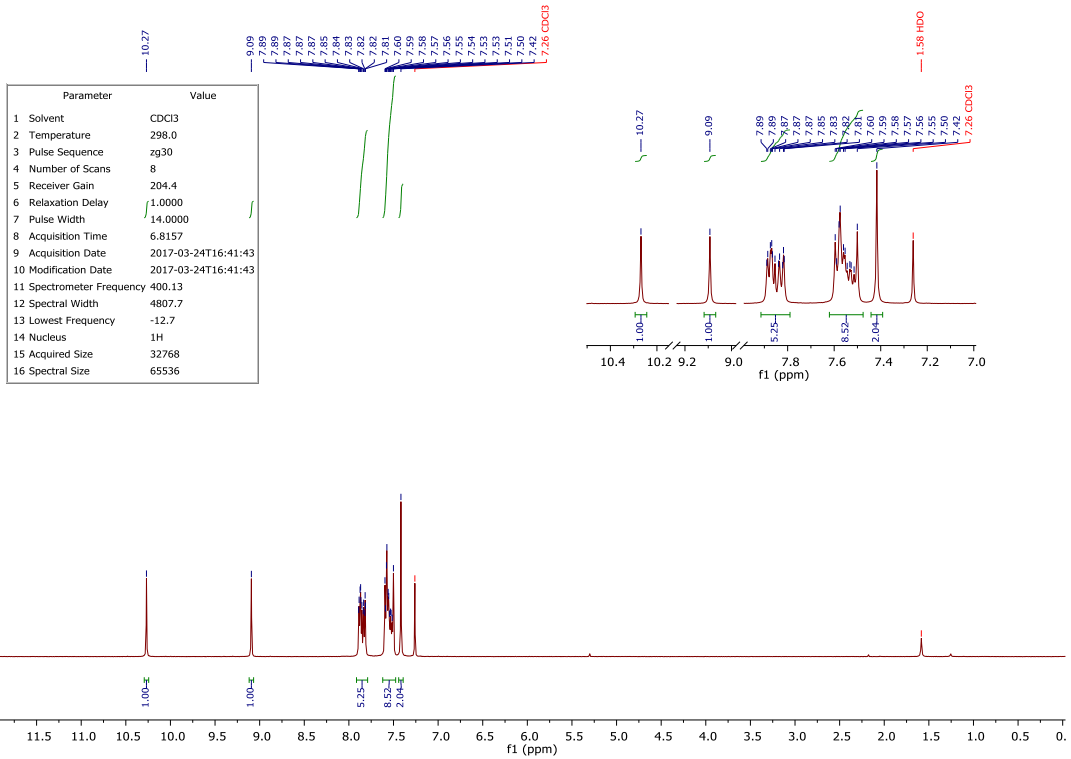
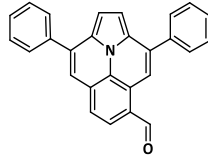
APPENDIX



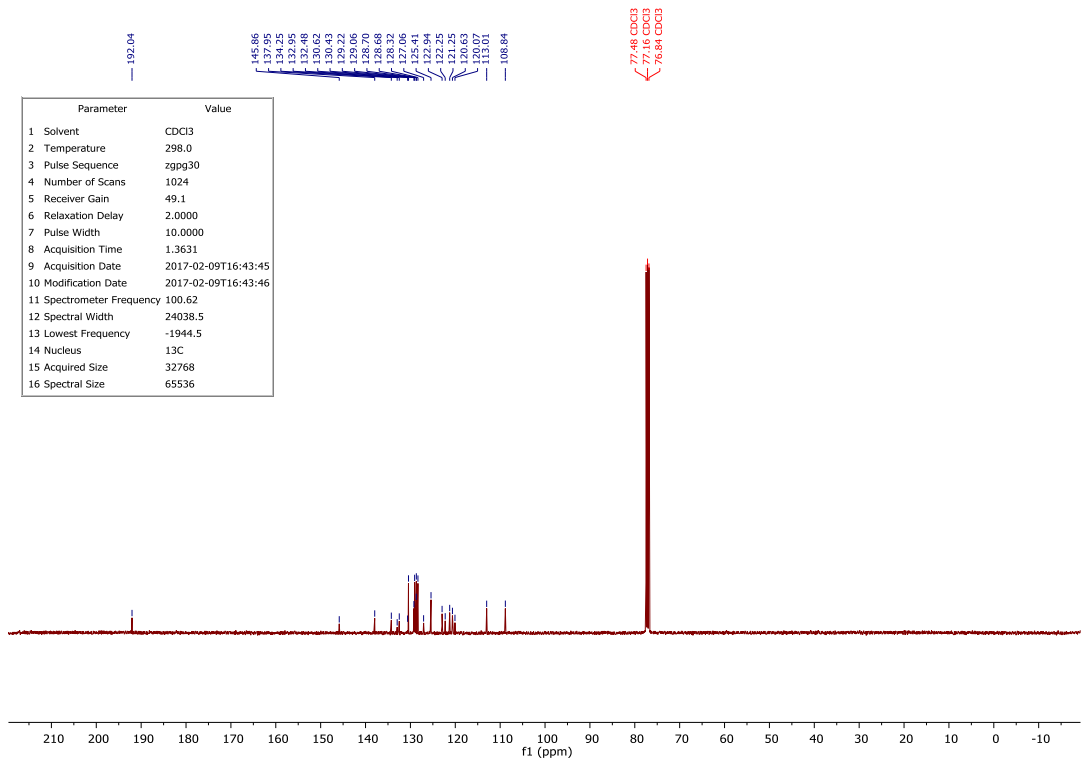
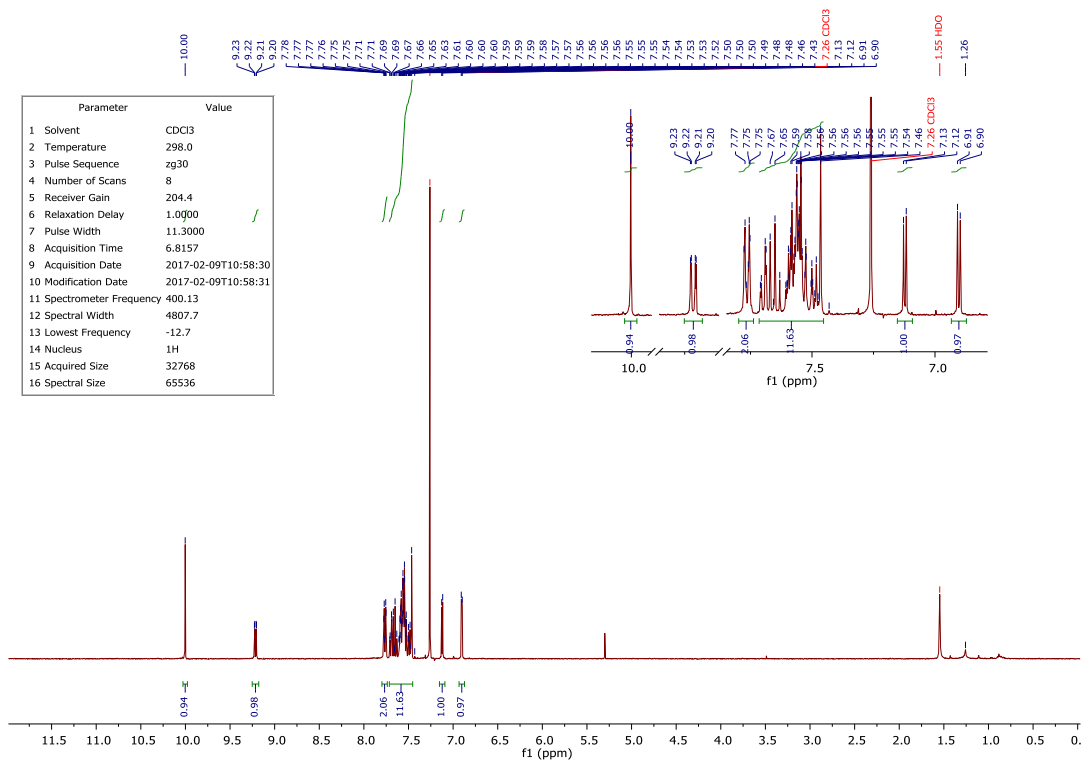
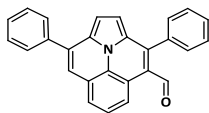
APPENDIX



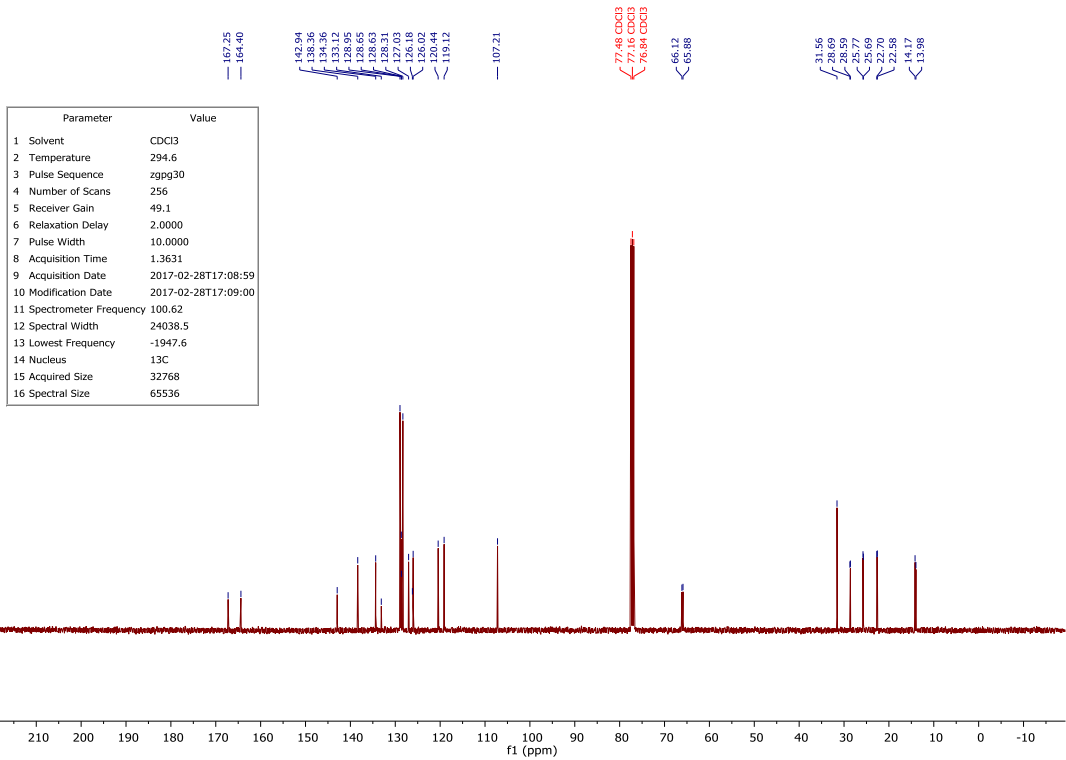
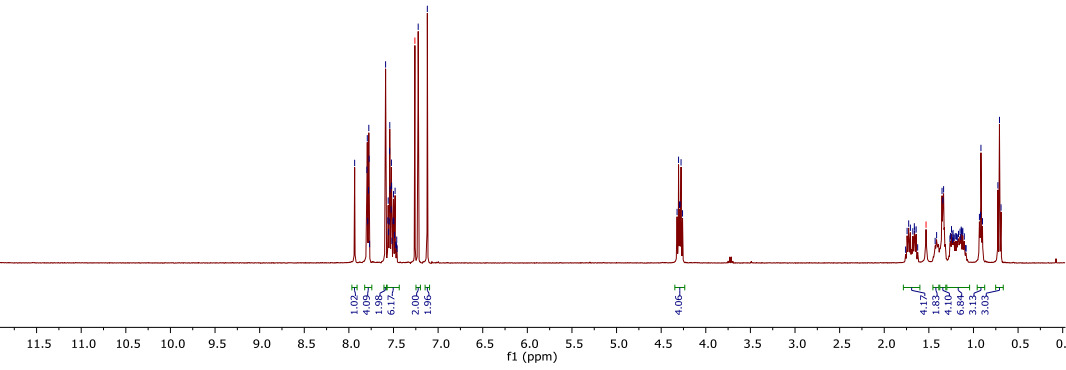
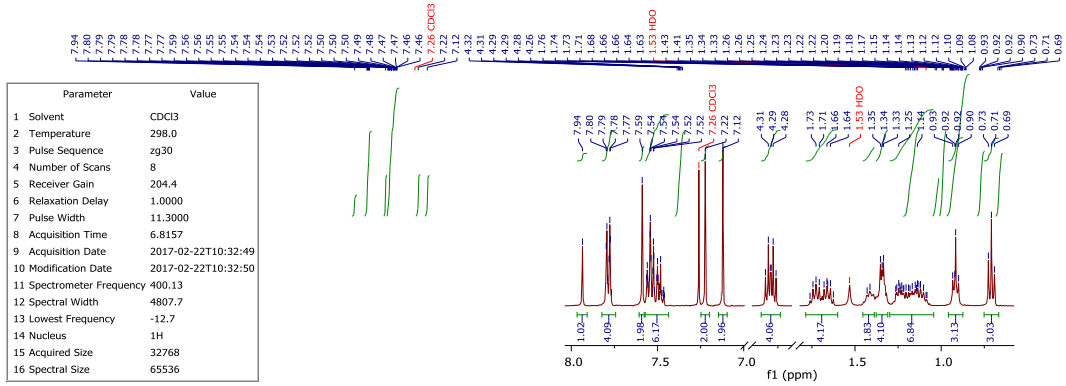
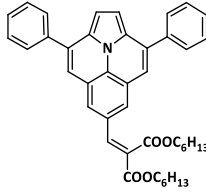
APPENDIX



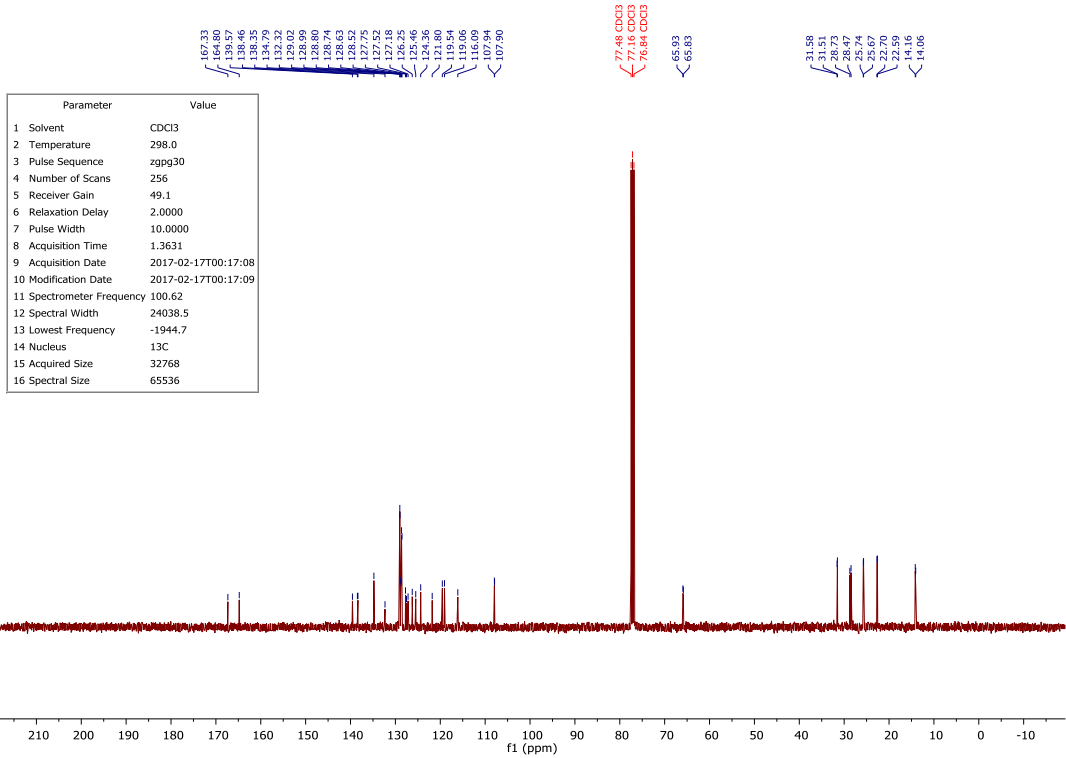
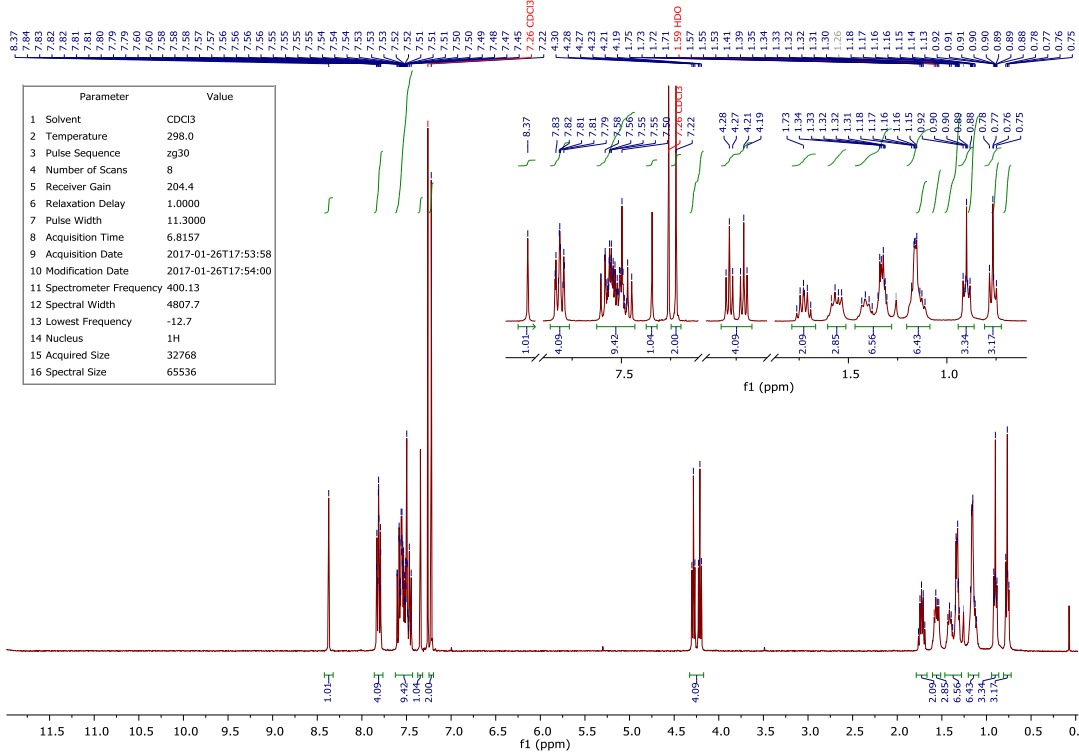
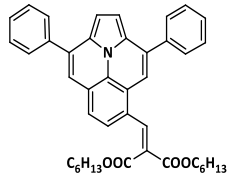
APPENDIX



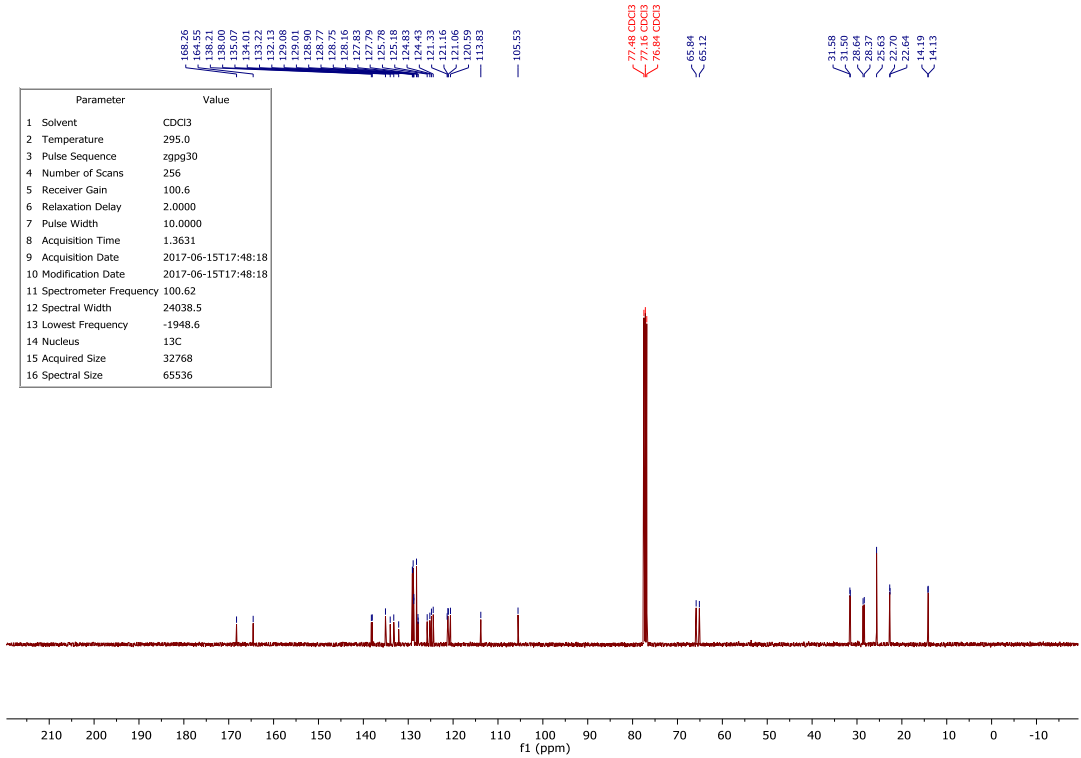
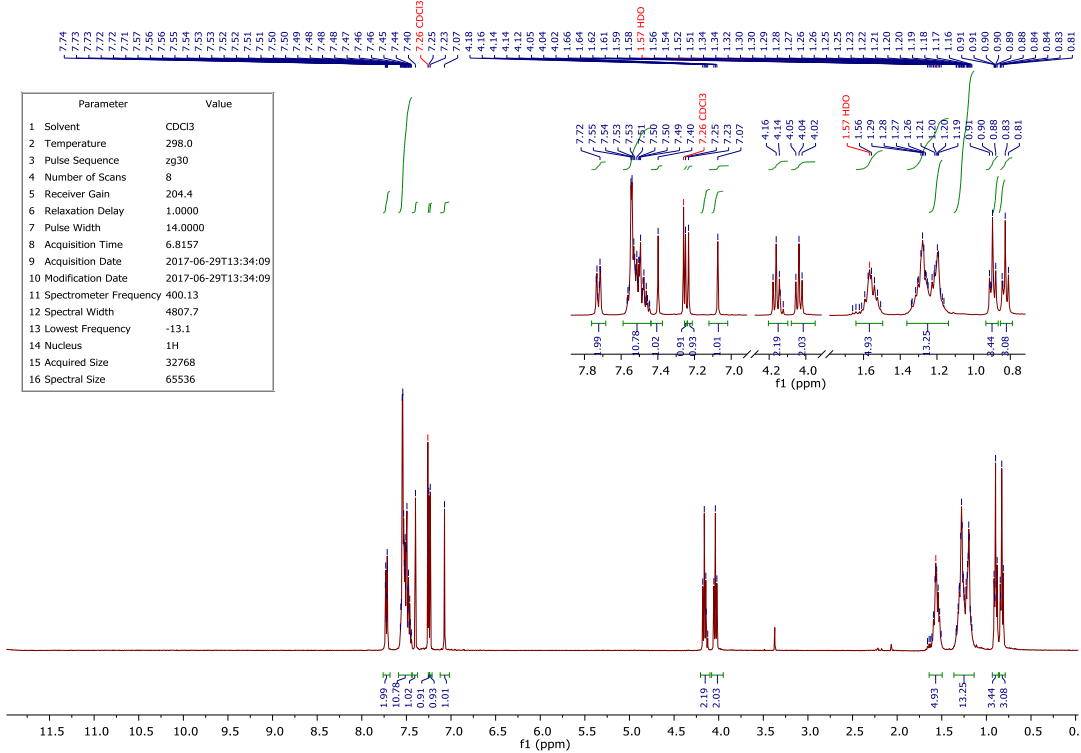
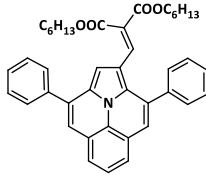
APPENDIX



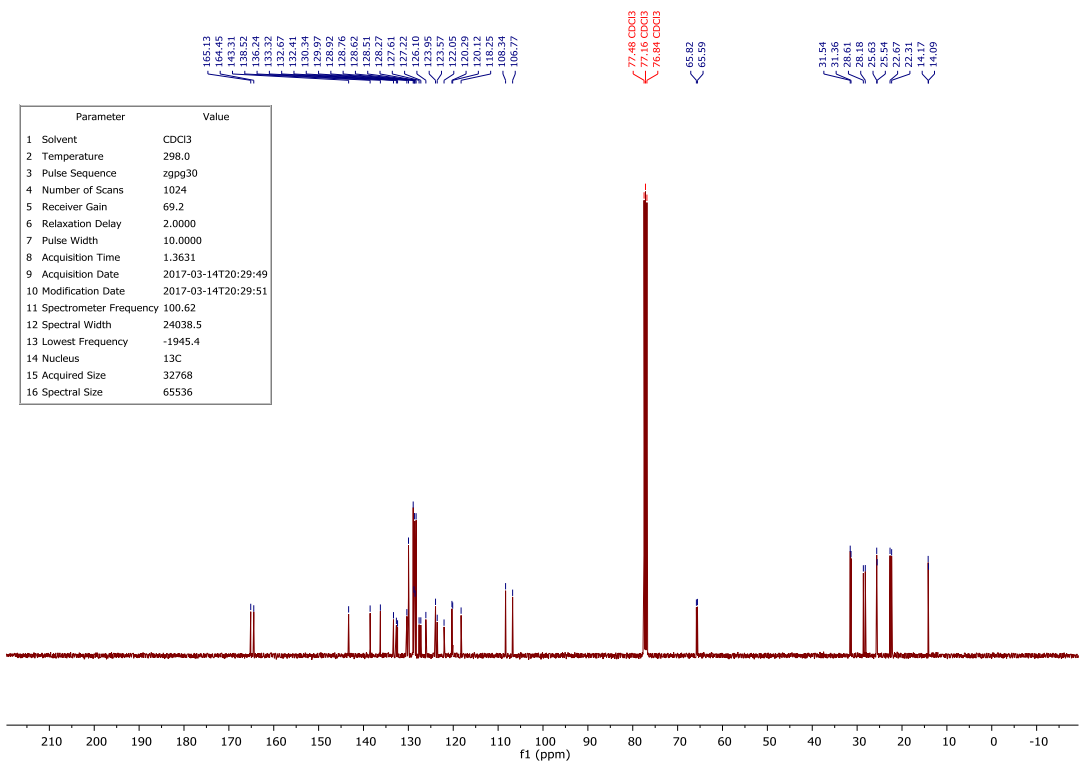
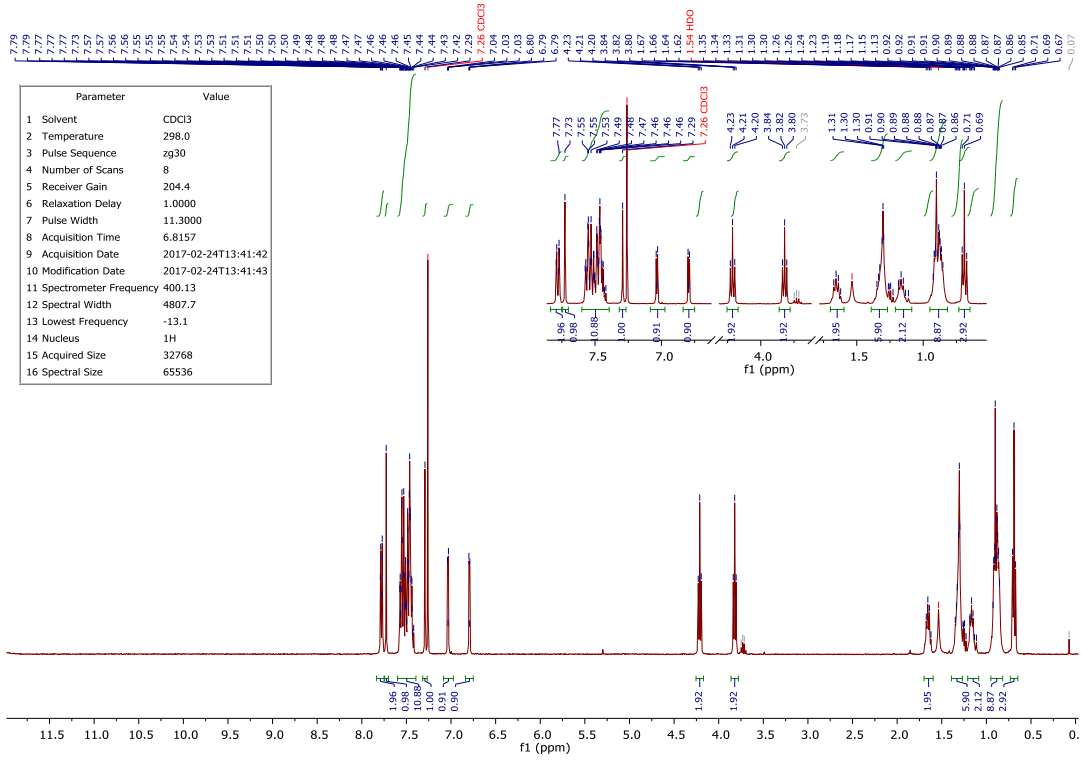
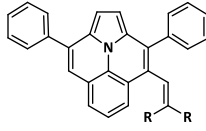
APPENDIX



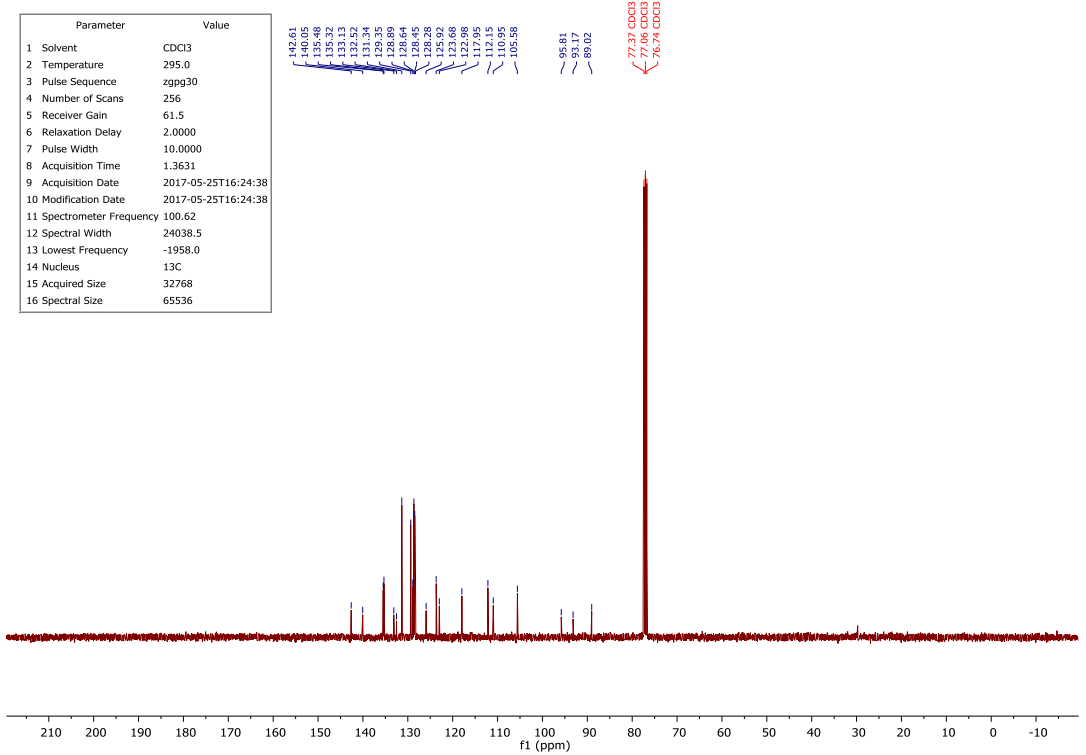
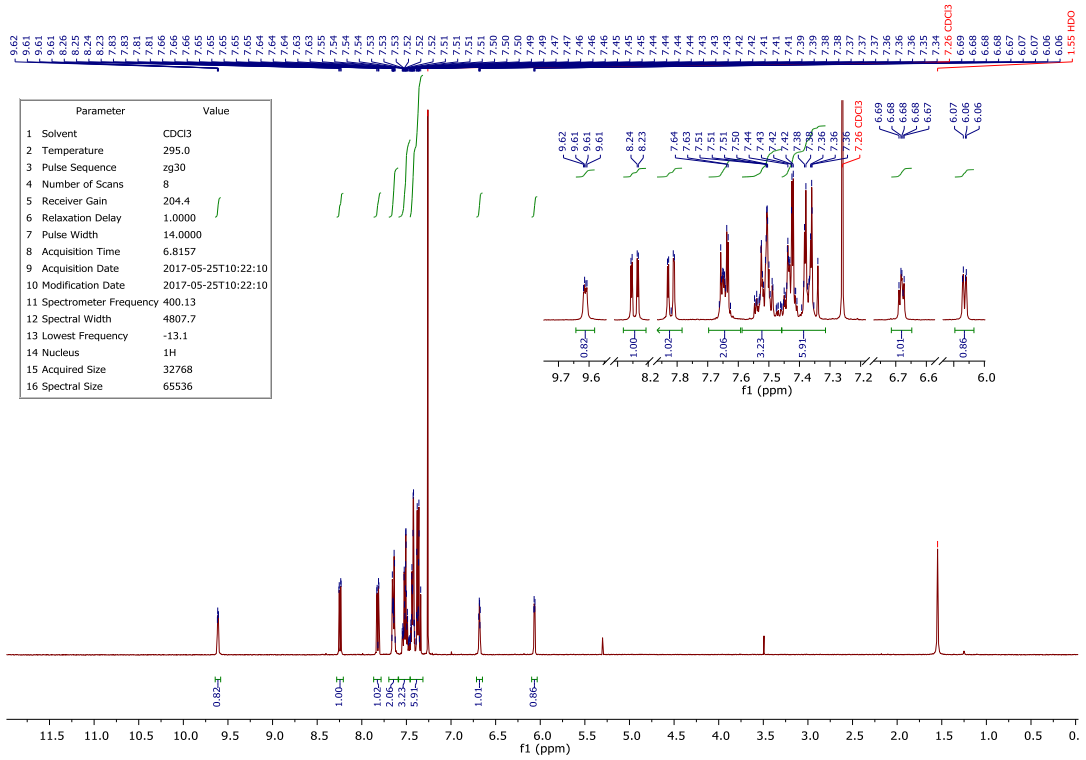
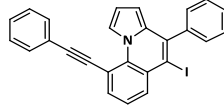
APPENDIX



APPENDIX



APPENDIX



APPENDIX

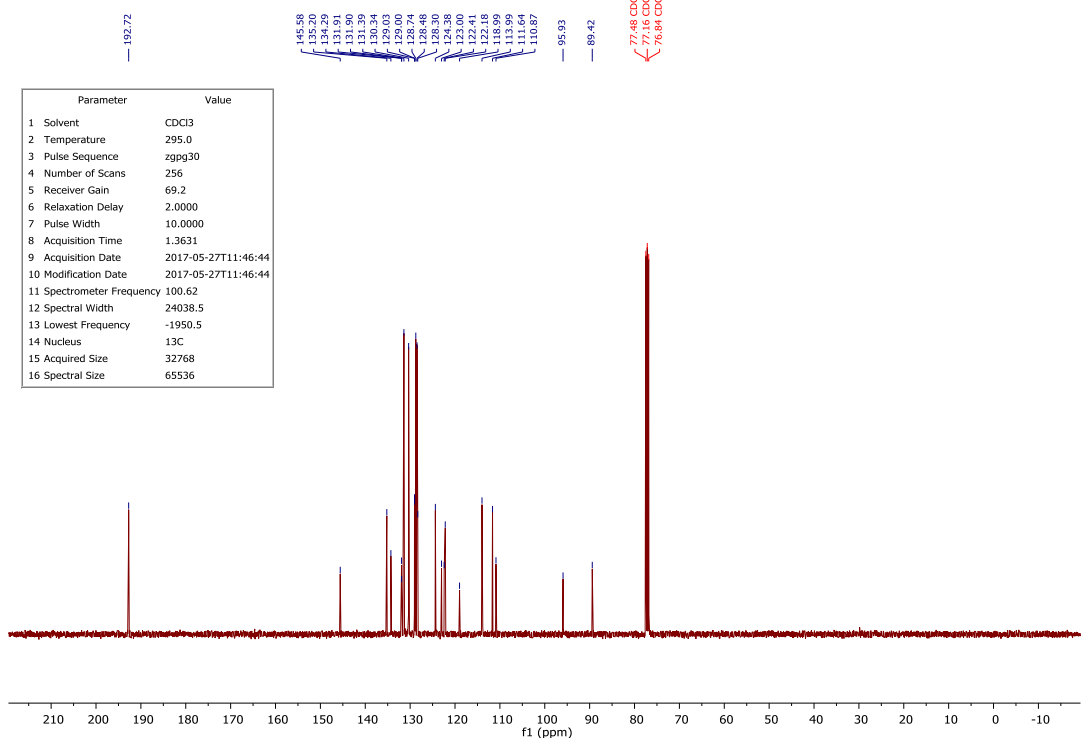
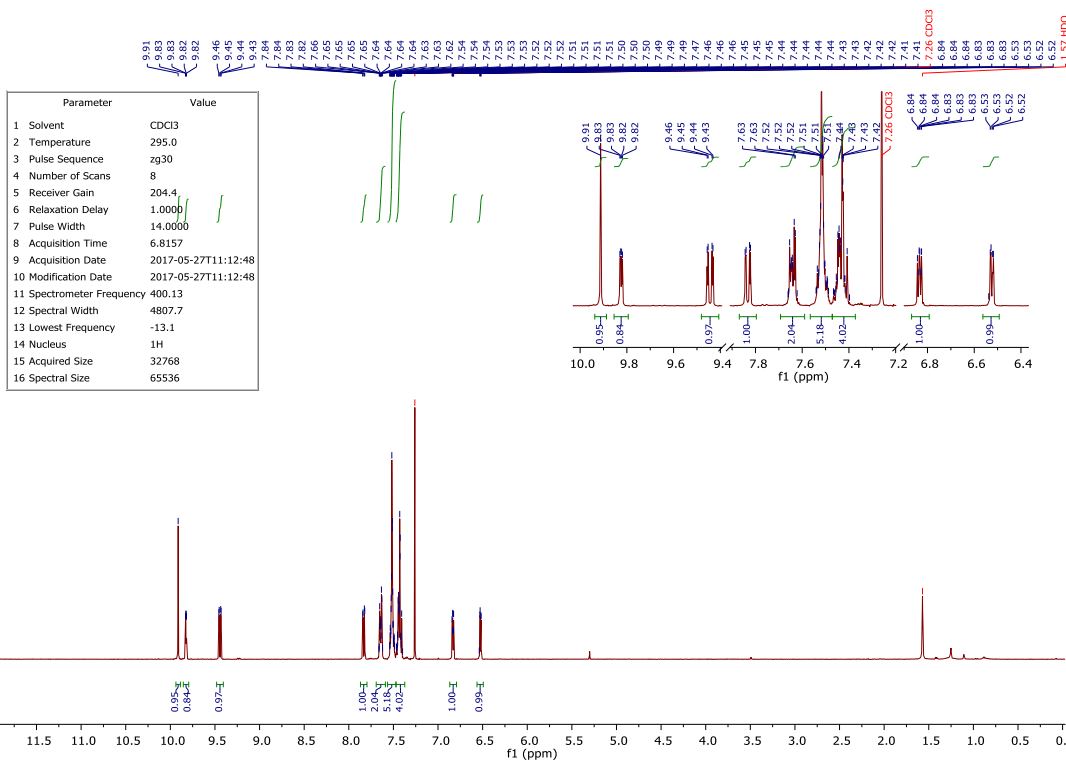
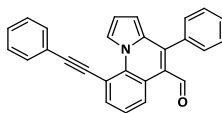


Table 13. Crystal structure and refinement for **5c** and **9**.

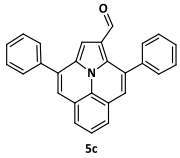
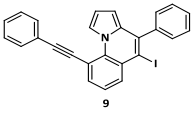
Compound		
Formula	C ₂₇ H ₁₇ NO	C ₂₆ H ₁₆ IN
Crystal system	Monoclinic	Triclinic
Space group	P2 ₁ /c	P-1
Temperature / K	130(2)	130(2)
Lattice constants / Å and °	a = 12.0507(5) b = 19.7960(9) c = 8.1453(3) α = 90 β = 104.2930 γ = 90	a = 7.2056(6) b = 8.9773(7) c = 16.0309(14) α = 75.931(2) β = 78.418(2) γ = 78.817(2)
Volume / Å ³	1882.96(14)	973.84(14)
Z	4	4
Dcalculated / g·cm ⁻³	1.31	1.6004
Radiation	Mo-Kα (λ = 0.71069 Å)	Mo-Kα (λ = 0.71069 Å)
Crystal dimensions / mm	0.12 × 0.07 × 0.025	0.20 × 0.04 × 0.02
θ range / °	2.698–30.675	2.37–30.84
Min. / max. h k l	-17 ≤ h ≤ 16 -27 ≤ k ≤ 27 -11 ≤ l ≤ 10	-10 ≤ h ≤ 10 -12 ≤ k ≤ 12 -22 ≤ l ≤ 22
Reflections, measured	45507	30191
Reflections, independent	5271	5650
Absorption coefficient / mm ⁻¹	0.079	1.655
Absorption correction	Multi-Scan	Multi-Scan
Refined parameters	262	253
R ₁ [I > 2σ(I)]	0.0463	0.0305
wR ₂ (all data)	0.0683	0.0348
Max. / min. Residual	0.323 and -0.30	1.0576 and -1.034
Density / e ⁻ /Å ³		

Table 14. Absorption and PL data for unsubstituted ullazine **5b** and the ullazine dyes **8a-d**.

Ullazine	λ _{abs} , nm			λ _{PL} , nm		
	Cyclohexane	THF	Acetonitrile	Cyclohexane	THF	Acetonitrile
5b	374, 391 ^[b]	374, 392	374, 389	478, 513 , 553	488 , 520 , 559	491, 521 , 560
8a	395	396	396	519	592	nd ^[b]
8b	446, 466	471	471	530 , 560	579	606
8c	416 , 439	419 , 439	420	474, 502	520	560
8d	386, 401	386, 404	386, 401	492, 529 , 570	500, 534 , 572	511, 540

[a] Bold corresponds to the highest intensity in a band. [b] not detected

6.4.3. Solar cell fabrication.

The etched FTO glass (Nippon Sheet Glass) was cleaned sequentially by sonication in a 2 % Hellmanex solution, acetone and ethanol, followed by a 15 min UV-ozone treatment. A 30 nm thick TiO₂ compact layer was deposited by spray pyrolysis at 450°C from a precursor solution of diluted titanium diisopropoxide bis(acetylacetonate) (TAA) solution (Sigma-Aldrich) in isopropanol. On the top of it, a 150 nm mesoporous TiO₂ layer was made by spin coating method using a commercially available TiO₂ paste (Dyesol 30NRD). The Substrates were sintered at 500°C for 30 min in air. Then, Li-doping of the mesoporous TiO₂ is done by spin coating a 0.03 M solution of LiTFSI (in acetonitrile) at 3000 rpm for 10 s, followed by sintering at 500°C for 20 min before use. The mixed perovskite precursor solution was prepared by dissolving PbI₂ (1.15 M), FAI (1.10 M), PbBr₂ (0.2 M), and MABr (0.2 M) in anhydrous solvent DMF: DMSO = 4 : 1 (volume ratio). The perovskite precursor solution was spin coated at 2000 rpm for 10 s, followed by 6000 rpm for 30 s. Trifluorotoluene (110 µl) was dropped on the spinning substrate at the 20 s in the second step.²⁸⁴ The films were annealed at 100°C for 90 min in the glove box. The hole-transporting material, consisting of 15 mM **8b** in tetrachloroethane, was spin-coated on the top of the perovskite layer with a spin speed of 4000 rpm.²⁸⁵ Finally, 80 nm of Au was deposited by thermal evaporation as the back electrode.

6.4.4. Photovoltaic characterization

The current-voltage curves were measured under AM 1.5 simulated light source connecting with a source meter (Keithley 2400). The light intensity was calibrated with an NREL certified KG5 filtered Si reference diode. *J-V* curves were obtained at a scan rate of 50 mV s⁻¹. The devices were measured by using a black mask with an active area of 0.16 cm².

REFERENCES

- (1) International Energy Agency (IEA) Electricity Information-2019: Overview. <https://webstore.iea.org/electricity-information-2019-overview>.
- (2) International Energy Agency (IEA) CO₂ emissions from fuel combustion 2018 Highlights <https://webstore.iea.org/co2-emissions-from-fuel-combustion-2018-highlights>.
- (3) Greenhouse Gas Concentrations <https://www.climatecentral.org/gallery/graphics/greenhouse-gas-concentrations>.
- (4) Lewis, N. S.; Nocera, D. G. Powering the Planet: Chemical Challenges in Solar Energy Utilization. *PNAS* **2006**, *103* (43), 15729–15735.
- (5) Lighting Tracking Clean Energy Progress <https://www.iea.org/tcep/buildings/lighting/>.
- (6) International Energy Agency (IEA) Energy Efficiency Indicators 2018 Highlights <https://webstore.iea.org/energy-efficiency-indicators-2018-highlights>.
- (7) Popovich, N. America's Light Bulb Revolution <https://www.nytimes.com/interactive/2019/03/08/climate/light-bulb-efficiency.html>.
- (8) The Nobel Prize in Chemistry 2000 <https://www.nobelprize.org/prizes/chemistry/2000/summary/>.
- (9) Liu, D.; Yang, J.; Kelly, T. L. Compact Layer Free Perovskite Solar Cells with 13.5% Efficiency. *J. Am. Chem. Soc.* **2014**, *136* (49), 17116–17122. <https://doi.org/10.1021/ja508758k>.
- (10) Zhou, X.; Bao, C.; Li, F.; Gao, H.; Yu, T.; Yang, J.; Zhu, W.; Zou, Z. Hole-Transport-Material-Free Perovskite Solar Cells Based on Nanoporous Gold Back Electrode. *RSC Adv.* **2015**, *5* (72), 58543–58548. <https://doi.org/10.1039/c5ra11720h>.
- (11) Zuo, C.; Bolink, H. J.; Han, H.; Huang, J.; Cahen, D.; Ding, L. Advances in Perovskite Solar Cells. *Adv. Sci.* **2016**, *3* (7), 1500324. <https://doi.org/10.1002/advs.201500324>.
- (12) Maniarasu, S.; Bhavani, T.; Manjunath, V.; Ramasamy, E.; Ramesh, M.; Veerappan, G. Recent Advancement in Metal Cathode and Hole-Conductor-Free Perovskite Solar Cells for Low-Cost and High Stability: A Route towards Commercialization. *Renew. Sustain. Energy Rev.* **2018**, *82* (Part 1), 845–857. <https://doi.org/10.1016/j.rser.2017.09.095>.
- (13) Pope, M.; Kallmann, H. P.; Magnante, P. Electroluminescence in Organic Crystals. *J. Chem. Phys.* **1963**, *38* (8), 2042–2043. <https://doi.org/10.1063/1.1733929>.

-
- (14) Tang, C. W.; VanSlyke, S. A. Organic Electroluminescent Diodes. *Appl. Phys. Lett.* **1987**, *51* (12), 913–915. <https://doi.org/10.1063/1.98799>.
- (15) Raay, V. Der; Cortes, R.; Jr, E. J.; Livingston, A. N. Light-Emitting Diodes Based on Conjugated Polymers. *Nature* **1990**, *347*, 539–541.
- (16) Forrest, S. R.; O'Brien, D. F. Excitonic Singlet-Triplet Ratio in a Semiconducting Organic Thin Film. *Phys. Rev. B - Condens. Matter Mater. Phys.* **1999**, *60* (20), 14422–14428. <https://doi.org/10.1103/PhysRevB.60.14422>.
- (17) Segal, M.; Baldo, A.; Holmes, J.; Forrest, R.; Soos, G. Excitonic Singlet-Triplet Ratios in Molecular and Polymeric Organic Materials. *Phys. Rev. B - Condens. Matter Mater. Phys.* **2003**, *68* (7), 1–14. <https://doi.org/10.1103/PhysRevB.68.075211>.
- (18) Smith, L. H.; Wasey, J. A. E.; Barnes, W. L. Light Outcoupling Efficiency of Top-Emitting Organic Light-Emitting Diodes. *Appl. Phys. Lett.* **2004**, *84* (16), 2986–2988. <https://doi.org/10.1063/1.1712036>.
- (19) Baldo, M. A.; O'Brien, D. F.; You, Y.; Shoustikov, A.; Sibley, S.; Thompson, M. E.; Forrest, S. R. Highly Efficient Phosphorescent Emission from Organic Electroluminescent Devices. *Nature* **1998**, *395* (6698), 151–154. <https://doi.org/10.1038/25954>.
- (20) Adachi, C.; Baldo, M. A.; Thompson, M. E.; Forrest, S. R. Nearly 100% Internal Phosphorescence Efficiency in an Organic Light Emitting Device. *J. Appl. Phys.* **2001**, *90* (10), 5048–5051. <https://doi.org/10.1063/1.1409582>.
- (21) Bizzarri, C.; Hundemer, F.; Busch, J.; Bräse, S. Triplet Emitters versus TADF Emitters in OLEDs : A Comparative Study. *Polyhedron* **2018**, *140*, 51–66. <https://doi.org/10.1016/j.poly.2017.11.032>.
- (22) Chou, P.; Chi, Y. Phosphorescent Dyes for Organic Light-Emitting Diodes. *Chem. - A Eur. J.* **2007**, *13* (2), 380–395. <https://doi.org/10.1002/chem.200601272>.
- (23) Zhang, Y.; Lee, J.; Forrest, S. R. Tenfold Increase in the Lifetime of Blue Phosphorescent Organic Light-Emitting Diodes. *Nat. Commun.* **2014**, *5*, 5008. <https://doi.org/10.1038/ncomms6008>.
- (24) Lee, J.; Jeong, C.; Batagoda, T.; Coburn, C.; Thompson, M. E.; Forrest, S. R. Hot Excited State Management for Long-Lived Blue Phosphorescent Organic Light-Emitting Diodes. *Nat. Commun.* **2017**, *8*, 15566. <https://doi.org/10.1038/ncomms15566>.
- (25) Schmidbauer, S.; Hohenleutner, A.; König, B. Chemical Degradation in Organic Light-Emitting Devices: Mechanisms and Implications for the Design of New Materials. *Adv. Mater.* **2013**, *25* (15), 2114–2129. <https://doi.org/10.1002/adma.201205022>.
- (26) Volz, D.; Wallesch, M.; Fléchon, C.; Danz, M.; Verma, A.; Navarro, J. M.; Zink, D. M.; Bräse, S.; Baumann, T. From Iridium and Platinum to Copper and Carbon: New Avenues for More Sustainability in Organic Light-Emitting Diodes. *Green Chem.* **2015**, *17* (4), 1988–2011. <https://doi.org/10.1039/c4gc02195a>.

-
- (27) Lewis, N.; Lipkin, D.; Magel, T. T.; Lewis, N.; Lipkin, D. Reversible Photochemical Processes in Rigid Media . By Gilbert A Study of the Phosphorescent. *J. Am. Chem. Soc.* **1941**, *920* (5), 3005–3018. <https://doi.org/10.1021/ja01856a043>.
- (28) Hatchard, C. G. Triplet-Singlet Emission in Fluid Solutions. **1961**, 1894–1904.
- (29) Yamanashi, B. S.; Hercules, D. M. Solution Luminescence of Anthraquinone , Naphthoquinone , and Some Derivatives at Room Temperature *. *Appl. Spectrosc.* **1971**, *25* (4), 457–460.
- (30) Sikorski, M.; Khmelinskii, I. V; Augustyniak, W.; Wilkinson, F. Triplet State Decay of Some Thioketones in Solution. *J. Chem. Soc. Faraday Trans.* **1996**, *92* (3), 3487–3490.
- (31) States, T.; Maciejewski, M. S. A. Radiationless Decay of Aromatic Thiones In Solution Selectively Excited to Their. *J. Phys. Chem.* **1988**, *92* (22), 2485–2489. <https://doi.org/10.1021/j100320a019>.
- (32) Berberan-Santos, M. N.; Garcia, J. M. M. Unusually Strong Delayed Fluorescence of C70. *J. Am. Chem. Soc.* **1996**, *118* (39), 9391–9394. <https://doi.org/10.1021/ja961782s>.
- (33) Jones, P. F.; Calloway, A. R. Temperature Effects On The Intramolecular Decay Of The Lowest Triplet State Of Benzophenone. *Chem. Phys. Lett.* **1971**, *10* (4), 438–443.
- (34) Blasse, G.; Copper, O.; Mcmillin, D. R.; Lafayette, W. On The Luminescence Of Bis (Triphenylphosphine) Phenanthroline Copper (I). *Chem. Phys. Lett.* **1980**, *70* (1), 4–6.
- (35) Yersin, H.; Czerwieniec, R.; Shafikov, M. Z.; Suleymanova, A. F. TADF Material Design : Photophysical Background and Case Studies Focusing on Cu I and Ag I Complexes. *ChemPhysChem* **2017**, *18* (24), 3508–3535. <https://doi.org/10.1002/cphc.201700872>.
- (36) Endo, A.; Ogasawara, M.; Takahashi, A.; Yokoyama, D.; Kato, Y.; Adachi, C. Thermally Activated Delayed Fluorescence from Sn4+-Porphyrin Complexes and Their Application to Organic Light Emitting Diodes - A Novel Mechanism for Electroluminescence. *Adv. Mater.* **2009**, *21* (47), 4802–4806. <https://doi.org/10.1002/adma.200900983>.
- (37) Endo, A.; Sato, K.; Yoshimura, K.; Kai, T.; Kawada, A.; Miyazaki, H.; Adachi, C. Efficient Up-Conversion of Triplet Excitons into a Singlet State and Its Application for Organic Light Emitting Diodes. *Appl. Phys. Lett.* **2011**, *98* (8), 2009–2012. <https://doi.org/10.1063/1.3558906>.
- (38) Uoyama, H.; Goushi, K.; Shizu, K.; Nomura, H.; Adachi, C. Highly Efficient Organic Light-Emitting Diodes from Delayed Fluorescence. *Nature* **2012**, *492* (7428), 234–238. <https://doi.org/10.1038/nature11687>.
- (39) Kwon, J. H. Highly Efficient Blue Thermally Activated Delayed Fluorescence Emitters Based on Symmetrical and Rigid Oxygen-Bridged Boron Acceptors. *Nat. Photonics* **2019**, *13*, 540–546. <https://doi.org/10.1038/s41566-019-0415-5>.

-
- (40) Wu, T.; Huang, M.; Lin, C.; Huang, P.; Chou, T.; Lin, H.; Liu, R.; Cheng, C. Diboron Compound-Based Organic Light-Emitting Diodes with High Efficiency and Reduced Efficiency Roll-Off. *Nat. Photonics* **2018**, *12*, 235–240. <https://doi.org/10.1038/s41566-018-0112-9>.
- (41) Zeng, W.; Lai, H.; Lee, W.; Jiao, M.; Shiu, Y.; Zhong, C.; Gong, S.; Zhou, T.; Xie, G.; Sarma, M.; et al. Achieving Nearly 30 % External Quantum Efficiency for Orange – Red Organic Light Emitting Diodes by Employing Thermally Activated Delayed Fluorescence Emitters Composed of 1, 8-Naphthalimide-Acridine Hybrids. *Adv. Mater.* **2018**, *30* (5), 1704961. <https://doi.org/10.1002/adma.201704961>.
- (42) Turro, N.; Ramamurthy, V.; C., S. J. *Modern Molecular Photochemistry of Organic Molecules*; Science, 2010.
- (43) Zhang, Q.; Li, J.; Shizu, K.; Huang, S.; Hirata, S.; Miyazaki, H.; Adachi, C. Design of Efficient Thermally Activated Delayed Fluorescence Materials for Pure Blue Organic Light Emitting Diodes. *J. Am. Chem. Soc.* **2012**, *134* (36), 14706–14709. <https://doi.org/10.1021/ja306538w>.
- (44) Milián-medina, B.; Gierschner, J. Computational Design of Low Singlet–Triplet Gap All-Organic Molecules for OLED Application. *Org. Electron.* **2012**, *13* (6), 985–991. <https://doi.org/10.1016/j.orgel.2012.02.010>.
- (45) Baba, M. Intersystem Crossing in the $n\pi^*$ and $\pi\pi^*$ States. *J. Phys. Chem. A* **2011**, *115* (34), 9514–9519. <https://doi.org/10.1021/jp111892y>.
- (46) Gibson, J.; Monkman, A. P.; Penfold, T. J. The Importance of Vibronic Coupling for Efficient Reverse Intersystem Crossing in Thermally Activated Delayed Fluorescence Molecules. *ChemPhysChem* **2016**, *17* (1), 2956–2961. <https://doi.org/10.1002/cphc.201600662>.
- (47) Etherington, M. K.; Gibson, J.; Higginbotham, H. F.; Penfold, T. J.; Monkman, A. P. Revealing the Spin–Vibronic Coupling Mechanism of Thermally Activated Delayed Fluorescenc. *Nat. Commun.* **2016**, *7*, 13680. <https://doi.org/10.1038/ncomms13680>.
- (48) Gibson, J.; Penfold, T. J. Nonadiabatic Coupling Reduces the Activation Energy in Thermally Activated Delayed Fluorescence. *Phys. Chem. Chem. Phys.* **2017**, *19* (12), 8428–8434. <https://doi.org/10.1039/c7cp00719a>.
- (49) Lyskov, I.; Marian, C. M. Climbing up the Ladder: Intermediate Triplet States Promote the Reverse Intersystem Crossing in the Efficient TADF Emitter ACRSA. *J. Phys. Chem. C* **2017**, *121* (39), 21145–21153. <https://doi.org/10.1021/acs.jpcc.7b06187>.
- (50) Cai, X.; Chen, D.; Gao, K.; Gan, L.; Yin, Q.; Qiao, Z.; Chen, Z.; Jiang, X.; Su, S.-J. “Trade-Off” Hidden in Condensed State Solvation: Multiradiative Channels Design for Highly Efficient Solution-Processed Purely Organic Electroluminescence at High Brightness. *Adv. Funct. Mater.* **2017**, *28* (7), 1704927. <https://doi.org/10.1002/adfm.201704927>.
- (51) Santos, P. L.; Ward, J. S.; Congrave, D. G.; Batsanov, A. S.; Eng, J.; Stacey, J. E.;

- Penfold, T. J.; Monkman, A. P.; Bryce, M. R. Triazatruxene: A Rigid Central Donor Unit for a D–A₃ Thermally Activated Delayed Fluorescence Material Exhibiting Sub-Microsecond Reverse Intersystem Crossing and Unity Quantum Yield via Multiple Singlet–Triplet State Pairs. *Adv. Sci.* **2018**, *5* (6), 1700989. <https://doi.org/10.1002/advs.201700989>.
- (52) Zhang, Q.; Li, B.; Huang, S.; Nomura, H.; Tanaka, H.; Adachi, C. Efficient Blue Organic Light-Emitting Diodes Employing Thermally Activated Delayed Fluorescence. *Nat. Photonics* **2014**, *8* (4), 326–332. <https://doi.org/10.1038/nphoton.2014.12>.
- (53) Geng, Y.; Aleo, A. D.; Inada, K.; Cui, L.; Kim, J. U.; Nakanotani, H.; Adachi, C. Donor–s–Acceptor Motifs: Thermally Activated Delayed Fluorescence Emitters with Dual Upconversion. *Angew. Chemie - Int. Ed.* **2017**, *129* (52), 16763–16767. <https://doi.org/10.1002/ange.201708876>.
- (54) Valchanov, G.; Ivanova, A.; Tadjer, A.; Chercka, D.; Baumgarten, M. Understanding the Fluorescence of TADF Light-Emitting Dyes. *J. Phys. Chem. A* **2016**, *120* (35), 6944–6955. <https://doi.org/10.1021/acs.jpca.6b06680>.
- (55) Hatakeyama, T.; Shiren, K.; Nakajima, K.; Nomura, S.; Nakatsuka, S.; Kinoshita, K.; Ni, J.; Ono, Y.; Ikuta, T. Ultrapure Blue Thermally Activated Delayed Fluorescence Molecules: Efficient HOMO–LUMO Separation by the Multiple Resonance Effect. *Adv. Mater.* **2016**, *28* (14), 2777–2781. <https://doi.org/10.1002/adma.201505491>.
- (56) Yuan, Y.; Tang, X.; Du, X.; Hu, Y.; Yu, Y.; Jiang, Z.; Liao, L.; Lee, S.-T. The Design of Fused Amine/Carbonyl System for Efficient Thermally Activated Delayed Fluorescence: Novel Multiple Resonance Core and Electron Acceptor. *Adv. Opt. Mater.* **2019**, *7* (7), 1801536. <https://doi.org/10.1002/adom.201801536>.
- (57) Oda, S.; Kawakami, B.; Kawasumi, R.; Okita, R.; Hatakeyama, T. Multiple Resonance Effect-Induced Sky-Blue Thermally Activated Delayed Fluorescence with a Narrow Emission Band. *Org. Lett.* **2019**, *21* (23), 9311–9314. <https://doi.org/10.1021/acs.orglett.9b03342>.
- (58) Mamada, M.; Inada, K.; Komino, T.; Potscavage, W. J.; Nakanotani, H.; Adachi, C. Highly Efficient Thermally Activated Delayed Fluorescence from an Excited-State Intramolecular Proton Transfer System. *ACS Cent. Sci.* **2017**, *3* (7), 769–777. <https://doi.org/10.1021/acscentsci.7b00183>.
- (59) Kitamoto, Y.; Suzuki, T.; Miyata, Y.; Kita, H.; Funaki, K.; Oi, S. The First Synthesis and X-Ray Crystallographic Analysis of an Oxygen-Bridged Planarized Triphenylborane. *Chem. Commun.* **2016**, *52* (44), 7098–7101. <https://doi.org/10.1039/c6cc02440h>.
- (60) Hirai, H.; Nakajima, K.; Nakatsuka, S.; Shiren, K.; Ni, J.; Nomura, S.; Ikuta, T.; Hatakeyama, T. One-Step Borylation of 1,3-Diaryloxybenzenes Towards Efficient Materials for Organic Light-Emitting Diodes. *Angewandte. Angew. Chemie - Int. Ed.* **2015**, *54* (46), 13581–13585. <https://doi.org/10.1002/anie.201506335>.

-
- (61) Yang, Z.; Mao, Z.; Xie, Z.; Zhang, Y.; Liu, S.; Zhao, J.; Xu, J.; Chi, Z.; Aldred, M. P. Recent Advances in Organic Thermally Activated Delayed Fluorescence Materials. *Chem. Soc. Rev.* **2017**, *46* (3), 915–1016. <https://doi.org/10.1039/C6CS00368K>.
- (62) Im, Y.; Kim, M.; Cho, Y. J.; Seo, J.-A.; Yook, K. S.; Lee, J. Y. Molecular Design Strategy of Organic Thermally Activated Delayed Fluorescence Emitters. *Chem. Mater.* **2017**, *29* (5), 1946–1963. <https://doi.org/10.1021/acs.chemmater.6b05324>.
- (63) Wong, M. Y.; Zysman-Colman, E. Purely Organic Thermally Activated Delayed Fluorescence Materials for Organic Light-Emitting Diodes. *Adv. Mater.* **2017**, *29* (22), 1605444. <https://doi.org/10.1002/adma.201605444>.
- (64) Dias, F. B.; Bourdakos, K. N.; Jankus, V.; Moss, K. C.; Kamtekar, T.; Bhalla, V.; Santos, J.; Bryce, M. R.; Monkman, A. P. Triplet Harvesting with 100% Efficiency by Way of Thermally Activated Delayed Fluorescence in Charge Transfer OLED Emitters. *Adv. Mater.* **2013**, *25* (27), 3707–3714. <https://doi.org/10.1002/adma.201300753>.
- (65) Etherington, M. K.; Franchello, F.; Gibson, J.; Northey, T.; Santos, J.; Ward, J. S.; Higginbotham, H. F.; Data, P.; Kurowska, A.; Lays, P.; et al. Regio- and Conformational Isomerization Critical to Design of Efficient Thermally-Activated Delayed Fluorescence Emitters. *Nat. Commun.* **2017**, *8*, 14987. <https://doi.org/10.1038/ncomms14987>.
- (66) Cai, X.; Gao, B.; Li, X.; Cao, Y.; Su, S. Singlet – Triplet Splitting Energy Management via Acceptor Substitution : Complation Molecular Design for Deep- Blue Thermally Activated Delayed Fluorescence Emitters and Organic Light-Emitting Diodes Application. *Adv. Funct. Mater.* **2016**, *26* (44), 8042–8052. <https://doi.org/10.1002/adfm.201603520>.
- (67) Seo, J.; Im, Y.; Han, S. H.; Lee, C. W.; Lee, J. Y. Unconventional Molecular Design Approach of High-Efficiency Deep Blue Thermally Activated Delayed Fluorescent Emitters Using Indolocarbazole as an Acceptor. *ACS Appl. Mater. Interfaces* **2017**, *9* (43), 37864–37872. <https://doi.org/10.1021/acsami.7b09351>.
- (68) He, Z.; Cai, X.; Wang, Z.; Li, Y.; Xu, Z.; Liu, K.; Chen, D.; Su, S.-J. Sky-Blue Thermally Activated Delayed Fluorescence Material Employing a Diphenylethyne Acceptor for Organic Light-Emitting Diodes. *J. Mater. Chem. C* **2018**, *6* (1), 36–42. <https://doi.org/10.1039/c7tc02763j>.
- (69) Chan, C.; Cui, L.; Kim, J. U.; Nakanotani, H.; Adachi, C. Rational Molecular Design for Deep-Blue Thermally Activated Delayed Fluorescence Emitters. *Adv. Funct. Mater.* **2018**, *28* (11), 1706023. <https://doi.org/10.1002/adfm.201706023>.
- (70) Chen, R.; Tang, Y.; Wan, Y.; Chen, T.; Zheng, C.; Qi, Y.; Cheng, Y.; Huang, W. Promoting Singlet/Triplet Exciton Transformation in Organic Optoelectronic Molecules: Role of Excited State Transition Configuration. *Sci. Rep.* **2017**, *7*, 6225. <https://doi.org/10.1038/s41598-017-05339-4>.
- (71) Chen, C.; Huang, R.; Batsanov, A. S.; Pander, P.; Hsu, Y.; Chi, Z.; Dias, F. B.; Bryce, M. R. Intramolecular Charge Transfer Controls Switching Between Room

- Temperature Phosphorescence and Thermally Activated Delayed Fluorescence. *Angew. Chemie - Int. Ed.* **2018**, *130* (50), 16645–16649. <https://doi.org/10.1002/ange.201809945>.
- (72) Zhan, L.; Chen, Z.; Gong, S.; Xiang, Y.; Ni, F.; Zeng, X.; Xie, G.; Yang, C. A Simple Organic Molecule Realizing Simultaneous TADF, RTP, AIE, and Mechanoluminescence: Understanding the Mechanism Behind the Multifunctional Emitter. *Angew. Chemie - Int. Ed.* **2019**, *58* (49), 17651–17655. <https://doi.org/10.1002/ange.201910719>.
- (73) Takeda, Y.; Kaihara, T.; Okazaki, M.; Higginbotham, H.; Data, P.; Tohnai, N.; Minakata, S. Conformationally-Flexible and Moderately Electron-Donating Units-Installed D–A–D Triad Enabling Multicolor-Changing Mechanochromic Luminescence, TADF and Room-Temperature Phosphorescence. *Chem. Commun.* **2018**, *54* (50), 6847–6850. <https://doi.org/10.1039/c8cc02365d>.
- (74) Wang, K.; Zheng, C.; Liu, W.; Liang, K.; Shi, Y.; Tao, S.; Lee, C.-S.; Ou, X.-M.; Zhang, X.-H. Avoiding Energy Loss on TADF Emitters : Controlling the Dual Conformations of D – A Structure Molecules Based on the Pseudoplanar Segments. *Adv. Mater.* **2017**, *29* (47), 1701476. <https://doi.org/10.1002/adma.201701476>.
- (75) Tanaka, H.; Shizu, K.; Nakanotani, H.; Adachi, C. Dual Intramolecular Charge-Transfer Fluorescence Derived from a Phenothiazine-Triphenyltriazine Derivative. *J. Phys. Chem. C* **2014**, *118* (29), 15985–15994. <https://doi.org/10.1021/jp501017f>.
- (76) Noda, H.; Nakanotani, H.; Adachi, C. Excited State Engineering for Efficient Reverse Intersystem Crossing. *Sci. Adv.* **2018**, *4* (6), 6910.
- (77) Shizu, K.; Noda, H.; Tanaka, H.; Taneda, M.; Uejima, M.; Sato, T.; Tanaka, K.; Kaji, H.; Adachi, C. Highly Efficient Blue Electroluminescence Using Delayed-Fluorescence Emitters with Large Overlap Density between Luminescent and Ground States. *J. Phys. Chem. C* **2015**, *119* (47), 26283–26289. <https://doi.org/10.1021/acs.jpcc.5b07798>.
- (78) Cui, L. S.; Nomura, H.; Geng, Y.; Kim, J. U. k.; Nakanotani, H.; Adachi, C. Controlling Singlet–Triplet Energy Splitting for Deep-Blue Thermally Activated Delayed Fluorescence Emitters. *Angew. Chemie - Int. Ed.* **2017**, *56* (6), 1571–1575. <https://doi.org/10.1002/anie.201609459>.
- (79) Baikie, T.; Fang, Y.; Kadro, J. M.; Schreyer, M.; Wei, F.; Mhaisalkar, S. G.; Graetzel, M.; White, T. J. Synthesis and Crystal Chemistry of the Hybrid Perovskite (CH₃NH₃)PbI₃ for Solid-State Sensitised Solar Cell Applications. *J. Mater. Chem. A Chem.* **2013**, *1* (18), 5628–5641. <https://doi.org/10.1039/c3ta10518k>.
- (80) Jeon, N. J.; Noh, J. H.; Kim, Y. C.; Yang, W. S.; Ryu, S.; Seok, S. Il. Solvent Engineering for High-Performance Inorganic–Organic Hybrid Perovskite Solar Cells. *Nat. Mater.* **2014**, *13*, 897–903. <https://doi.org/10.1038/NMAT4014>.
- (81) Eperon, G. E.; Stranks, S. D.; Menelaou, C.; Johnston, M. B.; Herz, L. M.; Snaith,

- H. J. Formamidinium Lead Trihalide: A Broadly Tunable Perovskite for Efficient Planar Heterojunction Solar Cells. *Energy Environ. Sci.* **2014**, *7* (3), 982–988. <https://doi.org/10.1039/c3ee43822h>.
- (82) Noh, J. H.; Im, S. H.; Heo, J. H.; Mandal, T. N.; Seok, S. Il. Chemical Management for Colorful, Efficient, and Stable Inorganic–Organic Hybrid Nanostructured Solar Cells. *Nano Lett.* **2013**, *13* (4), 1764–1769. <https://doi.org/10.1021/nl400349b>.
- (83) Seo, J.; Noh, J. H.; Seok, S. Il. Rational Strategies for Efficient Perovskite Solar Cells. *Acc. Chem. Res.* **2016**, *49* (3), 562–572. <https://doi.org/10.1021/acs.accounts.5b00444>.
- (84) Giorgi, G.; Yamashita, K. Organic–Inorganic Halide Perovskites: An Ambipolar Class of Materials with Enhanced Photovoltaic Performances. *J. Mater. Chem. A* **2015**, *3* (15), 8981–8991. <https://doi.org/10.1039/c4ta05046k>.
- (85) Sum, T. C.; Mathews, N. Advancements in Perovskite Solar Cells : Photophysics behind the Photovoltaics. *Energy Environ. Sci.* **2014**, *7* (8), 2518–2534. <https://doi.org/10.1039/c4ee00673a>.
- (86) Innocenzo, V. D.; Grancini, G.; Alcocer, M. J. P.; Ram, A.; Kandada, S.; Stranks, S. D.; Lee, M. M.; Lanzani, G.; Snaith, H. J.; Petrozza, A. Excitons versus Free Charges in Organo-Lead Tri-Halide Perovskites. *Nat. co* **2014**, *5*, 3586. <https://doi.org/10.1038/ncomms4586>.
- (87) Dong, Q.; Fang, Y.; Shao, Y.; Mulligan, P.; Qiu, J.; Cao, L.; Huang, J. Electron-Hole Diffusion Lengths >175 Mm in Solution-Grown CH₃NH₃PbI₃ Single Crystals. *Science*. **2015**, *347* (6225), 967–970.
- (88) Kojima, A.; Teshima, K.; Shirai, Y.; Miyasaka, T. Organometal Halide Perovskites as Visible-Light Sensitizers for Photovoltaic. *J. Am. Chem. Soc.* **2009**, *131* (17), 6050–6051.
- (89) Im, J.; Lee, C.; Lee, J.; Park, S.; Park, N. 6.5% Efficient Perovskite Quantum-Dot-Sensitized Solar Cell. *Nanoscale* **2011**, *3* (10), 4088–4093. <https://doi.org/10.1039/c1nr10867k>.
- (90) Kim, H.; Lee, C.; Im, J.; Lee, K.; Moehl, T.; Marchioro, A.; Moon, S.; Humphry-baker, R.; Yum, J.; Moser, J. E.; et al. Lead Iodide Perovskite Sensitized All-Solid-State Submicron Thin Film Mesoscopic Solar Cell with Efficiency Exceeding 9%. *Sci. Rep.* **2012**, *2*, 591. <https://doi.org/10.1038/srep00591>.
- (91) Lee, M. M.; Teuscher, J.; Miyasaka, T.; Murakami, T.; Snaith, H. J. Efficient Hybrid Solar Cells Based on Meso-Superstructured Organometal Halide Perovskites. *Science*. **2012**, *338* (6107), 643–648.
- (92) Zhou, Y.; Li, X.; Lin, H. To Be Higher and Stronger — Metal Oxide Electron Transport Materials for Perovskite Solar Cells. *Small* **2019**, 1902579. <https://doi.org/10.1002/sml.201902579>.
- (93) Said, A. A.; Xie, J.; Zhang, Q. Recent Progress in Organic Electron Transport Materials in Inverted Perovskite Solar Cells. *Small* **2019**, *15* (27), 1900854. <https://doi.org/10.1002/sml.201900854>.

-
- (94) Rakstys, K.; Igci, C.; Nazeeruddin, M. K. Efficiency vs. Stability: Dopant-Free Hole Transporting Materials towards Stabilized Perovskite Solar Cells. *Chem. Sci.* **2019**, *10* (28), 6748–6769. <https://doi.org/10.1039/c9sc01184f>.
- (95) Urieta-Mora, J.; García-Benito, I.; Molina-Ontoria, A.; Martín, N. Hole Transporting Materials for Perovskite Solar Cells: A Chemical Approach. *Chem. Soc. Rev.* **2018**, *47* (23), 8541–8571. <https://doi.org/10.1039/C8CS00262B>.
- (96) Gangala, S.; Misra, R. Spiro-Linked Organic Small Molecules as Hole-Transport Materials for Perovskite Solar Cells. *J. Mater. Chem. A* **2018**, *6* (39), 18750–18765. <https://doi.org/10.1039/c8ta08503j>.
- (97) Rodríguez-Seco, C.; Cabau, L.; Vidal-Ferran, A.; Palomares, E. Advances in the Synthesis of Small Molecules as Hole Transport Materials for Lead Halide Perovskite Solar Cells. *Acc. Chem. Res.* **2018**, *51* (4), 869–880. <https://doi.org/10.1021/acs.accounts.7b00597>.
- (98) Li, Y.; Ji, L.; Liu, R.; Zhang, C.; Mak, C. H.; Zou, X.; Shen, H.-H.; Leu, S.-Y.; Hsu, H.-Y. A Review on Morphology Engineering for Highly Efficient and Stable Hybrid Perovskite Solar Cells. *J. Mater. Chem. A* **2018**, *6* (27), 12842–12875. <https://doi.org/10.1039/c8ta04120b>.
- (99) Li, B.; Binks, D.; Cao, G.; Tian, J. Engineering Halide Perovskite Crystals through Precursor Chemistry. *Small* **2019**, *15* (47), 1903613. <https://doi.org/10.1002/smll.201903613>.
- (100) Grancini, G.; Nazeeruddin, M. K. Dimensional Tailoring of Hybrid Perovskites for Photovoltaics. *Nat. Rev. Mater.* **2018**, *4*, 4–22. <https://doi.org/10.1038/s41578-018-0065-0>.
- (101) Dubey, A.; Adhikari, N.; Mabrouk, S.; Wu, F.; Chen, K.; Yang, S.; Qiao, Q. A Strategic Review on Processing Routes towards Highly Efficient Perovskite Solar Cells. *J. Mater. Chem. A* **2018**, *6* (6), 2406–2431. <https://doi.org/10.1039/c7ta08277k>.
- (102) Cho, A.-N.; Park, N. Impact of Interfacial Layers in Perovskite Solar Cells. *ChemSusChem* **2017**, *10* (19), 3687–3704. <https://doi.org/10.1002/cssc.201701095>.
- (103) Zhao, P.; Kim, B. J.; Jung, H. S. Passivation in Perovskite Solar Cells : A Review. *Mater. Today Energy* **2018**, *7*, 267–286. <https://doi.org/10.1016/j.mtener.2018.01.004>.
- (104) Best Research-Cell Efficiency Chart <https://www.nrel.gov/pv/cell-efficiency.html>.
- (105) Agarwala, P.; Kabra, D. A Review on Triphenylamine (TPA) Based Organic Hole Transport Materials (HTMs) for Dye Sensitized Solar Cells (DSSCs) and Perovskite Solar Cells (PSCs): Evolution and Molecular Engineering. *J. Mater. Chem. A* **2017**, *5* (4), 1348–1373. <https://doi.org/10.1039/c6ta08449d>.
- (106) Naito, K.; Miura, A. Molecular Design for Nonpolymieric Organic Dye Glasses with Thermal Stability: Relations between Thermodynamic Parameters and Amorphous Properties. *J. Phys. Chem.* **1993**, *97* (23), 6240–6248. <https://doi.org/10.1021/j100125a025>.

-
- (107) Naito, K. Quantitative Relations between Glass Transition Temperatures and Thermodynamic Parameters for Various Materials: Molecular Design for Nonpolymeric Organic Dye Glasses with Thermal Stability. *Chem. Mater.* **1994**, *6* (12), 2343–2350. <https://doi.org/10.1021/cm00048a021>.
- (108) Paek, S.; Zimmermann, I.; Gao, P.; Gratia, P.; Rakstys, K.; Grancini, G.; Nazeeruddin, M. K.; Rub, M. A.; Kosa, S. A.; Alamry, K. A.; et al. Donor–p–Donor Type Hole Transporting Materials: Marked p-Bridge Effects on Optoelectronic Properties, Solid-State Structure, and Perovskite Solar Cell Efficiency. *Chem. Sci.* **2016**, *7* (9), 6068–6075. <https://doi.org/10.1039/c6sc01478j>.
- (109) Shirota, Y.; Kuwabara, Y.; Okuda, D.; Okuda, R. Starburst Molecules Based on X-Electron Systems as Materials for Organic Electroluminescent Devices. *J. Lumin.* **1997**, *72–74*, 985–991.
- (110) Schmidt-Mende, L.; Fechtenkötter, A.; Mullen, K.; Moons, E.; Friend, R. H.; MacKenzie, J. D. Self-Organized Discotic Liquid Crystals for High-Efficiency Organic Photovoltaics. *Science*. **2001**, *293* (5532), 1119–1123.
- (111) Petrus, M. L.; Schutt, K.; Sirtl, M. T.; Hutter, E. M.; Closs, A. C.; Ball, J. M.; Bijleveld, J. C.; Petrozza, A.; Bein, T.; Dingemans, T. J.; et al. New Generation Hole Transporting Materials for Perovskite Solar Cells : Amide-Based Small-Molecules with Nonconjugated Backbones. *Adv. Energy Mater.* **2018**, *8* (32), 1801605. <https://doi.org/10.1002/aenm.201801605>.
- (112) Zhang, F.; Wang, Z.; Zhu, H.; Pellet, N.; Luo, J.; Yi, C.; Mohammed, S.; Bi, D.; Grätzel, M. Over 20 % PCE Perovskite Solar Cells with Superior Stability Achieved by Novel and Low-Cost Hole-Transporting Materials. *Nano Energy* **2017**, *41*, 469–475. <https://doi.org/10.1016/j.nanoen.2017.09.035>.
- (113) Cho, I.; Jeon, N. J.; Kwon, O. K.; Kim, D. W.; Jung, E. H.; Noh, J. H.; Seo, J.; Seok, S. Il; Park, S. Y. Indolo[3,2-b]Indole-Based Crystalline Hole- Transporting Material for Highly Efficient Perovskite Solar Cells. *Chem. Sci.* **2017**, *8* (1), 734–741. <https://doi.org/10.1039/c6sc02832b>.
- (114) Rakstys, K.; Paek, S.; Gao, P.; Gratia, P.; Marszalek, T.; Grancini, G.; Cho, K. T.; Genevicius, K.; Jankauskas, V.; Pisula, W.; et al. Molecular Engineering of Face-on Oriented Dopant-Free Hole Transporting Material for Perovskite Solar Cells with 19% PCE. *J. Mater. Chem. A* **2017**, *5* (17), 7811–7815. <https://doi.org/10.1039/c7ta01718a>.
- (115) Xu, P.; Liu, P.; Li, Y.; Xu, B.; Kloo, L.; Sun, L.; Hua, Y. D – A – D-Typed Hole Transport Materials for Efficient Perovskite Solar Cells: Tuning Photovoltaic Properties via the Acceptor Group. *ACS Appl. Mater. Interfaces* **2018**, *10* (23), 19697–19703. <https://doi.org/10.1021/acsami.8b04003>.
- (116) Ge, Q.; Shao, J.; Ding, J.; Deng, L.; Zhou, W.; Chen, Y.; Ma, Y.; Wan, L.; Yao, J.; Hu, J.; et al. A Two-Dimensional Hole-Transporting Material for High-Performance Perovskite Solar Cells with 20% Average Efficiency. *Angew. Chemie - Int. Ed.* **2018**, *57* (34), 10959–10965. <https://doi.org/10.1002/anie.201806392>.

- (117) Xu, B.; Zhang, J.; Hua, Y.; Liu, P.; Wang, L.; Ruan, C.; Li, Y.; Boschloo, G.; Johansson, E. M. J.; Kloo, L.; et al. Tailor-Making Low-Cost Spiro[Fluorene-9,9'-Xanthene]-Based 3D Oligomers for Perovskite Solar Cells. *Chem* **2017**, *2* (5), 676–687. <https://doi.org/10.1016/j.chempr.2017.03.011>.
- (118) Saliba, M.; Orlandi, S.; Matsui, T.; Aghazada, S.; Cavazzini, M.; Correa-Baena, J.-P.; Gao, P.; Scopelliti, R.; Mosconi, E.; Dahmen, K.-H.; et al. A Molecularly Engineered Hole-Transporting Material for Efficient Perovskite Solar Cells. *Nat. Energy* **2016**, *1* (2), 15017. <https://doi.org/10.1038/nenergy.2015.17>.
- (119) Jeon, N. J.; Na, H.; Jung, E. H.; Yang, T. Y.; Lee, Y. G.; Kim, G.; Shin, H. W.; Il Seok, S.; Lee, J.; Seo, J. A Fluorene-Terminated Hole-Transporting Material for Highly Efficient and Stable Perovskite Solar Cells. *Nat. Energy* **2018**, *3* (8), 682–689. <https://doi.org/10.1038/s41560-018-0200-6>.
- (120) Saragi, T. P. I.; Spehr, T.; Siebert, A.; Fuhrmann-lieker, T.; Salbeck, J. Spiro Compounds for Organic Optoelectronics. *Chem. Rev.* **2007**, *107* (4), 1011–1065. <https://doi.org/10.1021/cr0501341>.
- (121) Hawash, Z.; Ono, L. K.; Qi, Y. Recent Advances in Spiro-MeOTAD Hole Transport Material and Its Applications in Organic–Inorganic Halide Perovskite Solar Cells. *Adv. Mater. Interfaces* **2018**, *5* (1), 1–22. <https://doi.org/10.1002/admi.201700623>.
- (122) Li, H.; Fu, K.; Boix, P. P.; Wong, L. H.; Hagfeldt, A.; Grätzel, M.; Mhaisalkar, S. G.; Grimsdale, A. C. Hole-Transporting Small Molecules Based on Thiophene Cores for High Efficiency Perovskite Solar Cells. *ChemSusChem* **2014**, *7* (12), 3420–3425. <https://doi.org/10.1002/cssc.201402587>.
- (123) Sturm, E.; Kiesele, H. Elektrochemische Oxidation von Acridanen. *Chem. Ber.* **1978**, *111* (1), 227–239.
- (124) Tritschler, W.; Sturtn, E.; Kiesele, H. Synthese Und Konformation von Spiroacridanen. *Chem. Ber.* **1984**, *117* (8), 2703–2713.
- (125) Ooishi, M.; Seino, M.; Imachi, R.; Ishida, T.; Nogami, T. Convenient Synthesis and Host–Guest Compounds of 9,9'(10H,10'H)-Spirobiacridines. *Tetrahedron Lett.* **2002**, *43* (32), 5521–5524.
- (126) Wang, W.; Wan, H.; Du, G.; Dai, B.; He, L. Synthesis of Benzo[b]Fluoranthenes and Spiroacridines from Fluorene-Derived Alkenes and N-Arylimines via a Tandem Reaction with Benzyne. *Org. Lett.* **2019**, *21* (10), 3496–3500. <https://doi.org/10.1021/acs.orglett.9b00659>.
- (127) Wei, Y.; Tang, L.; Zhong, C.; Xie, X.; Sun, P.; Sun, C.; Zhang, H.; Zheng, X.; Wang, X.; Xie, L. Photooxygenations and Self-Sensitizations of Naphthylamines: Efficient Access to Iminoquinones. *J. Chem.* **2018**, *2018*, 9180671. <https://doi.org/https://doi.org/10.1155/2018/9180671>.
- (128) Xie, L.; Liu, F.; Tang, C.; Hou, X.; Hua, Y.; Fan, Q.-L.; Huang, W. Unexpected One-Pot Method to Building Blocks for Blue-Light-Emitting Materials. *Org. Lett.* **2006**, *8* (13), 2787–2790. <https://doi.org/10.1021/olo60871z>.
- (129) Liu, F.; Xie, L.; Tang, C.; Liang, J.; Chen, Q.; Peng, B.; Wei, W.; Cao, Y.; Huang, W.

- Facile Synthesis of Spirocyclic Aromatic Hydrocarbon Derivatives Based on *o*-Halobiaryl Route and Domino Reaction for Deep-Blue Organic Semiconductors. *Org. Lett.* **2009**, *11* (17), 3850–3853.
- (130) Ito, A.; Hata, K.; Kawamoto, K.; Hirao, Y.; Tanaka, K.; Shiro, M.; Furukawa, K.; Kato, T. Para-Phenylene-Bridged Spirobi(Triarylamine) Dimer with Four Perpendicularly Linked Redox-Active *p* Systems. *Chem. - A Eur. J.* **2010**, *16* (35), 10866–10878. <https://doi.org/10.1002/chem.201000848>.
- (131) Liu, X.; Tang, X.; Zhao, Y.; Zhao, D.; Fan, J.; Liao, L. Spirobi[Dibenzo[b,e][1,4]Azasiline]: A Novel Platform for Host Materials in Highly Efficient Organic Light-Emitting Diodes. *J. Mater. Chem. C* **2018**, *5* (6), 1023–1030. <https://doi.org/10.1039/c7tc05031c>.
- (132) Wasserman, D.; Jones, R. E.; Robinson, S. A.; Garber, J. D. A New Synthesis of 5,10-Dihydrophenazasilines. *J. Org. Chem.* **1965**, *30* (9), 3248–3250. <https://doi.org/10.1021/j001020a534>.
- (133) Gilman, H.; Zuech, E. A. Some 2,5,8-Trimethyl-5,10-Dihydrophenazasiline Derivatives. *J. Org. Chem.* **1962**, *27* (8), 2897–2899. <https://doi.org/10.1021/j001055a041>.
- (134) Corey, J. Y.; Trankler, K. A.; Braddock-Wilking, J.; Rath, N. P. Reactions of (Et₂NCH₂CH₂NEt₂)₃ H₂SiCl₂ with Selected Diorganometallic Reagents of Magnesium and Lithium. *Organometallics* **2010**, *29* (21), 5708–5713. <https://doi.org/10.1021/om100544f>.
- (135) Woo, S.; Kim, Y.; Kim, Y.; Kwon, S.; Kim, J. A Spiro-Silafluorene–Phenazasiline Donor-Based Efficient Blue Thermally Activated Delayed Fluorescence Emitter and Its Host-Dependent Device Characteristics. *J. Mater. Chem. C* **2019**, *7* (14), 4191–4198. <https://doi.org/10.1039/c9tc00193j>.
- (136) Gilman, H.; Zuech, E. A. Group IV-B Element Analogs of 5, 10-Dihydroacridine. *J. Am. Chem. Soc.* **1960**, *82* (10), 2522–2524. <https://doi.org/10.1021/ja01495a030>.
- (137) Kupchik, E. J.; Perciaccante, V. A. Some New 5,10-Dihydrophenazastannine Derivatives. The Novel Conversion of 5,10,10-Trimethyl-5,10-Dihydrophenazastannines into Their Phosphorus(III) Analogs. *J. Organomet. Chem.* **1967**, *10* (1), 181–187.
- (138) Stanoppi, M.; Lorbach, A. Boron-Based Donor-Spiro-Acceptor Compounds Exhibiting Thermally Activated Delayed Fluorescence (TADF). *Dalt. Trans.* **2018**, *47* (31), 10394–10398. <https://doi.org/10.1039/c8dt01255e>.
- (139) Crossley, D. L.; Cid, J.; Curless, L. D.; Turner, M. L.; Ingleson, M. J. Facile Arylation of Four-Coordinate Boron Halides by Borenium Cation Mediated Boro-Desilylation and -Destannylation. *Organometallics* **2015**, *34* (24), 5767–5774. <https://doi.org/10.1021/acs.organomet.5b00857>.
- (140) Bell, B. M.; Clark, T. P.; De Vries, T. S.; Lai, Y.; Laitar, D. S.; Gallagher, T. J.; Jeon, J. H.; Kearns, K. L.; McIntire, T.; Mukhopadhyay, S.; et al. Boron-Based TADF Emitters with Improved OLED Device Efficiency Roll-off and Long Lifetime. *Dye.*

- Pigment.* **2017**, *141*, 83–92. <https://doi.org/10.1016/j.dyepig.2017.01.055>.
- (141) Tao, Y.; Yuan, K.; Chen, T.; Xu, P.; Li, H.; Chen, R.; Zheng, C.; Zhang, L.; Huang, W. Thermally Activated Delayed Fluorescence Materials towards the Breakthrough of Organoelectronics. *Adv. Mater.* **2014**, *26* (47), 7931–7958. <https://doi.org/10.1002/adma.201402532>.
- (142) Bui, T.-T.; Goubard, F.; Ibrahim-Ouali, M.; Gigmès, D.; Dumur, F. Recent Advances on Organic Blue Thermally Activated Delayed Fluorescence (TADF) Emitters for Organic Light-Emitting Diodes (OLEDs). *Beilstein J. Org. Chem.* **2018**, *14*, 282–308. <https://doi.org/10.3762/bjoc.14.18>.
- (143) Kim, J. H.; Yun, J. H.; Lee, J. Y. Recent Progress of Highly Efficient Red and Near-Infrared Thermally Activated Delayed Fluorescent Emitters. *Adv. Opt. Mater.* **2018**, *6* (18), 1800255. <https://doi.org/10.1002/adom.201800255>.
- (144) Méhes, G.; Nomura, H.; Zhang, Q.; Nakagawa, T.; Adachi, C. Enhanced Electroluminescence Efficiency in a Spiro-Acridine Derivative through Thermally Activated Delayed Fluorescence. *Angew. Chemie - Int. Ed.* **2012**, *51* (45), 11311–11315. <https://doi.org/10.1002/anie.201206289>.
- (145) Nasu, K.; Nakagawa, T.; Nomura, H.; Lin, C.; Cheng, C.; Tseng, M.; Yasuda, T.; Adachi, C. A Highly Luminescent Spiro-Anthracenone-Based Organic Light-Emitting Diode Exhibiting Thermally Activated Delayed Fluorescence. *Chem. Commun.* **2013**, *49* (88), 10385–10387. <https://doi.org/10.1039/c3cc44179b>.
- (146) Wang, Y.; Wu, S.; Yuan, Y.; Li, S.; Fung, M.; Liao, L.; Jiang, Z. Donor – σ – Acceptor Molecules for Green Thermally Activated Delayed Fluorescence by Spatially Approaching Spiro Conformation. *Org. Lett.* **2017**, *19* (12), 3155–3158. <https://doi.org/10.1021/acs.orglett.7b01281>.
- (147) Ohkuma, H.; Nakagawa, T.; Shizu, K.; Yasuda, T.; Adachi, C. Thermally Activated Delayed Fluorescence from a Spiro-Diazafluorene Derivative. *Chem. Lett.* **2014**, *43* (7), 1017–1019. <https://doi.org/10.1246/cl.140360>.
- (148) Wang, Y.; Liu, W.; Qu, Z.; Tan, H.; Liu, Y.; Xie, G. Dyes and Pigments Spirotriphenylamine Based Star-Shaped D-A Molecules Meeting AIE Chromophore for Both Efficient Solution-Processed Doped and Nondoped Blue Organic Light-Emitting Diodes. *Dye. Pigment.* **2017**, *143*, 173–182. <https://doi.org/10.1016/j.dyepig.2017.04.030>.
- (149) Lu, J.; Zheng, Y.; Zhang, J. Tuning the Color of Thermally Activated Delayed Fluorescent Properties for Spiro-Acridine Derivatives by Structural Modification of the Acceptor Fragment: A DFT Study. *RSC Adv.* **2015**, *5* (24), 18588–18592. <https://doi.org/10.1039/c4ra15155k>.
- (150) Numata, M.; Yasuda, T.; Adachi, C. High Efficiency Pure Blue Thermally Activated Delayed Fluorescence Molecules Having 10H-Phenoxaborin and Acridan Units. *Chem. Commun.* **2015**, *51* (46), 9443–9446. <https://doi.org/10.1039/C5CC00307E>.
- (151) Lin, T.-A.; Chatterjee, T.; Tsai, W.-L.; Lee, W.-K.; Wu, M.-J.; Jiao, M.; Pan, K.-C.; Yi, C.-L.; Chung, C.-L.; Wong, K.-T.; et al. Sky-Blue Organic Light Emitting Diode

- with 37% External Quantum Efficiency Using Thermally Activated Delayed Fluorescence from Spiroacridine-Triazine Hybrid. *Adv. Mater.* **2016**, *28* (32), 6976–6983. <https://doi.org/10.1002/adma.201601675>.
- (152) Gan, L.; Xu, Z.; Wang, Z.; Li, B.; Li, W.; Cai, X.; Liu, K.; Liang, Q.; Su, S.-J. Utilizing a Spiro TADF Moiety as a Functional Electron Donor in TADF Molecular Design toward Efficient “Multichannel” Reverse Intersystem Crossing. *Adv. Funct. Mater.* **2019**, *29* (20), 1808088. <https://doi.org/10.1002/adfm.201808088>.
- (153) Li, W.; Li, B.; Cai, X.; Gan, L.; Xu, Z.; Li, W.; Liu, K.; Chen, D.; Su, S. Tri-Spiral Donor for High Efficiency and Versatile Blue Thermally Activated Delayed Fluorescence Materials. *Angew. Chemie - Int. Ed.* **2019**, *58* (33), 11301–11305. <https://doi.org/10.1002/anie.201904272>.
- (154) Sun, J. W.; Baek, J. Y.; Kim, K. H.; Moon, C. K.; Lee, J. H.; Kwon, S. K.; Kim, Y. H.; Kim, J. J. Thermally Activated Delayed Fluorescence from Azasiline Based Intramolecular Charge-Transfer Emitter (DTPDDA) and a Highly Efficient Blue Light Emitting Diode. *Chem. Mater.* **2015**, *27* (19), 6675–6681. <https://doi.org/10.1021/acs.chemmater.5b02515>.
- (155) Lien, Y.; Lin, T.; Yang, C.; Chiang, Y.; Chang, C.; Liu, S.; Chen, Y.; Lee, G.; Chou, P.; Lu, C.; et al. First N - Boronated Emitters Displaying Highly Efficient Thermally Activated Delayed Fluorescence and High-Performance OLEDs. *ACS Appl. Mater. Interfaces* **2017**, *9* (32), 27090–27101. <https://doi.org/10.1021/acsami.7b08258>.
- (156) Lee, J.; Aizawa, N.; Numata, M.; Adachi, C.; Yasuda, T. Versatile Molecular Functionalization for Inhibiting Concentration Quenching of Thermally Activated Delayed Fluorescence. *Adv. Mater.* **2017**, *29* (4), 1604856. <https://doi.org/10.1002/adma.201604856>.
- (157) Wada, Y.; Kubo, S.; Kaji, H. Adamantyl Substitution Strategy for Realizing Solution-Processable Thermally Stable Deep-Blue Thermally Activated Delayed Fluorescence Materials. *Adv. Mater.* **2018**, *30* (8), 1705641. <https://doi.org/10.1002/adma.201705641>.
- (158) Yu, Y.; Tang, X.; Ge, H.; Yuan, Y.; Jiang, Z.; Liao, L. Fluorenone-Based Thermally Activated Delayed Fluorescence Materials for Orange-Red Emission. *Org. Electron.* **2019**, *73*, 240–246. <https://doi.org/10.1016/j.orgel.2019.06.008>.
- (159) Liu, M.; Komatsu, R.; Cai, X.; Hotta, K.; Sato, S.; Liu, K.; Chen, D.; Kato, Y.; Sasabe, H.; Ohisa, S.; et al. Horizontally Orientated Sticklike Emitters: Enhancement of Intrinsic Out-Coupling Factor and Electroluminescence Performance. *Chem. Mater.* **2017**, *29* (20), 8630–8636. <https://doi.org/10.1021/acs.chemmater.7b02403>.
- (160) Lee, J.; Aizawa, N.; Yasuda, T. Isobenzofuranone- and Chromone-Based Blue Delayed Fluorescence Emitters with Low Efficiency Roll-Off in Organic Light-Emitting Diodes. *Chem. Mater.* **2017**, *29* (18), 8012–8020. <https://doi.org/10.1021/acs.chemmater.7b03371>.
- (161) Ganesan, P.; Chen, D.; Liao, J.; Li, W.; Lai, Y.; Luo, D.; Chang, C.; Ko, C.; Hung, W.; Liu, S.; et al. Isomeric Spiro-[Acridine-9,90-Fluorene]-2,6- Dipyridylpyrimidine

- Based TADF Emitters: Insights into Photophysical Behaviors and OLED Performances. *J. Mater. Chem. A* **2018**, *6* (37), 10088–10100. <https://doi.org/10.1039/c8tc03645d>.
- (162) Woo, S.; Kim, Y.; Kwon, S.; Kim, Y.; Kim, J. Phenazasiline / Spiroacridine Donor Combined with Methyl- Substituted Linkers for Efficient Deep Blue Thermally Activated Delayed Fluorescence Emitters. *ACS Appl. Mater. Interfaces* **2019**, *11* (7), 7199–7207. <https://doi.org/10.1021/acsami.8b20009>.
- (163) Ganesan, P.; Ranganathan, R.; Chi, Y.; Liu, X. K.; Lee, C. S.; Liu, S. H.; Lee, G. H.; Lin, T. C.; Chen, Y. T.; Chou, P. T. Functional Pyrimidine-Based Thermally Activated Delay Fluorescence Emitters: Photophysics, Mechanochromism, and Fabrication of Organic Light-Emitting Diodes. *Chem. - A Eur. J.* **2017**, *23* (12), 2858–2866. <https://doi.org/10.1002/chem.201604883>.
- (164) Lee, S. Y.; Adachi, C.; Yasuda, T. High-Efficiency Blue Organic Light-Emitting Diodes Based on Thermally Activated Delayed Fluorescence from Phenoxaphosphine and Phenoxathiin Derivatives. *Adv. Mater.* **2016**, *28* (23), 4626–4631. <https://doi.org/10.1002/adma.201506391>.
- (165) Zeng, X.; Pan, K.; Lee, W.; Gong, S.; Ni, F.; Xiao, X.; Zeng, W.; Xiang, Y.; Zhan, L.; Zhang, Y.; et al. High-Efficiency Pure Blue Thermally Activated Delayed Fluorescence Emitters with a Preferentially Horizontal Emitting Dipole Orientation via a Spiro-Linked Double D–A. *J. Mater. Chem. C* **2019**, *7* (35), 10851–10859. <https://doi.org/10.1039/c9tc03582f>.
- (166) Li, M.; Hsu, C.; Shen, P.; Cheng, H.; Chi, Y.; Chen, P.; Guo, T.-F. Novel Spiro-Based Hole Transporting Materials for Efficient Perovskite Solar Cells. *Chem. Commun.* **2015**, *51* (85), 15518–15521. <https://doi.org/10.1039/c5cc04405g>.
- (167) Wang, Y.-K.; Yuan, Z.-C.; Shi, G.-Z.; Li, Y.-X.; Li, Q.; Hui, F.; Sun, B.-Q.; Jiang, Z.-Q.; Liao, L.-S. Dopant-Free Spiro-Triphenylamine/Fluorene as Hole-Transporting Material for Perovskite Solar Cells with Enhanced Efficiency and Stability. *Adv. Funct. Mater.* **2016**, *26* (9), 1375–1381. <https://doi.org/10.1002/adfm.201504245>.
- (168) Zhu, X.; Ma, X.; Wang, Y.; Li, Y.; Gao, C.; Wang, Z.; Jiang, Z.; Liao, L. Hole-Transporting Materials Incorporating Carbazole into Spiro-Core for Highly Efficient Perovskite Solar Cells. *Adv. Funct. Mater.* **2019**, *29* (5), 1807094. <https://doi.org/10.1002/adfm.201807094>.
- (169) Wang, Y.; Zhu, Z.; Chueh, C.; Jen, A. K.; Chi, Y. Spiro-Phenylpyrazole-9,9 '-Thioxanthene Analogues as Hole-Transporting Materials for Efficient Planar Perovskite Solar Cells. *Adv. Energy Mater.* **2017**, *7* (19), 1700823. <https://doi.org/10.1002/aenm.201700823>.
- (170) Kaji, H.; Suzuki, H.; Fukushima, T.; Shizu, K.; Suzuki, K.; Kubo, S.; Komino, T.; Oiwa, H.; Suzuki, F.; Wakamiya, A.; et al. Purely Organic Electroluminescent Material Realizing 100% Conversion from Electricity to Light. *Nat. Commun.* **2015**, *6*, 8476. <https://doi.org/10.1038/ncomms9476>.
- (171) Zhang, Q.; Tsang, D.; Kuwabara, H.; Hatae, Y.; Li, B.; Takahashi, T.; Lee, S. Y.;

- Yasuda, T.; Adachi, C. Nearly 100% Internal Quantum Efficiency in Undoped Electroluminescent Devices Employing Pure Organic Emitters. *Adv. Mater.* **2015**, *27* (12), 2096–2100. <https://doi.org/10.1002/adma.201405474>.
- (172) Rajamalli, P.; Senthilkumar, N.; Huang, P. Y.; Ren-Wu, C. C.; Lin, H. W.; Cheng, C. H. New Molecular Design Concurrently Providing Superior Pure Blue, Thermally Activated Delayed Fluorescence and Optical Out-Coupling Efficiencies. *J. Am. Chem. Soc.* **2017**, *139* (32), 10948–10951. <https://doi.org/10.1021/jacs.7b03848>.
- (173) Byeon, S. Y.; Kim, J.; Lee, D. R.; Han, S. H.; Forrest, S. R.; Lee, J. Y. Nearly 100 % Horizontal Dipole Orientation and Upconversion Efficiency in Blue Thermally Activated Delayed Fluorescent Emitters. *Adv. Opt. Mater.* **2018**, *6* (15), 1701340. <https://doi.org/10.1002/adom.201701340>.
- (174) Kondakov, D. Y. Characterization of Triplet-Triplet Annihilation in Organic Light-Emitting Diodes Based on Anthracene Derivatives. *J. Appl. Phys.* **2007**, *102*, 114504. <https://doi.org/10.1063/1.2818362>.
- (175) Hu, J.; Pu, Y.; Satoh, F.; Kawata, S.; Katagiri, H.; Sasabe, H.; Kido, J. Bisanthracene-Based Donor – Acceptor-Type Light-Emitting Dopants : Highly Efficient Deep-Blue Emission in Organic Light-Emitting Devices. *Adv. Funct. Mater.* **2014**, *24* (14), 2064–2071. <https://doi.org/10.1002/adfm.201302907>.
- (176) Ma, Y.; Zhang, H.; Shen, J.; Che, C. Electroluminescence from Triplet Metal—Ligand Charge-Transfer Excited State of Transition Metal Complexes. *Synth. Met.* **1998**, *94* (3), 245–248. [https://doi.org/10.1016/S0379-6779\(97\)04166-0](https://doi.org/10.1016/S0379-6779(97)04166-0).
- (177) Köhler, A.; Wilson, J. S.; Friend, R. H. Fluorescence and Phosphorescence in Organic Materials. *Adv. Mater.* **2002**, *14* (10), 701–707. [https://doi.org/10.1002/1521-4095\(20020517\)14:10<701::AID-ADMA701>3.0.CO;2-4](https://doi.org/10.1002/1521-4095(20020517)14:10<701::AID-ADMA701>3.0.CO;2-4).
- (178) Beljonne, D.; Shuai, Z.; Pourtois, G.; Bredas, J. L. Spin-Orbit Coupling and Intersystem Crossing in Conjugated Polymers: A Configuration Interaction Description. *J. Phys. Chem. A* **2001**, *105* (15), 3899–3907. <https://doi.org/10.1021/jp010187w>.
- (179) Dos Santos, P. L.; Ward, J. S.; Bryce, M. R.; Monkman, A. P. Using Guest-Host Interactions to Optimize the Efficiency of TADF OLEDs. *J. Phys. Chem. Lett.* **2016**, *7* (17), 3341–3346. <https://doi.org/10.1021/acs.jpcclett.6b01542>.
- (180) Cho, Y. J.; Jeon, S. K.; Chin, B. D.; Yu, E.; Lee, J. Y. The Design of Dual Emitting Cores for Green Thermally Activated Delayed Fluorescent Materials. *Angew. Chemie - Int. Ed.* **2015**, *54* (17), 5201–5204. <https://doi.org/10.1002/anie.201412107>.
- (181) Kim, M.; Jeon, S. K.; Hwang, S. H.; Lee, S. S.; Yu, E.; Lee, J. Y. Correlation of Molecular Structure with Photophysical Properties and Device Performances of Thermally Activated Delayed Fluorescent Emitters. *J. Phys. Chem. C* **2016**, *120* (5), 2485–2493. <https://doi.org/10.1021/acs.jpcc.5b09114>.
- (182) Ohisa, S. Horizontally Orientated Sticklike Emitters: Enhancement of Intrinsic Out-Coupling Factor and Electroluminescence Performance. **2017**, 8630–8636.

- <https://doi.org/10.1021/acs.chemmater.7b02403>.
- (183) Han, C.; Zhao, Y.; Xu, H.; Chen, J.; Deng, Z.; Ma, D.; Li, Q.; Yan, P. A Simple Phosphine-Oxide Host with a Multi-Insulating Structure: High Triplet Energy Level for Efficient Blue Electrophosphorescence. *Chem. - A Eur. J.* **2011**, *17* (21), 5800–5803. <https://doi.org/10.1002/chem.201100254>.
- (184) Noda, H.; Kabe, R.; Adachi, C. Blue Thermally Activated Delayed Fluorescence Molecule Having Acridane and Cyanobenzene Units. *Chem. Lett.* **2016**, *45* (12), 1463–1466. <https://doi.org/10.1246/cl.160814>.
- (185) Tanaka, T.; Tasaki, T.; Aoyama, Y. Acridinylresorcinol as a Self-Complementary Building Block of Robust Hydrogen-Bonded 2D Nets with Coordinative Saturation. Preservation of Crystal Structures upon Guest Alteration, Guest Removal, and Host Modification. *J. Am. Chem. Soc.* **2002**, *124* (42), 12453–12462. <https://doi.org/10.1021/jao26704l>.
- (186) Ghoneim, N.; Suppan, P. Solvation of TICT* States in Solvent Mixtures. *Pure Appl. Chem.* **1993**, *65* (8), 1739–1743.
- (187) Ryoo, C. H.; Cho, I.; Han, J.; Yang, J.; Kwon, J. E.; Kim, S.; Jeong, H.; Lee, C.; Park, S. Y. Structure–Property Correlation in Luminescent Indolo[3,2- b]Indole (IDID) Derivatives: Unraveling the Mechanism of High Efficiency Thermally Activated Delayed Fluorescence (TADF). *ACS Appl. Mater. Interfaces* **2017**, *9* (47), 41413–41420. <https://doi.org/10.1021/acsami.7b13158>.
- (188) Mayr, C.; Lee, S. Y.; Schmidt, T. D.; Yasuda, T.; Adachi, C.; Brütting, W. Efficiency Enhancement of Organic Light-Emitting Diodes Incorporating a Highly Oriented Thermally Activated Delayed Fluorescence Emitter. *Adv. Funct. Mater.* **2014**, *24* (33), 5232–5239. <https://doi.org/10.1002/adfm.201400495>.
- (189) Goushi, K.; Yoshida, K.; Sato, K.; Adachi, C. Organic Light-Emitting Diodes Employing Efficient Reverse Intersystem Crossing for Triplet-to-Singlet State Conversion. *Nat. Photonics* **2012**, *6* (4), 253–258. <https://doi.org/10.1038/nphoton.2012.31>.
- (190) Leo, K. Signs of Stability. *Nat. Nanotechnol.* **2015**, *10* (7), 574–575. <https://doi.org/10.1038/nnano.2015.139>.
- (191) Zhu, K.; Miyasaka, T.; Kim, J. Y.; Mora-Seró, I. Trend of Perovskite Solar Cells: Dig Deeper to Build Higher. *J. Phys. Chem. Lett.* **2015**, *6* (12), 2315–2317. <https://doi.org/10.1021/acs.jpcllett.5b01033>.
- (192) Park, N. G.; Grätzel, M.; Miyasaka, T.; Zhu, K.; Emery, K. Towards Stable and Commercially Available Perovskite Solar Cells. *Nat. Energy* **2016**, *1* (11), 1–8. <https://doi.org/10.1038/nenergy.2016.152>.
- (193) Wang, D.; Wright, M.; Elumalai, N. K.; Uddin, A. Solar Energy Materials & Solar Cells Stability of Perovskite Solar Cells. *Sol. Energy Mater. Sol. Cells* **2016**, *147*, 255–275. <https://doi.org/10.1016/j.solmat.2015.12.025>.
- (194) Berhe, T. A.; Su, W. N.; Chen, C. H.; Pan, C. J.; Cheng, J. H.; Chen, H. M.; Tsai, M. C.; Chen, L. Y.; Dubale, A. A.; Hwang, B. J. Organometal Halide Perovskite Solar

- Cells: Degradation and Stability. *Energy Environ. Sci.* **2016**, *9* (2), 323–356. <https://doi.org/10.1039/c5ee02733k>.
- (195) Niu, G.; Guo, X.; Wang, L. Review of Recent Progress in Chemical Stability of Perovskite Solar Cells. *J. Mater. Chem. A* **2015**, *3* (17), 8970–8980. <https://doi.org/10.1039/c4ta04994b>.
- (196) Saliba, M.; Matsui, T.; Seo, J.-Y.; Domanski, K.; Correa-Baena, J.-P.; Nazeeruddin, M. K.; Zakeeruddin, S. M.; Tress, W.; Abate, A.; Hagfeldt, A.; et al. Cesium-Containing Triple Cation Perovskite Solar Cells: Improved Stability, Reproducibility and High Efficiency. *Energy Environ. Sci.* **2016**, *9* (6), 1989–1997. <https://doi.org/10.1039/c5ee03874j>.
- (197) Jeon, N. J.; Noh, J. H.; Yang, W. S.; Kim, Y. C.; Ryu, S.; Seo, J.; Seok, S. II. Compositional Engineering of Perovskite Materials for High-Performance Solar Cells. *Nature* **2014**, *517* (1), 476–480. <https://doi.org/10.1038/nature14133>.
- (198) Jodlowski, A. D.; Roldán-Carmona, C.; Grancini, G.; Salado, M.; Ralaiarisoa, M.; Ahmad, S.; Koch, N.; Camacho, L.; De Miguel, G.; Nazeeruddin, M. K. Large Guanidinium Cation Mixed with Methylammonium in Lead Iodide Perovskites for 19% Efficient Solar Cells. *Nat. Energy* **2017**, *2* (12), 972–979. <https://doi.org/10.1038/s41560-017-0054-3>.
- (199) Saliba, M.; Matsui, T.; Domanski, K.; Seo, J.-Y.; Amita Ummadisingu; Zakeeruddin, S. M.; Correa-Baena, J.-P.; Tress, W.; Abate, A.; Hagfeldt, A.; et al. Incorporation of Rubidium Cations into Perovskite Solar Cells Improves Photovoltaic Performance. *Science* **2016**, *354* (6309), 206–209. <https://doi.org/10.1126/science.aah5557>.
- (200) Salado, M.; Idigoras, J.; Calio, L.; Kazim, S.; Nazeeruddin, M. K.; Anta, J. A.; Ahmad, S. Interface Play between Perovskite and Hole Selective Layer on the Performance and Stability of Perovskite Solar Cells. *ACS Appl. Mater. Interfaces* **2016**, *8* (50), 34414–34421. <https://doi.org/10.1021/acsami.6b12236>.
- (201) Kim, H. S.; Seo, J. Y.; Park, N. G. Impact of Selective Contacts on Long-Term Stability of CH₃NH₃PbI₃ Perovskite Solar Cells. *J. Phys. Chem. C* **2016**, *120* (49), 27840–27848. <https://doi.org/10.1021/acs.jpcc.6b09412>.
- (202) Wei, D.; Wang, T.; Ji, J.; Li, M.; Cui, P.; Li, Y.; Li, G.; Mbengue, J. M.; Song, D. Photo-Induced Degradation of Lead Halide Perovskite Solar Cells Caused by the Hole Transport Layer/Metal Electrode Interface. *J. Mater. Chem. A* **2016**, *4* (5), 1991–1998. <https://doi.org/10.1039/c5ta08622a>.
- (203) Domanski, K.; Correa-Baena, J. P.; Mine, N.; Nazeeruddin, M. K.; Abate, A.; Saliba, M.; Tress, W.; Hagfeldt, A.; Grätzel, M. Not All That Glitters Is Gold: Metal-Migration-Induced Degradation in Perovskite Solar Cells. *ACS Nano* **2016**, *10* (6), 6306–6314. <https://doi.org/10.1021/acs.nano.6b02613>.
- (204) Guarnera, S.; Abate, A.; Zhang, W.; Foster, J. M.; Richardson, G.; Petrozza, A.; Snaith, H. J. Improving the Long-Term Stability of Perovskite Solar Cells with a Porous Al₂O₃ Buffer Layer. *J. Phys. Chem. Lett.* **2015**, *6* (3), 432–437.

- <https://doi.org/10.1021/jz502703p>.
- (205) Kim, S.; Bae, S.; Lee, S. W.; Cho, K.; Lee, K. D.; Kim, H.; Park, S.; Kwon, G.; Ahn, S. W.; Lee, H. M.; et al. Relationship between Ion Migration and Interfacial Degradation of CH₃NH₃PbI₃ Perovskite Solar Cells under Thermal Conditions. *Sci. Rep.* **2017**, *7* (1), 1200. <https://doi.org/10.1038/s41598-017-00866-6>.
- (206) Divitini, G.; Cacovich, S.; Matteocci, F.; Cinà, L.; Di Carlo, A.; Ducati, C. In Situ Observation of Heat-Induced Degradation of Perovskite Solar Cells. *Nat. Energy* **2016**, *1* (2), 15012. <https://doi.org/10.1038/NENERGY.2015.12>.
- (207) Li, Z.; Xiao, C.; Yang, Y.; Harvey, S. P.; Kim, D. H.; Christians, J. A.; Yang, M.; Schulz, P.; Nanayakkara, S. U.; Jiang, C. S.; et al. Extrinsic Ion Migration in Perovskite Solar Cells. *Energy Environ. Sci.* **2017**, *10* (5), 1234–1242. <https://doi.org/10.1039/c7ee00358g>.
- (208) Kasparavicius, E.; Magomedov, A.; Malinauskas, T.; Getautis, V. Long-Term Stability of the Oxidized Hole-Transporting Materials Used in Perovskite Solar Cells. *Chem. - A Eur. J.* **2018**, *24* (39), 9910–9918. <https://doi.org/10.1002/chem.201801441>.
- (209) Schloemer, T. H.; Gehan, T. S.; Christians, A.; Mitchell, D. G.; Dixon, A.; Li, Z.; Zhu, K.; Berry, J. J.; Luther, J. M.; Sellinger, A. Thermally Stable Perovskite Solar Cells by Systematic Molecular Design of the Hole-Transport Layer. *ACS Energy Lett.* **2019**, *4* (2), 473–482. <https://doi.org/10.1021/acsenergylett.8b02431>.
- (210) Carrillo, J.; Guerrero, A.; Rahimnejad, S.; Almora, O.; Zarazua, I.; Mas-Marza, E.; Bisquert, J.; Garcia-Belmonte, G. Ionic Reactivity at Contacts and Aging of Methylammonium Lead Triiodide Perovskite Solar Cells. *Adv. Energy Mater.* **2016**, *6* (9), 1502246. <https://doi.org/10.1002/aenm.201502246>.
- (211) Wang, Y.; Yue, Y.; Yang, X.; Han, L. Toward Long-Term Stable and Highly Efficient Perovskite Solar Cells via Effective Charge Transporting Materials. *Adv. Energy Mater.* **2018**, *8* (22), 1800249. <https://doi.org/10.1002/aenm.201800249>.
- (212) Magomedov, A.; Paek, S.; Gratia, P.; Kasparavicius, E.; Daskeviciene, M.; Kamarauskas, E.; Gruodis, A.; Jankauskas, V.; Kantminiene, K.; Cho, K. T.; et al. Diphenylamine-Substituted Carbazole-Based Hole Transporting Materials for Perovskite Solar Cells: Influence of Isomeric Derivatives. *Adv. Funct. Mater.* **2018**, *28* (9), 1704351. <https://doi.org/10.1002/adfm.201704351>.
- (213) García-Benito, I.; Zimmermann, I.; Urieta-Mora, J.; Aragón, J.; Molina-Ontoria, A.; Ortí, E.; Martín, N.; Nazeeruddin, M. K. Isomerism Effect on the Photovoltaic Properties of Benzotrithiophene-Based Hole-Transporting Materials. *J. Mater. Chem. A* **2017**, *5* (18), 8317–8324. <https://doi.org/10.1039/c7ta00997f>.
- (214) Seok, S. Il. O-Methoxy Substituents in Spiro-OMeTAD for Efficient Inorganic–Organic Hybrid Perovskite Solar Cells. *J. Am. Chem. Soc.* **2014**, *136* (22), 7837–7840. <https://doi.org/10.1021/ja502824c>.
- (215) Gao, K.; Xu, B.; Hong, C.; Shi, X.; Liu, H.; Li, X.; Xie, L.; Jen, A. K. Y. Di-Spiro-Based Hole-Transporting Materials for Highly Efficient Perovskite Solar Cells. *Adv.*

- Energy Mater.* **2018**, *8* (22), 1800809. <https://doi.org/10.1002/aenm.201800809>.
- (216) Zhang, J.; Xu, B.; Yang, L.; Ruan, C.; Wang, L.; Liu, P.; Zhang, W.; Vlachopoulos, N.; Kloo, L.; Boschloo, G.; et al. The Importance of Pendant Groups on Triphenylamine-Based Hole Transport Materials for Obtaining Perovskite Solar Cells with over 20% Efficiency. *Adv. Energy Mater.* **2018**, *8* (2), 1701209. <https://doi.org/10.1002/aenm.201701209>.
- (217) Rakstys, K.; Paek, S.; Sohail, M.; Gao, P.; Cho, K. T.; Gratia, P.; Lee, Y.; Dahmen, K. H.; Nazeeruddin, M. K. A Highly Hindered Bithiophene-Functionalized Dispiro-Oxepine Derivative as an Efficient Hole Transporting Material for Perovskite Solar Cells. *J. Mater. Chem. A* **2016**, *4* (47), 18259–18264. <https://doi.org/10.1039/C6TA09028A>.
- (218) Lin, K.; Prlj, A.; Corminboeuf, C. A Rising Star: Truxene as a Promising Hole Transport Material in Perovskite Solar Cells. *J. Phys. Chem. C* **2017**, *121* (39), 21729–21739. <https://doi.org/10.1021/acs.jpcc.7b07355>.
- (219) Lin, K.; Prlj, A.; Corminboeuf, C. How Does Alkyl Chain Length Modify the Properties of Triphenylamine-Based Hole Transport Materials? *J. Mater. Chem. C* **2018**, *6* (5), 960–965. <https://doi.org/10.1039/c7tc05318e>.
- (220) Zhang, M.; Wang, G.; Zhao, D.; Huang, C.; Cao, H.; Chen, M. 3D Hole-Transporting Materials Based on Coplanar Quinolizino Acridine for Highly Efficient Perovskite Solar Cells. *Chem. Sci.* **2017**, *8* (11), 7807–7814. <https://doi.org/10.1039/c7sc03543h>.
- (221) Huang, C.; Fu, W.; Li, C. Z.; Zhang, Z.; Qiu, W.; Shi, M.; Heremans, P.; Jen, A. K. Y.; Chen, H. Dopant-Free Hole-Transporting Material with a C_{3h}Symmetrical Truxene Core for Highly Efficient Perovskite Solar Cells. *J. Am. Chem. Soc.* **2016**, *138* (8), 2528–2531. <https://doi.org/10.1021/jacs.6b00039>.
- (222) Zhang, J.; Xu, B.; Johansson, M. B.; Hadadian, M.; Correa Baena, J. P.; Liu, P.; Hua, Y.; Vlachopoulos, N.; Johansson, E. M. J.; Boschloo, G.; et al. Constructive Effects of Alkyl Chains: A Strategy to Design Simple and Non-Spiro Hole Transporting Materials for High-Efficiency Mixed-Ion Perovskite Solar Cells. *Adv. Energy Mater.* **2016**, *6* (13), 1502536. <https://doi.org/10.1002/aenm.201502536>.
- (223) Abate, A.; Paek, S.; Giordano, F.; Correa-Baena, J. P.; Saliba, M.; Gao, P.; Matsui, T.; Ko, J.; Zakeeruddin, S. M.; Dahmen, K. H.; et al. Silolothiophene-Linked Triphenylamines as Stable Hole Transporting Materials for High Efficiency Perovskite Solar Cells. *Energy Environ. Sci.* **2015**, *8* (10), 2946–2953. <https://doi.org/10.1039/c5ee02014j>.
- (224) Mabrouk, S.; Zhang, M.; Wang, Z.; Liang, M.; Bahrami, B.; Wu, Y.; Wu, J.; Qiao, Q.; Yang, S. Dithieno[3,2-b:2',3'-d] Pyrrole-Based Hole Transport Materials for Perovskite Solar Cells with Efficiencies over 18%. *J. Mater. Chem. A* **2018**, *6* (17), 7950–7958. <https://doi.org/10.1039/c8ta01773e>.
- (225) Wu, Y.; Wang, Z.; Liang, M.; Cheng, H.; Li, M.; Liu, L.; Wang, B.; Wu, J.; Prasad Ghimire, R.; Wang, X.; et al. Influence of Nonfused Cores on the Photovoltaic

- Performance of Linear Triphenylamine-Based Hole-Transporting Materials for Perovskite Solar Cells. *ACS Appl. Mater. Interfaces* **2018**, *10* (21), 17883–17895. <https://doi.org/10.1021/acsmi.8bo2090>.
- (226) Malinauskas, T.; Tomkute-Luksiene, D.; Sens, R.; Daskeviciene, M.; Send, R.; Wonneberger, H.; Jankauskas, V.; Bruder, I.; Getautis, V. Enhancing Thermal Stability and Lifetime of Solid-State Dye-Sensitized Solar Cells via Molecular Engineering of the Hole-Transporting Material Spiro-OMeTAD. *ACS Appl. Mater. Interfaces* **2015**, *7* (21), 11107–11116. <https://doi.org/10.1021/am5090385>.
- (227) Christians, J. A.; Schulz, P.; Tinkham, J. S.; Schloemer, T. H.; Harvey, S. P.; Tremolet De Villers, B. J.; Sellinger, A.; Berry, J. J.; Luther, J. M. Tailored Interfaces of Unencapsulated Perovskite Solar Cells for >1,000 Hour Operational Stability. *Nat. Energy* **2018**, *3* (1), 68–74. <https://doi.org/10.1038/s41560-017-0067-y>.
- (228) Drigo, N. A.; Kudriashova, L. G.; Weissenseel, S.; Sperlich, A.; Huckaba, A. J.; Nazeeruddin, M. K.; Dyakonov, V. Photophysics of Deep Blue Acridane- and Benzonitrile-Based Emitter Employing Thermally Activated Delayed Fluorescence. *J. Phys. Chem. C* **2018**, *122* (39), 22796–22801. <https://doi.org/10.1021/acs.jpcc.8bo8716>.
- (229) Ganesan, P.; Fu, K.; Gao, P.; Raabe, I.; Schenk, K.; Scopelliti, R.; Luo, J.; Wong, L. H.; Grätzel, M.; Nazeeruddin, M. K. A Simple Spiro-Type Hole Transporting Material for Efficient Perovskite Solar Cells. *Energy Environ. Sci.* **2015**, *8* (7), 1986–1991. <https://doi.org/10.1039/c4ee03773a>.
- (230) Lin, K.; Prlj, A.; Yao, L.; Drigo, N.; Cho, H.; Nazeeruddin, M. K.; Sivula, K.; Corminboeuf, C. Multiarm and Substituent Effects on Charge Transport of Organic Hole Transport Materials. *Chem. Mater.* **2019**, *31* (17), 6605–6614. <https://doi.org/10.1021/acs.chemmater.9b00438>.
- (231) Leijtens, T.; Eperon, G. E.; Barker, A. J.; Grancini, G.; Zhang, W.; Ball, J. M.; Srimath, R.; Snaith, J.; Petrozza, A. Environmental Science Carrier Trapping and Recombination: The Role of Defect Physics in Enhancing the Open Circuit Voltage of Metal Halide Perovskite Solar Cells. *Energy Environ. Sci.* **2016**, *9* (11), 3472–3481. <https://doi.org/10.1039/c6ee01729k>.
- (232) Baloch, A. A. B.; Alharbi, F. H.; Grancini, G.; Hossain, M. I.; Nazeeruddin, K.; Tabet, N. Analysis of Photocarrier Dynamics at Interfaces in Perovskite Solar Cells by Time-Resolved Photoluminescence. *J. Phys. Chem. C* **2018**, *122* (47), 26805–26815. <https://doi.org/10.1021/acs.jpcc.8bo7069>.
- (233) Motta, C.; El-mellouhi, F.; Sanvito, S. Charge Carrier Mobility in Hybrid Halide Perovskites. *Sci. Rep.* **2015**, *5*, 12746. <https://doi.org/10.1038/srep12746>.
- (234) Stępien, M.; Gońka, E.; Żyła, M.; Sprutta, N. Heterocyclic Nanographenes and Other Polycyclic Heteroaromatic Compounds: Synthetic Routes, Properties, and Applications. *Chem. Rev.* **2017**, *117* (4), 3479–3716. <https://doi.org/10.1021/acs.chemrev.6b00076>.
- (235) Anthony, J. E. Functionalized Acenes and Heteroacenes for Organic Electronics.

- Chem. Rev.* **2006**, *106* (12), 5028–5048. <https://doi.org/10.1021/cro50966z>.
- (236) Bendikov, M.; Wudl, F.; Perepichka, D. F. Tetrathiafulvalenes, Oligoacenes, and Their Buckminsterfullerene Derivatives: The Brick and Mortar of Organic Electronics. *Chem. Rev.* **2004**, *104* (11), 4891–4945. <https://doi.org/10.1021/cro30666m>.
- (237) Gerson, F.; Basel, U. Fasc. 7 (1983) -. *Helv. Chim. Acta* **1983**, *66* (200), 2031–2043.
- (238) Balli, H. Vol.66,. *Helv. Chim. Acta* **1983**, *66* (210), 2035–2139.
- (239) Kanno, K. I.; Liu, Y.; Iesato, A.; Nakajima, K.; Takahashi, T. Chromium-Mediated Synthesis of Polycyclic Aromatic Compounds from Halobiaryls. *Org. Lett.* **2005**, *7* (24), 5453–5456. <https://doi.org/10.1021/olo52214x>.
- (240) Delcamp, J. H.; Yella, A.; Holcombe, T. W.; Nazeeruddin, M. K.; Grätzel, M. The Molecular Engineering of Organic Sensitizers for Solar-Cell Applications. *Angew. Chemie - Int. Ed.* **2013**, *52* (1), 376–380. <https://doi.org/10.1002/anie.201205007>.
- (241) Dualeh, A.; Humphry-Baker, R.; Delcamp, J. H.; Nazeeruddin, M. K.; Grätzel, M. Solid-State Dye-Sensitized Solar Cells Using a Novel Class of Ullazine Dyes as Sensitizers. *Adv. Energy Mater.* **2013**, *3* (4), 496–504. <https://doi.org/10.1002/aenm.201200701>.
- (242) Feng, J.; Jiao, Y.; Ma, W.; Nazeeruddin, M. K.; Grätzel, M.; Meng, S. First Principles Design of Dye Molecules with Ullazine Donor for Dye Sensitized Solar Cells. *J. Phys. Chem. C* **2013**, *117* (8), 3772–3778. <https://doi.org/10.1021/jp310504n>.
- (243) Ma, W.; Jiao, Y.; Meng, S. Predicting Energy Conversion Efficiency of Dye Solar Cells from First Principles. *J. Phys. Chem. C* **2014**, *118* (30), 16447–16457. <https://doi.org/10.1021/jp410982e>.
- (244) Yang, L.; Li, S.; Li, Z.; Li, Q. Molecular Engineering of Quinoxaline Dyes toward More Efficient Sensitizers for Dye-Sensitized Solar. *RSC Adv.* **2015**, *5* (32), 25079–25088. <https://doi.org/10.1039/C5RA00587F>.
- (245) Mathew, S.; Astani, N. A.; Curchod, B. F. E.; Delcamp, J. H.; Marszalek, M.; Frey, J.; Rothlisberger, U.; Nazeeruddin, M. K.; Grätzel, M. Synthesis, Characterization and Ab Initio Investigation of a Panchromatic Ullazine–Porphyrin Photosensitizer for Dye-Sensitized Solar Cells. *J. Mater. Chem. A* **2016**, *4* (6), 2332–2339. <https://doi.org/10.1039/C5TA08728G>.
- (246) Wan, D.; Li, X.; Jiang, R.; Feng, B.; Lan, J.; Wang, R.; You, J. Palladium-Catalyzed Annulation of Internal Alkynes: Direct Access to π -Conjugated Ullazines. *Org. Lett.* **2016**, *18* (12), 2876–2879. <https://doi.org/10.1021/acs.orglett.6b01182>.
- (247) Ito, S.; Tokimaru, Y.; Nozaki, K. Isoquinolino[4,3,2-de]Phenanthridine: Synthesis and Its Use in 1,3-Dipolar Cycloadditions to Form Nitrogen-Containing Polyaromatic Hydrocarbons. *Chem. Commun.* **2015**, *51* (1), 221–224. <https://doi.org/10.1039/c4cc06643j>.
- (248) Thenarukandiyil, R.; Choudhury, J. Rhodium(III)-Catalyzed Activation and Functionalization of Pyridine C–H Bond by Exploring a Unique Double Role of

- “N-Heterocyclic Carbene–Pyridyl” Ligand Platform. *Organometallics* **2015**, *34* (10), 1890–1897. <https://doi.org/10.1021/acs.organomet.5b00157>.
- (249) Villar, J. M.; Suárez, J.; Varela, J. A.; Saá, C. N-Doped Cationic PAHs by Rh(III)-Catalyzed Double C-H Activation and Annulation of 2-Arylbenzimidazoles with Alkynes. *Org. Lett.* **2017**, *19* (7), 1702–1705. <https://doi.org/10.1021/acs.orglett.7b00478>.
- (250) Boldt, S.; Parpart, S.; Villinger, A.; Ehlers, P.; Langer, P. Synthesis and Properties of Aza-Ullazines. *Angew. Chemie - Int. Ed.* **2017**, *56* (16), 4575–4578. <https://doi.org/10.1002/anie.201701347>.
- (251) Davies, D. L.; Ellul, C. E.; MacGregor, S. A.; McMullin, C. L.; Singh, K. Experimental and DFT Studies Explain Solvent Control of C-h Activation and Product Selectivity in the Rh(III)-Catalyzed Formation of Neutral and Cationic Heterocycles. *J. Am. Chem. Soc.* **2015**, *137* (30), 9659–9669. <https://doi.org/10.1021/jacs.5b04858>.
- (252) Ghorai, D.; Choudhury, J. Rhodium(III)-N-Heterocyclic Carbene-Driven Cascade C-H Activation Catalysis. *ACS Catal.* **2015**, *5* (4), 2692–2696. <https://doi.org/10.1021/acscatal.5b00243>.
- (253) Li, R.; Hu, Y.; Liu, R.; Hu, R.; Li, B.; Wang, B. Ruthenium(II)-Catalyzed Oxidative Annulation Reactions of Arylimidazolium Salts via N-Heterocyclic Carbene-Directed C-H Activation. *Adv. Synth. Catal.* **2015**, *357* (18), 3885–3892. <https://doi.org/10.1002/adsc.201500788>.
- (254) Ge, Q.; Li, B.; Song, H.; Wang, B. Rhodium(III)-Catalyzed Cascade Oxidative Annulation Reactions of Aryl Imidazolium Salts with Alkynes Involving Multiple C–H Bond Activation. *Org. Biomol. Chem.* **2015**, *13* (28), 7695–7710. <https://doi.org/10.1039/C5OB00823A>.
- (255) Berger, R.; Wagner, M.; Feng, X.; Müllen, K. Polycyclic Aromatic Azomethine Ylides: A Unique Entry to Extended Polycyclic Heteroaromatics. *Chem. Sci.* **2015**, *6* (1), 436–441. <https://doi.org/10.1039/C4SC02793K>.
- (256) Ge, Q.; Li, B.; Wang, B. Synthesis of Substituted Benzo[*l*]imidazo[2,1-*b*]quinolizine by Rhodium(III)-Catalyzed Multiple C–H Activation and Annulations. *Org. Biomol. Chem.* **2016**, *14* (5), 1814–1821. <https://doi.org/10.1039/C5OB02515J>.
- (257) Das, A.; Ghosh, I.; König, B. Synthesis of Pyrrolo[1,2-*a*]quinolines and Ullazines by Visible Light Mediated One- and Twofold Annulation of N-Arylpyrroles with Arylalkynes. *Chem. Commun.* **2016**, *52* (56), 8695–8698. <https://doi.org/10.1039/C6CC04366F>.
- (258) Xia, Y. Q.; Dong, L. Ruthenium(II)-Catalyzed Indolo[2,1-*a*]isoquinolines Synthesis by Tandem C-H Allylation and Oxidative Cyclization of 2-Phenylindoles with Allyl Carbonates. *Org. Lett.* **2017**, *19* (9), 2258–2261. <https://doi.org/10.1021/acs.orglett.7b00762>.
- (259) Lim, Y.-K.; Jiang, X.; Bollinger, J. C.; Lee, D. Molecular Engineering of Two-Dimensional Pi-Conjugation: Expected and Unexpected Photophysical

- Consequences of a Simple Particle-in-a-Box Approach. *J. Mater. Chem.* **2007**, *17* (19), 1969–1980. <https://doi.org/10.1039/b617353e>.
- (260) Huckaba, A. J.; Giordano, F.; McNamara, L. E.; Dreux, K. M.; Hammer, N. I.; Tschumper, G. S.; Zakeeruddin, S. M.; Grätzel, M.; Nazeeruddin, M. K.; Delcamp, J. H. Indolizine-Based Donors as Organic Sensitizer Components for Dye-Sensitized Solar Cells. *Adv. Energy Mater.* **2015**, *5* (7), 1401629. <https://doi.org/10.1002/aenm.201401629>.
- (261) Verma, A. K.; Shukla, S. P.; Singh, J.; Rustagi, V. Synthesis of 5-Iodopyrrolo[1,2-a]Quinolines and Indolo[1,2-a]Quinolines via Iodine-Mediated Electrophilic and Regioselective 6-Endo-Dig Ring Closure. **2011**, *76* (14), 5670–5684. <https://doi.org/10.1002/anie.201602491>.
- (262) Fulmer, G. R.; Miller, A. J. M.; Sherden, N. H.; Gottlieb, H. E.; Nudelman, A.; Stoltz, B. M.; Bercaw, J. E.; Goldberg, K. I. NMR Chemical Shifts of Trace Impurities: Common Laboratory Solvents, Organics, and Gases in Deuterated Solvents Relevant to the Organometallic Chemist. *Organometallics* **2010**, *29* (9), 2176–2179. <https://doi.org/10.1021/om100106e>.
- (263) Burfield, D. R.; Smithers, R. H. Desiccant Efficiency in Solvent Drying. 3. Dipolar Aprotic Solvents. *J. Org. Chem.* **1978**, *43* (20), 3966–3968. <https://doi.org/10.1021/jo00414a038>.
- (264) Armarego, W. L. F.; Chai, C. L. L. *Purification of Organic Chemicals*; 2009. <https://doi.org/10.1016/B978-075067571-0/50008-9>.
- (265) Bagriantsev, S. N.; Ang, K. H.; Gallardo-Godoy, A.; Clark, K. A.; Arkin, M. R.; Renslo, A. R.; Minor, D. L. A High-Throughput Functional Screen Identifies Small Molecule Regulators of Temperature- and Mechano-Sensitive K₂Pchannels. *ACS Chem. Biol.* **2013**, *8* (8), 1841–1851. <https://doi.org/10.1021/cb400289x>.
- (266) Zhang, Q.; Kuwabara, H.; Potscavage, W. J.; Huang, S.; Hatae, Y.; Shibata, T.; Adachi, C. Anthraquinone-Based Intramolecular Charge-Transfer Compounds: Computational Molecular Design, Thermally Activated Delayed Fluorescence, and Highly Efficient Red Electroluminescence. *J. Am. Chem. Soc.* **2014**, *136* (52), 18070–18081. <https://doi.org/10.1021/ja510144h>.
- (267) Sheldrick, G. M. SADABS. Program for Empirical Absorption Correction. University of Gottingen 1996.
- (268) Sheldrick, G. M. XPREP. Bruker-AXS: Madison, Wisconsin, USA 2001.
- (269) Sheldrick, G. M. Research Papers SHELXT – Integrated Space-Group and Crystal-Structure Determination Research Papers. *Acta Crystallogr. Sect. A* **2014**, *A71*, 3–8. <https://doi.org/10.1107/S2053273314026370>.
- (270) Sheldrick, G. M. Crystal Structure Refinement with SHELXL. *Acta Crystallogr. Sect. C* **2014**, *C71*, 3–8. <https://doi.org/10.1107/S2053229614024218>.
- (271) Dolomanov, O. V; Bourhis, L. J.; Gildea, R. J.; Howard, J. A. K.; Puschmann, H. OLEX₂: A Complete Structure Solution, Refinement and Analysis Program. *J. Appl. Crystallogr.* **2009**, *42*, 339–341. <https://doi.org/10.1107/S0021889808042726>.

- (272) Grimme, S.; Ehrlich, S.; Goerigk, L. Effect of the Damping Function in Dispersion Corrected Density Functional Theory. *J. Comput. Chem.* **2011**, *32* (7), 1456–1465. <https://doi.org/10.1002/jcc>.
- (273) Frisch, M. J.; Trucks, G. W.; Schlegel, H. B.; Scuseria, G. E.; Robb, M. A.; Cheeseman, J. R.; Scalmani, G.; Barone, V.; Petersson, G. A.; Nakatsuji, H.; et al. Gaussian 16, Revision B.01. Gaussian, Inc: Wallingford CT 2016.
- (274) Martínez, L.; Andrade, R.; Birgin, E. G.; Martínez, J. M. Software News and Update Packmol : A Package for Building Initial Configurations. *J. Comput. Chem.* **2009**, *30* (13), 2157–2164. <https://doi.org/10.1002/jcc>.
- (275) Spoel, D. V. A. N. D. E. R.; Lindahl, E.; Hess, B.; Groenhof, G.; Mark, A. E.; BERENDSEN, H. J. C. GROMACS: Fast, Flexible, and Free. *J. Comput. Chem.* **2005**, *26* (16), 1701–1718. <https://doi.org/10.1002/jcc.20291>.
- (276) Abraham, M. J.; Murtola, T.; Schulz, R.; Pall, S.; Smith, J. C.; Hess, B.; Lindahl, E. GROMACS: High Performance Molecular Simulations through Multi-Level Parallelism from Laptops to Supercomputers. *SoftwareX* **2015**, *1–2*, 19–25. <https://doi.org/10.1016/j.softx.2015.06.001>.
- (277) Wang, J.; Wolf, R. M.; Caldwell, J. W.; Kollman, P. A.; Case, D. A. Development and Testing of a General Amber Force Field. *J. Comput. Chem.* **2004**, *25* (9), 1157–1174.
- (278) Bussi, G.; Donadio, D.; Parrinello, M. Canonical Sampling through Velocity Rescaling. *J. Chem. Phys.* **2007**, *126*, 014101. <https://doi.org/10.1063/1.2408420>.
- (279) Marcus, R. A. Electron Transfer Reactions in Chemistry : Theory and Experiment. *Angew. Chemie - Int. Ed.* **1993**, *32* (8), 1111–1121.
- (280) Victor, R.; Lukyanov, A.; May, F.; Schrader, M.; Veho, T.; Kirkpatrick, J.; Andrienko, D. Microscopic Simulations of Charge Transport in Disordered Organic Semiconductors. *J. Chem. Theory Comput.* **2011**, *7* (10), 3335–3345. <https://doi.org/10.1021/ct200388s>.
- (281) Kirkpatrick, J. An Approximate Method for Calculating Transfer Integrals Based on the ZINDO Hamiltonian. *Int. J. Quantum Chem.* **2008**, *108* (1), 51–56. <https://doi.org/10.1002/qua>.
- (282) Bondi, A. Van Der Waals Volumes and Radii. *J. Phys. Chem.* **1964**, *68* (3), 441–451. <https://doi.org/10.1021/j100785a001>.
- (283) Bäessler, H. Charge Transport in Disordered Organic Photoconductors a Monte Carlo Simulation Study. *Phys. status solidi* **1993**, *175* (1), 15–56.
- (284) Paek, S.; Schouwink, P.; Athanasopoulou, E. N.; Cho, K. T.; Grancini, G.; Lee, Y.; Zhang, Y.; Stellacci, F.; Nazeeruddin, M. K.; Gao, P. From Nano- to Micrometer Scale: The Role of Antisolvent Treatment on High Performance Perovskite Solar Cells. *Chem. Mater.* **2017**, *29* (8), 3490–3498. <https://doi.org/10.1021/acs.chemmater.6b05353>.
- (285) Paek, S.; Qin, P.; Lee, Y.; Cho, K. T.; Gao, P.; Grancini, G.; Oveisi, E.; Gratia, P.;

Rakstys, K.; Al-Muhtaseb, S. A.; et al. Dopant-Free Hole-Transporting Materials for Stable and Efficient Perovskite Solar Cells. *Adv. Mater.* **2017**, *29* (35), 1606555. <https://doi.org/10.1002/adma.201606555>.

CURRICULUM VITAE

Nikita Drigo

📍 CH-1950 Sion, Switzerland
✉ nikita.drigo@epfl.ch
🌐 <https://www.linkedin.com/in/nikita-drigo/>

Date of birth: June 22nd 1993
Nationality: Russian

EDUCATION

- 07.2015 – 12.2019 **PhD in chemistry**
EPFL Valais Wallis
Supervisor: Prof. Mohammad Khaja Nazeeruddin
Thesis: Molecular engineering of functional materials for optoelectronic applications
- 09.2010 – 06.2015 **Specialist in chemistry (equal to MSc)**
Moscow State University
Graduated with distinctions (GPA: 4.82/5.00)
Thesis: Polyfunctional molecular receptors and sensors based on triazole-containing calix[4]arenes

PUBLICATIONS

- 1) **Drigo, N. A.**; Roldán-Carmona, C.; Franckevičius M.; Lin, K.; Gegevičius R.; Kim H.; Schouwink, P. A.; Sutanto A. A.; Olthof S.; Sohail M.; Meerholz K.; Gulbinas V.; Corminboeuf, C.; Paek, S.; Nazeeruddin, M. K. Spirobisacridine hole transporting materials for hysteresis-free and stable perovskite solar cells. *Accepted (J. Am. Chem. Soc., 2019, <https://doi.org/10.1021/jacs.9b07166>)*
- 2) Weißenseel S.*; **Drigo N. A.***; Kudriashova, L. G.; Schmid M.; Morgenstern T.; Lin, K.; Prlj, A.; Corminboeuf, C.; Sperlich, A.; Brütting W.; Nazeeruddin, M. K.; Dyakonov, V. Getting the Right Twist: Influence of Donor–Acceptor Dihedral Angle on Exciton Kinetics and Singlet–Triplet Gap in Deep Blue Thermally Activated Delayed Fluorescence Emitter. *J. Phys. Chem. C* **2019**, 123 (45), 27778-27784. (*Equal contribution with Weißenseel S.)
<https://doi.org/10.1021/acs.jpcc.9b08269>

- 3) **Drigo, N. A.***; Kudriashova, L. G.*; Weissenseel, S.; Sperlich, A.; Huckaba, A. J.; Nazeeruddin, M. K.; Dyakonov, V. Photophysics of Deep Blue Acridane- and Benzonitrile-Based Emitter Employing Thermally Activated Delayed Fluorescence. *J. Phys. Chem. C* **2018**, *122* (39), 22796–22801. (*Equal contribution with Kudriashova, L. G.) <https://doi.org/10.1021/acs.jpcc.8b08716>
- 4) **Drigo, N. A.**; Paek, S.; Huckaba, A. J.; Schouwink, P. A.; Tabet, N.; Nazeeruddin, M. K. Approaches for Selective Synthesis of Ullazine Donor–Acceptor Systems. *Chem. - A Eur. J.* **2017**, *23* (68), 17209–17212. <https://doi.org/10.1002/chem.201704694>
- 5) **Drigo, N. A.**; Gorbunov, A. N.; Gorbunov, D. N.; Talanova, M. Y.; Kardasheva, Y. S.; Kovalev, V. V; Maximov, A. L.; Vatsouro, I. M. Synthesis of Polyfunctional Phosphorus-Containing Calixarenes in Cycloaddition Reactions of Azides to Alkynes. *Chem. Heterocycl. Comp.* **2016**, *52* (12), 1042–1053. <https://doi.org/10.1007/s10593-017-2005-0>
- 6) Lin, K.; Prlj, A.; Yao, L.; **Drigo, N.**; Cho, H.; Nazeeruddin, M. K.; Sivula, K.; Corminboeuf, C. Multiarm and Substituent Effects on Charge Transport of Organic Hole Transport Materials. *Chem. Mater.* **2019**, *31*, (17), 6605-6614. <https://doi.org/10.1021/acs.chemmater.9b00438>
- 7) Xia, R.; Fei, Z.; **Drigo, N.**; Bobbink, F. D.; Huang, Z.; Jasiu, R.; Roldán-carmona, C.; Nazeeruddin, M. K.; Dyson, P. J. Retarding Thermal Degradation in Hybrid Perovskites by Ionic Liquid Additives. *Adv. Funct. Mater.* **2019**, *29*, 1902021. <https://doi.org/10.1002/adfm.201902021>.
- 8) Fedorovskiy, A.E.; **Drigo, N.**; Nazeeruddin, M. K. The role of Goldschmidt's tolerance factor in the formation of A_2BX_6 double halide perovskites and its optimal range. *Small Methods*, **2019**, 1900426. <https://doi.org/10.1002/smt.201900426>
- 9) Sutanto A. A.; **Drigo N.**; Queloz V.I.E.; Garcia-Benito I.; Kirmani A. R., Richter L. J.; Cho K. T.; Nazeeruddin, M. K.; Grancini G. Dynamical Evolution of the 2D/3D Interface: A Hidden Driver behind Perovskite Solar Cell Instability. *Accepted (J. Mater. Chem. A, 2020* <https://doi.org/10.1039/C9TA12489F>).

PRESENTATIONS

- 2019 5th International Conference on Perovskite Solar Cells and Optoelectronics (Poster)
- 2019 Swiss Snow Symposium 2019 (Poster)